



Creating highly entangled states with ultracold bosonic atoms through resonance- and chaos-assisted tunneling

Guillaume VANHAELE

Supervisor:

Peter Schlagheck

Jury:

Arnd Bäcker, TU Dresden, Germany

Srihari Keshavamurthy, IIT Kanpur, India

John Martin, University of Liège, Belgium

Matthieu Verstraete, University of Liège, Belgium (Secretary)

Thierry Bastin, University of Liège, Belgium (President)

Université de Liège
Faculté des Sciences
Département de Physique
Unité de recherche CESAM – IPNAS

A thesis submitted in partial fulfillment of the requirements for
the degree of Doctor in Sciences
October 2021

Copyright © 2021 Guillaume Vanhaele, Université de Liège – Faculté des Sciences, Place du 20 août, 7, B-4000 Liège, Belgique

Tous droits réservés. Aucune partie de ce document ne peut être reproduite sous forme d'imprimé, de photocopie ou par n'importe quels autres moyens, sans l'autorisation écrite de l'auteur ou du promoteur.

All Rights Reserved. No part of this publication may be reproduced in any form by print, photo print or any other means without permission in writing from the author or the supervisor.

Acknowledgments

Before anything else, I would like to thank my supervisor Peter Schlagheck that gave me the opportunity to begin a doctorate. His vast knowing of physics paved the way to me to discover various fields that didn't seem a priori related. Moreover, his profound physical intuition drove me to original discoveries. During these five years of thesis, he devoted a part of his precious time to dispense me valuable advice without which I couldn't have completed my research project.

I thank Arnd Bäcker and Roland Ketzmerick that welcomed me in their research group in TU Dresden for a two-month stay. When I was there, Arnd gave me determinant guidance for the visualization of multiple degree-of-freedom system. He initiated me to his software program built for this purpose, which was necessary to achieve decisive parts of my research. I am also glad to have met Felix Fritzsche and Markus Firmbach. Our frequent discussions during the stay led me to a better understanding of nonlinear physics.

I thank the members of the jury, namely Arnd Bäcker, Srihari Keshavamurthy, John Martin, Matthieu Verstraete and Thierry Bastin, who accepted to evaluate the dissertation and to participate in the defense. I hope that the reading will be sufficiently pleasant and relatively comprehensible.

I also had the chance to supervise lessons for physics and geographic students with Renaud. Our frequent interactions and the pertinence of his points made this supervision an enjoyable moment. Moreover, our tonic debates about physics, among others, have led me to novel and interesting ideas. Even if, unfortunately, its presence in Liège were quite short because of the outbreak, I also met Quirin with which I have shared lively discussions mixing humor and physics. Thomas had the kindness to proofread my manuscript and to make countless pertinent remarks on it. Moreover, we shared inspiring conversations on our respective topics. During my thesis, I shared numerous and animated midday time with Florence, Sébastien, Alexandre, Cyril, Céline, Pierre and Thomas. Each time it was the occasion of lively debates, stimulating discussions on various topics, such as politics, physics, science etc. Even with these seemingly serious subjects, the humor had always its place without altering the depth of these exchanges. I have had also the occasion to share my thought with Sacha and Florian, which have brought me points of view external to my academic field.

I would like to thank also my family, especially my parents, that has given me their support for all these years. Every time I went to see them, they were always very welcoming even when my mood was not at the top.

All these interactions have forged my vision of the world and constitute surely a part of myself.

Belgian F.R.S.-FNRS is gratefully acknowledged. Without their financial support via FNRS aspirant grant, this research project wouldn't have been possible.

Contents

Résumé	v
Abstract	vii
Introduction	1
1 Bose-Einstein condensate in an optical lattice	7
1.1 Bose-Einstein condensation	7
1.2 Optical (super)lattice	12
1.2.1 Interaction between an atom and an electric field	12
1.2.2 Double-well potential	13
1.2.3 Triple-well potential	14
1.3 Bose-Hubbard model	16
1.3.1 Scattering at low energy	16
1.3.2 Derivation of the Bose-Hubbard model via second quantization	17
1.3.3 Bose-Hubbard parameters in the laboratory units	20
1.3.4 Mean-field approximation	22
2 Periodically driven two-site Bose-Hubbard model	27
2.1 Two-site Bose-Hubbard Hamiltonian	27
2.1.1 Discrete symmetry	28
2.1.2 Structure of the spectrum	29
2.1.3 Periodically-driven two-site Bose-Hubbard Hamiltonian	31
2.2 Floquet theory	32
2.3 Floquet theory for a periodic tilting of the double-well potential	34
2.3.1 Discrete symmetry and Floquet matrix	35
2.3.2 Structure of the Floquet spectrum	36
2.4 Coherent renormalization and destruction of tunneling	37
2.4.1 High-frequency regime	37
2.4.2 Low-frequency regime	42

3	Mean-field analysis of the two-site Bose-Hubbard model	45
3.1	Classical limit	45
3.2	Josephson oscillations to self-trapping regime	47
3.3	Phase space and coherent destruction of tunneling	49
3.4	Canonical perturbation theory	51
3.5	Toward mean-field approximation: semiclassical limit	54
3.5.1	Husimi functions	54
3.5.2	N_p as the semiclassical parameter	56
4	NOON states via resonance- and chaos-assisted tunneling	59
4.1	Semiclassical evaluation of the wavefunction	60
4.2	Tunneling rate in integrable systems	62
4.2.1	Size-varying phase space	63
4.2.2	Fixed phase space	65
4.3	Resonance-assisted tunneling	66
4.3.1	Secular perturbation theory	67
4.3.2	Pendulum approximation	69
4.3.3	Quantization of the pendulum Hamiltonian	71
4.3.4	Tunneling rate modification via resonance-assisted tunneling	74
4.3.5	NOON states in near-integrable phase spaces	75
4.3.6	Multiple resonance case	77
4.3.7	Application to the two-site Bose-Hubbard system	77
4.4	Beyond weak perturbations	80
4.4.1	Semiclassical evaluation of the four-level oscillations	86
4.4.2	Improvement of the resonant condition	87
4.5	Resonance- and chaos-assisted tunneling	89
4.5.1	NOON states in mixed phase spaces	89
4.5.2	Modeling of the chaotic sea	93
5	Unperturbed three-site Bose-Hubbard model	99
5.1	Classical limit	100
5.2	Analysis of the phase space	102
5.3	NOON states via resonance-assisted tunneling	106
6	Triple-NOON states via resonance- and chaos-assisted tunneling	111
6.1	Structure of the spectrum	111
6.2	Three-level approximation	113

6.3	Classical limit of the three-site Bose-Hubbard Hamiltonian	115
6.4	Analysis of the phase space	117
6.5	Triple-NOON states in near-integrable phase spaces	121
6.6	Triple-NOON states in mixed phase spaces	122
Conclusion		127
A Floquet theory and two-site Bose-Hubbard Hamiltonian		131
A.1	General solutions of Floquet systems	131
A.2	Two-site Bose-Hubbard Hamiltonian in the Fock basis	132
A.2.1	Measurement	132
A.2.2	Average of the measurements	133
A.3	Two-site Bose-Hubbard Hamiltonian in the symmetry-adapted basis	134
A.3.1	N_p odd	135
A.3.2	N_p even	135
A.3.3	Measurement	136
A.3.4	Average of the measurements	137
B Monodromy matrix		139
C Two-level approximation		141
D Matrix representation of the unperturbed three-site Bose-Hubbard Hamiltonian		143
Bibliography		147

Résumé

Cette thèse de doctorat investigate d'un point de vue théorique la génération d'états intriqués avec des atomes bosoniques ultrafroids. Elle se focalise plus spécifiquement sur les états NOON dans un double puits de potentiel, qui représentent la superposition cohérente et équivalente de $|N, 0\rangle$ et $|0, N\rangle$ avec N atomes, et également sur les états triple-NOON dans un piège optique à trois sites, qui représentent la superposition cohérente et équivalente de $|N, 0, 0\rangle$, $|0, N, 0\rangle$ et $|0, 0, N\rangle$. Ces états peuvent être vus comme des manifestations à larges échelles de l'intrication quantique. L'effet tunnel collectif des atomes dans le régime d'auto-piégeage est rendu possible par les interactions atome-atome. Par exemple, l'état NOON est formé après la moitié du temps d'effet tunnel, c'est-à-dire le temps nécessaire pour obtenir un transfert total des atomes vers l'autre site. Le message principal que ce document voudrait faire passer est que l'échelle de temps requise pour générer cette transition peut être considérablement réduite via une perturbation périodique externe sans modifier qualitativement la dynamique quantique. De plus, des indications de cette réduction sont clairement visible dans l'espace des phases correspondant. La présence de résonances non-linéaires au niveau classique induit des couplages perturbatifs au niveau quantique. Il en résulte une réorganisation du spectre quantique qui permet d'expliquer la modification du temps d'effet tunnel. Ces modifications peuvent aussi être produites par une proéminente mer chaotique connue pour accueillir des états fortement connectés. Bâtie sur les caractéristiques de l'espace des phases, l'effet tunnel assisté par résonance et par chaos est une théorie semiclassique qui peut être utilisée comme un guide dans la quête des paramètres idoines.

Abstract

The present dissertation theoretically investigates the generation of entangled states with ultracold bosonic atoms. Specifically, that focuses on the NOON states in a double-well potential, which are the coherent and equivalent superposition of $|N, 0\rangle$ and $|0, N\rangle$ with N atoms, and on the triple-NOON states in a three-site optical trap, which are the coherent and equivalent superposition of $|N, 0, 0\rangle$, $|0, N, 0\rangle$ and $|0, 0, N\rangle$. These states can be seen as large manifestations of entanglement. The collective tunneling in the self-trapping regime is made possible by the atom-atom interactions. For example, the NOON state is formed after half the tunneling time, i.e. the time needed to obtain a total transfer of population to the other site. The main message of this dissertation is that the timescale required to generate this transition can be considerably reduced by means of an external periodic driving without qualitatively altering the quantum dynamics. Moreover, indications of this speedup are available in the corresponding classical phase space. The presence of nonlinear resonances at the classical level induces perturbative couplings at the quantum level. The subsequent reorganization of the eigenspectrum enables one to explain the modifications of the tunneling time. These modifications can also be produced by prominent chaotic layer known to welcome strongly connected states. Built upon the phase space features, resonance- and chaos-assisted tunneling is a semiclassical theory which can be used as a guideline in the quest of suitable parameters.

Introduction

Entanglement is an astonishing manifestation of quantum mechanics. This very counterintuitive phenomenon mainly takes place at the microscopic level. If two particles are entangled, it means that a measurement of one of them projects the other one on a specific state depending on the result of this measurement. Quite surprisingly, this phenomenon is non-local, meaning that this interaction is instantaneous and doesn't depend on the distance between the two particles. To take the measure of how strange the entanglement is, some well-known physicists were doubtful about this phenomenon, like Einstein who called this non-local interaction a "spooky action at distance" [1]. Instead of assuming that there exist instantaneous interactions between particles, one can imagine the existence of hidden variables. These are related to a lack of knowledge of the underlying mechanisms at stake with entanglement and even with the superposition of states. This was the idea of the Einstein-Podolsky-Rosen (EPR) paradox formulated in 1935 [2]. Nevertheless, the experiments of Freedman and Clauser in 1972 [3] and Aspect in 1981 [4] demonstrated the non-local behavior of entangled photons. These experiments were based on that of Kocher and Commins realized in 1967 [5] and confirmed the phenomenon of non-locality through the violation of the Bell inequalities [6]. Moreover, entanglement has been experimentally demonstrated in various systems including electrons separated by 1.3 km [7], an atom and a molecule [8], and macroscopic diamonds [9], to mention some examples.

In practice, we have no intuition of entanglement at the macroscopic level. An open question is the realization of this phenomenon at larger scale. For instance, two spatially separated millimeter-sized diamonds have been entangled in some of their vibrational states [9]. This kind of entanglement is giant in a sense that the material supports, namely the diamonds, are macroscopic. Another kind of giant entangled state is built when the number of entangled quanta is significant. This is the case of the NOON states, where two bosonic modes are entangled in such a way that one of them is totally full with N quanta while the other one is empty. It has been experimentally demonstrated in bosonic systems using photons [10, 11] and phonons [12], for example.

This dissertation theoretically investigates the generation of entangled states with a Bose-Einstein condensate by focusing on large entanglement. A Bose-Einstein condensate is in general made of ultracold atoms. It can be seen as a new state of matter which behaves like a coherent wave. From an experimental point of view, this coherent matter wave can have a macroscopic scale with a spatial extension of the order of a millimeter [13, 14]. Historically, Bose-Einstein condensation was theoretically predicted in 1924-1925 by Einstein [15, 16] in the wake of the work of Bose on photons published in 1924 [17]. Seventy years later, the first experimental realizations were performed with the atomic species ^{87}Rb in the Wieman and Cornell group [13] and with ^{23}Na in the Ketterle group [14]. Section 1.1 will give a general overview about the different experimental realizations of the Bose-Einstein condensation by emphasizing the typical length, temperature and density scales.

Optical lattices

Once a Bose-Einstein condensate is created, it can be loaded in a periodic configuration of potential wells, which can be generated by an optical lattice [18, 19]. With this potential, it becomes possible to conceive protocols to entangle the spatially separated parts of the ultracold gas. Contrary to laser cooling based on cycles of absorption-spontaneous emission of photons by the atom, an optical lattice is made of lasers where frequencies are sufficiently detuned away from an atomic transition in order to avoid these cycles, but sufficiently close to this transition to modify substantially the ground state energy of the atoms [20]. This leads to a spatially periodic trapping of the Bose-Einstein condensate. The lattice parameters, such as for example the laser intensities, determine the coupling between wells and the degree of confinement of the atoms on a site. An additional harmonic trap can produce a dimer [21]. An alternative is based on the superlattice techniques where the multiple periodicities of the lattice can lead to, for example, dimers or trimers relatively well separated from each other [22–24]. In this context, it is possible to conceive a spatial entanglement between the different sites of the dimer or the trimer in which the Bose-Einstein condensate is trapped.

Historically, the Hubbard model was introduced in order to model interacting electrons in a solid [25]. Like a crystal, the optical lattice is a periodic potential. In the crystal, the electrons are trapped by the electromagnetic potential produced by the spatially periodic atomic nuclei while, in the optical lattice, the atoms are trapped because of the laser fields. That is why the Hubbard model was adapted to describe spinless interaction atoms, leading to the Bose-Hubbard model [26, 27]. This model is able to explain the quantum phase transition at zero temperature between the superfluid phase to the Mott-insulator phase [27–29]. Thus, there is an analogy between the optical lattice and the crystal and between the ultracold atoms and the electrons. Nevertheless, the scales are very different. The temperature scale is $1\ \mu\text{K}$ for the optical lattice compared to $10^4\ \text{K}$ for solid, the mass scale is $10^{-25}\ \text{kg}$ for an atom and $9.1 \times 10^{-31}\ \text{kg}$ for an electron. The lattice spacing is typically $500\ \text{nm}$ for an optical lattice compared to $0.1\ \text{nm}$ for a crystal. Moreover, the optical lattices are easily controllable by means of the intensities and the wavelengths of the lasers, and they present almost no defect which constitutes an asset over crystals.

NOON states

Entangled states are very fragile, which explains why it is almost impossible (for the moment) to observe them at the mesoscopic or macroscopic scale. The NOON states are a specific class of entangled states. They are made of two bosonic modes where one of them is totally full of N quanta while the other is empty. The NOON state made up of the two quantum states $|N, 0\rangle$ and $|0, N\rangle$ can be written as

$$|\text{NOON}\rangle = e^{i\varphi_1}|N, 0\rangle + e^{i\varphi_2}|0, N\rangle. \quad (0.0.1)$$

This kind of state becomes more and more impressive as the number of quanta increases. Indeed, if N is sufficiently large, it could potentially lead to a mesoscopic manifestation of entanglement. The usefulness of this state is related to the field of quantum metrology [30, 31]. Although the NOON states are very unstable toward any interaction with the environment, they have been experimentally observed with the nuclear spins of a molecule [32], with two optical paths of photons [10], with the two polarization states of photons [11], with qubits in superconducting circuits [33], and with phonons in ions traps [12].

When describing Bose-Einstein condensation, the atom-atom interactions must in general be taken into account. These interactions are far from being a nuisance as they allow one to conceive protocols for the generation of entangled states that are based on the internal dynamics of the ultracold atoms. Several proposals have been made to build a NOON state with a Bose-Einstein condensate. With attractive ultracold atoms, the NOON state is the ground state. In this context, it could be possible to build it by adiabatically decreasing the hopping between both modes [34]. Nevertheless, two problems arise. As it is the ground state, it requires very low temperature to reach that. Moreover, an attractive condensate is unstable as it can collapse on itself [35], and the contraction on itself [36] leads to the proliferation of inelastic scattering [37]. That is why several other proposals have been made for repulsive condensates, based on the dynamical redistribution of atoms after applying a suitable phase shift [38–44]. The NOON state could also be produced by some specific measurement processes [45–47], via an adiabatic passage from an excited state [48], with a two-component Bose-Einstein condensate in a double-well potential [49] or via the scattering of solitonic wave packet [50, 51].

The idea proposed in our work [52] consists in loading all atoms on any site of a symmetric double-well potential. At the transition time, all atoms tunnel to the other site. At half this waiting time, called the NOON time, the large coherent superposition of states, i.e. the NOON state, is obtained. This can be achieved in the self-trapping regime [21, 53–61] where the effective on-site interaction energy is much larger than the coupling between both parts of the dimer. In this regime, the atoms tunnel collectively and not individually. This phenomenon is due to the mismatch of the chemical potentials in the two wells. Besides the need of a perfect symmetry, the problem in collective tunneling is the extremely long timescale required [62]. Moreover, this time increases with the population imbalance, which makes it more complicated to reach entanglement at a mesoscopic scale.

Resonance- and chaos-assisted tunneling

We claim that it is possible to speed up the production of the NOON states by means of an additional periodic modulation of the double-well potential [63, 64]. This modulation is expected to modify significantly the NOON time for some parameters. The Bose-Hubbard model describes from a pure quantum point of view the dynamics of ultracold atoms trapped in an optical lattice. As this model focuses on spinless particles, one can define a classical counterpart as shown in Sec. 1.3.4. An appealing idea is to use the related classical dynamics as a guideline for the choice of suitable driving parameters. The purpose is to build nonlinear resonances [65, 66] in the phase space via the periodic driving. A nonlinear resonance induces perturbative couplings of the states $|N, 0\rangle$ and $|0, N\rangle$ with other states $|n_1, n_2\rangle$. These couplings can lead to a reduction of the NOON time by several orders of magnitude via the phenomenon of resonance-assisted tunneling [67–71] valid for near-integrable systems. In the framework of this theory, the NOON time τ can be semiclassically evaluated in terms of the energies $\epsilon_q^{(0)}$ of the unperturbed system and the corresponding unperturbed entanglement times $\tau_q^{(0)}$, i.e. the times required to produce perfectly balanced entangled states between $|n_1, n_2\rangle$ and $|n_2, n_1\rangle$. For a one-step process, it reads

$$\tau \sim \frac{\epsilon_n^{(0)} - \epsilon_m^{(0)} - l\hbar\omega}{A} \tau_m^{(0)}, \quad (0.0.2)$$

where n is an integer labeling the NOON state, m and l are integers depending, among others, on the rank of the nonlinear resonance. Here ω is the frequency of the periodic

perturbation and A depends on the characteristics of the resonance, such as its size in phase space.

The perturbed NOON time is evaluated by means of the unperturbed parameters, using standard perturbation theory. What is remarkable with Eq. (0.0.2) is that its evaluation can be performed exclusively with the characteristics of the underlying classical dynamics. The constant A depends only on the phase-space features of the resonance [67, 68], the unperturbed energies can be evaluated by means of the canonical perturbation theory [66], and the unperturbed entanglement times by means of analytic continuations of the phase-space tori in the complex domain [68, 72].

The transition related to the NOON state can also be sped up by means of a prominent layer of chaotic motion in the phase space. The perturbative couplings of the regular $|N, 0\rangle$ and $|0, N\rangle$ states to the strongly connected chaotic states lead to the phenomenon of chaos-assisted tunneling [73–77]. In the framework of this theory, the NOON time is determined by means of the coupling V to the chaotic sea,

$$\tau \sim \frac{1}{V^2}. \quad (0.0.3)$$

Both phenomena can be combined in order to obtain the semiclassical theory of resonance- and chaos-assisted tunneling [71, 72, 78–83]. In this theory, the coupling to the chaotic sea in Eq. (0.0.3) becomes an effective coupling taking into account the contributions of the different resonance paths.

Due to the particle conservation, the classical counterpart of the driven two-site Bose-Hubbard model is an effective periodically driven one degree-of-freedom system, such that the phase space has two dimensions. Resonance-assisted tunneling has been extensively studied for this kind of low-dimensional system. In the near-integrable regime, it was applied to the kicked Harper model [67, 68] and in deformed optical microcavities [70, 71], for example. In the mixed regime, i.e. the regime where there is a coexistence between regular and chaotic trajectories in the phase space, it was applied to molecular systems [69], the kicked Harper model [79], the periodically-driven pendulum [84], the standard map [72, 81–83] and optical microcavities [71, 80].

Resonance-assisted tunneling in high-dimensional systems

Concerning the classical counterpart of the three-site Bose-Hubbard model, the phase space has four dimensions as it is an effective periodically-perturbed two degree-of-freedom system. In this context, some complications arise due to additional connections between different parts of the phase space. Even if it is no longer possible to have a global visualization of the dynamics by means of a 2D plane, the phase space can still be visualized by slicing the 4D phase space to extract a 3D subspace [85, 86]. The 3D phase space slices can be obtained by projecting the orbits (q_1, q_2, p_1, p_2) on a 2ε width around an arbitrary point \bar{p}_2 ,

$$\{(q_1, q_2, p_1, p_2) \mid |p_2 - \bar{p}_2| \leq \varepsilon\}. \quad (0.0.4)$$

Indeed, before studying resonance- and chaos-assisted tunneling, it is valuable to know which regions in phase space are chaotic and which tori are still preserved. Moreover, the set of resonances, called the Arnold web, must be known in order to determine which perturbative couplings are dominant. The Arnold web can be computed through frequency-analysis techniques, and it has been applied, for example, in the case of two coupled standard maps [85, 86].

In the case of a 4D phase space with a periodic perturbation (meaning that stroboscopic sections must be done to obtain the 4D space), the resonance lines $k_0:k_1:m$, coming from the destruction of an ensemble of tori, are given by [87]

$$k_0\Omega_0 + k_1\Omega_1 = m\omega, \quad (0.0.5)$$

where (Ω_0, Ω_1) are the frequencies of the tori and ω is the external frequency. Here k_0, k_1 and m are integers of which at least one of them is non-zero. Equation (0.0.5) determines the set of resonances. With the Arnold web, resonance-assisted tunneling has been studied in a three degree-of-freedom Hamiltonian [88]. Another technique to compute the Arnold web is called the fast Lyapunov indicator [89, 90]. With this kind of technique, resonance- and chaos-assisted tunneling has been studied in high-dimensional molecular systems in the context of intramolecular vibrational energy redistribution [91–93] or in a three-site Bose-Hubbard model weakly coupled with an additional fourth site [94]. In Ref. [95], resonance-assisted tunneling mechanisms were investigated in four-dimensional normal-form Hamiltonians. As these latter Hamiltonians are time independent, it is possible to perform 3D slices for $\varepsilon = 0$.

Except for the work cited above, resonance- and chaos-assisted tunneling has not yet been studied much for high-dimensional systems. We will add our contribution to this research field by studying this phenomenon for the three-site Bose-Hubbard model by focusing on the effect of an external driving on tunneling.

Triple-NOON states

In a three-site Bose-Hubbard model, a natural way to study entanglement is by introducing three modes. From a general point of view, a triple-NOON state is an entangled state where one mode is totally populated with N quanta while the other ones are empty. It is formally written as

$$|\text{t-NOON}\rangle = e^{i\varphi_1}|N, 0, 0\rangle + e^{i\varphi_2}|0, N, 0\rangle + e^{i\varphi_3}|0, 0, N\rangle. \quad (0.0.6)$$

In the specific case of the trimer, the N quanta are assimilated to the total number of particles and a measurement of the system will give an equal probability to obtain all particles on one of the three sites.

Few proposals have been made for realizing this kind of state with a Bose-Einstein condensate confined on three sites. In Ref. [96], it was proposed to produce the triple-NOON state by an adiabatic decrease of the coupling between sites. This protocol is possible with an attractive condensate for which the triple-NOON state is the ground state. Nevertheless, the same problems arise as for the double-NOON state case, namely the potential collapse of the condensate on itself [35] and the extremely low temperatures and slow parameter variations required.

Our proposal here is the same as for the NOON states in a dimer. All atoms are loaded on one of the three sites of the symmetric optical trap, and the triple-NOON state is generated after the triple-NOON time. This protocol must be performed in the self-trapping regime where the strong effective on-site interactions force the atoms to tunnel as a whole. Nevertheless, the time required to observe such a transition is prohibitively long. The idea is then to add a periodic perturbation of the trimer which preserves its symmetry. In this context, nonlinear resonances and chaos are produced by the periodic driving in the related classical phase space. From resonance and chaos-assisted tunneling theory, these phase space modifications are expected to reduce by several orders of magnitude the NOON time. Thus,

the classical counterpart of the three-site Bose-Hubbard model is used as a guideline in the quest of suitable parameters.

Outline of the chapters

Chapter 1 is devoted to the general Bose-Hubbard model describing a Bose-Einstein condensate trapped in an optical lattice. This model can be derived through second quantization procedure, and when the total number of particles is pretty high, the classical limit is enough to capture the features of the dynamics. The beginning of this chapter gives a general overview about the experiments related to the Bose-Einstein condensation as well as the typical length, temperature, and density scales.

Chapter 2 is devoted to the two-site Bose-Hubbard model. It focuses on the case of weak coupling between sites for which the spectrum displays a doublet structure. The addition of a periodic tilting of the double-well potential can be dealt with within Floquet theory. At the end of this chapter, it is shown how it is feasible to prevent the formation of an entangled state by means of a periodic perturbation.

Chapter 3 introduces the classical counterpart of the two-site Bose-Hubbard model. While the mean-field approximation is not able to explain the formation of entangled states, some features of the dynamics can still be captured with this model, namely the self-trapping dynamics and the Josephson oscillations. These two qualitatively different dynamics are displayed through the phase space for which the canonical perturbation theory is applied in order to obtain an analytical approximation of its structure.

Chapter 4 introduces the notion of NOON state in the two-site Bose-Hubbard model. As the unperturbed two-site Bose-Hubbard model is integrable, the tunneling rate (the inverse of the NOON time) is expected to decrease exponentially with the semiclassical parameter, i.e. the total number of particles as shown in Secs. 3.5.2 and 4.1. With the periodic driving, chaos and nonlinear resonances arise in the phases space. The semiclassical theory of resonance- and chaos-assisted tunneling is developed by highlighting the mechanisms that boost the NOON state production.

Chapter 5 is devoted to the production of NOON states in the unperturbed three-site Bose-Hubbard model. The 3D slices of a 4D phase space enable one to obtain a global visualization of the classical dynamics. The non-congruent third site introduces new resonance channels clearly visible in phase space leading to the speedup of the NOON-state production.

Chapter 6 introduces the notion of triple-NOON state in the symmetric three-site Bose-Hubbard model. A part of its spectrum displays a triplet organization for which the three-level approximation is valid in the weak coupling regime. An additional periodic driving preserving the symmetries of the system can lead to substantial decrease of the triple-NOON time through resonance- and chaos-assisted tunneling mechanisms.

Chapter 1

Bose-Einstein condensate in an optical lattice

The experiments and the typical orders of magnitude related to Bose-Einstein condensation are presented at the beginning of this chapter. It is possible to trap a Bose-Einstein condensate in an optical lattice, which produces spatial separations of its different parts enabling one to develop protocols for entanglement. Historically, the introduction of the Hubbard model was motivated by the study of interacting electrons in a solid [25]. The Bose-Hubbard model was developed in order to describe interacting ultracold atoms trapped in a periodic potential [27–29]. This periodic potential, called an optical lattice, can be produced by lasers whose frequency is slightly detuned from an atomic transition. The subsequent modifications of the ground state energy lead to a periodic lattice of sites [18–20]. The addition of a harmonic confinement is able to produce, for example, a two-site optical trap [21]. An alternative is the superlattices which are optical lattices characterized by different periodicities. This can produce dimers or trimers well separated from each other [22–24].

The Bose-Hubbard model is one of the simplest model describing interacting ultracold atoms trapped in a periodic potential. As the gas is very dilute, only the two-atom interaction is taken into account while the three-body collisions are neglected. The assumption of a dilute gas also allows one to model the atom-atom interaction by a two-atom contact potential. Moreover, the combination of a low temperature gas with a deep optical-lattice potential enables one to only consider the first energy band of the system.

1.1 Bose-Einstein condensation

In 1905, Einstein describes the photoelectric effect by assuming that light behaves not only like a wave but is made of particles called photons [97]. Conversely, de Broglie postulated in 1924 in his well-known thesis [98] that matter presents also a wave behavior. This leads to the concept of wave-particle duality for which each particle is characterized by a wavelength given by $\lambda_{\text{dB}} = h/p$, where h is the Planck constant and p is the momentum of the particle. This theory was able to explain the experiment of Davisson and Germer conducted in 1927 concerning the diffraction of electrons through a crystal [99, 100]. Based on the work of de Broglie, Schrödinger proposed in 1926 the eponymous equation describing the wave behavior of massive particles in the context of the first quantization [101].

There are two classes of quantum particles, namely the bosons and the fermions. The former are described by a totally symmetric wave function while the latter by a totally anti-

symmetric wave function. It means that the permutation between two identical particles in the wave function $\psi(\mathbf{r}_1, \mathbf{r}_2, \dots, \mathbf{r}_N)$ describing N particles leads to a prefactor ± 1 , respectively, in the symmetric and antisymmetric case. By assuming that \mathbf{r}_l is the position of the particle l (which takes into account its possible spin), this condition leads to

$$\psi(\mathbf{r}_1, \dots, \mathbf{r}_i, \dots, \mathbf{r}_j, \dots, \mathbf{r}_N) = \pm \psi(\mathbf{r}_1, \dots, \mathbf{r}_j, \dots, \mathbf{r}_i, \dots, \mathbf{r}_N). \quad (1.1.1)$$

This matter property leads to the fact that two fermions cannot share the same position with the same spin. In other terms, the exclusion principle stipulates that two fermions cannot occupy the same quantum state.

In practice, an ensemble of particles that are sufficiently far from each other can be described without introducing a common wave function and the wave functions of the particles can be treated separately. The de Broglie wavelength λ_{dB} gives a measure of the spatial extension of a particle of mass m at the temperature T ,

$$\lambda_{dB} = \sqrt{\frac{2\pi\hbar^2}{mk_B T}}. \quad (1.1.2)$$

At high temperature, the typical particle interdistance is very large in comparison to the de Broglie wavelength. This condition, which can be formally written as $\lambda_{dB} \ll (V/N)^{1/3}$ with V the volume, is fulfilled in a gas for normal temperature and pressure. Thus, the particles can be seen as points and the Maxwell-Boltzmann distribution is applicable. At low temperature, the wave spatial extensions of particles begin to overlap and the quantum properties of matter must be taken into account. For a de Broglie wavelength reaching the particle interdistance such that

$$\lambda_{dB} \gtrsim \left(\frac{V}{N}\right)^{1/3}, \quad (1.1.3)$$

the Maxwell-Boltzmann distribution must be replaced by the either Bose-Einstein distribution in the bosononic case or the Fermi-Dirac distribution in the fermionic case.

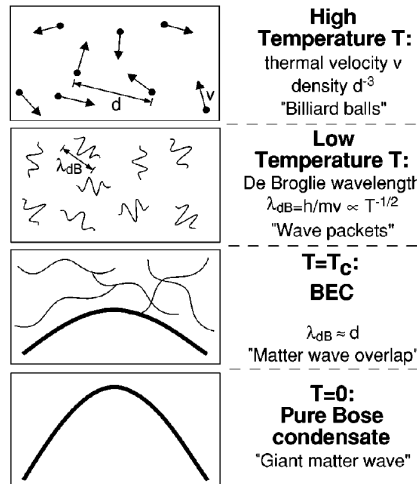


Figure 1.1.1: Sketch of the Bose-Einstein condensation that takes place when the wave spatial extensions of the bosonic particles are sufficiently overlapped. The Bose-Einstein condensate is a wave manifestation of matter that appears at low temperature. This image comes from Ref. [102].

In an ideal bosonic gas, the Bose-Einstein distribution gives the mean number of occupations $\langle n_k \rangle$ of the energy level ϵ_k , which is controlled by the temperature T and the chemical potential μ ,

$$\langle n_k \rangle = \frac{1}{\exp\left(\frac{\epsilon_k - \mu}{k_B T}\right) - 1}. \quad (1.1.4)$$

Unlike fermions, several bosons can occupy the same quantum state. This means that for low temperature, an important part of the particles occupies the ground state energy ϵ_0 . Moreover, as the temperature decreases the chemical potential tends to reach ϵ_0 , and a singularity arises at the critical temperature T_c . For $\mu \rightarrow \epsilon_0$, the occupancy of the ground state begins to diverge. This is the signature of the Bose-Einstein condensation. In this context, the particles lose their individuality and condense into the ground state to form a giant coherent matter wave as illustrated in Fig. 1.1.1.

The first Bose-Einstein condensates were realized in 1995 with a ^{87}Rb cloud of 2×10^4 atoms characterized by a density of $2.6 \times 10^{12} \text{ cm}^{-3}$ and a temperature of 170 nK [13] as well as a ^{23}Na cloud of 5×10^5 atoms characterized by a density of 10^{14} cm^{-3} and a temperature of 2 nK [14]. The same year, indirect evidence was also obtained for the atomic species ^7Li [103]. Other condensates have also been obtained for the spin-polarized hydrogen [104], for the ^4He in a metastable state [105] and for the species ^{41}K [106], to mention some examples. The alkalis are an interesting class of atoms for experimental construction of a Bose-Einstein condensate. Indeed, they display one valence electron whose magnetic moment of spin can interact with an external magnetic field leading to the possibility to realize a Ioffe-Pritchard trap [20]. This electron can be treated to a certain measure independently of the filled electronic inner shells. Moreover, these atoms have in general an optical transition in the visible or in the infrared, i.e. the range in which lasers are available for optical traps. For instance, some intra-atomic transitions from the electronic ground state exploitable for cooling are given by roughly 780 nm for Rubidium [13] or 671 nm for Lithium [103].

A Bose-Einstein condensate is obtained by means of a dilute gas of ultracold particles. The fact of being dilute prevents the phase change toward the liquid or solid configuration even at small temperature. The typical particle density of an ultracold atomic gas amounts to 10^{13} – 10^{15} cm^{-3} . To compare, the density of molecules in the air at room temperature is about 10^{19} cm^{-3} , about 10^{22} cm^{-3} for liquid and solid while it amounts to 10^{38} cm^{-3} for nucleons in atomic nuclei.

Bose-Einstein condensates are obtained for temperature scales below $10 \mu\text{K}$. Before reaching condensation, the standard technique is first to use laser cooling to trap an atomic cloud. The laser cooling refers to the trapping techniques based on cycles of absorption of a photon by an atom and spontaneous emission [20] which enables one to reach temperature of roughly $10 \mu\text{K}$. Unfortunately, this temperature is not enough to produce a Bose-Einstein condensate. That is why a second step is needed, which consists in the evaporative cooling. This cooling technique is used after turning off the lasers by replacing them by a purely magnetic trap. Then, the more energetic atoms are removed from the trap by means of radio-frequency radiations [20]. This enables one to reach temperature below $10 \mu\text{K}$. To compare, the quantum effect related to electrons in a metal is below the Fermi temperature, i.e. below 10^4 – 10^5 K in general, and for the phonons in a solid, it is below the Debye temperature i.e. below 10^2 K . The superfluidity of the ^4He is obtained for roughly 1 K , and the degeneracy temperature for the atomic nuclei is roughly 10^{11} K owing to their higher density.

Below a certain critical temperature T_c , the atoms condense in the ground state and form a coherent matter wave. By treating correctly the divergence when the chemical potential tends to the ground state energy, the evaluation of $N = \sum_k \langle n_k \rangle$ in a non-interacting bosonic gas leads to the condensed population [20, 107],

$$N_0 = N \left(1 - \left(\frac{T}{T_c} \right)^\alpha \right). \quad (1.1.5)$$

In 3D without an external trapping, we have $\alpha = 3/2$, and the critical temperature reads

$$T_c = \frac{2\pi\hbar^2}{mk_B} \left(\frac{N}{V\zeta(3/2)} \right)^{2/3}. \quad (1.1.6)$$

Here $\zeta(x)$ is the Riemann zeta function for which $\zeta(3/2) \simeq 2.612$. The evaporative cooling that enables one to reach the Bose-Einstein condensation consists in removing the more energetic atoms. The subsequent decrease of the atomic density N/V implies a decrease of the critical temperature. This contradictory effect required an atomic cloud that is sufficiently dense before performing the evaporative cooling in order to produce a Bose-Einstein condensate. For the first realization of a Bose-Einstein condensate in the Cornell and Wieman experiment [13], Eq. (1.1.6) leads to $T_c \approx 35$ nK and $\lambda_{dB}(T_c) \approx 1 \mu\text{m}$ knowing that the cloud density is $2.6 \times 10^{12} \text{ cm}^{-3}$ and the mass of ^{87}Rb is $m = 1.443 \times 10^{-25} \text{ kg}$.

In the case of a 3D harmonic trapping $m\omega^2(x^2 + y^2 + z^2)/2$, which is closer to the experimental context, the critical temperature reads [20, 107]

$$T_c = \frac{\hbar\omega}{k_B} \left(\frac{N}{\zeta(3)} \right)^{1/3}, \quad (1.1.7)$$

with $\alpha = 3$. Equation (1.1.7) is obtained with the assumption $k_B T \gg \hbar\omega$, meaning that the typical energy scale related to the temperature is larger than the typical distance between the levels in the discrete spectrum. Equation (1.1.7) becomes then valid for $N \gg 1$. In a typical experiment, the atomic cloud is composed of $N \sim 10^5$ particles and the frequency trap amounts to $\omega \sim 10^4 \text{ s}^{-1}$. These values correspond to $\hbar\omega/k_B$ of few nK and $T_c \sim 10^2 \text{ nK}$, which is the typical critical temperature for the condensation of an ultracold atomic cloud.

Because the fermions are subjected to the Pauli exclusion principle, it is not possible to perform a Bose-Einstein condensate with the fermionic atomic species. Nevertheless, the combination of two fermionic atoms leads to a bosonic molecule. The first realization of Bose-Einstein condensates with molecules were performed with $^{40}\text{K}_2$ [108] and with $^6\text{Li}_2$ [109, 110]. On the other hand, the ultracold properties of fermionic atoms can also be studied. In this context, it is possible to build a degenerate fermionic gas. The Fermi pressure resulting from the exclusion principle tends to induce a broader spatial extension of the fermionic atomic cloud than the one of a bosonic atomic cloud [111]. The same phenomenon avoids, at another length and density scale, the gravitational collapse of a white dwarf or a neutron star into a black hole [111, 112]. The Fermi degeneracy was observed for the first time in gas of ^{40}K where two hyperfine states were represented [113, 114] and in a gas mixing two isotopes of lithium, namely the fermions ^6Li with the bosons ^7Li [111, 115]. The sympathetic cooling is the term used to refer to the cooling with several atomic species.

A specific feature of the Bose-Einstein condensate is its coherence at long length scales. The idea is to introduce the one-body density matrix in order to characterize the long-range

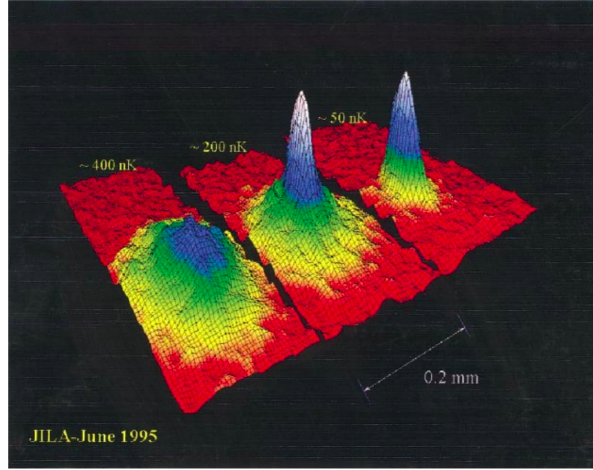


Figure 1.1.2: Time-of-flight absorption images of ultracold atomic clouds of ^{87}Rb for different temperatures. These distributions can also be seen as distributions in the reciprocal space. The Bose-Einstein condensation is obtained below a certain critical temperature from which the ultracold atoms follow a bimodal distribution roughly given by Eq. (1.1.11) characterized by a zero-momentum peak. These measures were experimentally obtained in the experiment of Cornell and Weiman [13,116]. This image comes from Ref. [116].

order of the condensate. This one-body density matrix is defined as [107]

$$n^{(1)}(\mathbf{r}, \mathbf{r}') = \langle \hat{\psi}^\dagger(\mathbf{r}) \hat{\psi}(\mathbf{r}') \rangle. \quad (1.1.8)$$

Here $\hat{\psi}(\mathbf{r})$ is the field operator that destroys a particle in \mathbf{r} while $\hat{\psi}^\dagger(\mathbf{r})$ creates a particle in \mathbf{r} . This quantity gives a measure of the coherence between the creation of particle at a certain point and a destruction of particle of another place. If the $\phi_{\mathbf{k}}(\mathbf{r})$ constitutes an orthonormal basis of the one-body Hamiltonian, the field operator can be expressed in terms of the ladder operators

$$\hat{\psi}(\mathbf{r}) = \sum_{\mathbf{k}} \phi_{\mathbf{k}}(\mathbf{r}) \hat{a}_{\mathbf{k}}. \quad (1.1.9)$$

Here $\hat{a}_{\mathbf{k}}$ destroys a particle characterized by the orbital $\phi_{\mathbf{k}}(\mathbf{r})$ while $\hat{a}_{\mathbf{k}}^\dagger$ creates a particle characterized by this orbital. Let us assume that we have a non-interacting gas without external trapping. Therefore, the one-body orbitals are plane waves, $\phi_{\mathbf{k}}(\mathbf{r}) = 1/\sqrt{V} e^{i\mathbf{k}\cdot\mathbf{r}}$. Moreover, the covariance between the ladder operators is given by $\langle \hat{a}_{\mathbf{k}}^\dagger \hat{a}_{\mathbf{k}'} \rangle = \langle n_{\mathbf{k}} \rangle \delta_{\mathbf{k}\mathbf{k}'}$ where $\langle n_{\mathbf{k}} \rangle$ is the mean number of particles in the orbital $\phi_{\mathbf{k}}(\mathbf{r})$. If \mathbf{p} is the momentum, $\langle n_{\mathbf{k}} \rangle$ can also be written as $n(\mathbf{p})$, and the one-body density matrix reads

$$n^{(1)}(\mathbf{r}, \mathbf{r}') = \frac{1}{V} \int d^3p \, n(\mathbf{p}) e^{\frac{i}{\hbar} \mathbf{p} \cdot (\mathbf{r} - \mathbf{r}')}. \quad (1.1.10)$$

The result depends only on the interdistance $\mathbf{r} - \mathbf{r}'$.

If $n(\mathbf{p})$ is a smooth function as it is the case for the Maxwell-Boltzmann statistics or the Bose-Einstein statistics above T_c , the one-body density matrix vanishes for $|\mathbf{r} - \mathbf{r}'| \rightarrow \infty$. Nevertheless, a divergence arises at T_c and below for the Bose-Einstein distribution. It means that $n(\mathbf{p})$ contains a delta function,

$$n(\mathbf{p}) = N_0 \delta(\mathbf{p}) + \tilde{n}(\mathbf{p}). \quad (1.1.11)$$

This bimodal distribution is peaked at zero-momentum where the condensed particles accumulate with N_0 the number of condensed particles. The second part $\tilde{n}(\mathbf{p})$ is a smooth function. In the context of the Bose-Einstein statistic, $\tilde{n}(\mathbf{p})$ is Gaussian in the free space. This bimodal distribution is illustrated in Fig. 1.1.2. The one-body density matrix becomes a non-zero value asymptotically below T_c ,

$$\lim_{|\mathbf{r}-\mathbf{r}'| \rightarrow \infty} n^{(1)}(\mathbf{r}, \mathbf{r}') = \frac{N_0}{V}. \quad (1.1.12)$$

This long-range behavior is called the off-diagonal long-range order and was highlighted by Penrose and Onsager in 1956 [117].

The result (1.1.12) highlights the long-range order of the ultracold atoms below the critical temperature. This coherence is the key to understand the difference with the Maxwell-Boltzmann statistics. For this one, it is possible to have almost all particles in the ground state at very low temperature. Nevertheless, the long-range order vanishes meaning that there is no coherence between particles. Conversely, for the Bose-Einstein statistics case, the one-body density matrix tends to the density of condensed bosonic atoms below the critical temperature. This indicates that a Bose-Einstein condensate is a coherent matter wave. The ultracold bosonic atoms become a useful resource for studying atomic interference and atom optics as illustrated in Fig. 1.1.3.

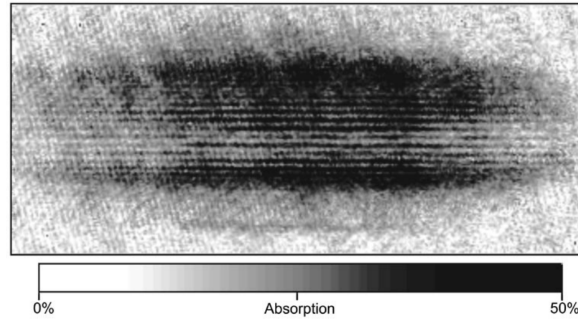


Figure 1.1.3: Interference fringes obtained with two expanding condensates of sodium after a time-of-flight of 40 ms [102]. The distance between two fringes is $15 \mu\text{m}$ and the width of the picture is 1.1 mm. The interference pattern suggests that the coherence is conserved on a long range. This image comes from Ref. [102].

1.2 Optical (super)lattice

1.2.1 Interaction between an atom and an electric field

The ground state of an atom can be modified by the presence of an external electric field, $\mathcal{E}(\mathbf{r}, t)$. Here the time-dependent part of the electrical field is determined by the frequency ω . The general Fourier decomposition of an electrical field characterized by one mode is given by

$$\mathcal{E}(\mathbf{r}, t) = \mathcal{E}_\omega e^{i\omega t} + \mathcal{E}_\omega^* e^{-i\omega t}. \quad (1.2.1)$$

In the framework of time-dependent perturbation theory the shift of the ground state energy reads [20]

$$\Delta E_g = -\frac{1}{2} \alpha(\omega) < \mathcal{E}(\mathbf{r}, t)^2 >_t, \quad (1.2.2)$$

where $\langle \dots \rangle_t = \omega/(2\pi) \int_0^{2\pi/\omega} dt$ is the temporal mean. The atoms subjected to an external electric field will display an electric dipole moment \mathbf{d} . The ground state shift is due to the coupling between this dipole and the electrical field. The laser frequency is assumed to be close to the transition between the ground state $|g\rangle$ and an excited state $|e\rangle$, which leads to the polarizability in the second order of the time-dependent perturbation theory with the following form [20],

$$\alpha(\omega) \simeq \frac{|\langle e | \hat{\mathbf{d}} \cdot \boldsymbol{\varepsilon} | g \rangle|^2}{(E_e - E_g) - \hbar\omega}. \quad (1.2.3)$$

Here $\boldsymbol{\varepsilon}$ is the polarization vector. Note that the expression (1.2.3) is valid when the rate of spontaneous emission from the excited state is much smaller than the laser frequency [20].

In the case of an electrical field modeled by a plane wave, we have $\boldsymbol{\mathcal{E}}_\omega = \mathcal{E}_0 \boldsymbol{\varepsilon} \exp(-i\mathbf{k} \cdot \mathbf{r})$ with \mathcal{E}_0 the amplitude and \mathbf{k} the wavevector. There are two qualitatively different behaviors which depend on the sign of the polarizability according to the relation (1.2.2).

1. Red-shift: $E_e - E_g > \hbar\omega$. As ΔE_g is negative, the laser tends to attract the atom.
2. Blue-shift: $E_e - E_g < \hbar\omega$. As ΔE_g is positive, the laser tends to repel the atom.

This energy shift is known as the AC Stark effect. The resulting energy gradient enables one to build optical traps for neutral atoms.

1.2.2 Double-well potential

An electrical field is able to attract an atom by inducing a level shift of its ground state. The key mechanism of this phenomenon is related to the interaction between the electric dipole moment and the electrical field as displayed in Eq. (1.2.3). When the electrical field is time-dependent, this phenomenon is called the AC Stark effect. The combination of different sources can create an optical lattice. The resulting electrical field of two opposite lasers linearly polarized along the same direction leads to a standing wave,

$$\mathcal{E}(x, t) = \mathcal{E}_0 \cos(kx - \omega t) + \mathcal{E}_0 \cos(-kx - \omega t) = 2\mathcal{E}_0 \cos(kx) \cos(\omega t), \quad (1.2.4)$$

with $k = 2\pi/\lambda$. The ground state energy shift of the atom is determined by the temporal mean of the square of the electric field,

$$\langle \mathcal{E}(x, t)^2 \rangle_t = 2\mathcal{E}_0^2 \cos^2(kx). \quad (1.2.5)$$

This evaluation enables one to determine the effective potential that acts on the atom,

$$V(x) = V_0 \cos^2(kx) = V_0 \cos^2(2\pi x/\lambda), \quad (1.2.6)$$

with $V_0 = -\frac{1}{2}\alpha(\omega)\mathcal{E}_0$. This is a periodic potential with a period $\lambda/2$.

As displayed in Fig. 1.2.1(a), a standing wave can be added in the y direction in order to create a *square lattice* [19],

$$V(x, y) = V_x \cos^2(k_x x) + V_y \cos^2(k_y y). \quad (1.2.7)$$

One way to achieve a two-site optical trap is to create a square lattice according to the previous relation by adding a harmonic confinement. This type of confinement can be achieved, for

example, by means an optical dipole trap, for which a focusing lens creates a local maximum of the laser intensity [21].

Another way to reach a double-well potential is to use the superlattice techniques, which consist in superimposing lasers with different wavelengths [24, 118]. In the case of square lattice, a two-site system can be generated by adding a second standing wave along the x direction.

$$V(x, y) = V_x \cos^2(k_{x,1}x) + V_x \cos^2(k_{x,2}x) + V_y \cos^2(k_y y) \quad (1.2.8)$$

Figure 1.2.1(b) shows the superlattice generated by the previous relation for $k_{x,2} = k_{x,1}/2$. The different dimers are relatively well separated from each other. In this context, if an atom is trapped in one of them, the description of the dynamics can be restricted to this dimer.

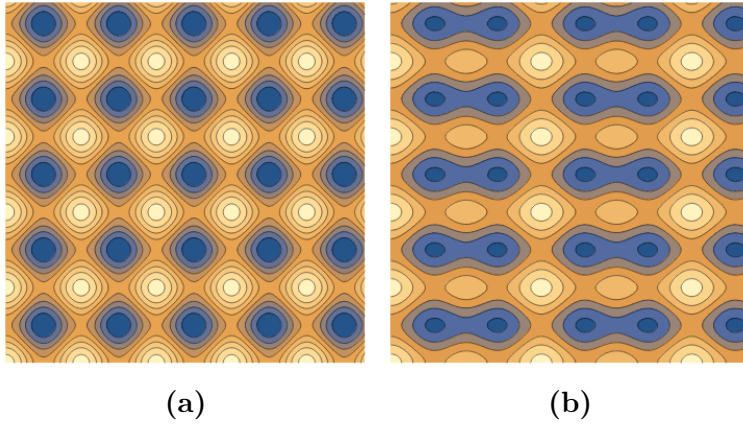


Figure 1.2.1: (a) Square optical lattice obtained with the relation (1.2.7) for $k_x = k_y$ and $V_x = V_y$. (b) Optical superlattice obtained with the relation (1.2.8) for $k_{x,2} = k_{x,1}/2$ and $V_x = 0.57V_y$.

1.2.3 Triple-well potential

The temporal mean in Eq. (1.2.2) can also be evaluated for a general configuration of lasers with arbitrary polarizations and wavevectors. The total electric field created by a set of lasers having the same frequency is given by the superposition of the individual fields,

$$\mathcal{E}(\mathbf{r}, t) = \sum_i \mathcal{E}_i \cos(\mathbf{k}_i \cdot \mathbf{r} - \omega t + \delta_i), \quad (1.2.9)$$

where δ_i is the phase shift of the laser i and \mathcal{E}_i contains its amplitude and its polarization. The temporal mean reads¹

$$\langle \mathcal{E}(\mathbf{r}, t)^2 \rangle_t = \frac{1}{2} \sum_i \mathcal{E}_i^2 + \sum_{i < j} \mathcal{E}_i \cdot \mathcal{E}_j \cos[(\mathbf{k}_i - \mathbf{k}_j) \cdot \mathbf{r} + \delta_i - \delta_j]. \quad (1.2.10)$$

One can thus play with the relative orientations and the number of lasers to create some specific optical lattices.

¹The mean of $\cos^2(\mathbf{k}_i \cdot \mathbf{r} - \omega t + \delta_i)$ over one period is equal to 1/2. To compute the other terms, we have to use $\cos a \cos b = \frac{1}{2}(\cos(a+b) + \cos(a-b))$ before the temporal mean.

A *triangular lattice* (see Fig. 1.2.2(a)) is built by using three lasers in a plane with a 120° angle between each wavevector. Their polarization must be perpendicular to this plane. The expressions of the wavevectors read $\mathbf{k}_1 = k(\cos(\frac{\pi}{6}), \sin(\frac{\pi}{6}), 0) = k(\sqrt{3}/2, 1/2, 0)$, $\mathbf{k}_2 = k(\cos(\frac{5\pi}{6}), \sin(\frac{5\pi}{6}), 0) = k(-\sqrt{3}/2, 1/2, 0)$, $\mathbf{k}_3 = k(0, -1, 0)$. The amplitudes are assumed to be equal to $\mathcal{E}_i = (0, 0, \mathcal{E}_0)$. The temporal mean of the square of the electric field reads

$$\langle \mathcal{E}(\mathbf{r}, t)^2 \rangle_t = \frac{3}{2} \mathcal{E}_0^2 + \mathcal{E}_0^2 (\cos[(\mathbf{k}_1 - \mathbf{k}_2) \cdot \mathbf{r}] + \cos[(\mathbf{k}_1 - \mathbf{k}_3) \cdot \mathbf{r}] + \cos[(\mathbf{k}_2 - \mathbf{k}_3) \cdot \mathbf{r}]), \quad (1.2.11)$$

for the triangular lattice. The previous expression enables one to evaluate the effective potential which acts on the atom.

$$\begin{aligned} V(\mathbf{r}) &= V_0 (\cos[(\mathbf{k}_1 - \mathbf{k}_2) \cdot \mathbf{r}] + \cos[(\mathbf{k}_1 - \mathbf{k}_3) \cdot \mathbf{r}] + \cos[(\mathbf{k}_2 - \mathbf{k}_3) \cdot \mathbf{r}]) \\ &= V_0 \left(\cos \left[k\sqrt{3} \begin{pmatrix} 1 \\ 0 \\ 0 \end{pmatrix} \cdot \mathbf{r} \right] + \cos \left[k\sqrt{3} \begin{pmatrix} -\frac{1}{2} \\ -\frac{\sqrt{3}}{2} \\ 0 \end{pmatrix} \cdot \mathbf{r} \right] + \cos \left[k\sqrt{3} \begin{pmatrix} -\frac{1}{2} \\ \frac{\sqrt{3}}{2} \\ 0 \end{pmatrix} \cdot \mathbf{r} \right] \right). \end{aligned} \quad (1.2.12)$$

The potential pattern of Eq. (1.2.12) would have been the same with a scale factor and with a global rotation if the initial configuration of \mathbf{k}_j had been used. In this case, the potential would read $V_0 \sum_{j=1}^3 \cos(\mathbf{k}_j \cdot \mathbf{r})$. This remark is also true, again with a scale factor, for a potential of the form

$$V(\mathbf{r}) = V_0 \sum_{j=1}^3 \cos^2(\mathbf{k}_j \cdot \mathbf{r}). \quad (1.2.13)$$

In this context, the potential (1.2.13) is a triangular lattice and is generated by means of three standing waves separated by a 120° angle from each other.

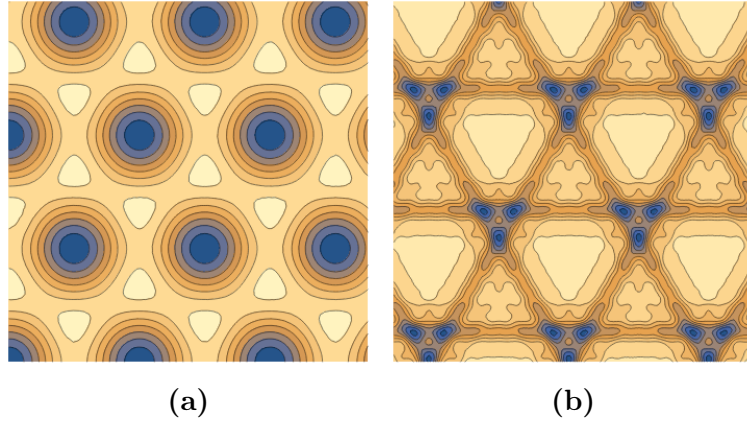


Figure 1.2.2: (a) Triangular optical lattice obtained with the relation (1.2.13). (b) Triangular optical superlattice obtained with the relation (1.2.14) for $\phi = 3\pi/2$.

The generation of the *triangular superlattice* in Fig. 1.2.2(b) is more technical. That can be achieved by using the superlattice techniques. It consists in substituting each standing wave $\cos^2(\mathbf{k}_j \cdot \mathbf{r})$ of the triangular lattice by $[\cos(\mathbf{k}_i \cdot \mathbf{r} + 3\sigma_i\phi/2) + 2\cos(\mathbf{k}_i \cdot \mathbf{r}/3 + \sigma_i\phi/2) + 4\cos(\mathbf{k}_i \cdot \mathbf{r}/9 + \sigma_i\phi/6)]^2$ with $\boldsymbol{\sigma} = (1, -1, 1)$ [22, 23]. The \mathbf{k}_j are the same as in the triangular

lattice case. The triangular superlattice potential reads

$$V(\mathbf{r}) = V_0 \sum_{i=1}^3 [\cos(\mathbf{k}_i \cdot \mathbf{r} + 3\sigma_i\phi/2) + 2\cos(\mathbf{k}_i \cdot \mathbf{r}/3 + \sigma_i\phi/2) + 4\cos(\mathbf{k}_i \cdot \mathbf{r}/9 + \sigma_i\phi/6)]^2. \quad (1.2.14)$$

In practice, there are three standing waves with an angle of 120° between each other. Each standing wave is generated by three lasers in a configuration explained in Ref. [22, 23]. The main advantage of the optical superlattice is to directly produce trimers well separated from each other. In this context, if an atom is trapped in one trimer, its dynamics will take place only on this trimer.

1.3 Bose-Hubbard model

1.3.1 Scattering at low energy

In an ultracold gas the typical distance between atoms is $d = 100$ nm. In this section, we will characterize the typical length scale over which the atoms interact. In a dilute gas, this typical length scale is much smaller than d . That is why the three-body interactions and more can be safely neglected, and the two-body interaction is modeled by a potential of the form $U(\mathbf{r}, \mathbf{r}')$ depending on the position \mathbf{r} of the first particle and the position \mathbf{r}' of the second one. In practice, this interaction depends only on the relative distance between both particles $\bar{\mathbf{r}} = \mathbf{r} - \mathbf{r}'$ such that $U(\mathbf{r}, \mathbf{r}') = U(\bar{\mathbf{r}})$. To deal with a two-body problem, it is convenient to study the dynamics in the center of mass coordinate $(\mathbf{r} + \mathbf{r}')/2$ and in the relative coordinate $\bar{\mathbf{r}}$. On one hand, the wave function related to the center of mass coordinate behaves like a free particle such that it is characterized by plane waves. On the other hand, the wave function related to the relative coordinate is described by a typical one-body Schrödinger equation where $U(\bar{\mathbf{r}})$ is treated like an external potential. In the context of the two-body scattering, it is possible to write the wave function as an incident plane wave (assumed to be oriented along the \bar{z} axis) plus a scattering part such that² [20, 107]

$$\psi = e^{ik\bar{z}} + f(\theta) \frac{e^{ik\bar{r}}}{\bar{r}} \quad (1.3.1)$$

for $\bar{r} \rightarrow \infty$. Here the potential characterizing the atom-atom interaction is supposed to be spherically symmetric, $U(\bar{\mathbf{r}}) = U(\bar{r})$, such that the scattering amplitude $f(\theta)$ depends only on the scattering angle θ . This is the angle between the incident motion and the motion after the scattering.

At very low energies, the wave function is delocalized in comparison to the spatial extension of $U(\bar{r})$. In this context, it is enough considering that $f(\theta)$ amounts to a constant $-a_s$ [20]. The wave function becomes

$$\psi = 1 - \frac{a_s}{\bar{r}} \quad (1.3.2)$$

for $k \rightarrow 0$, $\bar{r} \rightarrow \infty$ and $k\bar{r} \rightarrow 0$. The constant a_s , called the s-wave scattering length, describes entirely the collisions at very low temperature between two atoms for a dilute gas.

²Equation (1.3.1) is valid if the particles are distinguishable. As it not the case, the exact form should be $\psi = e^{ikz} \pm e^{-ikz} + |f(\theta) \pm f(\pi - \theta)| \frac{e^{ikr}}{r}$ respectively for bosons and fermions. If the $f(\theta)$ is a constant as it is the case at low energy scattering, the scattering part of the wave function vanishes for identical fermions.

The alkali atoms are characterized by one electron on the valence shell. When two atoms interact, their interaction can take place with respect to the singlet spin state or the triplet spin state of the two valence electrons. That is why there are s-wave scattering lengths related to the singlet and to the triplet. Some typical s-wave scattering lengths can be found in Table 1.1.

	$a_s^{(s)}/a_B$	$a_s^{(t)}/a_B$
H	0.41	1.2
^7Li	33	-27
^{23}Na	19	65
^{41}K	85	65
^{85}Rb	2400	-370
^{87}Rb	90	106
^{133}Cs	280	2400

Table 1.1: S-wave scattering lengths for different atomic species. Here $a_s^{(s)}$ makes reference to the singlet spin state while $a_s^{(t)}$ to the triplet spin state of the two valence electrons. The values are given in unit of the Bohr radius, $a_B = 5.29 \times 10^{-2}$ nm. These values come from [20].

The s-wave scattering length is the typical distance on which the atoms interact by pair. Thus, a_s is compared to the typical interdistance d , and the dilute gas condition is written as

$$|a_s| \ll d. \quad (1.3.3)$$

For typical d separation, atoms don't see each other. In the context of a dilute gas, it is convenient to get rid of all specific details concerning the atom-atom interaction and to model this one by a contact potential such that

$$U(\mathbf{r}, \mathbf{r}') = g\delta(\mathbf{r} - \mathbf{r}'). \quad (1.3.4)$$

From this assumption, it is possible to derive the relation between the coupling g and the s-wave scattering length [19, 20, 58, 119],

$$g = \frac{4\pi\hbar^2 a_s}{m}, \quad (1.3.5)$$

where m is the mass of the atomic species. A negative a_s leads to effectively attractive atoms while a positive a_s leads to repulsive ones. Although it is possible experimentally to cool attractive atoms to a Bose-Einstein condensate [103], the contraction on itself of the ultracold atomic cloud can lead to the collapse of the condensate with atomic losses [35, 36]. That is why the gases with an attractive inter-atomic interaction are more unstable than the repulsive one.

1.3.2 Derivation of the Bose-Hubbard model via second quantization

The idea of this section is to build a model to describe a gas of atoms trapped in optical lattice characterized by the one-body potential $V(\mathbf{r}) = V(\mathbf{r} + \mathbf{R})$. Here \mathbf{R} is the periodicity

of the optical lattice. Moreover, there is an additional trap potential $V_T(\mathbf{r})$. The gas is assumed to be diluted in order to only take into account the two-body interaction $U(\mathbf{r}, \mathbf{r}')$. In the framework of second quantization, the Hamiltonian of a sufficiently dilute ultracold atomic gas is given by [28, 120]

$$\begin{aligned} \hat{H} = & \int d^3r \, \hat{\psi}^\dagger(\mathbf{r}) \left(\frac{-\hbar^2}{2m} \Delta + V(\mathbf{r}) + V_T(\mathbf{r}) \right) \hat{\psi}(\mathbf{r}) \\ & + \frac{1}{2} \int d^3r \int d^3r' \, \hat{\psi}^\dagger(\mathbf{r}) \hat{\psi}^\dagger(\mathbf{r}') U(\mathbf{r}, \mathbf{r}') \hat{\psi}(\mathbf{r}') \hat{\psi}(\mathbf{r}), \end{aligned} \quad (1.3.6)$$

where $\hat{\psi}(\mathbf{r})$ and $\hat{\psi}^\dagger(\mathbf{r})$ are the field operators. The former destroys a spinless particle at the position \mathbf{r} while the latter creates a spinless particle at the position \mathbf{r} . They are characterized by the commutation relations $[\hat{\psi}(\mathbf{r}), \hat{\psi}^\dagger(\mathbf{r}')] = \delta(\mathbf{r} - \mathbf{r}')$ and $[\hat{\psi}^\dagger(\mathbf{r}), \hat{\psi}^\dagger(\mathbf{r}')] = [\hat{\psi}(\mathbf{r}), \hat{\psi}(\mathbf{r}')] = 0 \quad \forall \mathbf{r}, \mathbf{r}' \in \mathbb{R}^3$. These operators are able to count the total number of particles.

$$\int_{\mathbb{R}^3} d^3r \, \hat{\psi}^\dagger(\mathbf{r}) \hat{\psi}(\mathbf{r}) = \hat{N}_p \quad (1.3.7)$$

The one-body potential $V(\mathbf{r}) + V_T(\mathbf{r})$ is separated in two parts, one representing the periodic optical lattice potential $V(\mathbf{r})$ and the other one the trap potential $V_T(\mathbf{r})$. In the framework of the tight-binding approximation [20], the depth of the potential is sufficiently large that the system can be described by focusing only on the first energy band. Indeed, as the temperature is assumed to be very low, the energy of the particles is much smaller than the energy gap to the first excited band. The destructive field operator can be expanded in terms of the annihilation operators by means of the orthonormal single-particle basis $\{w_j(\mathbf{r}) | j = 1, \dots, N_s\}$ restricted to the first energy band,

$$\hat{\psi}(\mathbf{r}) = \sum_{j=1}^{N_s} w_j(\mathbf{r}) \hat{a}_j, \quad (1.3.8)$$

where N_s is the number of sites on the lattice. By assuming that the function $w_j(\mathbf{r})$ is relatively well localized on site j ³, the ladder operator \hat{a}_j can be associated to the destruction of one particle on site j .

In the framework of the scattering of two atoms at low energy, the collisions are mainly determined by the s-wave component of the eigenfunctions of the radial equation (knowing that the two-body interaction is modeled by a spherically symmetric potential). With the low energy assumption, it follows that the collisions can be characterized by an unique parameter, namely the s-wave scattering length a_s [19, 20]. As the atomic gas is strongly diluted, the two-body interaction is modeled by a contact potential according to Eq. (1.3.4) [20, 119].

By using the previous assumptions, the Hamiltonian (1.3.6) can now be expressed in terms of the ladder operators,

$$\hat{H} = \sum_{i,j=1}^{N_s} J_{ij} \hat{a}_i^\dagger \hat{a}_j + \frac{1}{2} \sum_{i,j,k,l=1}^{N_s} U_{ijkl} \hat{a}_i^\dagger \hat{a}_j^\dagger \hat{a}_k \hat{a}_l + \sum_{i,j=1}^{N_s} V_{ij} \hat{a}_i^\dagger \hat{a}_j, \quad (1.3.9)$$

³In the literature the Wannier functions are often used [19, 28, 120], which depend only on the relative distance $\mathbf{r} - \mathbf{r}_j$ with \mathbf{r}_j the position of the lattice site j , such that $w_j(\mathbf{r}) = w(\mathbf{r} - \mathbf{r}_j)$.

with

$$J_{ij} = \int d^3r w_i^*(\mathbf{r}) \left(\frac{-\hbar^2}{2m} \Delta + V(\mathbf{r}) \right) w_j(\mathbf{r}), \quad (1.3.10)$$

$$U_{ijkl} = g \int d^3r w_i^*(\mathbf{r}) w_j^*(\mathbf{r}) w_k(\mathbf{r}) w_l(\mathbf{r}), \quad (1.3.11)$$

$$V_{ij} = \int d^3r w_i^*(\mathbf{r}) V_T(\mathbf{r}) w_j(\mathbf{r}). \quad (1.3.12)$$

The terms J_{ii} represents a part of the on-site energy of site i as it will be discussed below. In order to obtain the Bose-Hubbard Hamiltonian, several assumptions are introduced.

- The hopping is restricted to the nearest neighbor sites. If the lattice is one dimensional, this assumption leads to $J_{i,i+1} \neq 0$ and $J_{i,i+l} = 0 \quad \forall l \geq 2, \forall i$.

$$-J_i \equiv J_{i,i+1} = \int d^3r w_i^*(\mathbf{r}) \left(\frac{-\hbar^2}{2m} \Delta + V(\mathbf{r}) \right) w_{i+1}(\mathbf{r}) \quad (1.3.13)$$

- The two-body interactions are restricted to the particles on a same site. The non-local interactions are neglected meaning that $U_{ijkl} \neq 0$ if and only if $i = j = k = l$.

$$U_i \equiv U_{iiii} = g \int d^3r |w_i(\mathbf{r})|^4 \quad (1.3.14)$$

- The trap potential varies slowly. It is constant on a site: $V_{ij} \approx V_T(\mathbf{r}_i) \int d^3r w_i^*(\mathbf{r}) w_j(\mathbf{r})$. By defining $V_i = V_T(\mathbf{r}_i)$, we obtain

$$V_{ij} \approx V_i \delta_{ij}. \quad (1.3.15)$$

The on-site energy is then defined as $\xi_i = J_{ii} + V_i$. The previous assumptions give rise to the Bose-Hubbard Hamiltonian,

$$\hat{H} = - \sum_{l=1}^{N_s} J_l (\hat{a}_l^\dagger \hat{a}_{l+1} + \hat{a}_{l+1}^\dagger \hat{a}_l) + \frac{1}{2} \sum_{l=1}^{N_s} U_l \hat{a}_l^\dagger \hat{a}_l^\dagger \hat{a}_l \hat{a}_l + \sum_{l=1}^{N_s} \xi_l \hat{a}_l^\dagger \hat{a}_l. \quad (1.3.16)$$

In the case of periodic boundary conditions, we have $\hat{a}_{N_s+1} = \hat{a}_1$. If the boundary conditions are fixed, the sum for the hopping goes to $N_s - 1$ instead of N_s .

In a homogeneous optical lattice made of ultracold atoms, there are two main parameters which will lead to different qualitative dynamics, namely the on-site interaction U and the hopping J^4 . On one hand, the former describing the interaction of two atoms on a same site tends to localize the system. On the other hand, the latter describing the tunneling of atoms one by one tends to delocalize the system over the entire lattice. It means that the system may stay in its initial configuration for $U/J \gg 1$ [19, 27, 29, 121, 122]. This configuration is called a Mott state for an infinite lattice. The phenomenon by which interactions between atoms leads to a localization is also called self-trapping. In this case, the phases of the sites are uncorrelated. On the other hand, the giant matter wave displays a superfluid behavior for $U/J \ll 1$, where all atoms are delocalized over the entire lattice [19, 27, 29, 121, 122].

⁴The lattice is assumed to be homogeneous according to U and J such that $J_l = J$ and $U_l = U \quad \forall l$.

1.3.3 Bose-Hubbard parameters in the laboratory units

An atom trapped in an optical lattice made of a standing wave defined along the x direction (see Eq. (1.2.6)) will be subjected to the potential

$$V(x) = V_0 \frac{\hbar^2 k_\varphi^2}{2m} \sin^2(k_\varphi x) = V_0 \frac{\hbar^2 k^2}{m} (1 - \cos(kx)), \quad (1.3.17)$$

where m is the mass of the atom, $k_\varphi = 2\pi/\lambda$ is the wavevector of the laser photons and $k = 2\pi/d$ the wavevector of the lattice for which the distance between two successive sites is given by $d = \lambda/2$ leading to $k = 2k_\varphi$. The typical energy scale is the recoil energy $E_r = \hbar^2 k_\varphi^2/(2m)$, which represents the kinetic energy of an atom, initially at rest, after the emission of a photon.

The addition of a harmonic confinement along the two other directions gives rise to the following Hamiltonian,

$$H = -\frac{\hbar^2}{2m} \Delta + V_0 \frac{\hbar^2 k^2}{m} (1 - \cos(kx)) + \frac{1}{2} m \omega_\perp^2 (y^2 + z^2). \quad (1.3.18)$$

As $H = H_x + H_y + H_z$ is separable, the different parts of the Hamiltonian read

$$H_x = -\frac{\hbar^2}{2m} \frac{\partial^2}{\partial x^2} + V_0 \frac{\hbar^2 k^2}{m} (1 - \cos(kx)), \quad (1.3.19)$$

$$H_y = -\frac{\hbar^2}{2m} \frac{\partial^2}{\partial y^2} + \frac{1}{2} m \omega_\perp^2 y^2, \quad (1.3.20)$$

$$H_z = -\frac{\hbar^2}{2m} \frac{\partial^2}{\partial z^2} + \frac{1}{2} m \omega_\perp^2 z^2. \quad (1.3.21)$$

If the oscillations inside the well are small, a harmonic approximation can be made and the ground state on site l reads $w_l(\mathbf{r}) = w(\mathbf{r} - l \frac{2\pi}{k} \mathbf{e}_x)$, where

$$w(\mathbf{r}) \simeq \frac{1}{\sqrt{\sqrt{\pi} \sigma_\parallel}} \exp\left(-\frac{x^2}{2\sigma_\parallel^2}\right) \frac{1}{\sqrt{\pi} \sigma_\perp} \exp\left(-\frac{y^2 + z^2}{2\sigma_\perp^2}\right), \quad (1.3.22)$$

with $\sigma_\parallel = 1/(kV_0^{1/4})$ and $\sigma_\perp = \sqrt{\hbar/(m\omega_\perp)}$. In the tight-binding approximation the potential is sufficiently deep such that the $w_l(\mathbf{r})$ are approximately orthonormal,

$$\int_{\mathbb{R}^3} d^3r w^*(\mathbf{r}) w(\mathbf{r} - l 2\pi/k \mathbf{e}_x) = \exp\left(-\left(\frac{l\pi}{k\sigma_\parallel}\right)^2\right) \xrightarrow{\sigma_\parallel \rightarrow 0} 0 \quad \forall l \neq 0. \quad (1.3.23)$$

Still in the harmonic approximation, the longitudinal trap frequency takes the form $\omega_\parallel = \sqrt{V_0 \hbar k^2/m}$ with $\sigma_\parallel = \sqrt{\hbar/(m\omega_\parallel)}$. Within this approximation, the ground state energy

$E_0 = E_{0,x} + E_{0,y} + E_{0,z}$ can be evaluated analytically.

$$E_{0,x} = \int_{\mathbb{R}^3} w^*(\mathbf{r}) H_x w(\mathbf{r}) d^3r \simeq \sqrt{V_0}(1 - \eta) \hbar \omega_{\parallel} \quad (1.3.24)$$

$$E_{0,y} = \int_{\mathbb{R}^3} w^*(\mathbf{r}) H_y w(\mathbf{r}) d^3r = \frac{\hbar \omega_{\perp}}{2} \quad (1.3.25)$$

$$E_{0,z} = \int_{\mathbb{R}^3} w^*(\mathbf{r}) H_z w(\mathbf{r}) d^3r = \frac{\hbar \omega_{\perp}}{2} \quad (1.3.26)$$

Here $\eta = \exp(-1/(4\sqrt{V_0})) - 1/(4\sqrt{V_0})$. By means of Eq. (1.3.14), the evaluation of the on-site interaction is given by

$$U = g \int_{\mathbb{R}^3} |w(\mathbf{r})|^4 d^3r = 2\hbar \omega_{\perp} k a_s \sqrt{\frac{\sqrt{V_0}}{2\pi}}, \quad (1.3.27)$$

with a_s the s-wave scattering length, $g = 4\pi \hbar^2 a_s / m$ [119] and ω_{\perp} the transverse trap frequency.

The use of Eq. (1.3.13) is a way to evaluate the hopping. An alternative is the semi-classical theory called WKB (Wentzel-Kramers-Brillouin) [66] enabling one to calculate the transmission coefficient through a potential barrier for a particle in its ground state. This transmission coefficient can be related to the hopping parameter [123–125],

$$J = \frac{\hbar \omega_{\parallel}}{\sqrt{e\pi}} \exp\left(-\frac{2}{\hbar} \int_a^{\pi/k} \sqrt{2m(V(x) - E_{0,x})} dx\right) \quad (1.3.28)$$

$$= \sqrt{\frac{V_0}{e\pi}} \frac{\hbar^2 k^2}{m} \exp\left(-2\sqrt{2V_0} \int_{\arccos \eta}^{\pi} \sqrt{\eta - \cos \phi} d\phi\right), \quad (1.3.29)$$

with $V(a) = E_{0,x}$ the ground state energy of the one dimensional system. By assuming $\omega_{\perp} = \omega_{\parallel}$, V_0 can be determined by solving

$$\frac{U}{J} = \sqrt{2e\sqrt{V_0}} k a_s \exp\left(2\sqrt{2V_0} \int_{\arccos \eta}^{\pi} \sqrt{\eta - \cos \phi} d\phi\right). \quad (1.3.30)$$

The energy scale is then obtained by means of Eqs. (1.3.27) or (1.3.29).

The wavelength of the laser is assumed to be equal to $\lambda = 1064$ nm. The s-wave scattering length and the mass of ^{87}Rb are $a_s = 5.313$ nm and $m = 1.443 \times 10^{-25}$ kg, respectively. The solution of Eq. (1.3.30) for $U/J = 20$ gives $V_0 = 0.8586$. This leads to $\omega_{\parallel} = \omega_{\perp} = 9.4 \times 10^4$ s $^{-1}$ and $\hbar/J = 4.4 \times 10^{-3}$ s. Figure 1.3.1 illustrates the increase of the tunneling timescale \hbar/J of a particle as a function of the on-site interaction. A harmonic approximation of the energy bands takes the form

$$E_{n,x} \approx \sqrt{V_0} \left(n + \frac{1}{2}\right) \frac{\hbar^2 k^2}{m}, \quad (1.3.31)$$

with n the band index. Knowing that the strength of the potential is $2V_0 \simeq 1.7$, the system displays two binding states inside a well, namely $E_{0,x} \approx 0.46 \hbar^2 k^2 / m$ and $E_{1,x} \approx 1.39 \hbar^2 k^2 / m$.

So far we have assumed that the atomic cloud is diluted such that the frequency of the collisions is relatively small. In this context, it is possible to take only into account the two-body collisions, which occur much more often than the three-body ones. The dilute gas

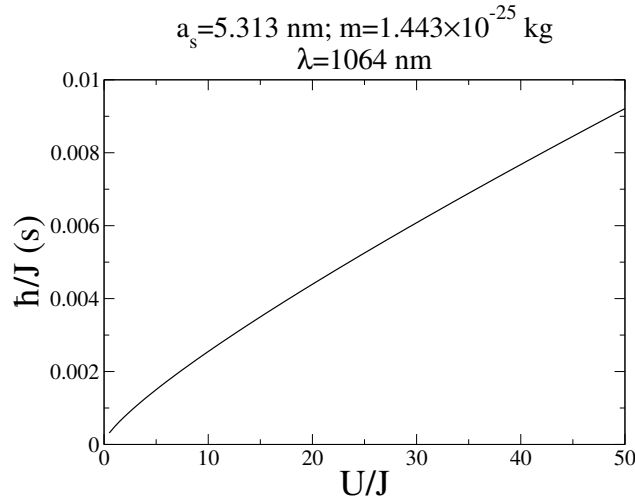


Figure 1.3.1: The tunneling timescale, here in seconds, tends to increase with the on-site interaction. This plot was obtained for a typical optical lattice of wavelength λ filled with ^{87}Rb atoms.

condition reads [126, 127]

$$|a_s| \ll d, \quad (1.3.32)$$

where $d = 1/\bar{n}^{1/3}$ is the typical interdistance between two atoms and $\bar{n} = N_p/((\sqrt{2\pi}\sigma_\perp)^2\sqrt{2\pi}\sigma_\parallel)$ is the average density of atoms. Here N_p is the total number of particles on the lattice. As calculated previously, $\omega_\parallel = 9.4 \times 10^4 \text{ s}^{-1}$, which leads to $\sigma_\parallel = \sqrt{\hbar/(m\omega_\parallel)} = 88 \text{ nm}$ for the oscillator length for ^{87}Rb atoms.

To simplify the calculus, we can assume $\omega_\parallel = \omega_\perp$ such that $\sigma_\parallel = \sigma_\perp$. In some results of the next chapters, the scale of the number of particles is $N_p \sim 10$. It corresponds to a density of $\bar{n} = 9.3 \times 10^{14} \text{ cm}^{-3}$ and to $d = 100 \text{ nm}$, which is the typical orders of magnitude encounters in experiments with ultracold atoms. The dilute gas condition (1.3.32) can be used to set an upper limit on the number of atoms. This gives rise to

$$N_p \ll \frac{\sqrt{2\pi}^3 \sigma_\perp^3}{a_s^3} \simeq 72000. \quad (1.3.33)$$

Thus, this assumption can be safely done for roughly 10 atoms.

1.3.4 Mean-field approximation

Before taking the classical limit of the Bose-Hubbard Hamiltonian (1.3.16), we will explain how this can be achieved with the harmonic oscillator. Its Hamiltonian reads

$$\hat{H}_{\text{ho}} = \hbar\omega \left(\hat{a}^\dagger \hat{a} + \frac{1}{2} \right). \quad (1.3.34)$$

One way to obtain the classical limit is to replace the ladder operators by complex numbers such that

$$\begin{aligned} \langle \hat{a} \rangle &\sim \psi = \sqrt{I/\hbar} e^{i\theta}, \\ \langle \hat{a}^\dagger \rangle &\sim \psi^* = \sqrt{I/\hbar} e^{-i\theta}. \end{aligned} \quad (1.3.35)$$

Nevertheless, the Hamiltonian must be symmetrized before replacing the ladder operators by complex numbers. Knowing that the commutator is $[\hat{a}, \hat{a}^\dagger] = 1$, this can be achieved by ordering the ladder operators according to

$$\hat{H}_{\text{ho}} = \hbar\omega \left(\frac{\hat{a}^\dagger \hat{a} + \hat{a} \hat{a}^\dagger}{2} \right). \quad (1.3.36)$$

With the expression (1.3.36), the classical limit of \hat{H}_{ho} reads

$$H_{\text{ho}} = \omega I. \quad (1.3.37)$$

A rapid way to compute the spectrum is to use the semiclassical method called the Bohr-Sommerfeld quantization ($n \in \mathbb{N}$) [65, 66],

$$\frac{1}{2\pi} \int_0^{2\pi} I d\theta = \hbar \left(n + \frac{1}{2} \right), \quad (1.3.38)$$

where I is the conjugate momenta and θ is the generalized coordinate. In this case, the spectrum of the harmonic oscillator is reproduced with the correct zero-point energy.

$$E = \hbar\omega \left(n + \frac{1}{2} \right) \quad (1.3.39)$$

The ordering of the operators is crucial to obtain the correct classical equivalent. The goal of this section is to take the classical limit of the Bose-Hubbard Hamiltonian (1.3.16),

$$\hat{H} = - \sum_{l=1}^{N_s} J_l (\hat{a}_l^\dagger \hat{a}_{l+1} + \hat{a}_{l+1}^\dagger \hat{a}_l) + \frac{1}{2} \sum_{l=1}^{N_s} U_l \hat{a}_l^\dagger \hat{a}_l^\dagger \hat{a}_l \hat{a}_l + \sum_{l=1}^{N_s} \xi_l \hat{a}_l^\dagger \hat{a}_l, \quad (1.3.40)$$

while keeping the correct zero-point energy. The parts that must be ordered are the on-site interaction part and the on-site energy part. By realizing that this term can be expressed as $U_l \hat{a}_l^\dagger \hat{a}_l^\dagger \hat{a}_l \hat{a}_l = U_l \hat{n}_l (\hat{n}_l - 1)$ with $\hat{n}_l = \hat{a}_l^\dagger \hat{a}_l$, the Hamiltonian becomes

$$\begin{aligned} \hat{H} = & \frac{1}{2} \sum_{l=1}^{N_s} U_l \left(\frac{\hat{a}_l^\dagger \hat{a}_l + \hat{a}_l \hat{a}_l^\dagger}{2} - \frac{1}{2} \right) \left(\frac{\hat{a}_l^\dagger \hat{a}_l + \hat{a}_l \hat{a}_l^\dagger}{2} - \frac{1}{2} - 1 \right) \\ & - \sum_{l=1}^{N_s} J_l (\hat{a}_l^\dagger \hat{a}_{l+1} + \hat{a}_{l+1}^\dagger \hat{a}_l) + \sum_{l=1}^{N_s} \xi_l \left(\frac{\hat{a}_l^\dagger \hat{a}_l + \hat{a}_l \hat{a}_l^\dagger}{2} - \frac{1}{2} \right). \end{aligned} \quad (1.3.41)$$

In Ref. [128], the classical limit is obtained by introducing the quadrature operators, which can be seen as a Cartesian representation of the system. Another way to achieve that is to replace the ladder operators by complex numbers [129, 130] in the limit of an infinite amount of particles, which is called the mean-field approximation,

$$\begin{aligned} \langle \hat{a}_l \rangle & \sim \psi_l = \sqrt{I_l} e^{i\theta_l}, \\ \langle \hat{a}_l^\dagger \rangle & \sim \psi_l^* = \sqrt{I_l} e^{-i\theta_l}, \end{aligned} \quad (1.3.42)$$

where the ψ_l represents the condensate amplitude on site l , θ_l the phase on the site l and I_l is proportional to n_l , the number of particles on site l such that $I_l = n_l + 1/2$. As N_p is

conserved, the sum of the I_l amounts to a constant $N = N_p + N_s/2$.

$$\sum_{l=1}^{N_s} I_l = N \quad (1.3.43)$$

Those preliminary explanations lead to the classical limit of (1.3.40).

$$H(\psi_l, \psi_l^*) = - \sum_{l=1}^{N_s} J_l (\psi_l^* \psi_{l+1} + \psi_{l+1}^* \psi_l) + \frac{1}{2} \sum_{l=1}^{N_s} U_l \left(|\psi_l|^4 - 2|\psi_l|^2 + \frac{3}{4} \right) + \sum_{l=1}^{N_s} \xi_l \left(|\psi_l|^2 - \frac{1}{2} \right) \quad (1.3.44)$$

The ordering of the ladder operators reproduces the correct zero-point energy and the interaction terms at the classical limit lead to a contribution to the on-site energy through the term $U_l |\psi_l|^2$. The discrete Gross-Pitaevskii equation is then calculated by the Hamiltonian equations of (1.3.44) with $l = 1, 2, \dots, N_s$.

$$i\hbar \frac{d\psi_l}{dt} = -(J_l \psi_{l+1} + J_{l-1} \psi_{l-1}) + U_l (|\psi_l|^2 - 1) \psi_l + \xi_l \psi_l \quad (1.3.45)$$

Note that ψ_0 corresponds to ψ_{N_s} and ψ_{N_s+1} corresponds to ψ_1 for periodic boundary conditions.

The variables $(\boldsymbol{\theta}, \mathbf{I})$ are known as the action-angle canonical variables, and can be used as a representation of the classical dynamics. This representation makes a clear distinction between the angle-independent part $H(\mathbf{I})$ and the angle-dependent part $V(\boldsymbol{\theta}, \mathbf{I})$ of the Hamiltonian such that $H(\boldsymbol{\theta}, \mathbf{I}) = H(\mathbf{I}) + V(\boldsymbol{\theta}, \mathbf{I})$.

$$H(\boldsymbol{\theta}, \mathbf{I}) = \frac{1}{2} \sum_{l=1}^{N_s} U_l \left(I_l^2 - 2I_l + \frac{3}{4} \right) - 2 \sum_{l=1}^{N_s} J_l \sqrt{I_l I_{l+1}} \cos(\theta_l - \theta_{l+1}) + \sum_{l=1}^{N_s} \xi_l \left(I_l - \frac{1}{2} \right) \quad (1.3.46)$$

Here I_{N_s+1} corresponds to I_1 for periodic boundary conditions.

The total number of particles is a conserved quantity such that the sum of each action is a constant amounting to N . Therefore, it becomes possible to reduce the number of degrees of freedom by performing a canonical transformation to a set of variables where N plays the role of a conjugate momentum. For example, the third class generating function $F(\mathbf{I}, \boldsymbol{\phi})$ can perform this process and generates the identity for the other action variables. This generating function accomplishes the transformation $(\boldsymbol{\theta}, \mathbf{I}) \rightarrow (\boldsymbol{\phi}, \mathbf{z})$ and reads

$$F(\mathbf{I}, \boldsymbol{\phi}) = \sum_{j=1}^{N_s-1} I_j \phi_j + \left(\sum_{j=1}^{N_s} I_j \right) \phi_{N_s}. \quad (1.3.47)$$

From this generating function, the link between the old and the new canonical variables is obtained through $(l = 1, 2, \dots, N_s)$

$$\theta_l = \frac{\partial F(\mathbf{I}, \boldsymbol{\phi})}{\partial I_l}; \quad z_l = \frac{\partial F(\mathbf{I}, \boldsymbol{\phi})}{\partial \phi_l}. \quad (1.3.48)$$

This leads to the new set of canonical variables expressed in terms of the old ones.

$$\begin{aligned}
\phi_l &= \theta_l - \theta_{N_s} & l &= 1, 2, \dots, N_s - 1 \\
\phi_{N_s} &= \theta_{N_s} \\
z_l &= I_l & l &= 1, 2, \dots, N_s - 1 \\
z_{N_s} &= \sum_{j=1}^{N_s} I_j = N
\end{aligned} \tag{1.3.49}$$

In this case, the new momentum z_{N_s} is a constant of motion amounting to N such that ϕ_{N_s} is a cyclic variable. Therefore, the new Hamiltonian is given by $H(\phi_1, \dots, \phi_{N_s-1}, z_1, \dots, z_{N_s})$ where z_{N_s} is treated like a parameter.

That kind of transformation demands an analytic treatment. Nevertheless, that enables one to visualize the whole dynamics from an easier point of view. For example, the two-site system is an effective one degree-of-freedom system such that the phase space has two dimensions. The unperturbed one is an integrable system⁵ owing to the energy conservation. If the two-site system is periodically driven, it is still possible to visualize the dynamics in a plane with the stroboscopic map as it will be described in Eq. (3.3.3). A canonical transformation similar to Eq. (1.3.47) will be particularized to the two-site system in Eq. (3.1.8). The three-site one is an effective two-degree-freedom system owing to the conservation of the number of particles. It is a non-integrable system as it possesses two constants of motion for three degrees of freedom. However, it is still possible to visualize the dynamics by means of Poincaré section [66]. A canonical transformation similar to Eq. (1.3.47) will be particularized to the three-site system in Eq. (5.2.13). The stroboscopic map of the periodically-driven three-site system can be designed in order to have a 4D phase space. Then, the dynamics can be visualized in 3D by means of slices introduced in Eq. (0.0.4). This will be discussed in Sec. 6.4.

⁵An integrable system is system where there exists as many independent constants of motion as degrees of freedom. In this context, it becomes possible to define a canonical transformation to the action-angle variables where all generalized coordinates are cyclic. For more details, see [66].

Chapter 2

Periodically driven two-site Bose-Hubbard model

The general Bose-Hubbard Hamiltonian introduced in the previous chapter is particularized here to the symmetric two-site case. In the framework of weak coupling between both sites in comparison to the on-site interaction, the atoms are no longer able to tunnel one by one because of the mismatch of chemical potentials of the two sites. Nevertheless, collective tunneling can occur because of the quasidegeneracy between the symmetric and antisymmetric combination of $|n_1, n_2\rangle$ and $|n_2, n_1\rangle$, namely $1/\sqrt{2}(|n_1, n_2\rangle \pm |n_2, n_1\rangle)$, respectively. For a Fock state $|n_1, n_2\rangle$, n_l represents the number of particles on site l . The energetic signature of this phenomenon is the doublet structure of the eigenspectrum where each group of two levels are relatively well separated from each other such that the standard two-level approximation is applicable.

An additional external periodic driving can be treated in the framework of Floquet theory [131]. For a time-independent Hamiltonian, the system is characterized by means of these eigenvalues and eigenvectors. Although the energy is not conserved in the time-dependent one, it is still possible to build an eigenvalue Schrödinger equation in terms of the quasienergies and of the time-periodic Floquet eigenvectors. Even if the dimension is infinite in the Floquet space, it is possible to focus only on a frequency-size block of the eigenspectrum owing to the periodicity of the quasienergies. The Floquet spectrum is made of an infinite number of frequency-shifted unperturbed spectra coupled by the amplitude of the periodic perturbation. The subsequent modification of the unperturbed eigenspectrum is expected to play a role on the quantum dynamics, especially the tunneling between sites. The end of this chapter will present original results concerning the total suppression of tunneling by means of the periodic driving.

2.1 Two-site Bose-Hubbard Hamiltonian

A collection of spinless atoms can be trapped in a double-well potential, whose representation is shown in Fig. 1.2.1(b). In the optical superlattice case, the plaquettes are well separated without an additional harmonic confinement such that the system can be seen as a two-mode system in which the atoms are either trapped on site 1 or on site 2. For example, Fig. 2.1.1 represents a Bose-Einstein condensate with 2 atoms on site 1 and 4 atoms on site 2. A site coupling, modeled by J , enables the atoms to tunnel from one site to the other. In the context of a dilute atomic gas the on-site two-body interaction U is enough to model

the collisions between atoms. If the temperature is sufficiently low, the atoms stay on the lowest-energy band and the Hamiltonian of the two-site system reads [54, 58, 132]

$$\hat{H}_0 = -J(\hat{a}_1^\dagger \hat{a}_2 + \hat{a}_2^\dagger \hat{a}_1) + \frac{U}{2}(\hat{a}_1^\dagger \hat{a}_1^\dagger \hat{a}_1 \hat{a}_1 + \hat{a}_2^\dagger \hat{a}_2^\dagger \hat{a}_2 \hat{a}_2), \quad (2.1.1)$$

where \hat{a}_l and \hat{a}_l^\dagger are respectively the annihilation and the destruction operators of a particle on site l . In addition to the conservation of energy, the Hamiltonian (2.1.1) describes a system where the total number of particles N_p is a conserved quantity,

$$[\hat{N}_p, \hat{H}_0] = 0. \quad (2.1.2)$$

Here we have $\hat{N}_p = \hat{a}_1^\dagger \hat{a}_1 + \hat{a}_2^\dagger \hat{a}_2$. As the system is time-independent and the total amount of particles is constant, the two-site Bose-Hubbard model is integrable owing that there are two constants of motion for two degrees of freedom (one degree of freedom for each site). A more detailed derivation of the Hamiltonian (2.1.1) is presented in Sec. 1.3.2. Incidentally, the Hamiltonian (2.1.1) is a specific case of the Hamiltonian (1.3.16) for $N_s = 2$, $U_l = U$, $J_l = J$ and $\xi_l = 0 \ \forall l$.

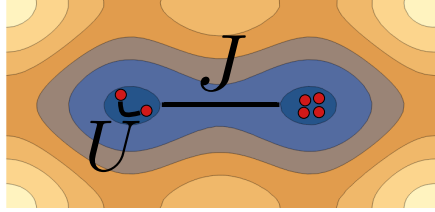


Figure 2.1.1: Contour plot of the potential landscape of an optical superlattice introduced for the first in time in Fig. 1.2.1(b). Two ultracold atoms are trapped on the first site while four ones are trapped on the second site. The atoms are able to tunnel to the other site via the hopping parameter J while the on-site interaction U tends to localize the atoms.

2.1.1 Discrete symmetry

One of the simplest basis choice for the decomposition of the Hamiltonian (2.1.1) is the Fock basis according to the one-body site basis,

$$\{|n_1, n_2\rangle \mid n_1 = 0, 1, \dots, N_p; \ n_2 = N_p - n_1\}. \quad (2.1.3)$$

Here n_l is the number of particles on site l . From this basis, the dimension of the Hilbert space is directly obtained,

$$\dim \hat{H}_0 = N_p + 1. \quad (2.1.4)$$

Nevertheless, in some circumstances, it could be valuable to choose an unperturbed basis that takes into account the symmetries of the system, which enables one to decrease the size of the matrix to diagonalize. As the double-well potential is symmetric, the system must be invariant under the permutation of both sites. That is why the permutation operator, \hat{P} , which inverts the site 1 and the site 2 such that

$$\hat{P}|n_1, n_2\rangle = |n_2, n_1\rangle, \quad (2.1.5)$$

is introduced. An eigenbasis of this operator are the symmetric, $|\psi_+\rangle$, and antisymmetric states, $|\psi_-\rangle$.

$$\hat{P}|\psi_\pm\rangle = \pm|\psi_\pm\rangle \quad (2.1.6)$$

In the context of the Bose-Hubbard Hamiltonian (2.1.1), the basis of the symmetric and antisymmetric states (for N_p odd¹) reads

$$\left\{ \dots, \frac{1}{\sqrt{2}}(|n_1, n_2\rangle + |n_2, n_1\rangle), \dots, \frac{1}{\sqrt{2}}(|n_1, n_2\rangle - |n_2, n_1\rangle), \dots \mid n_1 = 0, 1, \dots, (N_p - 1)/2 \right\}, \quad (2.1.7)$$

with $n_2 = N_p - n_1$.

The Hamiltonian (2.1.1) is invariant under the discrete symmetry \hat{P} . From a physical point of view, it means that this operation has no influence on the underlying dynamics. From a mathematical point of view, if the Hamiltonian commutes with a discrete operator, this Hamiltonian is block diagonal in the operator's eigenbases [66] such that

$$[\hat{H}_0, \hat{P}] = 0 \quad (2.1.8)$$

$$\implies (\hat{H}_0) = \begin{pmatrix} S & 0 \\ 0 & A \end{pmatrix}. \quad (2.1.9)$$

Here S and A are respectively the symmetric and antisymmetric blocks. This property can for instance be used from a numerical point of view. In this context, the matrices that must be diagonalized are twice smaller than that one decomposed in the Fock basis (2.1.3).

2.1.2 Structure of the spectrum

The site permutation operator (2.1.5) turns out to be a symmetry of the unperturbed Hamiltonian (2.1.1). That means that each eigenbasis $\{|\psi_{n_1, n_2}^\pm\rangle\}$ of the Hamiltonian are made of symmetric and antisymmetric states obeying the Schrödinger eigenvalue equation,

$$\begin{aligned} \hat{H}_0|\psi_{n_1, n_2}^\pm\rangle &= \epsilon_{n_1, n_2}^\pm|\psi_{n_1, n_2}^\pm\rangle, & n_1 &= 0, 1, \dots, d^\pm, \\ & & n_2 &= N_p - n_1, \end{aligned} \quad (2.1.10)$$

with $|\psi_{n_1, n_2}^\pm\rangle = \pm|\psi_{n_2, n_1}^\pm\rangle$. Here we have $d^+ = d^- = (N_p - 1)/2$ for N_p odd and $d^+ = N_p/2$ and $d^- = N_p/2 - 1$ for N_p even (more details are given in Appx. A.3). If $U = 0$ in the Hamiltonian (2.1.1), then the atoms do not see each other. There is no interaction and the ultracold gas can be seen as an ideal gas. If $J = 0$, there is no transfer of particles from a site to another one. The system is totally frozen. In this framework, the Fock basis (2.3.5) is an eigenbasis of the Hamiltonian as well as the symmetric and antisymmetric basis (2.1.7). Each eigenvalue of the spectrum, which is solely determined by the non-interacting term $U/2(\hat{a}_1^\dagger\hat{a}_1^\dagger\hat{a}_1\hat{a}_1 + \hat{a}_2^\dagger\hat{a}_2^\dagger\hat{a}_2\hat{a}_2)$, is twice degenerate, meaning that the states $1/\sqrt{2}(|n_1, n_2\rangle \pm |n_2, n_1\rangle)$ have the same eigenvalue.

$$\epsilon_{n_1, n_2}^\pm(J = 0) = \frac{U}{2}(n_1(n_1 - 1) + n_2(n_2 - 1)) \quad (2.1.11)$$

If the hopping is slightly turned on, such that $(N_p + 1)U/J \gg 1$, the symmetric and antisymmetric basis (2.1.7) becomes an approximation of the exact eigenbasis $\{|\psi_{n_1, n_2}^\pm\rangle\}$

¹To build a basis for N_p even, one must add the state $|N_p/2, N_p/2\rangle$ as shown in Eq. (A.3.5). The following reasoning is also correct in this basis.

such that

$$|\psi_{n_1, n_2}^\pm\rangle = \sum_{n'_1=0}^{N_p} c_{n'_1}^\pm |n'_1, n'_2\rangle \quad (2.1.12)$$

$$\simeq \frac{1}{\sqrt{2}}(|n_1, n_2\rangle \pm |n_2, n_1\rangle). \quad (2.1.13)$$

In this configuration, the coupling matrix elements related to J give rise to non-zero (but small) coefficients for $n'_1 \neq n_1$ and $n'_1 \neq n_2$. These non-zero coefficients lead to transitions between the Fock states. Incidentally, as the system is unchanged under the site inversion, we have $c_n^\pm = \pm c_{N_p-n}^\pm$. The coupling between sites removes the degeneracy of each pair of levels. For example, the unperturbed spectrum for $N_p = 5$ and $U/J = 20$ is numerically given by

$$\begin{aligned} \epsilon_{0,5}^- &= 200.06250456J, \\ \epsilon_{0,5}^+ &= 200.06250196J, \\ \epsilon_{1,4}^- &= 120.1527J, \\ \epsilon_{1,4}^+ &= 120.1229J, \\ \epsilon_{2,3}^- &= 82.78J, \\ \epsilon_{2,3}^+ &= 76.81J. \end{aligned} \quad (2.1.14)$$

In this context, the eigenvalues are organized by doublets relatively well separated from each other for which the two-level approximation is still valid. If the system is initially in $|\phi(0)\rangle = |n_1, n_2\rangle$, then it will oscillate between the states $|n_1, n_2\rangle$ and $|n_2, n_1\rangle$. One can thus use the formalism introduced in Appx. C and write the following time evolution,

$$|\phi(t)\rangle = \cos\left(\frac{\Delta\epsilon_{n_1, n_2}}{2\hbar}t\right) |n_1, n_2\rangle + i \sin\left(\frac{\Delta\epsilon_{n_1, n_2}}{2\hbar}t\right) |n_2, n_1\rangle, \quad (2.1.15)$$

with the splitting $\Delta\epsilon_{n_1, n_2} = \epsilon_{n_1, n_2}^- - \epsilon_{n_1, n_2}^+$. Figure 2.1.2 gives an example for which the dynamics is largely dominated by $|0, 5\rangle$ and $|5, 0\rangle$. The time τ_{n_1, n_2} required to obtain a perfectly balanced entangled state,

$$|\phi(\tau_{n_1, n_2})\rangle = \frac{1}{\sqrt{2}}(|n_1, n_2\rangle + i|n_2, n_1\rangle), \quad (2.1.16)$$

is given by

$$\tau_{n_1, n_2} = \frac{\pi\hbar}{2|\Delta\epsilon_{n_1, n_2}|}. \quad (2.1.17)$$

This time is called the entanglement time.

The unperturbed spectrum (2.1.14) shows that the higher the energies are, the smaller the doublet splitting is. It means that the greater the particle difference between sites is, the greater τ_{n_1, n_2} is. Moreover, this time can be expressed in laboratory units for the atomic species ^{87}Rb whose mass is $m = 1.443 \times 10^{-25}$ kg and s-wave scattering length is $a_s = 5.313$ nm. If the wavelength of the lasers used to build the optical lattice is $\lambda = 1064$ nm, we obtain

$$\frac{\hbar}{J} = 4.4 \times 10^{-3} \text{ s}. \quad (2.1.18)$$

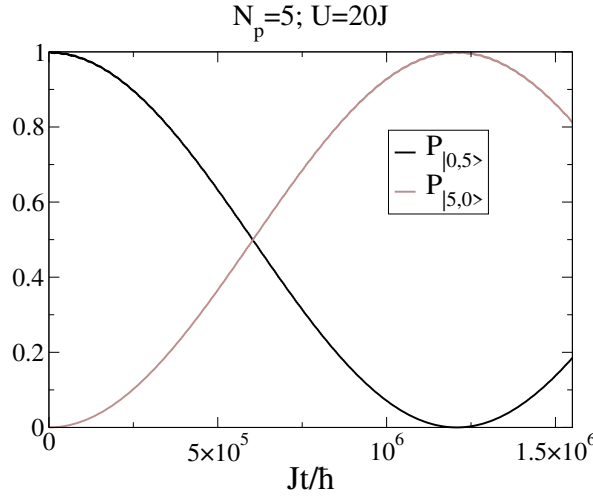


Figure 2.1.2: The numerical detection probabilities are computed for the unperturbed two-site Bose-Hubbard Hamiltonian (2.1.1). This indicates that the two-level approximation is suitable for describing the dynamics. For this example, we have $J\tau_{0,5}/\hbar = 6.0 \times 10^5$.

For the derivation of the result (2.1.18), see Sec. 1.3.3. The evaluations of the entanglement times τ_{n_1, n_2} for spectrum (2.1.14) read

$$\begin{aligned} \tau_{0,5} &= 6.0 \times 10^5 \hbar/J & \longrightarrow & \tau_{0,5} = 2.6 \times 10^3 \text{ s} \\ \tau_{1,4} &= 53 \hbar/J & \longrightarrow & \tau_{1,4} = 0.23 \text{ s} \\ \tau_{2,3} &= 0.26 \hbar/J & \longrightarrow & \tau_{2,3} = 1.1 \times 10^{-3} \text{ s} \end{aligned} \quad (2.1.19)$$

These evaluations illustrate the difficulty to build giant entangled state as τ_{n_1, n_2} increases exponentially with the particle imbalance $|n_1 - n_2|$. Moreover, there is an additional exponential increase with the total number of particles as it will be explained in Sec. 4.2. In a typical optical lattice experiment, the lifetime of a Bose-Einstein condensate has the order of magnitude of 10 s [133]. It means that the entangled states related to $\tau_{2,3}$ and $\tau_{1,4}$ could be observable, but it is definitely not the case for $\tau_{0,5}$. Sections 4.3–4.5 will deal with this problem by studying the effect of an external coupling on the tunneling rate.

2.1.3 Periodically-driven two-site Bose-Hubbard Hamiltonian

A periodic tilting of the double-well potential (see Fig. 2.1.3) characterized by an amplitude δ and a frequency ω is an external perturbation breaking the energy conservation and, thus, breaking the integrability of the system. From an experimental point of view this can be achieved by introducing a periodic modulation of the frequency difference of the lasers designing the optical lattice [131, 134–136],

$$\hat{H}(t) = \hat{H}_0 + \delta \cos(\omega t)(\hat{a}_1^\dagger \hat{a}_1 - \hat{a}_2^\dagger \hat{a}_2). \quad (2.1.20)$$

As shown in the relations (2.1.19), the entanglement time $\tau_{0,5}$ is prohibitively large in comparison to the lifetime of a condensate. One of the goals of this periodic driving is to reduce substantially this entanglement time. This can be achieved by finding the appropriate parameters for the frequency and the amplitude. This question is addressed in Secs. 4.3–4.5.

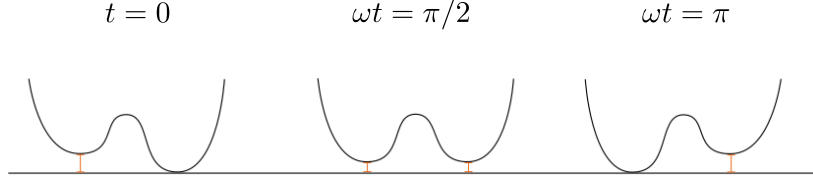


Figure 2.1.3: Schematic representation of the periodic tilting of the double-well potential. Ultracold atoms trapped in this potential are described by the Hamiltonian (2.1.20).

On the opposite side, the external perturbation can be used to prevent the formation of an entangled state, meaning that the entanglement time becomes infinite. This question is addressed in Sec. 2.4.

2.2 Floquet theory

Floquet theory was developed for the first time in 1883 by Floquet [137]. It is a suitable framework to solve the Schrödinger equation with a time-dependent periodic Hamiltonian $\hat{H}(t) = \hat{H}_0 + \hat{V}(t)$,

$$i\hbar \frac{d}{dt} |\psi(t)\rangle = \hat{H}(t) |\psi(t)\rangle. \quad (2.2.1)$$

Knowing that T is the periodicity of the Hamiltonian such that $\hat{H}(t+T) = \hat{H}(t)$, it can be decomposed in Fourier series,

$$\hat{H}(t) = \sum_{k=-\infty}^{\infty} \hat{H}_k e^{ik\omega t}, \quad (2.2.2)$$

$$\hat{H}_k = \frac{1}{T} \int_{-T/2}^{T/2} \hat{H}(t) e^{-ik\omega t} dt, \quad (2.2.3)$$

where $\omega = 2\pi/T$ is the frequency, and \hat{H}_k are the Fourier coefficients.

The periodicity insures that the solutions of (2.2.1) (denoted with $\nu \in \mathbb{Z}$) are given by the combination of an imaginary exponential and a function, $|u_\nu(t)\rangle = |u_\nu(t+T)\rangle$, with the periodicity of $\hat{H}(t)$ [138] (see Appx. A.1 for a demonstration),

$$|\psi_\nu(t)\rangle = e^{-i\epsilon_\nu t/\hbar} |u_\nu(t)\rangle, \quad (2.2.4)$$

with ϵ_ν the quasienergies, which perform the time translation over one period through $|\psi_\nu(t+T)\rangle = e^{-i\epsilon_\nu T/\hbar} |\psi_\nu(t)\rangle$. The Schrödinger equation becomes [131]

$$\left(\hat{H}(t) - i\hbar \frac{d}{dt} \right) |u_\nu(t)\rangle = \epsilon_\nu |u_\nu(t)\rangle. \quad (2.2.5)$$

By means of the following Fourier series, $|u_\nu(t)\rangle = \sum_{k=-\infty}^{\infty} e^{ik\omega t} |\tilde{u}_{\nu,k}\rangle$, the time-dependent Schrödinger equation becomes a time-independent eigenvalue problem,

$$\sum_{k'=-\infty}^{+\infty} \left(\hat{H}_{k-k'} + k\hbar\omega \delta_{kk'} \hat{1} \right) |\tilde{u}_{\nu,k'}\rangle = \epsilon_\nu |\tilde{u}_{\nu,k}\rangle. \quad (2.2.6)$$

The knowledge of the Fourier coefficients \hat{H}_k makes it possible to calculate the quasienergies ϵ_ν and the associated eigenvectors $(|f_\nu\rangle) = (\dots, (|\tilde{u}_{\nu,-1}\rangle), (|\tilde{u}_{\nu,0}\rangle), (|\tilde{u}_{\nu,1}\rangle), \dots)^T$. It corresponds to the diagonalization of the Floquet matrix.

$$(\hat{F}) = \left(\hat{H}_{k-k'} + k\hbar\omega\delta_{kk'}\hat{1} \right) = \begin{pmatrix} \ddots & \vdots & \vdots & \vdots & \\ \dots & (\hat{H}_0) + (k-1)\hbar\omega & (\hat{H}_1) & (\hat{H}_2) & \dots \\ \dots & (\hat{H}_{-1}) & (\hat{H}_0) + k\hbar\omega & (\hat{H}_1) & \dots \\ \dots & (\hat{H}_{-2}) & (\hat{H}_{-1}) & (\hat{H}_0) + (k+1)\hbar\omega & \dots \\ \vdots & \vdots & \vdots & \vdots & \ddots \end{pmatrix}. \quad (2.2.7)$$

By using the expression of the Hermitian Floquet matrix (2.2.7), the eigenvalue problem (2.2.6) can be expressed in a more concise way,

$$\hat{F}|f_\nu\rangle = \epsilon_\nu|f_\nu\rangle. \quad (2.2.8)$$

If $|u_\nu(t)\rangle$ solves Eq. (2.2.5) with the eigenvalue ϵ_ν , then $e^{in\omega t}|u_\nu(t)\rangle$ is also a solution with the eigenvalue $\epsilon_\nu + n\hbar\omega$. The following equation,

$$\left(\hat{H}(t) - i\frac{d}{dt} \right) e^{in\omega t}|u_\nu(t)\rangle = (\epsilon_\nu + n\hbar\omega)e^{in\omega t}|u_\nu(t)\rangle, \quad (2.2.9)$$

highlights the fact that the Floquet spectrum has a $\hbar\omega$ periodicity. Inside a $\hbar\omega$ range there are d quasienergies (d is assumed to be a finite number) such that $\epsilon_{\nu+nd} = \epsilon_\nu + n\hbar\omega$ and $|u_{\nu+nd}(t)\rangle = e^{in\omega t}|u_\nu(t)\rangle$. For the previous property, the quasienergies must be organized in ascending order. Moreover, the following expansion,

$$|u_{\nu+nd}(t)\rangle = \sum_{k=-\infty}^{\infty} e^{i(k+n)\omega t}|\tilde{u}_{\nu,k}\rangle \quad (2.2.10)$$

$$= \sum_{k=-\infty}^{\infty} e^{ik\omega t}|\tilde{u}_{\nu,k-n}\rangle, \quad (2.2.11)$$

indicates that $|u_\nu(t)\rangle$ and $|u_{\nu+nd}(t)\rangle$ are the same except that the Fourier coefficients are shifted of n elements. The structure of the matrix (2.2.7) shows that d is the dimension of the Hilbert space related to the unperturbed Hamiltonian \hat{H}_0 such that $d = \dim\hat{H}_0$.

The Floquet eigenvectors $|f_\nu\rangle$ are orthonormal by construction such that

$$\langle f_\nu | f_{\nu'+nd} \rangle = \sum_{k=-\infty}^{\infty} \langle \tilde{u}_{\nu,k} | \tilde{u}_{\nu',k-n} \rangle = \delta_{\nu,\nu'}\delta_{n,0}. \quad (2.2.12)$$

The indices ν and ν' refer to eigenvectors of a same block while the index nd enables one to make jump between these blocks. This leads to the equation

$$\langle u_\nu(0) | u_{\nu'}(0) \rangle = \sum_{k,k'=-\infty}^{\infty} \langle \tilde{u}_{\nu,k} | \tilde{u}_{\nu',k'} \rangle = \delta_{\nu,\nu'}. \quad (2.2.13)$$

This implies that the eigenvectors $|u_\nu(nT)\rangle$ satisfy the orthonormality relation with n integer. To obtain the orthonormality relation for all t , it is convenient to introduce the extended

Hilbert space $\mathcal{H} \otimes \mathcal{T}$ made of \mathcal{H} , the Hilbert space, and \mathcal{T} , the space of all time-periodic functions with the period T [139]. In this extended Hilbert space, the time is regarded as a coordinate such that the scalar product in this space is defined as $\langle\langle \cdot | \cdot \rangle\rangle = 1/T \int_0^T \langle \cdot | \cdot \rangle dt$. In this framework, the eigenvectors $|u_\nu(t)\rangle$ obey the orthonormality relation in the extended Hilbert space. This reads

$$\langle\langle u_\nu(t) | u_{\nu'}(t) \rangle\rangle = \frac{1}{T} \int_0^T dt \sum_{k,k'=-\infty}^{\infty} e^{i(k'-k)\omega t} \langle \tilde{u}_{\nu,k} | \tilde{u}_{\nu',k'} \rangle = \delta_{\nu,\nu'}. \quad (2.2.14)$$

Floquet theory consists in solving the time-independent Floquet equation (2.2.8) in order to solve the time-dependent Schrödinger equation (2.2.1). This eigenvalue problem gives rise to the quasienergies ϵ_ν and the Floquet eigenstates $|f_\nu\rangle$ enabling to build the solutions $|u_\nu(t)\rangle$. While the Floquet spectrum is infinite, it displays a $\hbar\omega$ periodicity, and $\dim \hat{H}_0$ is the number of quasienergies inside a range $\hbar\omega$. Moreover, two $\hbar\omega$ -related quasienergies have the same Floquet eigenstate with a shift. A time-periodic basis of solution of (2.2.5) is thus given by

$$\left\{ |u_\nu(t)\rangle = \sum_{k=-\infty}^{+\infty} e^{ik\omega t} |\tilde{u}_{\nu,k}\rangle \mid \zeta \leq \epsilon_\nu < \hbar\omega + \zeta \right\}, \quad (2.2.15)$$

where $\zeta \in \mathbb{R}$ is an arbitrary constant. In this framework, any $|\phi(t)\rangle$ can be decomposed in the time-periodic basis (2.2.15),

$$|\phi(t)\rangle = \sum_{\nu=1}^d c_\nu(t) |u_\nu(t)\rangle \quad (2.2.16)$$

$$= \sum_{\nu=1}^d c_\nu(t_0) e^{-i\epsilon_\nu(t-t_0)/\hbar} |u_\nu(t)\rangle, \quad (2.2.17)$$

with $c_\nu(t_0) = \langle u_\nu(t_0) | \phi(t_0) \rangle$ and t_0 the initial time.

2.3 Floquet theory for a periodic tilting of the double-well potential

The time-dependent Hamiltonian (2.1.20) describes a two-mode system with a periodic oscillation of the double-well potential. It reads

$$\hat{H}(t) = \hat{H}_0 + \delta \cos(\omega t) (\hat{a}_1^\dagger \hat{a}_1 - \hat{a}_2^\dagger \hat{a}_2). \quad (2.3.1)$$

In this case, the Fourier decomposition is determined by the only mode ω ,

$$\hat{H}(t) = \hat{H}_0 + \hat{H}_1 e^{i\omega t} + \hat{H}_{-1} e^{-i\omega t}, \quad (2.3.2)$$

$$\hat{H}_1 = \hat{H}_{-1} = \frac{\delta}{2} (\hat{a}_1^\dagger \hat{a}_1 - \hat{a}_2^\dagger \hat{a}_2). \quad (2.3.3)$$

The non-zero blocks of the Floquet matrix (2.2.7) are only the diagonal blocks and the blocks just above and under the diagonal.

$$(\hat{F}) = \begin{pmatrix} \ddots & \vdots & \vdots & \vdots & \\ \dots & (\hat{H}_0) + (k-1)\hbar\omega & (\hat{H}_1) & 0 & \dots \\ \dots & (\hat{H}_{-1}) & (\hat{H}_0) + k\hbar\omega & (\hat{H}_1) & \dots \\ \dots & 0 & (\hat{H}_{-1}) & (\hat{H}_0) + (k+1)\hbar\omega & \dots \\ \vdots & \vdots & \vdots & \vdots & \ddots \end{pmatrix}. \quad (2.3.4)$$

In order to build the Floquet matrix, a basis of the unperturbed system must be chosen. A simple basis is the collection of Fock states that take into account the conservation of the number of particles,

$$\{|n, N_p - n\rangle \mid n = 0, 1, 2, \dots, N_p\}. \quad (2.3.5)$$

Here the Fock state $|n_1, n_2\rangle$ represents a state with n_1 particles on site 1 and n_2 particles on site 2. Appendix A.2 presents the representations of the Fourier coefficients \hat{H}_k inside this basis.

2.3.1 Discrete symmetry and Floquet matrix

As in the unperturbed case, one can take advantage of the discrete symmetry of the system to simplify the Floquet matrix to diagonalize. Actually, the Hamiltonian (2.3.1) becomes invariant under the site permutation \hat{P} if this transformation is followed by the time translation $t \rightarrow t + T/2$. As in the unperturbed case, we will see in this section that the Floquet matrix is still separable in two blocks.

The idea is to use the symmetry-adapted basis (2.1.7) to decompose the different Floquet modes. As shown previously in Sec. 2.1.1 the unperturbed system is invariant under \hat{P} leading to

$$[\hat{H}_0, \hat{P}] = 0 \quad (2.3.6)$$

$$\implies (\hat{H}_0) = \left(\begin{array}{c|c} S & 0 \\ \hline 0 & A \end{array} \right). \quad (2.3.7)$$

The first mode (2.3.3) of the perturbed Hamiltonian anticommutes with \hat{P} , meaning that \hat{H}_1 is block counterdiagonal.

$$\{\hat{H}_1, \hat{P}\} = 0 \quad (2.3.8)$$

$$\implies (\hat{H}_1) = \left(\begin{array}{c|c} 0 & C \\ \hline C^\dagger & 0 \end{array} \right) \quad (2.3.9)$$

Here the block C couples the symmetric and antisymmetric states. As the matrix (\hat{H}_1) is symmetric, we have $C^\dagger = C$.

By combining the different Fourier coefficients \hat{H}_0 and \hat{H}_1 , the Floquet matrix (2.3.4) is formed, and it conserves the same shape as Eq. (2.3.6) after the reorganization of the blocks,

$$(\hat{F}) = \left(\begin{array}{c|c} F_S & 0 \\ \hline 0 & F_A \end{array} \right), \quad (2.3.10)$$

with

$$F_S = \begin{pmatrix} \ddots & \ddots & & & & & \\ \ddots & S_{-2} & C & & & & \\ & C & A_{-1} & C & & & \\ & & C & S_0 & C & & \\ & & & C & A_1 & C & \\ & & & & C & S_2 & \ddots \\ & & & & & \ddots & \ddots \end{pmatrix}, \quad (2.3.11)$$

$$F_A = \begin{pmatrix} \ddots & \ddots & & & & & \\ \ddots & A_{-2} & C & & & & \\ & C & S_{-1} & C & & & \\ & & C & A_0 & C & & \\ & & & C & S_1 & C & \\ & & & & C & A_2 & \ddots \\ & & & & & \ddots & \ddots \end{pmatrix}. \quad (2.3.12)$$

Here we have $S_k = S + k\hbar\omega\mathbb{1}$ and $A_k = A + k\hbar\omega\mathbb{1}$. By taking into account the symmetry, it is now possible to performing a separate diagonalization of the Floquet matrix. Appendix A.3 presents in more details the decomposition of the Floquet matrix of the two-site Bose-Hubbard Hamiltonian (2.1.20) into the symmetric and antisymmetric basis

2.3.2 Structure of the Floquet spectrum

A time-dependent perturbation breaks the conservation of energy. Nevertheless, if the perturbation is time periodic, it is still possible to define an eigenvalue Schrödinger equation in terms of the quasienergies ϵ_ν as shown in Eq. (2.2.5). The quasienergies are obtained through the diagonalization of the Floquet matrix (2.3.4) and display a periodicity $\hbar\omega$. A basis of the perturbed system can be built by focusing only on the Floquet eigenvectors related to the quasienergies of a Floquet block. This block is characterized by a width $\hbar\omega$. The unperturbed block is now coupled with other blocks through the amplitude of the driving. In this context, one expect that the unperturbed spectrum (2.1.14), for instance, will be modified owing to the presence of the other frequency-shifted Floquet blocks.

In the strong on-site interaction regime with a small perturbation, the Floquet eigenvectors can still be associated to the elements of the symmetry-adapted basis,

$$|u_{n_1, n_2}^\pm(t)\rangle \sim \frac{1}{\sqrt{2}}(|n_1, n_2\rangle \pm |n_2, n_1\rangle). \quad (2.3.13)$$

Here the symbol \pm refer to the two symmetric block of the Floquet matrix. Here $+$ refers to F_S , for which the symmetric unperturbed block S is centered, and $-$ refers to F_A , for which the antisymmetric unperturbed A block is centered. In this context, the quasienergies ϵ_ν^\pm can be denoted by ϵ_{n_1, n_2}^\pm (we keep the same symbols as those for the unperturbed energies to not overload the notations). Therefore, the two-level approximation Eq. (2.1.15) is still valid. The question now is how the driving parameters, namely δ and ω will influence the tunneling rate $\Delta\epsilon_{n_1, n_2}$. This modification will modify the typical timescale required to form an entangled state.

2.4 Coherent renormalization and destruction of tunneling

2.4.1 High-frequency regime

In Refs. [131, 135], it is shown that an external coupling applied to an optical lattice of any number of sites is able to perform a phase transition between Mott insulator and superfluid regime. The cosinusoidal driving produces a linear shaking of the optical lattice potential. A sufficiently large frequency of the driving induces a renormalization of the hopping such that the Bose-Hubbard system is now described by an effective hopping,

$$J_{\text{eff}} = J \mathcal{J}_0 \left(\frac{2\delta}{\hbar\omega} \right), \quad (2.4.1)$$

where \mathcal{J}_0 is the Bessel function of order 0². The periodic system is still described by the same model as the unperturbed one with the transformation $J \rightarrow J_{\text{eff}}$. The external coupling is able to totally destroy tunneling. This destruction is given by the zeros of the Bessel function and can be tracked in the Floquet spectrum when different bunches of quasienergies become degenerate [131, 134, 140]. In the two-site Bose-Hubbard case, the signature of this phenomenon is the degeneracies of the quasienergies of each doublet. Prior to these studies, the phenomenon of dynamic localization due to an external driving was studied for charged particle in a discrete lattice [141] and for a quartic double-well potential [142], to mention two examples.

The renormalization (2.4.1) is obtained when the periodic perturbation of the optical lattice is applied to the level of the on-site energies. Different renormalizations can be achieved for other configurations of the optical lattice. For instance, some specific linear tilts of the optical lattice potential beside the periodic modulation of the on-site energies lead to a renormalization with Bessel functions of different orders such that $J_{\text{eff}} \sim \mathcal{J}_n(2\delta/(\hbar\omega))$ [136]. On the other side, the periodic modulation of the on-site interaction leads to Bessel functions with an argument depending on the population imbalance such that $J_{\text{eff}} \sim \mathcal{J}_0(u(n_1 - n_2))$, where u is a constant depending on the on-site interaction [140, 143, 144]. This kind of periodic modulation can be achieved for instance by tuning a magnetic field close to a Feshbach resonance [19, 144]. All of these articles deal with the coherent control of tunneling in high frequency regime. We will derive the renormalization (2.4.1) in our case of interest, namely the two-site Bose-Hubbard model. Then, we will present our original contribution into this research field by showing how it is possible to coherently switch on and off an entangled state.

The representation of the Hamiltonian (2.1.20) in the Fock basis $\{|n_1, n_2\rangle\}$ reads

$$\left(\hat{H}(t) \right) = \begin{pmatrix} \ddots & -J\sqrt{n_1(n_2+1)} & 0 \\ -J\sqrt{n_1(n_2+1)} & (n_1 - n_2)\delta \cos(\omega t) & -J\sqrt{n_2(n_1+1)} \\ 0 & +U/2 [n_1(n_1-1) + n_2(n_2-1)] & \ddots \end{pmatrix}.$$

²The Bessel function of order N is defined as

$$\mathcal{J}_N(x) = \frac{1}{2\pi} \int_0^{2\pi} dt e^{-i(Nt - x \sin t)}, \quad (2.4.2)$$

with the property $\mathcal{J}_0(-x) = \mathcal{J}_0(x)$.

The temporal evolution of any state through the action of the Hamiltonian can be decomposed in the Fock basis as follows

$$|\psi(t)\rangle = \sum_{n_1=0}^{N_p} \psi_{n_1, n_2}(t) |n_1, n_2\rangle. \quad (2.4.3)$$

In this framework, the Schrödinger equation can be written in terms of the coefficients $\psi_{n_1, n_2}(t)$, which gives rise to $N_p + 1$ coupled equations,

$$\begin{aligned} i\hbar \frac{\partial}{\partial t} \psi_{n_1, n_2}(t) = & -J \left(\sqrt{n_1(n_2+1)} \psi_{n_1-1, n_2+1}(t) + \sqrt{n_2(n_1+1)} \psi_{n_1+1, n_2-1}(t) \right) \\ & + (n_1 - n_2) \delta \cos(\omega t) \psi_{n_1, n_2}(t) \\ & + \frac{U}{2} [n_1(n_1-1) + n_2(n_2-1)] \psi_{n_1, n_2}(t), \end{aligned} \quad (2.4.4)$$

with $n_1 = 0, 1, \dots, N_p$ and $n_2 = N_p - n_1$. The following gauge transformation is used,

$$\psi_{n_1, n_2}(t) = \phi_{n_1, n_2}(t) \exp \left(-\frac{i\delta}{\hbar\omega} (n_1 - n_2) \sin(\omega t) \right), \quad (2.4.5)$$

in order to obtain

$$\begin{aligned} i\hbar \frac{\partial}{\partial t} \phi_{n_1, n_2}(t) = & -J \left(\sqrt{n_1(n_2+1)} \exp \left(\frac{i\delta}{\hbar\omega} 2 \sin(\omega t) \right) \phi_{n_1-1, n_2+1}(t) \right. \\ & \left. + \sqrt{n_2(n_1+1)} \exp \left(-\frac{i\delta}{\hbar\omega} 2 \sin(\omega t) \right) \phi_{n_1+1, n_2-1}(t) \right) \\ & + \frac{U}{2} [n_1(n_1-1) + n_2(n_2-1)] \phi_{n_1, n_2}(t). \end{aligned} \quad (2.4.6)$$

This local gauge transformation doesn't change the experimental expectation values as $|\langle n_1, n_2 | \psi(t) \rangle|^2 = |\langle n_1, n_2 | \phi(t) \rangle|^2$ with $|\phi(t)\rangle = \sum_{n_1=0}^{N_p} \phi_{n_1, n_2}(t) |n_1, n_2\rangle$.

In the high-frequency regime, there are two time-evolution scales given by the fast oscillation of the sinus in the argument of the exponential and the slow oscillation of $\phi_{n_1, n_2}(t)$, which is roughly constant on the time-interval $T = 2\pi/\omega$. This leads to³

$$\frac{1}{T} \int_t^{t+T} \phi_{n_1, n_2}(t') dt' \simeq \phi_{n_1, n_2}(t). \quad (2.4.7)$$

Therefore, T is infinitesimal from the timescale point of view of $\phi_{n_1, n_2}(t)$. The integration of Eq. (2.4.6) on a period of the driving by taking into account Eq. (2.4.7) leads to

$$\begin{aligned} i\hbar \frac{\partial}{\partial t} \phi_{n_1, n_2}(t) = & -J_{\text{eff}} \left(\sqrt{n_1(n_2+1)} \phi_{n_1-1, n_2+1}(t) + \sqrt{n_2(n_1+1)} \phi_{n_1+1, n_2-1}(t) \right) \\ & + \frac{U}{2} [n_1(n_1-1) + n_2(n_2-1)] \phi_{n_1, n_2}(t), \end{aligned}$$

with $J_{\text{eff}} = J \mathcal{J}_0(\frac{2\delta}{\hbar\omega})$. These equations are exactly the same as those obtained in the unperturbed case with the transformation $J \rightarrow J_{\text{eff}}$.

³For any integrable function $f(t)$, we have $\lim_{T \rightarrow 0} \frac{1}{T} \int_t^{t+T} f(t') dt' = f(t)$.

Therefore, as announced above, the perturbed system in the high-frequency regime is described like the unperturbed one with the transformation $J \rightarrow J_{\text{eff}}$. The Hamiltonian in the high-frequency regime reads

$$\hat{H}_{(\omega \gg)} = -J_{\text{eff}}(\hat{a}_1^\dagger \hat{a}_2 + \hat{a}_2^\dagger \hat{a}_1) + \frac{U}{2}(\hat{a}_1^\dagger \hat{a}_1^\dagger \hat{a}_1 \hat{a}_1 + \hat{a}_2^\dagger \hat{a}_2^\dagger \hat{a}_2 \hat{a}_2). \quad (2.4.8)$$

This Hamiltonian takes a specific form in the Fock basis,

$$\left(\hat{H}_{(\omega \gg)} \right) = \begin{pmatrix} \frac{U}{2} N_p (N_p - 1) & -J_{\text{eff}} \sqrt{N_p} & & \\ -J_{\text{eff}} \sqrt{N_p} & \frac{U}{2} (N_p - 1)(N_p - 2) & -J_{\text{eff}} \sqrt{2(N_p - 1)} & \\ & -J_{\text{eff}} \sqrt{2(N_p - 1)} & \ddots & \end{pmatrix}, \quad (2.4.9)$$

which is symmetric and displays a discrete symmetric with respect to the counterdiagonal.

In the strong interaction regime $(N_p + 1)U/J \gg 1$, the eigenvalues are largely determined by the on-site interaction term such that $\epsilon_{n_1, n_2}^\pm \simeq U/2(n_1(n_1 - 1) + n_2(n_2 - 1))$. In the repulsive interaction case, the maximal eigenvalues correspond to the states where all particles are located on a site. By contrast, the minimum eigenvalues are the states where the particle difference is minimal. It becomes possible to approximately compute the width of the unperturbed spectrum,

$$L(U) = \epsilon_{0, N_p} - \epsilon_{N_p/2, N_p/2} \simeq N_p^2 \frac{U}{4}. \quad (2.4.10)$$

When the perturbation is turned on, the Floquet blocks will be mixed if the frequency is smaller than the width of the spectrum, i.e. $\hbar\omega \lesssim L(U)$. By contrast, the high-frequency regime can be defined when the Floquet blocks are relatively well separated, i.e. when the frequency is larger than the width, $\hbar\omega \gtrsim L(U)$.

The modification of the splitting $\Delta\epsilon_{n_1, n_2}$ in the context of a fast driving will depend on the number of steps to reach $|n_2, n_1\rangle$ from $|n_1, n_2\rangle$. As the hopping transfers the particles one by one, the most direct path for $n_1 < n_2$ reads

$$|n_1, n_2\rangle \rightarrow |n_1 + 1, n_2 - 1\rangle \rightarrow \dots \rightarrow |n_2, n_1\rangle. \quad (2.4.11)$$

The matrix (2.4.9) can be truncated by taking into account the dominant path which connects $|n_1, n_2\rangle$ with $|n_2, n_1\rangle$.

• Splitting of the population imbalance one, $\Delta\epsilon_{n, n+1}$

An analytical result for the splitting $\Delta\epsilon_{n, n+1} = \epsilon_{n, n+1}^- - \epsilon_{n, n+1}^+$ can be derived. To achieve that, the matrix (2.4.9) is truncated by keeping the dominant path which connects $|n, n+1\rangle$ with $|n+1, n\rangle$, meaning that its decomposition in the truncated subspace $\{|n, n+1\rangle, |n+1, n\rangle\}$ reads

$$\begin{pmatrix} U_1 & J_1 \\ J_1 & U_1 \end{pmatrix}. \quad (2.4.12)$$

The eigenvalues are $\epsilon_{n, n+1}^\pm = U_1 \pm J_1$, which leads to the splitting $\Delta\epsilon_{n, n+1} = -2J_1$.

In the specific case of $n = 2$, we have $U_1 = 4U$ and $J_1 = -3J_{\text{eff}}$ such that

$$\Delta\epsilon_{2,3}(\delta) = 6J\mathcal{J}_0\left(\frac{2\delta}{\hbar\omega}\right). \quad (2.4.13)$$

This relation is coherent with Eq. (2.4.1), which both describe the transfer of only one particle. The results of Fig. 2.4.1 is obtained through the diagonalization of the Floquet matrix (2.3.4) for $N_p = 5$, $U/J = 20$ and $\hbar\omega/J = 200$. It enables one to compare the analytical result in orange with the numerical computation of the splitting $\Delta\epsilon_{2,3}$ in black.

• Splitting of the population imbalance two, $\Delta\epsilon_{n,n+2}$

There are two steps to connect $|n, n+2\rangle$ to $|n+2, n\rangle$ with $n = N_p/2 - 1$. In this case, the truncation of the matrix (2.4.9) in the symmetric and antisymmetric subspace $\{1/\sqrt{2}(|n, n+2\rangle + |n+2, n\rangle), |n+1, n+1\rangle, 1/\sqrt{2}(|n, n+2\rangle - |n+2, n\rangle)\}$ reads

$$\begin{pmatrix} U_1 & J_1 & \\ J_1 & U_2 & \\ & & U_1 \end{pmatrix}. \quad (2.4.14)$$

The only antisymmetric eigenvalue reads $\epsilon_{n,n+2}^- = U_1$. Owing to the strong inter-atomic interaction, $(N_p + 1)U/J \gg 1$, the eigenvalues for the symmetric block can be evaluated up to the order one,

$$\epsilon_{\pm}^+ \simeq U_{1,2} \pm \frac{J_1^2}{U_1 - U_2}, \quad (2.4.15)$$

with $\epsilon_+^+ = \epsilon_{n,n+2}^+$. The splitting gives rise to

$$\Delta\epsilon_{n,n+2} \simeq -\frac{J_1^2}{U_1 - U_2}. \quad (2.4.16)$$

In the specific case of $n = 2$, we have $U_1 = 7U$, $U_2 = 6U$ and $J_1 = -\sqrt{12}J_{\text{eff}}$ such that

$$\Delta\epsilon_{2,4}(\delta) = -\frac{12J^2}{U} \mathcal{J}_0^2\left(\frac{2\delta}{\hbar\omega}\right). \quad (2.4.17)$$

• Splitting of the population imbalance three, $\Delta\epsilon_{n,n+3}$

There are three steps to connect $|n, n+3\rangle$ to $|n+3, n\rangle$. In this case, the truncation of the matrix (2.4.9) in the symmetric and antisymmetric subspace $\{1/\sqrt{2}(|n, n+3\rangle + |n+3, n\rangle), 1/\sqrt{2}(|n-1, n+2\rangle + |n+2, n-1\rangle), 1/\sqrt{2}(|n, n+3\rangle - |n+3, n\rangle), 1/\sqrt{2}(|n-1, n+2\rangle - |n+2, n-1\rangle)\}$ reads

$$\begin{pmatrix} U_1 & J_1 & & \\ J_1 & U_2 + J_2 & & \\ & & U_1 & J_1 \\ & & J_1 & U_2 - J_2 \end{pmatrix}. \quad (2.4.18)$$

The four eigenvalues can be calculated,

$$\epsilon_{\pm}^+ = \frac{U_1 + U_2 + J_2}{2} \pm \sqrt{\frac{(U_1 - U_2 - J_2)^2}{4} + J_1^2} \quad (2.4.19)$$

$$\epsilon_{\pm}^- = \frac{U_1 + U_2 - J_2}{2} \pm \sqrt{\frac{(U_1 - U_2 + J_2)^2}{4} + J_1^2}, \quad (2.4.20)$$

with $\epsilon_+^+ = \epsilon_{n,n+3}^+$ and $\epsilon_+^- = \epsilon_{n,n+3}^-$. Owing to the strong inter-atomic interaction, $(N_p + 1)U/J \gg 1$, and $U_1 > U_2$, the eigenvalues of interest can be evaluated up to the order one,

$$\epsilon_{n,n+3}^\pm \simeq U_1 + \frac{J_1^2}{U_1 - U_2 \mp J_2}. \quad (2.4.21)$$

The splitting at leading order is given by

$$\Delta\epsilon_{n,n+3} \simeq -\frac{2J_1^2 J_2}{(U_1 - U_2)^2}. \quad (2.4.22)$$

In the specific case of $n = 1$, we have $U_1 = 6U$, $U_2 = 4U$, $J_1 = -\sqrt{8}J_{\text{eff}}$ and $J_2 = -3J_{\text{eff}}$ such that

$$\Delta\epsilon_{1,4}(\delta) = \frac{12J^3}{U^2} \mathcal{J}_0^3\left(\frac{2\delta}{\hbar\omega}\right). \quad (2.4.23)$$

Figure 2.4.1 obtained through the diagonalization of the Floquet matrix (2.3.4) for $N_p = 5$, $U/J = 20$ and $\hbar\omega/J = 200$ illustrates this result valid in the high-frequency regime.

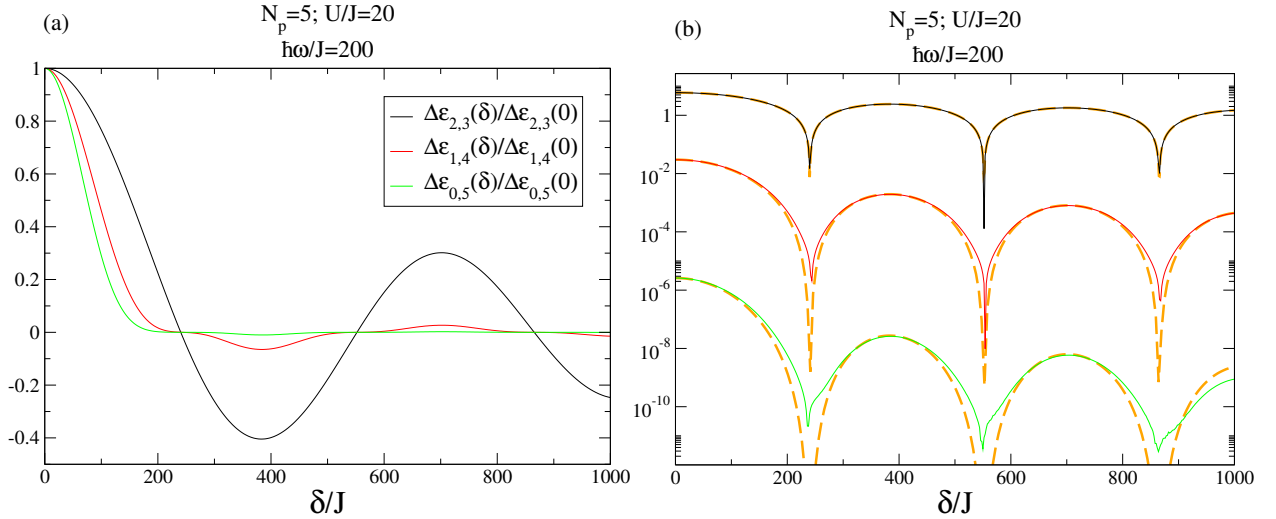


Figure 2.4.1: Energy splittings as a function of the amplitude of the perturbation. Panel (b) represents the absolute values of the energy splittings $|\Delta\epsilon_{2,3}(\delta)|$, $|\Delta\epsilon_{1,4}(\delta)|$ and $|\Delta\epsilon_{0,5}(\delta)|$ in black, red and green respectively. The dashed orange curves are the analytical functions (2.4.24). In the high-frequency regime, the splittings behave like Bessel functions with different exponents depending on the occupation number as displayed in the relation (2.4.24). This figure was obtained by computing the quasienergies associated to the time-periodic two-site Bose-Hubbard Hamiltonian (2.1.20).

• Splitting of the population imbalance k , $\Delta\epsilon_{n,n+k}$

When generalizing the splitting to $\Delta\epsilon_{n,n+k}$, it appears that it behaves like a Bessel function whose exponent is equal to the number of steps to connect $|n, n+k\rangle$ with $|n+k, n\rangle$, i.e. k steps. Therefore, the above results can be generalized as follows

$$\frac{\Delta\epsilon_{n,n+k}(\delta)}{\Delta\epsilon_{n,n+k}(0)} \simeq \mathcal{J}_0^k\left(\frac{2\delta}{\hbar\omega}\right). \quad (2.4.24)$$

This relation describes how the creation of the entangled states is influenced through the application of an external driving in the high-frequency regime. By contrast, the renormal-

ization (2.4.1) describes how the tunneling will be effected globally. Obviously, both results are not contradictory as $J_{\text{eff}} = 0$ implies automatically that all splittings will be equal to zero.

The unperturbed parameters (N_p and U/J) related to Fig. 2.4.1 are the same as those used to compute the unperturbed spectrum (2.1.14). By means of the relation (2.1.17), it is possible to compute the entanglement time τ_{n_1, n_2} , which are displayed in Eq. (2.1.19). Here $\tau_{2,3}(0)$ and $\tau_{1,4}(0)$ are smaller than one second. That is why it could be possible to experimentally reproduce Fig. 2.4.1, except for $\Delta\epsilon_{0,5}(0)$ for which $\tau_{0,5}(0)$ exceeds largely 10 s. This order of magnitude corresponds roughly to the lifetime of a Bose-Einstein condensate in an optical lattice [133].

2.4.2 Low-frequency regime

The heuristic result presented in this section was guessed from the numerical simulations. Further exploration and a better understanding of the low-frequency regime should lead to a more solid derivation. In the low-frequency regime (i.e. $L(U) \gg \hbar\omega/J$), there is no global renormalization like the one displayed in Eq. (2.4.1). Nevertheless, Fig. 2.4.2 seems to indicate that, for some range of parameters, the splittings still behave like Bessel functions as follows

$$\frac{\Delta\epsilon_{n,n+k}(\delta)}{\Delta\epsilon_{n,n+k}(0)} \simeq \mathcal{J}_0\left(k \frac{2\delta}{\hbar\omega}\right). \quad (2.4.25)$$

In this case, the zeros of the different Bessel function do not appear for the same δ , meaning that some transitions are prohibited and others are possible for a same amplitude of the perturbation.

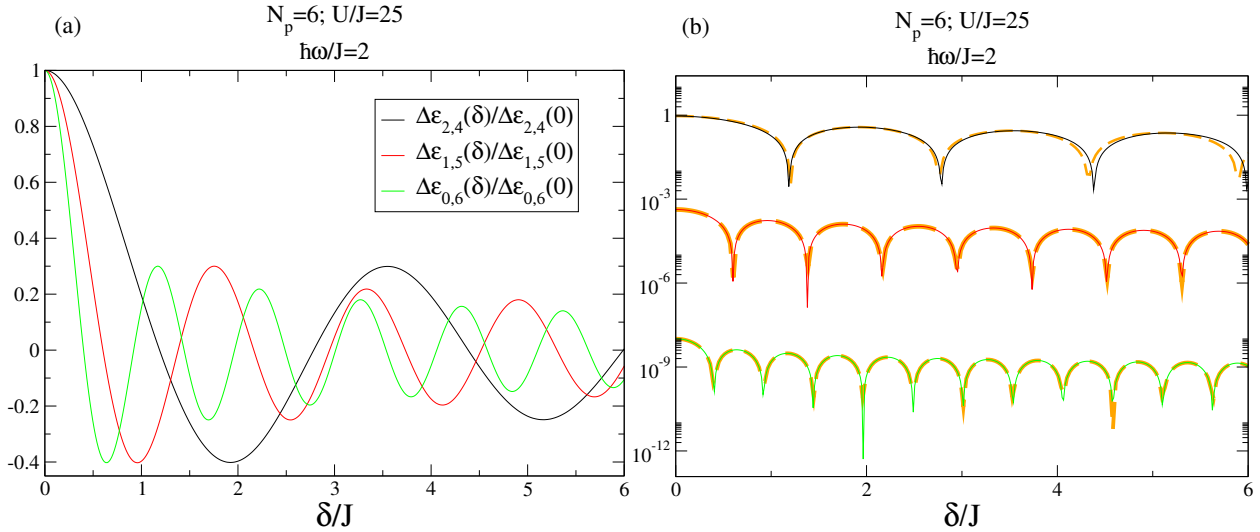


Figure 2.4.2: Energy splittings as a function of the amplitude of the perturbation. Panel (b) represents the absolute values of the energy splittings $|\Delta\epsilon_{2,4}(\delta)|$, $|\Delta\epsilon_{1,5}(\delta)|$ and $|\Delta\epsilon_{0,6}(\delta)|$ in black, red and green respectively. The dashed orange curves are the analytical functions (2.4.25). In the low-frequency regime, the splittings seem to behave like Bessel functions whose argument depends on the occupation number as displayed in the relation (2.4.25). This figure was obtained by computing the quasienergies associated to the time-periodic two-site Bose-Hubbard Hamiltonian (2.1.20).

We are going to present a model able to reproduce the result (2.4.25). We assume that we are in the strong interaction regime $(N_p + 1)U/J \gg 1$, where the two states $|n, n+k\rangle$

and $|n + k, n\rangle$ are coupled by an effective coupling matrix element V . This coupling takes into account all perturbations of the other Fock states. The truncated Hamiltonian in the basis $\{|n, n + k\rangle, |n + k, n\rangle\}$ reads

$$\begin{pmatrix} -k\delta \cos(\omega t) & V \\ V & k\delta \cos(\omega t) \end{pmatrix}. \quad (2.4.26)$$

Any state is decomposed in this basis according to $|\psi(t)\rangle = \psi_{-k}(t)|n, n + k\rangle + \psi_{+k}(t)|n + k, n\rangle$, and the Schrödinger is given by

$$\begin{aligned} i\hbar\dot{\psi}_{-k}(t) &= V\psi_{+k}(t) - k\delta \cos(\omega t)\psi_{-k}(t), \\ i\hbar\dot{\psi}_{+k}(t) &= V\psi_{-k}(t) + k\delta \cos(\omega t)\psi_{+k}(t). \end{aligned} \quad (2.4.27)$$

If the following gauge transformation is performed,

$$\psi_{\mp k}(t) = \phi_{\mp k}(t) \exp\left(\pm k \frac{i\delta}{\hbar\omega} \sin(\omega t)\right), \quad (2.4.28)$$

then the Schrödinger equation becomes

$$\begin{aligned} i\hbar\dot{\phi}_{-k}(t) &= V \exp\left(-k \frac{i2\delta}{\hbar\omega} \sin(\omega t)\right) \phi_{+k}(t), \\ i\hbar\dot{\phi}_{+k}(t) &= V \exp\left(+k \frac{i2\delta}{\hbar\omega} \sin(\omega t)\right) \phi_{-k}(t). \end{aligned} \quad (2.4.29)$$

The time variations of $\phi_{\mp k}(t)$ are determined by V . If the coupling V is sufficiently weak, the coefficients $\phi_{\mp k}(t)$ are constant on a period $T = 2\pi/\omega$. In this sense, the frequency is high. But we have to bear in mind that we are here in the low-frequency regime in the sense that $\hbar\omega$ is small in comparison to the width of the unperturbed spectrum $L(U)$. In this context, the integration over one period of the Schrödinger equation (2.4.29) leads to

$$\begin{aligned} i\hbar\dot{\phi}_{-k}(t) &= V \mathcal{J}_0\left(k \frac{2\delta}{\hbar\omega}\right) \phi_{+k}(t), \\ i\hbar\dot{\phi}_{+k}(t) &= V \mathcal{J}_0\left(k \frac{2\delta}{\hbar\omega}\right) \phi_{-k}(t), \end{aligned} \quad (2.4.30)$$

where $\mathcal{J}_0(x)$ are the Bessel function of order 0. The splitting related to the underlying effective Hamiltonian of Eq. (2.4.30) gives rise to the relation (2.4.25). Figure 2.4.2(b) compares the analytical results in dashed orange with numerical results $|\Delta\epsilon_{2,4}(\delta)|$ in black, $|\Delta\epsilon_{1,5}(\delta)|$ in red and $|\Delta\epsilon_{0,6}(\delta)|$ in green. There are visible deviations for the case $|\Delta\epsilon_{2,4}(\delta)|$ while it is not the case for the two others. Therefore, the results match better for large k . Indeed, in these cases, the coupling V is weaker as it is displayed in Fig. 2.4.2(b) by the values of those splittings in $\delta = 0$.

The entanglement time τ_{n_1, n_2} are inversely proportional to the tunneling rate $\Delta\epsilon_{n_1, n_2}$ according to Eq. (2.1.17). Moreover, this time can be expressed in physical units for the atomic species ^{87}Rb whose the mass is $m = 1.443 \times 10^{-25}$ kg and the s-wave scattering is $a_s = 5.313$ nm. If the wavelength of the lasers used to build the optical lattice is $\lambda = 1064$ nm, we obtain

$$\frac{\hbar}{J} = 5.2 \times 10^{-3} \text{ s}, \quad (2.4.31)$$

for $U = 25J$. For the derivation of the result (2.4.31), see Sec. 1.3.3. The evaluations of the unperturbed entanglement times $\tau_{n_1, n_2}(\delta = 0)$ read

$$\begin{aligned} \tau_{2,4} &= 1.7\hbar/J & \longrightarrow & \tau_{2,4} = 9.0 \times 10^{-3} \text{ s}, \\ \tau_{1,5} &= 3.7 \times 10^3 \hbar/J & \longrightarrow & \tau_{1,4} = 20 \text{ s}, \\ \tau_{0,6} &= 1.5 \times 10^8 \hbar/J & \longrightarrow & \tau_{0,6} = 7.9 \times 10^5 \text{ s}. \end{aligned} \tag{2.4.32}$$

The amount of time is prohibitive for $\tau_{0,6}$. Nevertheless, $\tau_{2,4}$ reaches the criteria for an experimental observation. A way to diminish this time would be to decrease the total number of particles. Decreasing the ratio U/J is another possibility, but we have to bear in mind that the approximation of strong effective on-site interactions limits this possibility.

Chapter 3

Mean-field analysis of the two-site Bose-Hubbard model

The classical limit for the general Bose-Hubbard model was presented in Sec. 1.3.4. The present chapter focuses on the specific two-site Bose-Hubbard model. For the unperturbed one, there are two main dynamics [21, 53]. If there is no on-site interaction, all phase space trajectories lead to Josephson oscillations. Conversely, if the coupling between sites is zero, the system is frozen and the atoms are in the self-trapping regime. Between both cases, there is a coexistence of Josephson oscillations for small population imbalances and self-trapping trajectories for significant population imbalances.

In the self-trapping regime, the atoms will be subjected, on a long timescale, to a collective tunneling while the mismatch between chemical potentials of the two sites prevents individual transfers of particles. Unfortunately, the mean-field approximation is not able to reproduce this phenomenon. Nevertheless, a careful analysis of the phase space indicates with which underlying mechanisms this collective tunneling takes place. These mechanisms lead to the production of entangled states.

3.1 Classical limit

The mean-field approximation of the general Bose-Hubbard Hamiltonian was developed in Sec. 1.3.4. This section will investigate the particular case of a two-site system [54, 58, 132], where the classical limit can be represented by a 2D phase space. Some features of the dynamics can be captured with the classical equivalent of the Hamiltonian

$$\hat{H}(t) = -J(\hat{a}_1^\dagger \hat{a}_2 + \hat{a}_2^\dagger \hat{a}_1) + \frac{U}{2}(\hat{a}_1^\dagger \hat{a}_1^\dagger \hat{a}_1 \hat{a}_1 + \hat{a}_2^\dagger \hat{a}_2^\dagger \hat{a}_2 \hat{a}_2) + \delta \cos(\omega t)(\hat{a}_1^\dagger \hat{a}_1 - \hat{a}_2^\dagger \hat{a}_2), \quad (3.1.1)$$

which appears for the first time in Eq. (2.1.20). In Ref. [128], the classical limit is obtained by introducing the quadrature operators, which can be seen as a Cartesian representation of the system. Otherwise, in the limit of an infinite number of particles the ladder operators can be replaced by complex numbers [129, 130], which corresponds to the mean-field approximation,

$$\langle \hat{a}_l \rangle \sim \psi_l = \sqrt{I_l} e^{i\theta_l}, \quad (3.1.2)$$

$$\langle \hat{a}_l^\dagger \rangle \sim \psi_l^* = \sqrt{I_l} e^{-i\theta_l}, \quad (3.1.3)$$

where the ψ_l ($l = 1, 2$) represents the condensate amplitude on site l , with θ_l the phase of the site l and I_l is proportional to n_l , the number of particles on site l , such that $I_l = n_l + 1/2$. As N_p is conserved, the sum of the I_l amounts to a constant $N = N_p + 1$,

$$I_1 + I_2 = N. \quad (3.1.4)$$

Therefore, the constant N is equal to the dimension of the Hilbert of the unperturbed two-site Bose-Hubbard Hamiltonian as shown in Eq. (2.1.4). In this case, we will see that there is one quantum eigenstate in each unit cell of the phase space.

In this framework, the classical limit of the Hamiltonian (3.1.1) reads¹

$$H(\psi_l, \psi_l^*, t) = -J(\psi_1^* \psi_2 + \psi_2^* \psi_1) + \frac{U}{2} (|\psi_1|^4 + |\psi_2|^4) + \delta \cos(\omega t)(|\psi_1|^2 - |\psi_2|^2). \quad (3.1.5)$$

The temporal evolution of the mean-field system is determined by the discrete Gross-Pitaevskii equation for a two-site optical lattice. This can be derived from the Hamiltonian equations of (3.1.5),

$$\begin{aligned} i\hbar \frac{d\psi_1}{dt} &= -J\psi_2 + U|\psi_1|^2\psi_1 + \delta \cos(\omega t)\psi_1, \\ i\hbar \frac{d\psi_2}{dt} &= -J\psi_1 + U|\psi_2|^2\psi_2 - \delta \cos(\omega t)\psi_2. \end{aligned} \quad (3.1.6)$$

The variables $(\boldsymbol{\theta}, \mathbf{I})$ are known as the action-angle canonical variables, and can be used as a representation of the classical dynamics. It enables one to separate the angle-independent part $H(\mathbf{I})$ from the rest of the Hamiltonian, such that $H(\boldsymbol{\theta}, \mathbf{I}, t) = H(\mathbf{I}) + V(\boldsymbol{\theta}, \mathbf{I}, t)$ with

$$H(\boldsymbol{\theta}, \mathbf{I}, t) = \frac{U}{2} (I_1^2 + I_2^2) - 2J\sqrt{I_1 I_2} \cos(\theta_1 - \theta_2) + \delta(I_1 - I_2) \cos(\omega t). \quad (3.1.7)$$

As the total number of particles is a constant of motion, it could be valuable to perform a canonical transformation in order to use N as a new conjugate momentum. In this case, the generalized coordinate associated to N is cyclic, and the dynamics behaves like an effective one degree-of-freedom system. The phase space has then two dimensions, and it becomes possible to visualize it in a plane. To achieve this purpose, the third class generating function that performs the transformation $(\boldsymbol{\theta}, \mathbf{I}) \mapsto (\boldsymbol{\phi}, \mathbf{z})$ is introduced,

$$F(\mathbf{I}, \boldsymbol{\phi}) = \frac{1}{2}(I_1 - I_2)\phi + (I_1 + I_2)\phi_2, \quad (3.1.8)$$

characterized by the following relations,

$$\theta_l = \frac{\partial F}{\partial I_l}; \quad z_l = \frac{\partial F}{\partial \phi_l}. \quad (3.1.9)$$

Here we introduce the notations $z = z_1$ and $\phi = \phi_1$.

¹The constants in the Hamiltonian were removed. The general version with the constants of motion is stated in Eq. (1.3.44).

The new canonical variables can be derived from the generating function.

$$\begin{cases} \theta_1 = \phi_2 + \frac{1}{2}\phi \\ \theta_2 = \phi_2 - \frac{1}{2}\phi \\ I_1 = z + \frac{z_2}{2} \\ I_2 = -z + \frac{z_2}{2} \end{cases} \Leftrightarrow \begin{cases} \phi = \theta_1 - \theta_2 \\ \phi_2 = \frac{1}{2}(\theta_1 + \theta_2) \\ z = \frac{1}{2}(I_1 - I_2) \\ z_2 = I_1 + I_2 = N \end{cases} \quad (3.1.10)$$

The constants are removed, and the Hamiltonian reads

$$H(\phi, z, t) = Uz^2 - 2J\sqrt{(N/2)^2 - z^2} \cos(\phi) + 2\delta \cos(\omega t)z. \quad (3.1.11)$$

As ϕ_2 doesn't appear in the new Hamiltonian, $z_2 = N$ is a constant of motion. This representation leads to a global visualization of the dynamics in two dimensions. The phase space can be built by propagating the Hamiltonian equations,

$$\begin{aligned} \dot{\phi} &= 2Uz + \frac{2Jz}{\sqrt{(N/2)^2 - z^2}} \cos(\phi) + 2\delta \cos(\omega t), \\ \dot{z} &= -2J\sqrt{(N/2)^2 - z^2} \sin(\phi). \end{aligned} \quad (3.1.12)$$

In the mean-field approximation the total number of particles is not relevant. That is why it becomes possible to write a dimensionless Hamiltonian where the factor N is no longer present,

$$\tilde{H}(\tilde{\phi}, \tilde{z}, \tilde{t}) = \frac{H}{NJ} = \frac{\Lambda}{4} \tilde{z}^2 - \sqrt{1 - \tilde{z}^2} \cos(\tilde{\phi}) + \tilde{\delta} \cos(\tilde{\omega} \tilde{t}) \tilde{z}. \quad (3.1.13)$$

Here we have $\tilde{\phi} = \phi$, $\tilde{z} = 2z/N$ and $\tilde{t} = 2Jt$. The Hamiltonian (3.1.13), depending only on the parameter Λ , $\tilde{\delta}$ and $\tilde{\omega}$, describes the same physical reality as (3.1.11). The three relevant parameters describing the dynamics are then given by

$$\Lambda = \frac{NU}{J}, \quad \tilde{\delta} = \frac{\delta}{J}, \quad \tilde{\omega} = \frac{\omega}{2J}. \quad (3.1.14)$$

A modification of the parameters N , U , J , δ and ω that leaves the parameters Λ , $\tilde{\delta}$ and $\tilde{\omega}$ unchanged leads to the same phase space and, therefore, leads to the same classical dynamics.

3.2 Josephson oscillations to self-trapping regime

Some features of the dynamics can be captured through the mean-field approximation. That is why the unperturbed Hamiltonian, given by

$$H(\phi, z) = Uz^2 - 2J\sqrt{(N/2)^2 - z^2} \cos(\phi), \quad (3.2.1)$$

is introduced [21, 53]. This is the unperturbed version of Eq. (3.1.11). It represents a kind of pendulum Hamiltonian where the prefactor of the $\cos(\phi)$ depends on the conjugate momentum. To some extent, it can be seen as a pendulum where the gravitational acceleration depends on the momentum. As displayed in Fig. 3.2.1, the term $\sqrt{(N/2)^2 - z^2}$ limits the phase space in the interval $z \in [-N/2; N/2]$. Those phase spaces were obtained for $N_p = 5$.

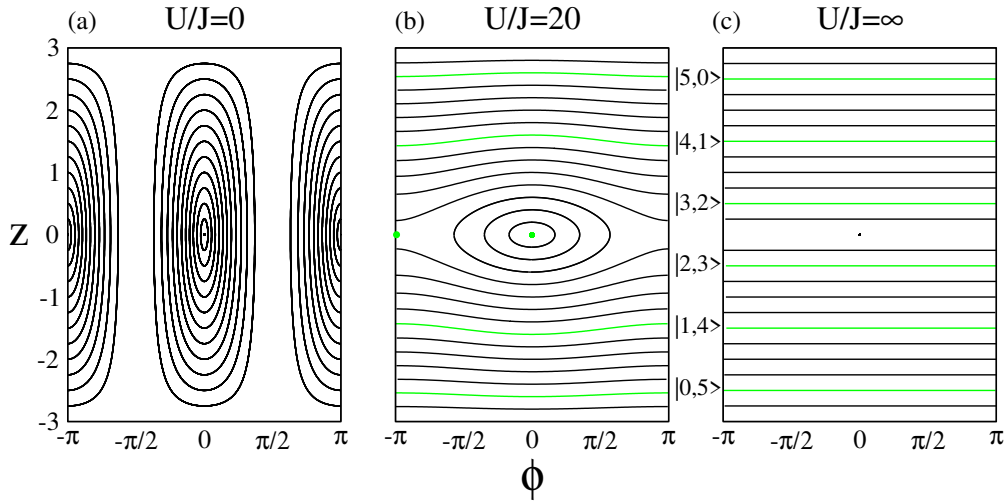


Figure 3.2.1: These phase-space plots were generated by means of the Hamiltonian (3.2.1) for $N_p = 5$. There is a coexistence in the case (b) between the self-trapping regime for high population imbalances and the Josephson oscillations for small population imbalances. By contrast, the case (a) displays only Josephson oscillations while the case (c) displays only self-trapping trajectories.

The green tori in Fig. 3.2.1 represent the classical counterparts of the Fock states $|n_1, n_2\rangle$, i.e. the tori on which those Fock states are anchored. As the energy is conserved, the one degree-of-freedom system (3.2.1) is integrable. In the case of a repulsive gas, the torus with the minimal energy is located at the center of the phase space, i.e. at the position of the central fixed point. On the other hand, the more significant the particle imbalance z is, the more energetic the torus is. Therefore, the most energetic tori are situated at the extremities of the phase space. Two kinds of dynamics can be distinguished.

- In the case of $U/J = 0$, particles are transferred one by one. The atoms do not see each other, and all initial conditions lead to Josephson oscillations [21, 53, 145, 146] characterized by a bounded phase difference ϕ as shown in Fig. 3.2.1(a). At the quantum level, the eigenstates display strong admixtures between the Fock states.
- In the case of no coupling between both orbitals ($J = 0$ or $U/J = \infty$), the transfer of particles is prohibited. That is why all tori in Fig. 3.2.1(c) are flat. The tori are characterized by unbounded phase differences. At the quantum level, the Fock states are an eigenbasis of the Hamiltonian.

Between these both extreme cases, there are intermediate phase spaces characterized by Josephson oscillations for low population imbalances and self-trapping trajectories for high population imbalances as displayed in Fig. 3.2.1(b).

In the self-trapping regime (or Fock regime) [21, 53–61, 147], there are few transfers of particles. At the quantum level, it is due to the mismatch between the particle removal energy on site 1 (or 2) and the particle additional energy on site 2 (or 1). By defining n_j the number of particles on site $j = 1, 2$, the particle removal energy is given by $U(n_j - 1)$ while the particle additional energy is given by Un_j . Both quantities, namely the particle removal energy and the particle additional energy, are equivalent to the chemical potential when N_p is large. In the strong interaction case, $(N_p + 1)U/J \gg 1$, the chemical potential on site j is largely dominated by U and is given by

$$\mu_j \simeq U(n_j - 1/2). \quad (3.2.2)$$

Those mismatches inhibit the atomic transfer one by one. From the Fock state $|n_1, n_2\rangle$, there will be no transition to another state, except to the $|n_2, n_1\rangle$ because there exists a quasidegeneracy between the symmetric and antisymmetric superposition of $|n_1, n_2\rangle$ and $|n_2, n_1\rangle$ as explained in Sec. 2.1.2. This phenomenon of collective transfers of particles is not reproduced by the mean-field approximation. For example, Figs 3.2.1(b) and (c) indicate that 5 particles initially on site 1 will stay indefinitely on this site. Nevertheless, when $U/J = \infty$, the eigenvalues related to the states $1/\sqrt{2}(|n_1, n_2\rangle + |n_2, n_1\rangle)$ and $1/\sqrt{2}(|n_1, n_2\rangle - |n_2, n_1\rangle)$ are degenerate, meaning that, even at the quantum level, there is no giant transfer of particles contrary to the U/J finite case. This remark enables one to interpret the central island in Fig 3.2.1(b) as the classical indicator for the presence of dynamical tunneling between $|n_1, n_2\rangle$ and $|n_2, n_1\rangle$ in the quantum dynamics. This constitutes the starting point of the semiclassical theory of resonance- and chaos-assisted tunneling, which will be discussed in Chap. 4.

3.3 Phase space and coherent destruction of tunneling

From a general perspective, a time-dependent Hamiltonian can be formally seen as a time-independent system with an additional degree of freedom [66, 87]. This additional degree of freedom is modeled by an extended phase space characterized by two additional canonical variables, namely the time and the energy. That is why a one degree-of-freedom time-dependent system is sometimes called a one-and-a-half degrees of freedom system. From a general point of view, a time-dependent Hamiltonian reads $H(\phi_i, z_i, t)$ with ϕ_i and z_i , respectively, the generalized coordinates and the conjugate momenta ($i = 1, \dots, f$). In practice, the purpose is to get rid of the temporal parameter by performing a canonical transformation $H(\phi_i, z_i, t) \rightarrow \bar{H}(\bar{\phi}_j, \bar{z}_j)$ to the extended phase space with

$$\begin{aligned} \bar{\phi}_i &= \phi_i, & \bar{z}_i &= z_i, & i &= 1, \dots, f, \\ \bar{\phi}_{f+1} &= t, & \bar{z}_{f+1} &= -H. \end{aligned} \quad (3.3.1)$$

The Hamiltonian equations in the new representation are given by

$$\frac{d\bar{\phi}_j}{d\bar{t}} = \frac{\partial \bar{H}}{\partial \bar{z}_j}, \quad \frac{d\bar{z}_j}{d\bar{t}} = -\frac{\partial \bar{H}}{\partial \bar{\phi}_j}, \quad j = 1, \dots, f+1. \quad (3.3.2)$$

The new Hamiltonian must be defined as $\bar{H}(\bar{\phi}_j, \bar{z}_j) = H(\phi_i, z_i, t) - H$ with $\bar{t} = t$ in order to preserve the structure of the Hamiltonian equations.

The stroboscopic map is a suitable way to visualize the phase space of a time-periodic system by taking a snapshot of the dynamics at each multiple of the period T . The idea behind the stroboscopic map is the same as for the Poincaré sections [65, 66], i.e. to fix a variable in order to see the dynamics on a hyperplane. Each time the trajectory in phase space passes through this hyperplane, a point is drawn. In the case of the Poincaré sections, we have to take into account some sign ambiguities that can arise on a fixed energy subshell [66]. In the case of a time-periodic system, a natural way to build the stroboscopic map is to fix the time modulo the period T . For a one degree-of-freedom system, the stroboscopic map is then defined as

$$\{(\phi, z, t) \in \mathbb{R}^3 \mid t = t_0 + nT, n \in \mathbb{N}\}, \quad (3.3.3)$$

where t_0 is an arbitrary constant in $[0, T[$. Stroboscopic sections are valuable tools as it enables one to have a global vision of the dynamics by means of a 2D plane. Indeed,

a continuous system can be explored by means of the stroboscopic map or the Poincaré sections, where the area are preserved according to the Poincaré-Cartan theorem [65,66].

The following Hamiltonian is time-dependent, implying that the phase space cannot be directly built in a 2D plane,

$$H(\phi, z, t) = Uz^2 - 2J\sqrt{(N/2)^2 - z^2} \cos(\phi) + 2\delta \cos(\omega t)z. \quad (3.3.4)$$

Nevertheless, the stroboscopic map of this system can be designed as the system is time-periodic. Figure 3.3.1(b) is an example of stroboscopic sections. At the quantum level, the splitting, which determines the oscillations between the Fock states $|n_1, n_2\rangle$ and $|n_2, n_1\rangle$, behaves like a Bessel function in the high-frequency regime as indicated by Eq. (2.4.24). This means that the transitions between $|n_1, n_2\rangle$ and $|n_2, n_1\rangle$ can be coherently destroyed by choosing a suitable amplitude of the driving δ . If the zeros of the Bessel function of order 0 are given by j_m ($m = 1, 2, \dots$), the amplitudes that destroy the oscillations between the two symmetrically-related Fock states read

$$\delta_m = \frac{j_m}{2} \hbar\omega. \quad (3.3.5)$$

As the first zero is given by $j_1 \simeq 2.4048$, we have $\delta_1/J \simeq 240.48$ for $\hbar\omega/J = 200$. As indicated in Fig. 3.3.1(b), there is a signature of the destruction of tunneling at the classical level. This signature is related to the absence of the central resonance. The tori being almost flat, there is almost no exchange of particles concerning the mean field dynamics, and we obtain again the qualitatively same phase space as in Fig. 3.2.1(c).

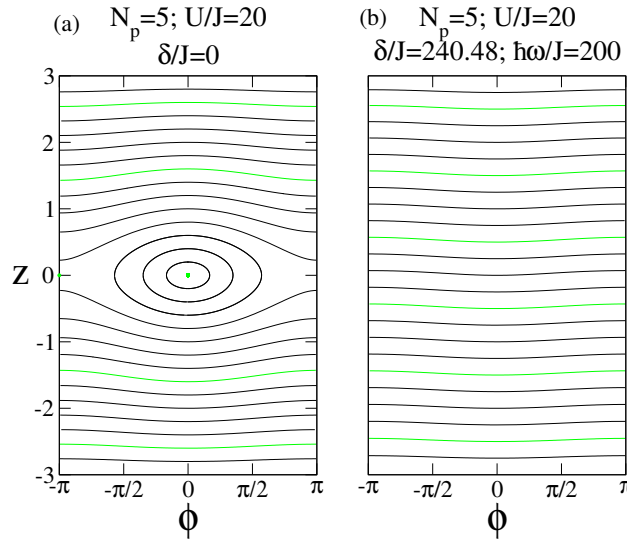


Figure 3.3.1: (a) Phase space generated by means of the unperturbed Hamiltonian (3.2.1). (b) Stroboscopic map numerically computed from the perturbed Hamiltonian (3.3.4). It is possible to coherently destroy tunneling between two weakly linked Bose-Einstein condensates by means of an external perturbation. In the stroboscopic sections (b), the central resonance is not present. This is the classical trigger for the absence of dynamical tunneling in the corresponding quantum dynamics.

3.4 Canonical perturbation theory

The canonical perturbation theory is useful for Hamiltonian systems composed of a solvable part $H_0(z)$ and a small additional perturbation $\epsilon H_1(\phi, z)$,

$$H(\phi, z) = H_0(z) + \epsilon H_1(\phi, z). \quad (3.4.1)$$

In the strong interaction case $NU/J \gg 1$, the two-mode Bose-Hubbard Hamiltonian (3.2.1) can be separated in two different parts,

$$H_0(z) = Uz^2, \quad (3.4.2)$$

$$\epsilon H_1(\phi, z) = -2J \sqrt{\left(\frac{N}{2}\right)^2 - z^2} \cos \phi. \quad (3.4.3)$$

The perturbation $\epsilon H_1(\phi, z)$ is assumed to be small in comparison to $H_0(z)$. This assumption is fulfilled for high population imbalances, i.e. $0 \ll |z| \leq N/2$, as well as for J small in comparison to NU . For the latter condition, the formal parameter ϵ is introduced and can be associated to $1/\Lambda = J/NU$ as shown by the dimensionless Hamiltonian (3.1.13). This parameter is supposed to be small.

The idea to solve the problem is to find a new set of canonical variables (α, Y) such that the new Hamiltonian has the form of $K(Y)$. The canonical variables (α, Y) become the new action-angle variables. To achieve this purpose, the generating function $S(\phi, Y)$, which performs the canonical transformation $(\phi, z) \mapsto (\alpha, Y)$, is developed from the identity transformation ϕY to which small corrections are added,

$$S(\phi, Y) = \phi Y + \bar{S}(\phi, Y), \quad (3.4.4)$$

with $\bar{S}(\phi, Y) = \bar{S}(\phi + 2\pi, Y)$ in order to preserve the periodicity of α . The link between the old and the new canonical variables is determined by the generating function according to

$$\alpha(\phi, Y) = \frac{\partial S(\phi, Y)}{\partial Y} = \phi + \frac{\partial \bar{S}(\phi, Y)}{\partial Y}, \quad (3.4.5)$$

$$z(\phi, Y) = \frac{\partial S(\phi, Y)}{\partial \phi} = Y + \frac{\partial \bar{S}(\phi, Y)}{\partial \phi}. \quad (3.4.6)$$

The generating function $S(\phi, Y)$ and the new Hamiltonian $K(Y)$ are developed in a power series in ϵ ,

$$K(Y) = K_0(Y) + \epsilon K_1(Y) + \epsilon^2 K_2(Y) + \mathcal{O}(\epsilon^3), \quad (3.4.7)$$

$$S(\phi, Y) = \phi Y + \epsilon S_1(\phi, Y) + \epsilon^2 S_2(\phi, Y) + \mathcal{O}(\epsilon^3). \quad (3.4.8)$$

By computing $K(Y) = H\left(z = \frac{\partial S(\phi, Y)}{\partial \phi}, \phi\right)$, it is possible to obtain the different corrections to $K_0(Y)$ by identifying the same power of ϵ [65, 66],

$$\mathcal{O}(\epsilon^0) : H_0(Y) = K_0(Y), \quad (3.4.9)$$

$$\mathcal{O}(\epsilon^1) : \hbar\Omega_0(Y) \frac{\partial S_1(\phi, Y)}{\partial \phi} + H_1(\phi, Y) = K_1(Y), \quad (3.4.10)$$

$$\mathcal{O}(\epsilon^2) : \hbar\Omega_0(Y) \frac{\partial S_2(\phi, Y)}{\partial \phi} + \frac{\hbar}{2} \frac{\partial \Omega_0(Y)}{\partial Y} \left(\frac{\partial S_1(\phi, Y)}{\partial \phi} \right)^2 + \frac{\partial H_1(\phi, Y)}{\partial Y} \frac{\partial S_1(\phi, Y)}{\partial \phi} = K_2(Y), \quad (3.4.11)$$

with $\hbar\Omega_0(Y) = \partial H_0(Y)/\partial Y = 2UY$. Here the Planck constant \hbar is introduced in order to have $\hbar Y$ with the unit of an action. By using the periodicity of \bar{S} , the corrections of the Hamiltonian can be computed,

$$K_0(Y) = UY^2, \quad (3.4.12)$$

$$K_1(Y) = \frac{1}{2\pi} \int_0^{2\pi} H_1(\phi, Y) d\phi \quad (3.4.13)$$

$$= 0, \quad (3.4.14)$$

$$K_2(Y) = \frac{\hbar}{2} \frac{\partial \Omega_0(Y)}{\partial Y} \frac{1}{2\pi} \int_0^{2\pi} \left(\frac{\partial S_1(\phi, Y)}{\partial \phi} \right)^2 d\phi + \frac{1}{2\pi} \int_0^{2\pi} \frac{\partial H_1(\phi, Y)}{\partial Y} \frac{\partial S_1(\phi, Y)}{\partial \phi} d\phi \quad (3.4.15)$$

$$= \frac{J^2}{\epsilon^2 2U} \left(\frac{N^2}{4Y^2} + 1 \right). \quad (3.4.16)$$

The total Hamiltonian included terms up to order 2 becomes

$$K(Y) = \underbrace{UY^2}_{\mathcal{O}(\epsilon^0)} + \underbrace{\frac{J^2}{2U} \left(\frac{N^2}{4Y^2} + 1 \right)}_{\mathcal{O}(\epsilon^2)} + \mathcal{O}(\epsilon^3). \quad (3.4.17)$$

In this context, \hbar times the frequency of the torus Y reads

$$\hbar\Omega(Y) = \frac{\partial K(Y)}{\partial Y} \quad (3.4.18)$$

$$= \underbrace{2UY}_{\mathcal{O}(\epsilon^0)} - \underbrace{\frac{J^2}{UY^3} \frac{N^2}{4}}_{\mathcal{O}(\epsilon^2)} + \mathcal{O}(\epsilon^3). \quad (3.4.19)$$

The previous results enable one to calculate the derivative of the generating function with respect to ϕ ,

$$\frac{\partial S_1(\phi, Y)}{\partial \phi} = -\frac{H_1(\phi, Y)}{\hbar\Omega_0(Y)} \quad (3.4.20)$$

$$= \frac{J}{\epsilon U Y} \sqrt{\left(\frac{N}{2} \right)^2 - Y^2} \cos \phi, \quad (3.4.21)$$

$$\frac{\partial S_2(\phi, Y)}{\partial \phi} = \frac{1}{\hbar \Omega_0(Y)} \left[K_2(Y) - \frac{\hbar}{2} \frac{\partial \Omega_0(Y)}{\partial Y} \left(\frac{\partial S_1(\phi, Y)}{\partial \phi} \right)^2 - \frac{\partial H_1(\phi, Y)}{\partial Y} \frac{\partial S_1(\phi, Y)}{\partial \phi} \right] \quad (3.4.22)$$

$$= \frac{-J^2}{\epsilon^2 4U^2 Y} \left(\frac{N^2}{4Y^2} + 1 \right) \cos(2\phi). \quad (3.4.23)$$

The tori $z(\phi, Y)$ of the phase space can be analytically approximated. The following parametrization is obtained up to the order ϵ^2 included,

$$z(\phi, Y) = Y + \frac{\partial \bar{S}(\phi, Y)}{\partial \phi} \quad (3.4.24)$$

$$= Y + \epsilon \frac{\partial S_1(\phi, Y)}{\partial \phi} + \epsilon^2 \frac{\partial S_2(\phi, Y)}{\partial \phi} + \mathcal{O}(\epsilon^3) \quad (3.4.25)$$

$$= \underbrace{Y}_{\mathcal{O}(\epsilon^0)} + \underbrace{\frac{J}{UY} \sqrt{\left(\frac{N}{2}\right)^2 - Y^2} \cos \phi}_{\mathcal{O}(\epsilon^1)} - \underbrace{\frac{J^2}{4U^2 Y} \left(\frac{N^2}{4Y^2} + 1 \right) \cos(2\phi)}_{\mathcal{O}(\epsilon^2)} + \mathcal{O}(\epsilon^3). \quad (3.4.26)$$

Note that Y is the action variable of the system such that

$$Y = \frac{1}{2\pi} \int_0^{2\pi} z(\phi, Y) d\phi. \quad (3.4.27)$$

Equation (3.4.26) makes possible to associate an action Y to each torus $z(\phi, Y)$. This formula indicates that the action is the phase-space area of the region inside the torus divided by 2π .

It becomes also possible to compute the different terms of the generating function by means of the relations (3.4.21) and (3.4.23),

$$S(\phi, Y) = \underbrace{\phi Y}_{\mathcal{O}(\epsilon^0)} + \underbrace{\frac{J}{UY} \sqrt{(N/2)^2 - Y^2} \sin \phi}_{\mathcal{O}(\epsilon^1)} + \underbrace{\frac{-J^2}{8U^2 Y} \left(\frac{N^2}{4Y^2} + 1 \right) \sin(2\phi)}_{\mathcal{O}(\epsilon^2)} + \mathcal{O}(\epsilon^3). \quad (3.4.28)$$

From the relation (3.4.28), the parametrization of the new angle is obtained,

$$\alpha(\phi, Y) = \underbrace{\phi}_{\mathcal{O}(\epsilon^0)} + \underbrace{\frac{-J}{U \sqrt{(N/2)^2 - Y^2}} \left(\frac{N}{2Y} \right)^2 \sin \phi}_{\mathcal{O}(\epsilon^1)} + \underbrace{\frac{3J^2}{8U^2 Y^2} \left(\frac{N^2}{4Y^2} + \frac{1}{3} \right) \sin(2\phi)}_{\mathcal{O}(\epsilon^2)} + \mathcal{O}(\epsilon^3). \quad (3.4.29)$$

As previously explained, the small parameter ϵ can be associated to $1/\Lambda$. To make it clear, the dimensionless relations and parametrizations are written for, respectively, the energy, \hbar times the frequency, the generating function, the population imbalance and the new angle with $\Lambda = NU/J$, $\tilde{\phi} = \phi$ and $\tilde{Y} = 2Y/N$,

$$\tilde{K}(\tilde{Y}) = \frac{K}{NJ} = \underbrace{\frac{\Lambda \tilde{Y}^2}{4}}_{\mathcal{O}(\epsilon^0)} + \underbrace{\frac{1}{2\Lambda} \left(\frac{1}{\tilde{Y}^2} + 1 \right)}_{\mathcal{O}(\epsilon^2)} + \mathcal{O}(\epsilon^3), \quad (3.4.30)$$

$$\tilde{\Omega}(\tilde{Y}) = \frac{\partial \tilde{K}(\tilde{Y})}{\partial \tilde{Y}} = \frac{\hbar\Omega}{2J} = \underbrace{\frac{\Lambda}{2}\tilde{Y}}_{\mathcal{O}(\epsilon^0)} + \underbrace{\frac{-1}{\Lambda\tilde{Y}}}_{\mathcal{O}(\epsilon^2)} + \mathcal{O}(\epsilon^3), \quad (3.4.31)$$

$$\tilde{S}(\tilde{\phi}, \tilde{Y}) = \frac{2S}{N} = \underbrace{\tilde{\phi}\tilde{Y}}_{\mathcal{O}(\epsilon^0)} + \underbrace{\frac{2}{\Lambda\tilde{Y}}\sqrt{1-\tilde{Y}^2}\sin\tilde{\phi}}_{\mathcal{O}(\epsilon^1)} + \underbrace{\frac{-1}{2\Lambda^2\tilde{Y}}\left(\frac{1}{\tilde{Y}^2}+1\right)\sin(2\tilde{\phi})}_{\mathcal{O}(\epsilon^2)} + \mathcal{O}(\epsilon^3), \quad (3.4.32)$$

$$\tilde{z}(\tilde{\phi}, \tilde{Y}) = \frac{2z}{N} = \underbrace{\tilde{Y}}_{\mathcal{O}(\epsilon^0)} + \underbrace{\frac{2}{\Lambda\tilde{Y}}\sqrt{1-\tilde{Y}^2}\cos\tilde{\phi}}_{\mathcal{O}(\epsilon^1)} + \underbrace{\frac{-1}{4\Lambda^2\tilde{Y}}\left(\frac{1}{\tilde{Y}^2}+1\right)\cos(2\tilde{\phi})}_{\mathcal{O}(\epsilon^2)} + \mathcal{O}(\epsilon^3), \quad (3.4.33)$$

$$\tilde{\alpha}(\tilde{\phi}, \tilde{Y}) = \alpha = \underbrace{\tilde{\phi}}_{\mathcal{O}(\epsilon^0)} + \underbrace{\frac{-2\sin\tilde{\phi}}{\Lambda\tilde{Y}^2\sqrt{1-\tilde{Y}^2}}}_{\mathcal{O}(\epsilon^1)} + \underbrace{\frac{3}{2\Lambda^2\tilde{Y}^2}\left(\frac{1}{\tilde{Y}^2}+\frac{1}{3}\right)\sin(2\tilde{\phi})}_{\mathcal{O}(\epsilon^2)} + \mathcal{O}(\epsilon^3). \quad (3.4.34)$$

As these equations suggest it, the higher the ratio Λ and the action \tilde{Y} are, the safer we are to neglect the terms of superior orders.

3.5 Toward mean-field approximation: semiclassical limit

3.5.1 Husimi functions

In quantum mechanics, the wave function is represented either in the configuration space or in the momentum space, but it is not possible to specify the generalized coordinates and the conjugate momenta at the same time. This implies that it is not possible to directly represent the wave function in the phase space. This fact is due to the Heisenberg indeterminacy principle related to the wave behavior of matter. Nevertheless, the Husimi function [66, 148], which depends on all canonical variables, can be used in order to achieve an indirect phase space representation of the wave function. This function is defined as the scalar product of the wave function $|\psi\rangle$ with a coherent state of the harmonic oscillator $|\alpha\rangle$,

$$H_{|\psi\rangle}(\phi_0, z_0) = |\langle\alpha|\psi\rangle|^2. \quad (3.5.1)$$

It is common to choose the coherent state that corresponds to the ground state of the harmonic oscillator [95] centered in (ϕ_0, z_0) . In z representation, this coherent state correspond to

$$\langle z|\alpha\rangle = \frac{1}{\sqrt{\sqrt{\pi}\sigma_g}} e^{-(z-z_0)^2/(2\sigma_g)} e^{i\phi_0(z-z_0)}, \quad (3.5.2)$$

where σ_g is the variance parameter enabling one to control the relative projection onto ϕ_0 and z_0 .

In the specific case of the two-site Bose-Hubbard system, $z = n - N_p/2$ is the population imbalance such that $\hat{z}|n, N_p - n\rangle = z|n, N_p - n\rangle$, where n is the population on site 1 and N_p the total number of particles. If the Floquet eigenstate $|u_\nu^\sigma(t)\rangle$ is decomposed into the Fock basis (2.3.5),

$$|u_\nu^\sigma(t)\rangle = \sum_{k=-\infty}^{+\infty} e^{ik\omega t} \sum_{n=0}^{N_p} F_{\nu,k,n}^\sigma |n, N_p - n\rangle, \quad (3.5.3)$$

its projection into the phase space by means of the Husimi function reads

$$H_{|u_\nu^\sigma(t)\rangle}(\phi_0, z_0) = \left| \sum_{k=-\infty}^{\infty} e^{ik\omega t} \sum_{n=0}^{N_p} F_{\nu,k,n}^\sigma g_n(\phi_0, z_0) \right|^2, \quad (3.5.4)$$

where

$$g_n^*(\phi_0, z_0) \equiv \langle z|\alpha \rangle = \frac{1}{\sqrt{\sqrt{\pi}\sigma_g}} \exp\left(-\frac{(n - N_p/2 - z_0)^2}{2\sigma_g}\right) \exp\left(i\phi_0\left(n - \frac{N_p}{2} - z_0\right)\right). \quad (3.5.5)$$

The symbol $\sigma = \pm$ is added and makes reference to the two possible symmetry blocks (see Sec. 2.3.1), and ν labeled the different eigenstates inside a same symmetry block.

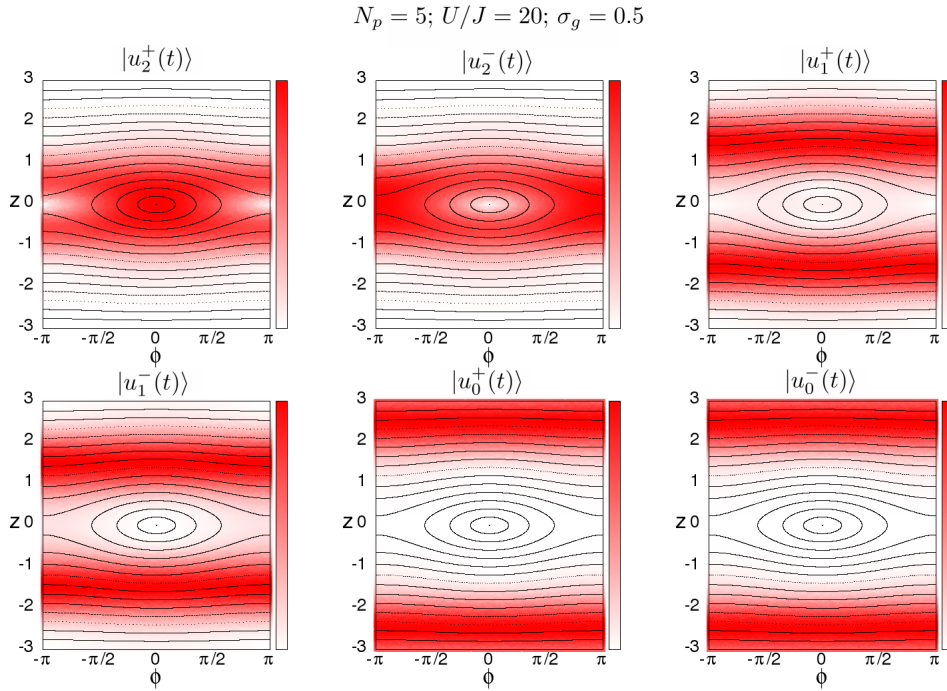


Figure 3.5.1: Husimi projections $H_{|u_\nu^\sigma(t)\rangle}(\phi, z)$ of the eigenstates $|u_\nu^\sigma(t)\rangle$ in the strong interaction regime $(N_p + 1)U/J \gg 1$ without perturbation, i.e. $\delta/J = 0$. The ground state is given by $|u_2^+(t)\rangle$ while the highest excited state is $|u_0^-(t)\rangle$. The eigenstates are relatively well localized in z , which justifies the approximation (3.5.6).

In the strong interaction regime $(N_p + 1)U/J \gg 1$, the unperturbed eigenstates stay close to the computational basis (see Eq. (2.1.13)). Concerning the perturbed eigenstates, this characteristic stays still valid as long as the perturbation δ is not too strong and the frequency of the driving ω not too small,

$$|u_\nu^\pm(t)\rangle \sim \frac{1}{\sqrt{2}}(|\nu, N_p - \nu\rangle \pm |N_p - \nu, \nu\rangle). \quad (3.5.6)$$

For example, Fig. 3.5.1 displays the Husimi functions of the eigenstates for $N_p = 5$, $U/J = 20$ and $\delta/J = 0$. As it is an unperturbed case, the shown projections of $|u_\nu^\sigma(t)\rangle$ are valid for all t . The repulsive interaction induces a ground state near the central fixed point of the phase space corresponding to a state where the population imbalance is low. The more the state is excited, the more the state is situated near the extremities of the phase space where the population imbalance is high. The eigenstates are relatively well localized in z , which justifies the approximation (3.5.6).

Incidentally, it is also possible to derive an expression of the Husimi function with the decomposition of $|u_\nu^\sigma(t)\rangle$ in the symmetric and antisymmetric basis (A.3.9)²,

$$|u_\nu^\sigma(t)\rangle = \sum_{k=-\infty}^{+\infty} e^{ik\omega t} \sum_{n=0}^{D_k^\sigma-1} F_{\nu,k,n}^\sigma \frac{1}{\sqrt{2}} (|n, N_p - n\rangle + p_k^\sigma |N_p - n, n\rangle). \quad (3.5.7)$$

In this framework, the Husimi function reads

$$H_{|u_\nu^\sigma(t)\rangle}(\phi_0, z_0) = \left| \sum_{k=-\infty}^{\infty} e^{ik\omega t} \sum_{n=0}^{D_k^\sigma-1} F_{\nu,k,n}^\sigma \frac{1}{\sqrt{2}} (g_n(\phi_0, z_0) + p_k^\sigma g_{N_p-n}(\phi_0, z_0)) \right|^2. \quad (3.5.8)$$

3.5.2 N_p as the semiclassical parameter

Figure 3.5.2 investigates the semiclassical limit. The Husimi functions of the centered eigenstates (in both symmetric parts of the phase space) are displayed for various values of N_p . As $(N_p + 1)U/J$ is fixed, the system stays the same at the classical level. Nevertheless, eigenstates have a certain width in the phase space at the quantum level. This width decreases as the total number of particles increases. At the limit $N_p \rightarrow \infty$, the Husimi function tends to correspond to a specific torus. This constitutes a graphical visualization of the mean-field approximation.

From a general point of view, an expansion in \hbar of the quantum mechanics can be done, and the 0th order gives rise to the classical dynamics. That is why the Planck constant can be seen as the semiclassical parameter. The classical system is obtained for the limit $\hbar \rightarrow 0$. To demonstrate that, the Schrödinger equation in the framework of the position representation,

$$i\hbar \frac{\partial \psi(\mathbf{q}, t)}{\partial t} = H(\hat{\mathbf{q}}, \hat{\mathbf{p}}, t) \psi(\mathbf{q}, t), \quad (3.5.9)$$

is introduced where $\hat{\mathbf{q}} \equiv \mathbf{q}$ and $\hat{\mathbf{p}} \equiv (\hbar/i)\partial/\partial\mathbf{q}$. In the context of the semiclassical theory [66, 149], the following ansatz is used,

$$\psi(\mathbf{q}, t) = A(\mathbf{q}, t) e^{\frac{i}{\hbar} S(\mathbf{q}, t)}. \quad (3.5.10)$$

Up to the order 0 in \hbar , the Hamilton-Jacobi equation is obtained,

$$H\left(\mathbf{q}, \frac{\partial S(\mathbf{q}, \mathbf{P}, t)}{\partial \mathbf{q}}, t\right) + \frac{\partial S(\mathbf{q}, \mathbf{P}, t)}{\partial t} = K(\mathbf{Q}, \mathbf{P}, t). \quad (3.5.11)$$

Here $S(\mathbf{q}, \mathbf{P}, t)$ is the generating function of the canonical transformation $(\mathbf{q}, \mathbf{p}) \rightarrow (\mathbf{Q}, \mathbf{P})$.

Solving the Hamilton-Jacobi equation consists in finding the function $S(\mathbf{q}, \mathbf{P}, t)$ by solving a partial differential equation. In general, the goal is to reach a simpler system by assuming that the new Hamiltonian $K(\mathbf{Q}, \mathbf{P}, t)$ is equal to 0. The generating function can be expressed with an integral along a trajectory γ where $\mathbf{q}_0 = \mathbf{q}(t_0)$ is the starting point and $\mathbf{q} = \mathbf{q}(t)$ is the endpoint [65, 66]

$$S(\mathbf{q}, \mathbf{P}, t) = \int_{\mathbf{q}_0}^{\mathbf{q}} \sum_j p_j(\mathbf{q}', \mathbf{P}) dq'_j + \int_{t_0}^t (K - H) dt'. \quad (3.5.12)$$

²See Appx. A.3.3 for the definitions of D_k^σ and p_k^σ .

Note that in the case of $K(\mathbf{Q}, \mathbf{P}, t) = 0$, the generating function becomes the action of the system.

As the Hamilton-Jacobi equation is an alternative to the Hamiltonian equations, the classical system is reproduced at \hbar^0 , i.e. for $\hbar \rightarrow 0$. By taking into account higher orders of \hbar , some corrections of $S(\mathbf{q}, t)$ and an approximated expression of $A(\mathbf{q}, t)$ can be obtained [66, 149]. In the specific case of the Bose-Hubbard model, N_p is the semiclassical parameter such that it becomes formally related to $1/\hbar$.

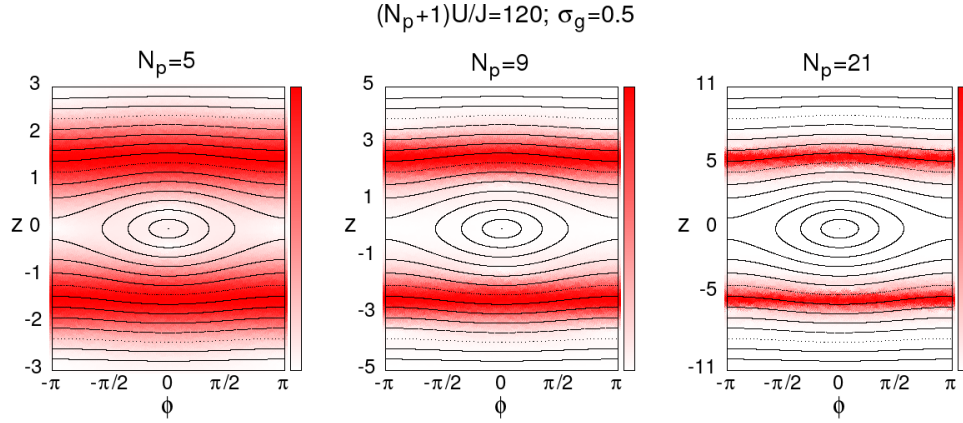


Figure 3.5.2: Husimi projections located on the same classical torus for various number of particles N_p . These Husimi projections $H_{|u_\nu^\sigma(t)\rangle}(\phi, z)$ are obtained for the eigenstates $|u_1^+(t)\rangle$, $|u_2^+(t)\rangle$ and $|u_5^+(t)\rangle$ (see Eq. (3.5.6)) related to $N_p = 5, 9, 21$ respectively. The mean-field approximation is reached when N_p tends to infinity.

Chapter 4

NOON states via resonance- and chaos-assisted tunneling

From a general point of view, a NOON state is entangled state made of two modes, namely $|N, 0\rangle$ and $|0, N\rangle$, one of which is totally full of N quanta while the other is totally empty. This highly entangled state can be formally written as $e^{i\varphi_1}|N, 0\rangle + e^{i\varphi_2}|0, N\rangle$. Even though this kind of state is very fragile, it has been realized with qubits in superconducting circuits [33], with photons [10, 11] and with phonons in ion traps [12], for example.

One theoretical proposal to build such a state with ultracold atoms is based on a adiabatic loading to the ground state [34], which is the NOON state for attractive atom-atom interaction. Nevertheless, the contraction of the Bose-Einstein [36] leads to some instabilities via the proliferation of inelastic collisions [37]. Moreover, it requires an extremely low temperature to reach the ground state. In this context, several other proposals have been formulated for repulsive atoms. For example, a phase shift is applied to the Bose-Einstein condensate, which consists in turning on the Josephson coupling during a certain period of time, and the subsequent dynamical redistribution of atoms reaches the NOON states [38–44]. The giant superposition of states can also be created by some specific measurement processes [45–47], via an adiabatic passage from an excited state [48], with a two-component Bose-Einstein condensate in a double-well potential [49] and through the scattering of a solitonic wave packet [50, 51].

Our proposal, which shares some similarities with [150], is to load all the atoms in one of the two wells and to wait half of the transition time in order to obtain the giant coherent superposition of states. Actually, the time evolution of the NOON state is a specific case of Eq. (2.1.15),

$$|\text{NOON}\rangle = \cos\left(\frac{\Delta\epsilon}{2\hbar}t\right)|0, N_p\rangle + i\sin\left(\frac{\Delta\epsilon}{2\hbar}t\right)|N_p, 0\rangle. \quad (4.0.1)$$

Here the tunneling rate is given by $\Delta\epsilon = \epsilon^- - \epsilon^+$, the NOON time by $\tau = \pi\hbar/(2|\Delta\epsilon|)$ and the total number of particles by N_p . The eigenvalue ϵ^- is related to the eigenvector roughly given by the antisymmetric combination of $|0, N_p\rangle$ and $|N_p, 0\rangle$ while the eigenvector of ϵ^+ is roughly given by the symmetric combination (see Sec. 2.1.2). This state can be produced in the self-trapping regime, where the inter-atomic repulsion prevents transfer of particles one by one. The problem, besides the requirement of a perfect symmetry of the two-site optical trap, is that the timescale of the NOON time is extremely long [62]. As indicated in Eq. (2.1.19), the higher the population imbalance is, the more time it takes to produce the entangled state. Moreover, Sec. 4.2 will show that the NOON time is characterized by an

exponential increase with the semiclassical parameter (i.e. N_p) as it is expected for integrable system.

The idea to speed up the process is to add a periodic modulation of the optical lattice [63, 64]. Section 4.3 investigates the decrease of the NOON time by means of resonance-assisted tunneling [67–69]. In the framework of near-integrable phase spaces, the quantization of the nonlinear resonances leads to coupling matrix elements boosting the transition. Moreover, the presence of a prominent chaotic layer in the classical phase space indicates the existence of strongly mixed eigenvectors, which can lead to chaos-assisted tunneling [73–77]. Section 4.5 will explain how it is possible to combine both phenomena to obtain transitions through resonance- and chaos-assisted tunneling [71, 72, 78, 79, 81–84].

4.1 Semiclassical evaluation of the wavefunction

When there is no inter-site hopping in the optical trap, the Fock basis $\{|n_1, n_2\rangle\}$ and the symmetry-adapted basis $\{1/\sqrt{2}|n_1, n_2\rangle \pm |n_2, n_1\rangle\}$ are two possible eigenbases of the Bose-Hubbard Hamiltonian as explained in Sec. 2.1.2. Indeed, a zero-hopping system doesn't induce coupling matrix element between them.

When the hopping is turned on such that $J \neq 0$, the symmetry-adapted basis and the Fock basis are no longer eigenbases. Nevertheless, the former stays close to the exact basis for small J in comparison to $(N_p + 1)U$ while the latter does not. Actually, the symmetries in the Hamiltonian induces symmetries throughout all the mathematical description of the system. For $J = 0$, the two sites can be treated separately. For $J \neq 0$, the Hamiltonian presents either symmetric eigenvectors or antisymmetric ones with respect to the permutation of both sites.

A discrete symmetry is an additional difficulty when the semiclassical eigenfunction of the problem is evaluated. From the semiclassical theory [65, 66, 68, 149, 151], it is possible to quantize a classical torus Γ of the phase space characterized by an action Y . Imagine that the system is integrable such that there exists a canonical transformation $(\phi, z) \rightarrow (\alpha, Y)$ to the action-angle coordinates by means of the generating function $S(\phi, Y)$. The semiclassical eigenfunction for the action variable Y reads

$$\psi_Y(\phi) = \frac{1}{\sqrt{2\pi}} \sqrt{\frac{\partial^2 S(\phi, Y)}{\partial Y \partial \phi}} \exp(iS(\phi, Y)). \quad (4.1.1)$$

In the case of the two-site Bose-Hubbard model, the generating function can be found in Eq. (3.4.28). The semiclassical eigenfunctions is defined for the actions that fulfill the following quantization condition,

$$Y = \frac{1}{2\pi} \int_{\Gamma} z(\phi, Y) d\phi = (m + \lambda_{N_p}) \equiv Y_m, \quad (4.1.2)$$

where λ_{N_p} is the Maslov index [66, 68, 149] and is given by $\lambda_{N_p} = 1/2$ for N_p odd^{1,2}. Here m are the integers bounded by the condition $-N/2 < Y_m < N/2$ where $N = N_p + 1$ is

¹The N_p even case will be introduced in Eq. (4.3.59).

²For the dimensionless system introduced in Eq. (3.1.13) and at the end of Sec. 3.4, the action reads $\tilde{Y} = 2Y/N$ with $N = N_p + 1$ the dimension of the Hilbert space. In this case, the quantization rule reads

$$\tilde{Y}_m = \hbar_{\text{eff}}(m + \lambda_{N_p}), \quad (4.1.3)$$

the dimension of the Hilbert space. This leads to $m = -(N_p - 1)/2, \dots, (N_p - 1)/2$. Note that each action is associated to its symmetric equivalent such that $Y_{-m} = -Y_m$. This is related to the fact that each torus $z(\phi, Y)$, for which an analytical approximation is given by Eq. (3.4.26), of the upper part of the phase space is symmetrically related to the torus $z(\phi, -Y)$ of the lower part according to $z(\phi, -Y) = -z(\phi, Y)$. Up to the order 1 of the canonical perturbation theory, the following parametrizations read for the two-site Bose-Hubbard Hamiltonian (see Eq. (3.4.28))

$$S(\phi, Y) = \int^\phi z(\phi', Y) d\phi' \simeq Y\phi + \frac{J}{UY} \sqrt{(N/2)^2 - Y^2} \sin \phi, \quad (4.1.4)$$

$$\frac{\partial^2 S(\phi, Y)}{\partial Y \partial \phi} = \frac{\partial z(\phi, Y)}{\partial Y} \simeq 1 - \frac{J \cos \phi}{U \sqrt{(N/2)^2 - Y^2}} \left(\frac{N}{2Y} \right)^2. \quad (4.1.5)$$

Equation (4.1.2) indicates that each quantum eigenstate will occupy a phase-space volume amounting to 2π . When the number of particles increases, the total phase-space volume $V_{\text{ps}} = 2\pi(N_p + 1)$ becomes larger and larger such that $2\pi/V_{\text{ps}} \rightarrow 0$ for $N_p \rightarrow \infty$. In this case, the classical limit is reached. For the dimensionless system (see Eq. (4.1.3)), the phase-space volume is fixed to 4π , and the quantization of the phase space admits an elementary cell of $2\pi\hbar_{\text{eff}}$ volume for each eigenstate. In this case, the classical limit is obtained for $\hbar_{\text{eff}} \rightarrow 0$, which corresponds to $N_p \rightarrow \infty$.

It is still possible to refine the approximation (4.1.1) by using the semiclassical theory, but there is no guarantee that it will converge to the exact eigenfunction. It is particularly striking when the system is constrained by a global symmetry. In the specific case of the two-site Bose-Hubbard system, the symmetry with respect to the inversion operator, $P : z \mapsto -z$, implies that the eigenfunctions must be either symmetric or antisymmetric with respect to P . Incidentally, the Husimi plots (3.5.1) illustrate this symmetry relation for the eigenstates. In this context, the wavefunction $\psi_Y(\phi)$ is called a local quasimode [68] and its symmetric equivalent is given by $\psi_{-Y}(\phi)$. A correct approximation of the eigenfunctions are then given by the (anti)symmetric linear combination of both quasimodes,

$$\psi_{\pm}(\phi) = \frac{1}{\sqrt{2}} (\psi_Y(\phi) \pm \psi_{-Y}(\phi)). \quad (4.1.6)$$

Incidentally, the semiclassical evaluation (4.1.1) up to the order 0 of the canonical perturbation theory reads

$$\psi_Y(\phi) \simeq \frac{1}{\sqrt{2\pi}} e^{iY\phi} = \langle \phi | n_1, n_2 \rangle, \quad (4.1.7)$$

with $Y = z \equiv (n_1 - n_2)/2$. The Fock states are then local quasimodes too.

The eigenspectrum can be approximated by means of the new Hamiltonian in terms of the action-angle coordinates, $K(Y)$. By using the classical relation (3.4.17), it becomes possible to evaluate the eigenvalues of the unperturbed two-site system with $N_p = 5$ and $U/J = 20$ for the quantized action $Y_2 = 2.5$, $Y_1 = 1.5$ and $Y_0 = 0.5$,

$$\begin{aligned} K(Y = \pm Y_2) + c &= 200.061J, \\ K(Y = \pm Y_1) + c &= 120.125J, \\ K(Y = \pm Y_0) + c &= 80.925J. \end{aligned} \quad (4.1.8)$$

with $\hbar_{\text{eff}} = 2/N$ is the effective Planck constant. In this case, the dimensionless generating function reads $\tilde{S} = \hbar_{\text{eff}} S$ as shown in Eq. (3.4.32).

As the constants in the Hamiltonian were removed when taking the classical limit, $c = -UN + 3U/4 + UN^2/4$ is added in order to reproduce the zero-point energy³. Energies (4.1.8) are close to the eigenspectrum (2.1.14). Nevertheless, the same energies are obtained by performing the transformation $Y \rightarrow -Y$. It means the doublets are still degenerate, which reflects the fact that no collective tunneling occurs in the mean-field approximation.

4.2 Tunneling rate in integrable systems

The two-mode Bose-Hubbard model described by the unperturbed Hamiltonian (3.2.1) has a global symmetry with respect to the sign inversion⁴ of z . This means that $H(\phi, z)$ stays unchanged under the operation $P : z \rightarrow -z$. In this context, the two symmetrically related tori Γ and Γ' are not necessarily connected in the phase space even if they have the same energy. They are separated by a dynamical barrier. For example, it is the case for the high population imbalance trajectories in the phase space 3.2.1(b) and for all trajectories in the phase space 3.2.1(c).

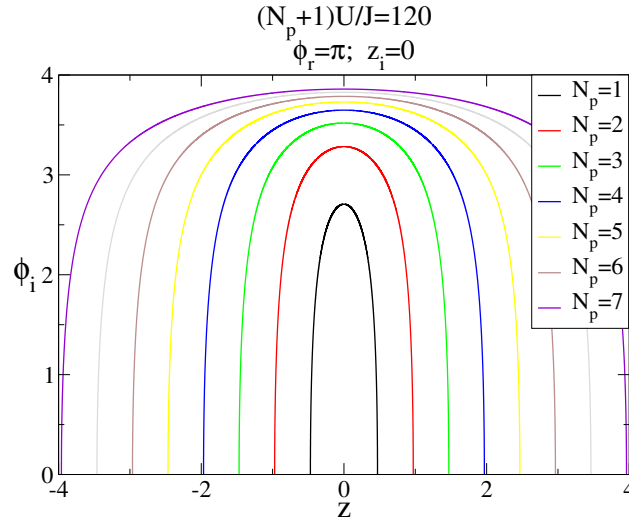


Figure 4.2.1: Analytic continuation of the canonical variable $\phi = \phi_r + i\phi_i$ into the complex domain for various N_p . This enables one to connect the two symmetrically-related parts of the phase space. Each path connects the two classical tori related to the NOON state for a given N_p .

If the initial conditions are chosen on the torus Γ , the temporal evolution will never reach Γ' . Nevertheless, an analytic continuation of the canonical variables into the complex plane is an elegant way to bypass this problem [68, 152],

$$\begin{aligned}\phi &= \phi_r + i\phi_i, \\ z &= z_r + iz_i, \\ t &= it_i.\end{aligned}\tag{4.2.1}$$

Here labels r and i make reference to the real and imaginary part respectively. By choosing initially the real part of the phase equal to π and the conjugate momentum purely real

³Section (1.3.4) derives the classical limit for the general Bose-Hubbard Hamiltonian with the correct zero-point energy.

⁴Concerning the time-periodic case (3.1.11), the Hamiltonian is symmetric under this operation if a temporal translation by an amount of $T/2$ is performed.

such that $\phi(0) = \pi + i\phi_i(0)$ and $z(0) = z_r(0)$, then $z_i(t)$ and $\phi_r(t)$ will stay constant⁵, i.e. $z_i(t) = z_i(0)$ and $\phi_r(t) = \phi_r(0) = \pi$. In this case, the analytic continuation will be able to connect Γ and Γ' . To demonstrate that, the Hamiltonian equations (3.1.12) (with $\delta = 0$) are written for that initial conditions⁶,

$$\begin{aligned} \left. \frac{d\phi_r}{d(it_i)} \right|_{t_i=0} + i \left. \frac{d\phi_i}{d(it_i)} \right|_{t_i=0} &= 2Uz_r(0) - \frac{2Jz_r(0)}{\sqrt{(N/2)^2 - z_r(0)^2}} \cosh \phi_i(0), \\ \left. \frac{dz_r}{d(it_i)} \right|_{t_i=0} + i \left. \frac{dz_i}{d(it_i)} \right|_{t_i=0} &= i 2J\sqrt{(N/2)^2 - z_r(0)^2} \sinh \phi_i(0). \end{aligned} \quad (4.2.2)$$

By matching the real parts on one side and the imaginary part on the other side, we obtain $d\phi_r/dt_i = dz_i/dt_i = 0$, and the temporal evolution reads

$$\begin{aligned} \frac{d\phi_i}{dt_i} &= 2Uz_r - \frac{2Jz_r}{\sqrt{(N/2)^2 - z_r^2}} \cosh \phi_i, \\ \frac{dz_r}{dt_i} &= -2J\sqrt{(N/2)^2 - z_r^2} \sinh \phi_i. \end{aligned} \quad (4.2.3)$$

The propagation of this system gives rise to the complex path $\Gamma \rightarrow \Gamma'$ that connects both tori normally disconnected at the classical level. Figure 4.2.1 illustrates this connection. It is worth to realize that in the non-integrable case (for $\delta \neq 0$), it is not guaranteed to have this smooth analytic continuation as the continuation from Γ does not necessarily reach Γ' [68].

The disconnection between Γ and Γ' at the classical level means that the splitting $\Delta\epsilon$ is equal to 0, leading to no dynamical tunneling. Nevertheless, there exists at the quantum level a coupling matrix element $C = |\langle \psi_Y | \hat{H}_0 | \psi_{-Y} \rangle|$ between the two symmetrically related quasimodes, which gives rise to a level splitting according to $C = \Delta\epsilon/2$. In the context of the Wentzel-Kramers-Brillouin (WKB) semiclassical method [65, 66, 151], the tunneling rate is expected to decrease exponentially with the action integral characterizing the barrier. In the framework of an imaginary path $\Gamma \rightarrow \Gamma'$ connecting the two symmetrically related tori Γ and Γ' , the splitting reads [68, 72, 151, 152]

$$\Delta\epsilon = \frac{\hbar|\Omega|}{\pi} \exp(-\sigma), \quad (4.2.4)$$

with the action integral of the analytic continuation given by

$$\sigma = \Im \left(\int_{\Gamma \rightarrow \Gamma'} \phi(z) dz \right). \quad (4.2.5)$$

Here Ω is the classical frequency on the torus Γ .

4.2.1 Size-varying phase space

As seen previously in Eq. (3.2.1), the size of the phase space with respect to the momentum is given by the dimension of the Hilbert space $N = N_p + 1$. This means that the size in the phase space of each eigenstate with respect to the momentum is equal to 1. If $\phi = \pi + i\phi_i$

⁵It remains true also for $\phi(0) = i\phi_i(0)$.

⁶ $\cos(ix) = \cosh(x)$ and $\sin(ix) = i \sinh(x)$ for $x \in \mathbb{C}$.

and $z = z_r$, the Hamiltonian (3.2.1) will determine the energy of the system according to

$$E = Uz^2 + 2J\sqrt{(N/2)^2 - z^2} \cosh \phi_i, \quad (4.2.6)$$

leading to the parametrization of the imaginary part of the phase difference,

$$\phi_i(z) = \operatorname{arccosh} \left(\frac{E - Uz^2}{2J\sqrt{(N/2)^2 - z^2}} \right). \quad (4.2.7)$$

Figure 4.2.1 displays complex paths emerging from the phase space for various N_p . These paths connect the two symmetrically-related parts of the phase space.

As the evaluation of σ becomes $\sigma = \int_{\Gamma \rightarrow \Gamma'} \phi_i dz$, the expression of the splitting takes the following form for the integrable case,

$$\Delta\epsilon = \frac{\hbar|\Omega(Y)|}{\pi} \exp \left(- \int_{-z(\pi,Y)}^{z(\pi,Y)} \operatorname{arccosh} \left(\frac{E(Y) - Uz^2}{2J\sqrt{(N/2)^2 - z^2}} \right) dz \right), \quad (4.2.8)$$

where Y is the action of the torus Γ' parametrized by $z(\phi, Y)$. By means of the canonical perturbation theory developed in Sec. 3.4, it is possible to obtain an analytical evaluation, from the classical mechanics, of the energy $E(Y)$, the frequency $\Omega(Y)$ and the parametrization $z(\phi, Y)$ of the torus characterized by an action Y . Up to the order 1, it reads

$$E(Y) \simeq UY^2, \quad (4.2.9)$$

$$\hbar\Omega(Y) \simeq 2UY, \quad (4.2.10)$$

$$z(\phi, Y) \simeq Y + \frac{J}{UY} \sqrt{(N/2)^2 - Y^2} \cos \phi. \quad (4.2.11)$$

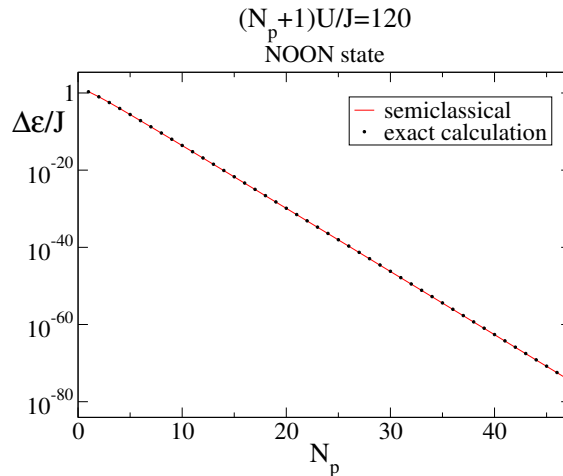


Figure 4.2.2: Tunneling rate of the NOON state defined in Eq. (4.0.1) for various N_p calculated from Eq. (4.2.8) for the red curve. The exact calculation is obtained through the diagonalization of the Hamiltonian (2.1.1).

In Fig. 4.2.2, the semiclassical limit of the NOON state defined in Eq. (4.0.1) is investigated in the integrable regime. As expected, the tunneling rate decreases exponentially with the total number of particles N_p . It means that the observation of a NOON state becomes harder and harder as the NOON time increases exponentially. The analytic continuation

was performed from the classical tori related to the quantum NOON state. In the above part of the phase space, its action reads

$$Y_{\text{NOON}} = \frac{N}{2} - \frac{1}{2}. \quad (4.2.12)$$

4.2.2 Fixed phase space

Equation (3.1.13) presents the dimensionless Hamiltonian characterized by the dimensionless parameters (we assume $\tilde{\delta} = 0$),

$$\Lambda = NU/J; \quad \tilde{\phi} = \phi; \quad \tilde{z} = 2z/N. \quad (4.2.13)$$

In the previous section, the size of the phase space changes with N . The idea is to express Eq. (4.2.8) in terms of a fixed phase space defined by that dimensionless Hamiltonian. In this framework, the tunneling rate reads

$$\Delta\tilde{\epsilon} = \frac{\Delta\epsilon}{NJ} = \frac{\hbar_{\text{eff}}|\tilde{\Omega}(\tilde{Y})|}{\pi} \exp\left(\frac{-1}{\hbar_{\text{eff}}} \int_{-\tilde{z}(\pi, \tilde{Y})}^{\tilde{z}(\pi, \tilde{Y})} \text{arccosh}\left(\frac{\tilde{E}(\tilde{Y}) - \frac{\Lambda}{4}\tilde{z}^2}{\sqrt{1 - \tilde{z}^2}}\right) d\tilde{z}\right), \quad (4.2.14)$$

with $\tilde{Y} = 2Y/N$, $\hbar_{\text{eff}} = 2/N$ and $N = N_p + 1$. The different dimensionless functions read up to the order 1

$$\tilde{E}(\tilde{Y}) = \frac{E}{NJ} \simeq \frac{\Lambda}{4}\tilde{Y}^2, \quad (4.2.15)$$

$$\tilde{\Omega}(\tilde{Y}) = \frac{\partial\tilde{E}(\tilde{Y})}{\partial\tilde{Y}} \simeq \frac{\Lambda}{2}\tilde{Y}, \quad (4.2.16)$$

$$\tilde{z}(\tilde{\phi}, \tilde{Y}) \simeq \tilde{Y} + \frac{2}{\Lambda\tilde{Y}}\sqrt{1 - \tilde{Y}^2}\cos\tilde{\phi}. \quad (4.2.17)$$

The prefactor of the exponential (4.2.14) was obtained by realizing that $\Omega(Y) = 2J\tilde{\Omega}(\tilde{Y})/\hbar$. Equation (4.2.14) confirms that N_p is the semiclassical parameter as the effective Planck constant is given by $\hbar_{\text{eff}} = 2/(N_p + 1)$. The tunneling rate $\Delta\tilde{\epsilon}$ is calculated from a fixed phase space. Nevertheless, as N_p increases, the number of quantum eigenstates contained inside the phase space increases. The widths of the Husimi function decrease with respect to z (see Fig. 3.5.2) such that, in the limit $N_p \rightarrow \infty$, the mean-field approximation becomes exact and $\Delta\epsilon \rightarrow 0$.

The corresponding classical action of the NOON state reads in the upper part of the phase space

$$\tilde{Y}_{\text{NOON}} = 1 - \frac{1}{N}. \quad (4.2.18)$$

This changing action implies that the frequency and the integral in Eq. (4.2.14) are not constant, but tend to be as N increases. Nevertheless, we have to bear in mind that we could have studied a fixed action (for example $\tilde{Y} = 0.5$ in the case of Husimi plots in Fig. 3.5.2) for which the frequency and the integral would have been constant.

4.3 Resonance-assisted tunneling

The addition of a time-periodic perturbation induces modifications of the dynamics, which leads to a modification of the structure of the phase space. In this context, the Kolmogorov-Arnold-Moser (KAM) theorem [153–156] states that the tori with incommensurable winding numbers $\beta \equiv \omega/\Omega$ are preserved with slight deformations if the perturbation is not too strong. Here ω is the external driving frequency while Ω is the frequency of the torus. Conversely, the Poincaré-Birkhoff theorem [157, 158] states that a torus with commensurable winding numbers $\beta = r/s$, with integers r and s , is destroyed. This torus gives rise to a nonlinear resonance with r stable and r unstable fixed points and chaos close to the unstable fixed points. In this context, the nonlinear resonance is called a $r:s$ resonance.

Figure 4.3.1 illustrates both theorems. Some tori are preserved in the perturbed case (panel (b)) in comparison to the unperturbed case (panel (a)) as it is demonstrated by the KAM theorem. Conversely, some structures like resonance chains emerge due to the Poincaré-Birkhoff theorem. In the specific case of panel (b), a nonlinear 2:1 resonance is present in the two symmetrically-related subregions. It is also possible to see a part of the 1:1 resonance in the extremities of the stroboscopic map.

For the two-site Bose-Hubbard model in the mean-field approximation, the frequency of the torus characterized by an action Y reads up to the order 1 (see Eq. (3.4.19))

$$\Omega(Y) = \frac{1}{\hbar} \frac{\partial K(Y)}{\partial Y} \simeq 2UY/\hbar. \quad (4.3.1)$$

As explained just previously the commensurable winding number leads to the following condition for the destroyed tori,

$$\frac{\omega}{\Omega_{r:s}} = \frac{r}{s}, \quad (4.3.2)$$

where $\Omega_{r:s} = \Omega(Y_{r:s})$ is the frequency of the torus $Y_{r:s}$. From this relation, the action of the torus that gives rise to the resonance chain $r:s$, and thus, its location in the phase space, reads

$$Y_{r:s} \simeq \frac{s}{r} \frac{\hbar\omega}{2U}, \quad (4.3.3)$$

The relation (4.3.3) makes possible to place at the wanted locations the nonlinear resonances in phase space by means of the external driving perturbation characterized by the frequency ω . In the case of Fig. 4.3.1(b), we obtain $Y_{2:1} = 1.5$ meaning that the 2:1 resonance is approximately situated in $z = 1.5$.

In the framework of resonance-assisted tunneling, the tunneling rate is determined semi-classically through the structure of the phase space. The positions of the $r:s$ resonances lead to coupling matrix elements between the local quasimodes. This is the key ingredient to explain why the tunneling rate will display plateaus and peaks instead of a smooth exponential decrease as illustrated in Fig. 4.3.4. In what follows, the Hamiltonian is assumed to be time-periodic, $H(\phi, z, t + T) = H(\phi, z, t)$ with $T = 2\pi/\omega$. Moreover, the phase space is expected to display a global symmetry such that the transition between two symmetrically-related quasimodes is determined by the splitting $\Delta\epsilon$ between the symmetric and antisymmetric eigenenergies. In the case of the two-site Bose-Hubbard Hamiltonian (3.1.11), this symmetry takes the form $H(\phi, -z, t + T/2) = H(\phi, z, t)$.

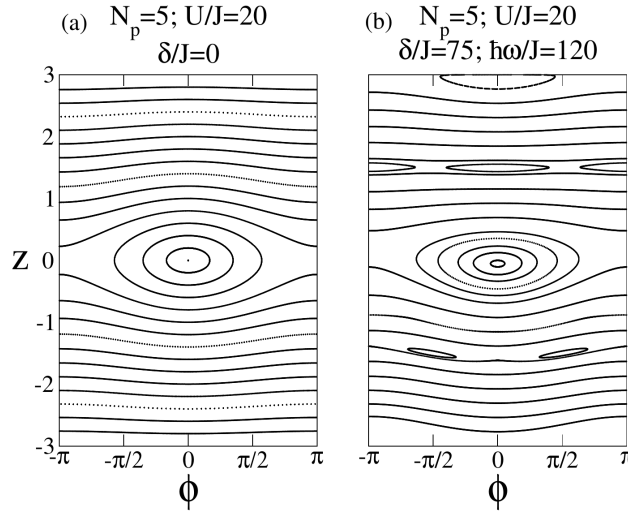


Figure 4.3.1: (a) Phase space computed from the unperturbed two-site Bose-Hubbard Hamiltonian (3.2.1). (b) Stroboscopic map computed from the periodically-driven Bose-Hubbard Hamiltonian (3.1.11). The stroboscopic sections of panel (b) display some conserved structures in comparison to the unperturbed panel (a) according to KAM theorem. Conversely, resonance chains emerge at some precise locations from destroyed tori according to Poincaré-Birkhoff theorem.

4.3.1 Secular perturbation theory

The purpose of the secular perturbation theory [66,68,72,79] is to describe from an analytical point of view, the dynamics of the system near a nonlinear $r:s$ resonance. Incidentally, the canonical perturbation theory is not adapted for this purpose because of divergences close to separatrices, for example. For the moment, we restrict ourselves to the one resonance case, where the frequency of the destroyed torus satisfies the relation (4.3.2). The system is assumed to be described by an integrable part and a weak time-periodic perturbation,

$$H(\alpha, Y, t) = K(Y) + V(\alpha, Y, t), \quad (4.3.4)$$

where (α, Y) are the action-angle variables and $V(\alpha, Y, t + T) = V(\alpha, Y, t)$ with $T = 2\pi/\omega$.

If the canonical transformation to the angle coordinate that cororates with the $r:s$ resonance is performed such that

$$\alpha_c = \alpha - \Omega_{r:s}t, \quad (4.3.5)$$

the Hamiltonian must be modified according to $H \mapsto \mathcal{H}(\alpha_c, Y, t) = H(\alpha_c + \Omega_{r:s}t, Y, t) - \hbar\Omega_{r:s}Y$ with α_c conjugated to Y . In this case, the new Hamiltonian takes the form

$$\mathcal{H}(\alpha_c, Y, t) = \mathcal{K}(Y) + \mathcal{V}(\alpha_c, Y, t), \quad (4.3.6)$$

with

$$\mathcal{K}(Y) = K(Y) - \hbar\Omega_{r:s}Y, \quad (4.3.7)$$

$$\mathcal{V}(\alpha_c, Y, t) = V(\alpha_c + \Omega_{r:s}t, Y, t). \quad (4.3.8)$$

The time variation of the corotating angle is given by the related Hamiltonian equation,

$$\dot{\alpha}_c = \frac{1}{\hbar} \frac{\partial \mathcal{H}}{\partial Y} = \Omega(Y) - \Omega_{r:s} + \frac{1}{\hbar} \frac{\partial \mathcal{V}}{\partial Y}. \quad (4.3.9)$$

As the perturbation is relatively weak, the variation $\partial\mathcal{V}/\partial Y$ is expected to be weak too. This leads to slow variations of the corotating angle close to the nonlinear resonance, i.e. for $Y \simeq Y_{r:s}$. Incidentally, α_c is fixed at the resonance in the unperturbed case. That is why $\mathcal{V}(\alpha_c, Y, t)$ varies rapidly in comparison to α_c such that the corotating angle can be seen as constant on a period of \mathcal{V} . These two significantly different timescales justify the application of the adiabatic perturbation theory [66, 68, 87]. As the periodicity of $V(\alpha_c + \Omega_{r:s}t, Y, t)$ is $rT = 2\pi s/\Omega_{r:s}$, the application of the adiabatic theory gives rise to the following Hamiltonian equation of the corotating angle,

$$\dot{\alpha}_c \simeq \frac{1}{rT} \int_0^{rT} \dot{\alpha}_c dt = \frac{1}{\hbar} \frac{\partial}{\partial Y} \left(\frac{1}{rT} \int_0^{rT} \mathcal{H}(\alpha_c, Y, t) dt \right). \quad (4.3.10)$$

In this framework, it is justified to work with a time-independent Hamiltonian,

$$\mathcal{H}(\alpha_c, Y) = \mathcal{K}(Y) + \mathcal{V}(\alpha_c, Y), \quad (4.3.11)$$

where the time-periodic part is integrated over one of its own period,

$$\mathcal{V}(\alpha_c, Y) = \frac{1}{rT} \int_0^{rT} \mathcal{V}(\alpha_c, Y, t) dt. \quad (4.3.12)$$

As the perturbation $V(\alpha, Y, t)$ is periodic with respect to the angle and the time such that $V(\alpha + 2\pi, Y, t) = V(\alpha, Y, t)$ and $V(\alpha, Y, t + T) = V(\alpha, Y, t)$, respectively, this perturbation can be developed in Fourier series according to

$$V(\alpha, Y, t) = \sum_{l,m=-\infty}^{\infty} V_{l,m}(Y) e^{il\alpha} e^{im\omega t}. \quad (4.3.13)$$

As the perturbation is real, we have $V_{l,m}(Y) = V_{-l,-m}^*(Y)$. The following calculation is obtained,

$$\mathcal{V}(\alpha_c, Y) = \frac{1}{rT} \int_0^{rT} V(\alpha_c + \Omega_{r:s}t, Y, t) dt \quad (4.3.14)$$

$$= V_{0,0}(Y) + \sum_{k=1}^{\infty} 2V_k(Y) \cos(kr\alpha_c + \varphi_k), \quad (4.3.15)$$

with

$$V_k(Y) e^{i\varphi_k} \equiv V_{rk, -sk}(Y), \quad (4.3.16)$$

such that $V_k(Y)$ is real. By defining $H_{\text{res}}(\alpha_c, Y) = 1/(rT) \int_0^{rT} \mathcal{H}(\alpha_c, Y, t) dt$ and by neglecting the term $V_{0,0}(Y)$, which does not depend on the corotating angle, the Hamiltonian that describes the dynamics close to the $r:s$ resonance is given by

$$H_{\text{res}}(\alpha_c, Y) = K(Y) - \hbar\Omega_{r:s}Y + \sum_{k=1}^{\infty} 2V_k(Y) \cos(kr\alpha_c + \varphi_k). \quad (4.3.17)$$

In the two-mode Bose-Hubbard case, we have already computed in a perturbative way $K(Y)$ in Eq. (3.4.17), and $\Omega_{r:s}$ can be deduced from Eq. (4.3.2). The Fourier coefficients can be obtained by performing a Fourier analysis of $V(\alpha, Y, t) = 2\delta \cos(\omega t) z(\phi(\alpha), Y)$. This solution implies to have a clear representation of $\phi(\alpha)$. Nevertheless, there is a more practical

way to obtain the different parameters, which is based on the phase space generated by $H(\phi, z, t)$.

4.3.2 Pendulum approximation

By adding another approximation, the nonlinear resonance can be described by an effective pendulum Hamiltonian. The resonance chains of Fig. 4.3.1(b) suggest that all Fourier coefficients of $V(\alpha, Y, t)$ can be neglected except $V_1(Y)$ in order to model a resonance by a pendulum-like Hamiltonian. The justification of that will be introduced during the quantization process, in Sec. (4.3.3) at the end of the part called *Action-independent case*. By defining $V_{r:s}(Y) \equiv V_1(Y)$ and $\varphi_{r:s} \equiv \varphi_1$, the Hamiltonian (4.3.17) becomes

$$H_{\text{res}}^{(r:s)}(\alpha_c, Y) = K(Y) - \hbar\Omega_{r:s}Y + 2V_{r:s}(Y) \cos(r\alpha_c + \varphi_{r:s}), \quad (4.3.18)$$

which constitutes a pendulum-like Hamiltonian.

Action-independent case

As the secular perturbation theory describes the dynamics near the nonlinear $r:s$ resonance, it is interesting to develop the unperturbed Hamiltonian around $Y_{r:s}$,

$$K(Y) \simeq K(Y_{r:s}) + \hbar\Omega_{r:s}(Y - Y_{r:s}) + \frac{1}{2m_{r:s}}(Y - Y_{r:s})^2, \quad (4.3.19)$$

with $1/m_{r:s} = d^2K(Y)/dY^2|_{Y=Y_{r:s}}$. Moreover, the amplitude $V_{r:s}(Y)$ is assumed for the moment to be independent of the action Y and to be equal to $V_{r:s}(Y_{r:s}) \equiv V_{r:s}$. By neglecting the constant, the Hamiltonian (4.3.18) takes the form of a pendulum Hamiltonian,

$$H_{\text{res}}^{(r:s)}(\alpha_c, Y) \simeq \frac{(Y - Y_{r:s})^2}{2m_{r:s}} + 2V_{r:s} \cos(r\alpha_c + \varphi_{r:s}). \quad (4.3.20)$$

It is notable that the Hamiltonian (4.3.20) provides a general way to describe any nonlinear resonance. Let us define $S_{r:s}^{\pm}$ as the areas below the outer and inner separatrices, respectively, of the $r:s$ resonance (see Fig. 4.3.2 as an example) in the (ϕ, z) representation. Moreover, $M_{r:s}$ denotes the monodromy matrix (see Appx. B) of the r -order stable fixed point of the nonlinear resonance. As both areas and the trace of the monodromy are preserved under the canonical transformations $(\phi, z) \rightarrow (\alpha, Y) \rightarrow (\alpha_c, Y)$, they can be used in the following relations derived from the dynamics generated by $H_{\text{res}}^{(r:s)}$ [72, 159],

$$Y_{r:s} = \frac{1}{4\pi}(S_{r:s}^+ + S_{r:s}^-), \quad (4.3.21)$$

$$\sqrt{2m_{r:s}V_{r:s}} = \frac{1}{16}(S_{r:s}^+ - S_{r:s}^-), \quad (4.3.22)$$

$$\sqrt{\frac{2V_{r:s}}{m_{r:s}}} = \frac{\hbar}{r^2T} \arccos(\text{Tr}(M_{r:s})/2). \quad (4.3.23)$$

In this framework, the different parameters of the pendulum Hamiltonian (4.3.20) can be extracted from the phase space of $H(\phi, z, t)$. This constitutes an alternative to the computation of $K(Y)$ with the canonical perturbation theory and to the Fourier analysis of $V(\alpha, Y, t)$.

In the context of the two-site Bose-Hubbard model, the canonical perturbation analysis has been already done for the unperturbed Hamiltonian $K(Y)$ through Eq. (3.4.17).

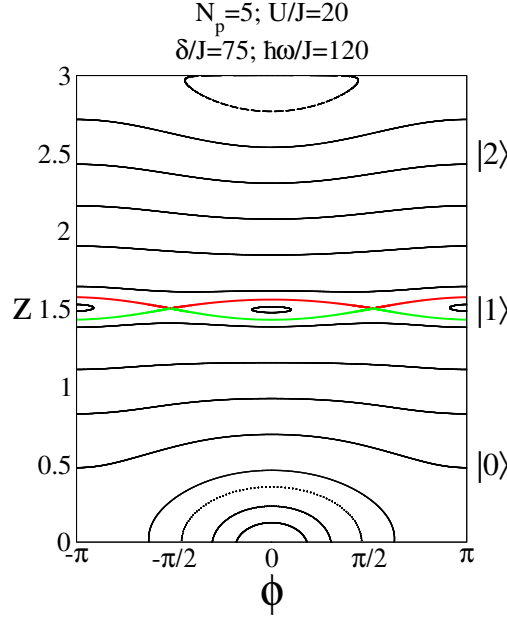


Figure 4.3.2: Upper half part of the phase space of the two-site Bose-Hubbard system for $N_p = 5$. The central 2:1 resonance is characterized by an outer separatrix in red and an inner separatrix in green. The areas below these separatrices are denoted by $S_{r:s}^{\pm}$ respectively. By using Eqs. (4.3.21)-(4.3.23), the characteristics of the 2:1 resonance are obtained leading to $Y_{2:1} = 1.5014$, $V_{2:1} = 0.02390J$ and $m_{2:1} = 0.02497J^{-1}$. In the right margin, the specific locations of the quasimodes are displayed such that $|2\rangle \leftrightarrow |5, 0\rangle$, $|1\rangle \leftrightarrow |4, 1\rangle$ and $|0\rangle \leftrightarrow |3, 2\rangle$.

Action-dependent case

If the dynamics is not directly near the $r:s$ resonance, the independence of the amplitude of the perturbation toward the action can be a crude approximation. In order to evaluate the action dependence of $V_{r:s}(Y)$, the Birkhoff-Gustavson normal-form coordinates (or quadrature variables) are introduced,

$$Q = \sqrt{2Y} \cos \alpha_c, \quad (4.3.24)$$

$$P = -\sqrt{2Y} \sin \alpha_c, \quad (4.3.25)$$

with $Y = (Q^2 + P^2)/2$. These conjugate canonical variables can be obtained through a canonical transformation from (ϕ, z) by assuming that $H(\phi, z, t)^7$ is analytic in ϕ and z in the vicinity of the resonance [72]. It becomes possible to derive

$$e^{\pm i\alpha_c} = \frac{Q \mp iP}{\sqrt{2Y}}, \quad (4.3.26)$$

⁷A canonical transformation from the action-angle variable (α_c, Y) must be done carefully because there is a singularity in $Y = 0$ for the derivatives.

from which the perturbed part of the Hamiltonian (4.3.18) is transformed,

$$H_{\text{res}}^{(r:s)}(\alpha_c, Y) = K(Y) - \hbar\Omega_{r:s}Y + \frac{V_{r:s}(Y)}{(2Y)^{r/2}} \left((Q - iP)^r e^{i\varphi_{r:s}} + (Q + iP)^r e^{-i\varphi_{r:s}} \right). \quad (4.3.27)$$

By assuming that $H_{\text{res}}^{(r:s)}$ is analytic in Q and P , the amplitude must at least be scaled in such manner that the divergence is avoided, i.e. $V_{r:s}(Y) \propto Y^{r/2}$ at least. In this framework, the following ansatz $V_{r:s}(Y) = Y^{r/2} \tilde{v}$ [81] is done, which assumes no action dependence of \tilde{v} , and it leads to

$$V_{r:s}(Y) = V_{r:s} \left(\frac{Y}{Y_{r:s}} \right)^{r/2}. \quad (4.3.28)$$

The action-independent case is obtained exactly at the resonance such that $V_{r:s}(Y_{r:s}) = V_{r:s}$. The action dependence gives in principle a better description in the vicinity of the resonance. Nevertheless, corrections of higher order of Y have been neglected, which could lead to an underestimation or an overestimation of the amplitude $V_{r:s}(Y)$ far from the resonance.

Equation (4.3.28) leads to the reformulation of the Hamiltonian (4.3.18),

$$H_{\text{res}}^{(r:s)}(\alpha_c, Y) = K(Y) - \hbar\Omega_{r:s}Y + 2V_{r:s} \left(\frac{Y}{Y_{r:s}} \right)^{r/2} \cos(r\alpha_c + \varphi_{r:s}). \quad (4.3.29)$$

Incidentally, this Hamiltonian for $r = 1$ is to some extent similar to the unperturbed Bose-Hubbard Hamiltonian (3.2.1), except that the former does not display a global symmetry with respect to the conjugate momentum.

4.3.3 Quantization of the pendulum Hamiltonian

Action-independent case

In this section, the amplitude $V_{r:s}(Y)$ is first assumed to be independent of the action and is replaced by $V_{r:s} \equiv V_{r:s}(Y_{r:s})$. In this framework, the quantization of the pendulum Hamiltonian (4.3.18) is given by

$$\hat{H}_{\text{res}}^{(r:s)} = K(\hat{Y}) - \hbar\Omega_{r:s}\hat{Y} + 2V_{r:s} \cos(r\hat{\alpha}_c + \varphi_{r:s}). \quad (4.3.30)$$

The quantization of the action-angle variable must obey the following commutation rule $[\hat{\alpha}_c, \hat{Y}] = i$ such that

$$\hat{\alpha}_c \equiv \alpha_c, \quad \hat{Y} \equiv \frac{1}{i} \frac{\partial}{\partial \alpha_c}. \quad (4.3.31)$$

The local quasimodes denoted by $|n\rangle^8$ represent plane waves in α_c representation, leading to $\langle\alpha_c|n\rangle = 1/\sqrt{2\pi} \exp(i(n+1/2)\alpha_c)$. The quantization of the action reads^{9,10}

$$\hat{Y}|n\rangle = Y_n|n\rangle = \left(n + \frac{1}{2}\right)|n\rangle. \quad (4.3.32)$$

Figure 4.3.2 displays an example of quantization of the action for three quasimodes related to the upper symmetric part of the phase space.

The perturbed part of the Hamiltonian introduces some admixture between the quasimodes [67, 79],

$$\langle n \pm r | \hat{H}_{\text{res}}^{(r:s)} | n \rangle = V_{r:s} e^{\pm i\varphi_{r:s}}. \quad (4.3.33)$$

As the perturbation is relatively weak, an accurate description of the eigenvectors can be obtained by means of the quantum perturbation theory [79],

$$\begin{aligned} |\psi_n\rangle = & |n\rangle + \sum_{l=\pm 1} \frac{\langle n+lr | \hat{H}_{\text{res}}^{(r:s)} | n \rangle}{\epsilon_n^{(0)} - \epsilon_{n+lr}^{(0)} + ls\hbar\omega} |n+lr\rangle \\ & + \sum_{l=\pm 1} \frac{\langle n+2lr | \hat{H}_{\text{res}}^{(r:s)} | n+lr \rangle}{\epsilon_n^{(0)} - \epsilon_{n+2lr}^{(0)} + 2ls\hbar\omega} \frac{\langle n+lr | \hat{H}_{\text{res}}^{(r:s)} | n \rangle}{\epsilon_n^{(0)} - \epsilon_{n+lr}^{(0)} + ls\hbar\omega} |n+2lr\rangle + \dots \end{aligned} \quad (4.3.34)$$

It becomes possible to couple the quasimodes $|n\rangle$ and $|n+kr\rangle$ by implying the $r:s$ resonance in a k -step process. This relation can be written in a more concise way,

$$|\psi_n\rangle = \sum_k \mathcal{A}_{n,n+kr}^{(r:s)} |n+kr\rangle, \quad (4.3.35)$$

with

$$\mathcal{A}_{n,n+kr}^{(r:s)} = \prod_{j=\text{sgn}(k)}^k \frac{\langle n+jr | \hat{H}_{\text{res}}^{(r:s)} | n+(j-\text{sgn}(j))r \rangle}{\epsilon_n^{(0)} - \epsilon_{n+jr}^{(0)} + js\hbar\omega} \quad k \neq 0. \quad (4.3.36)$$

Here we have $\mathcal{A}_{n,n}^{(r:s)} = 1$ for $k = 0$. Note that if $k < 0$, then we have $j = -1, -2, \dots, k$. Moreover, the unperturbed energies are given by $\epsilon_n^{(0)} = K(Y_n)$. The number of terms in Eq. (4.3.35) is finite for a bounded phase space.

The admixture between $|n\rangle$ and $|n+kr\rangle$ becomes significant if the denominator of Eq. (4.3.36) is close to zero. With the help of the quadratic expansion (4.3.19), the denominator can be expressed as

$$\epsilon_n^{(0)} - \epsilon_{n+jr}^{(0)} + js\hbar\omega \simeq \frac{1}{2m_{r:s}} (Y_n - Y_{n+jr})(Y_n + Y_{n+jr} - 2Y_{r:s}). \quad (4.3.37)$$

It is thus expected to obtain a strong admixture between $|n\rangle$ and $|n+jr\rangle$ if the $r:s$ resonance is symmetrically located between both coupled quasimodes.

⁸For the two-site Bose-Hubbard system, the link is given by $|n_1, n_2\rangle \leftrightarrow |n\rangle = |\frac{|n_1-n_2|}{2} - 1/2\rangle$ for N_p odd with $n = 0, 1, 2, \dots$. Concerning N_p even, the link is given by $|n_1, n_2\rangle \leftrightarrow |n\rangle = |\frac{|n_1-n_2|}{2} - 1\rangle$ with $n = 0, 1, 2, \dots$. The case $n = -1$ corresponds to the state $|n_1, n_1\rangle$ that doesn't have the antisymmetric equivalent. This case is omitted.

⁹The quantization can be applied to the dimensionless system such that $\hat{Y}|n\rangle = \hbar_{\text{eff}}(n+1/2)|n\rangle$ with $\hbar_{\text{eff}} = 2/(N_p+1)$.

¹⁰The additional factor $1/2$ is there to reproduce the zero-point energy for the N_p odd case. In the N_p even case, the eigenvalues read $Y_n = (n+1)$ with $n = 0, 1, 2, \dots$.

All Fourier coefficients have been neglected in the Hamiltonian (4.3.30) except the first one $V_1 \equiv V_{r:s}$ such that the only way to couple $|n\rangle$ with $|n + kr\rangle$ is through a k -step path. It would have been possible to have a one-step coupling with V_k such that $\langle n + kr | \hat{H}_{\text{res}}^{(r:s)} | n \rangle$ becomes a non-vanishing coupling matrix element. Nevertheless, it has been shown that V_k decreases exponentially with k and that this process is negligible compared to the one implying V_1 , especially in the semiclassical limit $\hbar_{\text{eff}} \rightarrow 0$ [68, 72, 79].

Action-dependent case

In order to compute the coupling matrix elements that take into account the action dependence of the coupling coefficient $V_{r:s}(Y)$, the Hamiltonian (4.3.29) is quantized in terms of the normal-form coordinates,

$$\hat{H}_{\text{res}}^{(r:s)} = K(\hat{Y}) - \hbar\Omega_{r:s}\hat{Y} + \frac{V_{r:s}}{(2Y_{r:s})^{r/2}} \left((\hat{Q} - i\hat{P})^r e^{i\varphi_{r:s}} + (\hat{Q} + i\hat{P})^r e^{-i\varphi_{r:s}} \right). \quad (4.3.38)$$

In this context, the ladders operators are expressed as a function of the normal-form operators according to

$$\hat{a} = \frac{1}{\sqrt{2}}(\hat{Q} + i\hat{P}), \quad (4.3.39)$$

$$\hat{a}^\dagger = \frac{1}{\sqrt{2}}(\hat{Q} - i\hat{P}). \quad (4.3.40)$$

This procedure of quantization is similar to the one used in Sec. 3.1 (in the opposite direction, i.e. the mean-field approximation). It consisted in replacing the ladder operators by complex numbers. In our present case, we would have $\langle \hat{a} \rangle \sim \psi = \sqrt{Y} e^{-i\alpha_c}$ and $\langle \hat{a} \rangle \sim \psi^* = \sqrt{Y} e^{i\alpha_c}$. The quantization in terms of the ladder operators reads

$$\hat{H}_{\text{res}}^{(r:s)} = K(\hat{Y}) - \hbar\Omega_{r:s}\hat{Y} + V_{r:s} \left(\frac{1}{Y_{r:s}} \right)^{r/2} \left((\hat{a}^\dagger)^r e^{i\varphi_{r:s}} + \hat{a}^r e^{-i\varphi_{r:s}} \right), \quad (4.3.41)$$

with $\hat{Y} = (\hat{a}^\dagger \hat{a} + 1/2)$. The coupling matrix elements become modified in comparison to the action-independent relation (4.3.33) [81],

$$\langle n + r | \hat{H}_{\text{res}}^{(r:s)} | n \rangle = V_{r:s} \left(\frac{1}{Y_{r:s}} \right)^{r/2} e^{i\varphi_{r:s}} \sqrt{\frac{(n+r)!}{n!}}, \quad (4.3.42)$$

$$\langle n - r | \hat{H}_{\text{res}}^{(r:s)} | n \rangle = V_{r:s} \left(\frac{1}{Y_{r:s}} \right)^{r/2} e^{-i\varphi_{r:s}} \sqrt{\frac{n!}{(n-r)!}}. \quad (4.3.43)$$

If the resonance is symmetrically located between both quasimodes $|n\rangle$ and $|n - r\rangle$ such that $Y_{r:s} \simeq (n - r/2)$, the difference of outcome with the coupling (4.3.33) is not expected to be significant. Nevertheless, important deviations arise when the resonance becomes close to either $|n\rangle$ or $|n - r\rangle$. The reasoning with $|n\rangle$ and $|n + r\rangle$ leads to the same conclusion.

By defining

$$V_{n+jr}^{(r:s)} \equiv \langle n + jr | \hat{H}_{\text{res}}^{(r:s)} | n + (j - \text{sgn}(j))r \rangle, \quad (4.3.44)$$

the expressions (4.3.42) and (4.3.43) can be generalized according to [81]

$$V_{n+jr}^{(r:s)} = \begin{cases} V_{r:s} \left(\frac{1}{Y_{r:s}} \right)^{r/2} e^{i\varphi_{r:s}} \sqrt{\frac{(n+jr)!}{(n+(j-\text{sgn}(j))r)!}} & j > 0 \\ V_{r:s} \left(\frac{1}{Y_{r:s}} \right)^{r/2} e^{-i\varphi_{r:s}} \sqrt{\frac{(n+(j-\text{sgn}(j))r)!}{(n+jr)!}} & j < 0 \end{cases}. \quad (4.3.45)$$

4.3.4 Tunneling rate modification via resonance-assisted tunneling

The unperturbed energy in the corotating frame $\tilde{\epsilon}_n^{(0)} = \epsilon_n^{(0)} - \hbar\Omega_{r:s}Y_n$ (where $\epsilon_n^{(0)} = K(Y_n)$ is the unperturbed energy) is modified by the coupling matrix elements $V_{n+jr}^{(r:s)}$, which are supposed to be weak. Moreover, we have to bear in mind that there are two symmetric parts in the phase space. Quantum mechanically speaking $|n\rangle$ possesses a symmetrically-related quasimode with the same eigenvalue. In this case, the matrix modeling the eigenenergy modification must be centrosymmetric, i.e. symmetric with respect to the counterdiagonal,

$$\begin{pmatrix} \tilde{\epsilon}_n^{(0)} & V_{n-r}^{(r:s)} & & & & & \Delta_n \\ V_{n-r}^{(r:s)*} & \tilde{\epsilon}_{n-r}^{(0)} & V_{n-2r}^{(r:s)} & & & & \Delta_{n-r} \\ & V_{n-2r}^{(r:s)*} & \tilde{\epsilon}_{n-2r}^{(0)} & \ddots & & & \Delta_{n-2r} \\ & & \ddots & \ddots & \ddots & & \\ & & & \ddots & \ddots & \ddots & \\ & & & & \ddots & \ddots & \\ & & \Delta_{n-2r} & & \ddots & \tilde{\epsilon}_{n-2r}^{(0)} & V_{n-2r}^{(r:s)} \\ & \Delta_{n-r} & & & V_{n-2r}^{(r:s)*} & \tilde{\epsilon}_{n-r}^{(0)} & V_{n-r}^{(r:s)} \\ \Delta_n & & & & V_{n-r}^{(r:s)*} & \tilde{\epsilon}_n^{(0)} \end{pmatrix}, \quad (4.3.46)$$

with $\tilde{\epsilon}_q^{(0)} = \epsilon_q^{(0)} - \hbar\Omega_{r:s}Y_q$, and the unperturbed splittings are given by $2\Delta_q = \Delta\epsilon_q^{(0)}$. If the index n in the matrix (4.3.46) refers to the highest energy state, i.e. the NOON state in the repulsive two-mode Bose-Hubbard case, this one is exact. If n is lower, the matrix is still a good approximation as the unperturbed splittings $\Delta\epsilon_l^{(0)}$ are expected to be weak in comparison to $\Delta\epsilon_n^{(0)}$ for $l > n$.

By assuming that the perturbation is weak, the modification of the tunneling rate through the presence of a $r:s$ resonance in the phase space reads [67, 79]

$$\Delta\epsilon_n = \sum_{k=k_c}^0 \left| \mathcal{A}_{n,n+kr}^{(r:s)} \right|^2 \Delta\epsilon_{n+kr}^{(0)}, \quad (4.3.47)$$

where $k_c \leq 0$ takes into account the finite number of quantum eigenstates in the phase space. The definition of $\mathcal{A}_{n,n+kr}^{(r:s)}$ is given by the expression (4.3.36). If $\epsilon_0^{(0)}$ is assumed to be the lower unperturbed energy, the expression of k_c will read

$$k_c = - \left[\frac{n}{r} \right], \quad (4.3.48)$$

where the square brackets represent the integer part of the expression.

The unperturbed parameters $\epsilon_q^{(0)}$ and $\Delta\epsilon_q^{(0)}$ can be extracted from the phase space. On one hand, the unperturbed energies can be computed through the canonical perturbation theory

through $\epsilon_q^{(0)} = K(Y_q)$. On the other hand, the unperturbed splitting $\Delta\epsilon_q^{(0)}$ can be computed by means of an analytic continuation of the symmetrically-related tori in the complex domain. This can be achieved by applying Eq. (4.2.4). An alternative is the unperturbed energies computed in terms of the unperturbed quantum Hamiltonian \hat{H}_0 . Moreover, the spectrum of the eigenvalue equation (2.1.10) gives directly rise to the unperturbed splittings.

4.3.5 NOON states in near-integrable phase spaces

The ultimate purpose of this section is to generate a NOON state in a reasonable time. The entanglement time is known to increase exponentially with the number of particles, which plays the role of the semiclassical parameter. Moreover, as illustrated in the evaluations (2.1.19), the higher the population imbalance is, the longer is the time τ_{n_1, n_2} required to produce an entangled state with the same probability for $|n_1, n_2\rangle$ and $|n_2, n_1\rangle$. Concerning the NOON state, its entanglement time, also called the NOON time, is higher than all other entanglement times of the states with smaller population imbalances. For $N_p = 5$ and $U/J = 20$, the NOON time amounts to $6.0 \times 10^5 \hbar/J$, which corresponds to 2.6×10^3 s for a typical optical lattice filled with ^{87}Rb (see the relations (2.1.19) and the explanations above). This time is prohibitively large knowing that the typical lifetime of a condensate in an optical lattice is roughly 10 s [133].

The idea is to add a time-periodic modulation of the double well as indicated in Eq. (2.1.20). This perturbation is able to produce nonlinear resonances in the mean-field approximation. The Poincaré-Birkhoff theorem leads to Eq. (4.3.3), which links the external frequency ω with the action $Y_{r:s}$ of the destroyed torus. This equation can be rewritten as

$$\hbar\omega \simeq \frac{r}{s} 2UY_{r:s}, \quad (4.3.49)$$

which indicates the frequency that must be applied in order to produce a $r:s$ resonance at the position $z \simeq Y_{r:s}$ in phase space. Moreover, in the context of resonance-assisted tunneling, the positions of resonances in phase space have a huge impact on the transition amplitude $\mathcal{A}_{n, n+kr}^{(r:s)}$ between quasimodes $|n\rangle$ and $|n+kr\rangle$ as displayed in Eq. (4.3.36). As indicated by development (4.3.37), the resonance must be symmetrically located between both quasimodes in order to have a maximal effect on the tunneling rate.

Concerning the $N_p = 5$ case, the equivalence between both notations of quasimodes reads

$$\begin{aligned} |2\rangle &\longleftrightarrow |5, 0\rangle, \\ |1\rangle &\longleftrightarrow |4, 1\rangle, \\ |0\rangle &\longleftrightarrow |3, 2\rangle. \end{aligned}$$

Figure (4.3.3) displays the positions of the quasimodes in phase space. Equation (4.3.49) indicates that the frequency giving rise to a huge coupling for the coupling path

$$|2\rangle \xrightarrow{2:1} |0\rangle \quad (4.3.50)$$

amounts to $\omega = 120 J/\hbar$ for $U/J = 20$. Indeed, as $Y_2 = 2.5$ and $Y_0 = 0.5$, the action $Y_{2:1}$ must be equal to 1.5 to be symmetrically located between Y_2 and Y_0 . The amplitude of the perturbation $\delta/J = 75$ is chosen such that the NOON time is minimal, which gives rise to

$$\tau_2 = 2.4 \times 10^3 \hbar/J \rightarrow \tau_2 = 11 \text{ s}. \quad (4.3.51)$$

The NOON time decreases by two orders of magnitude thanks to resonance-assisted tunneling induced by a suitably tuned perturbation. The typical lifetime of a condensate in an optical lattice presents the same order of magnitude, which may still be too long for an experimental observation. That is why chaos in phase space will be introduced later, in order to gain some more orders of magnitude.

In Fig. 4.3.3(b), the peak at $N_p = 5$ is explained by the 2:1 resonance situated symmetrically between $|2\rangle$ and $|0\rangle$. If N_p continues to increase, the number of quantum eigenstates in the phase space changes leading to a non-symmetrical position of the 2:1 resonance between some quasimodes. For N_p smaller than 5, there is no coupling matrix element implying the 2:1 resonance because of too few number of quasimodes.

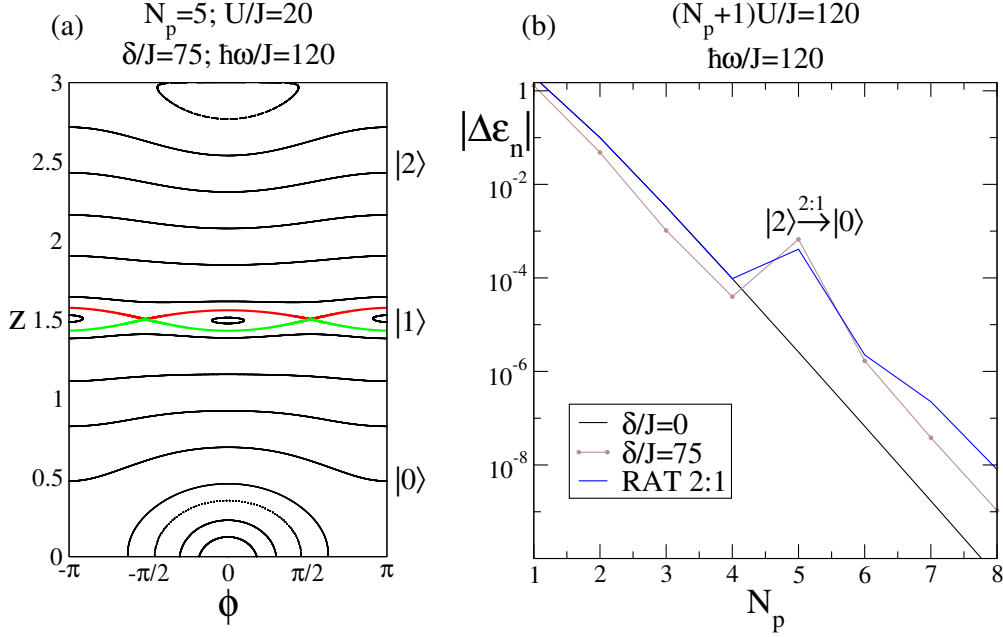


Figure 4.3.3: (a) Upper part of the phase space of the two-site Bose-Hubbard Hamiltonian in the mean-field approximation which displays a central 2:1 resonance. (b) Tunneling rate as a function of the number of particles. The pure quantum calculation of the tunneling rate (brown curve) is relatively well reproduced by the resonance-assisted tunneling (RAT) theory (blue curve) taking into account the 2:1 resonance. A peak is present for $N_p = 5$ and is due to the fact that the 2:1 resonance is symmetrically located between $|2\rangle$ and $|0\rangle$.

To model semiclassically the peak in $N_p = 5$, resonance-assisted tunneling can be described in terms of a matrix of the form

$$\begin{pmatrix} \tilde{\epsilon}_2^{(0)} & V_0^{(2:1)} & 0 & \Delta_2 \\ V_0^{(2:1)*} & \tilde{\epsilon}_0^{(0)} & \Delta_0 & 0 \\ 0 & \Delta_0 & \tilde{\epsilon}_0^{(0)} & V_0^{(2:1)} \\ \Delta_2 & 0 & V_0^{(2:1)*} & \tilde{\epsilon}_2^{(0)} \end{pmatrix}, \quad (4.3.52)$$

with $\tilde{\epsilon}_q^{(0)} = \epsilon_q^{(0)} - \hbar\Omega_{2:1}Y_q$, $V_0^{(2:1)} = \langle 0|H_{\text{res}}^{(2:1)}|2\rangle$ and the unperturbed splittings are given by $2\Delta_q = \Delta\epsilon_q^{(0)}$. In the case of weak perturbations, the modification of tunneling rate reads

$$\Delta\epsilon_2 \simeq \Delta\epsilon_2^{(0)} + \frac{|\langle 0|H_{\text{res}}^{(2:1)}|2\rangle|^2}{|\epsilon_2^{(0)} - \epsilon_0^{(0)} - \hbar\omega|^2} \Delta\epsilon_0^{(0)}. \quad (4.3.53)$$

This tunneling rate can be computed by using the characteristics of the 2:1 resonance, i.e. $Y_{2:1} = 1.5014$, $V_{2:1} = 0.02390J$ and $m_{2:1} = 0.02497J^{-1}$. Moreover, the unperturbed energies of the antisymmetric block, for example, can be used for the denominator. In this context, the semiclassical evaluation of the NOON time reads

$$\tau_2 = \frac{\pi\hbar}{2\Delta\epsilon_2} \simeq 3.8 \times 10^3 \hbar/J, \quad (4.3.54)$$

compared to the exact result $\tau_2 = 2.4 \times 10^3 \hbar/J$.

4.3.6 Multiple resonance case

The number of quantum eigenstates in phase space increases with $1/\hbar_{\text{eff}}$, the semiclassical parameter. For the one-resonance processes, it will favor the multistep transitions for large $1/\hbar_{\text{eff}}$ as it enables one to reach states that exhibit larger unperturbed tunneling rate (characterized by small q in expression $\Delta\epsilon_q^{(0)}$). More important, processes implying several resonances will appear and will be more and more frequent in the semiclassical limit $\hbar_{\text{eff}} \rightarrow 0$ as the number of paths increases.

The generalization of the single-resonance Hamiltonian (4.3.29) is obtained by adding the contributions of the other resonances. Introducing new resonances will introduce new coupling matrix elements, some of them implying several resonances. If there are m resonances denoted by $r_1:s_1, r_2:s_2, \dots, r_m:s_m$, then the modification of the tunneling rate follows [72]

$$\begin{aligned} \Delta\epsilon_n = & \sum_{k_1, k_2, \dots, k_m} \left| \mathcal{A}_{n, n+k_1 r_1}^{(r_1:s_1)} \right|^2 \left| \mathcal{A}_{n+k_1 r_1, n+k_1 r_1+k_2 r_2}^{(r_2:s_2)} \right|^2 \cdots \left| \mathcal{A}_{n+K_m, n+K_m+k_m r_m}^{(r_m:s_m)} \right|^2 \Delta\epsilon_{n+K_m+k_m r_m}^{(0)} \\ & + \text{perm}(1, 2, \dots, m), \end{aligned} \quad (4.3.55)$$

with $K_m = k_1 r_1 + k_2 r_2 + \dots + k_{m-1} r_{m-1}$. The $\text{perm}(1, 2, \dots, m)$ term takes into account all terms generated by the permutations between $r_1:s_1, r_2:s_2, \dots, r_m:s_m$. For $\text{perm}(1, 2, \dots, m)$, the terms with at least one $k_l = 0$ are removed in order to avoid multiple counting. Nevertheless, the $\text{perm}(1, 2, \dots, m)$ term is in general negligible if the $r_l:s_l$ are sorted according to their consecutive order of apparition in the phase space, i.e. according to their actions. The amplitudes read

$$\mathcal{A}_{n+K_l, n+K_l+k_l r_l}^{(r_l:s_l)} = \prod_{j=\text{sgn}(k_l)}^{k_l} \frac{\langle n+K_l+jr_l | \hat{H}_{\text{res}}^{(r_l:s_l)} | n+K_l+(j-\text{sgn}(j))r_l \rangle}{\epsilon_n^{(0)} - \epsilon_{n+K_l+jr_l}^{(0)} + (k_1 s_1 + k_2 s_2 + \dots + k_{l-1} s_{l-1} + j s_l) \hbar \omega} \quad k_l \neq 0, \quad (4.3.56)$$

with $K_l = k_1 r_1 + k_2 r_2 + \dots + k_{l-1} r_{l-1}$ and the prescription $\mathcal{A}_{\nu, \nu}^{(r_l:s_l)} = 1$.

The number of terms in Eq. (4.3.55) can be discouragingly large, especially in the semiclassical limit. Fortunately, there is in general one dominant contribution that drives the transition process. Equation (4.3.55) is mainly suitable to describe the tunneling rate in the near-integrable regime, i.e. a regime where chaos is almost absent from the phase space.

4.3.7 Application to the two-site Bose-Hubbard system

Resonance-assisted tunneling (RAT) has been extensively studied for the one degree-of-freedom systems, for which the phase space has the dimension two. In the near-integrable regime, it was applied in particular to the kicked Harper model [67,68] and for the deformed

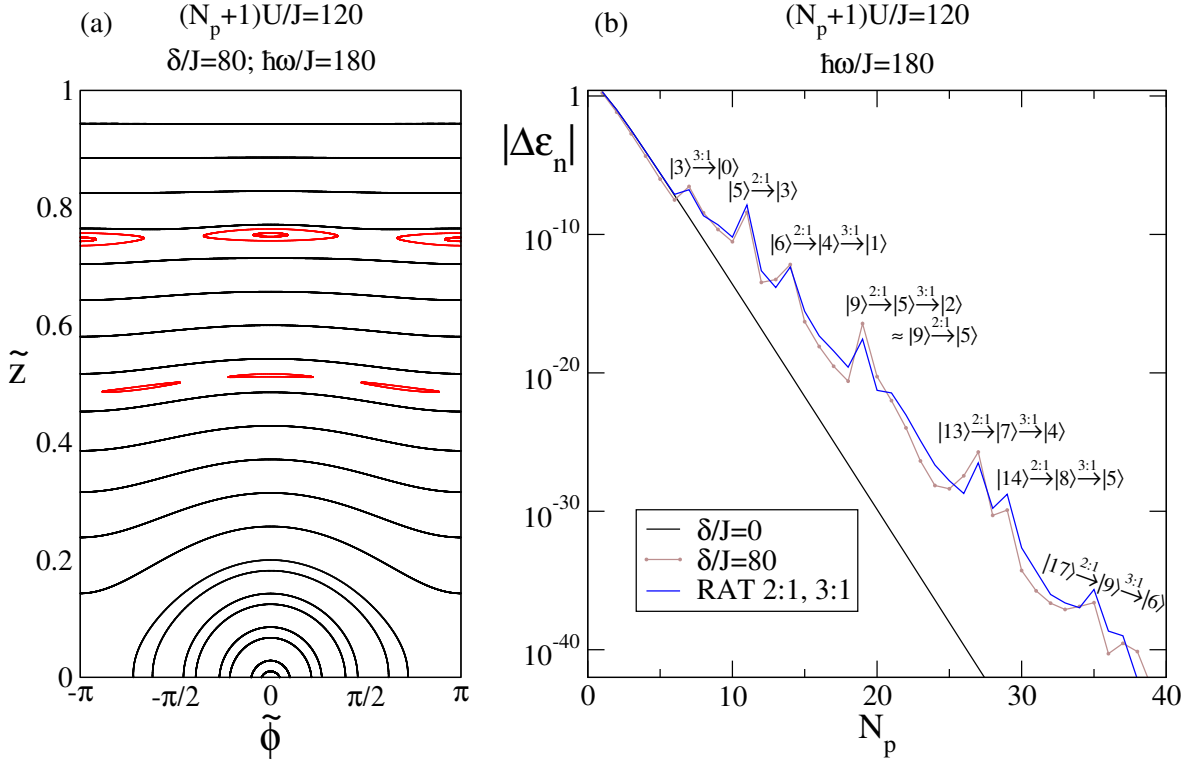


Figure 4.3.4: (a) Upper part of the phase space of the dimensionless two-site Bose-Hubbard Hamiltonian in the classical limit. Two main resonances are shown in red, namely the 2:1 and the 3:1 resonances. (b) Tunneling rate related to the NOON state as a function of the total number of particles. The semiclassical blue curve was obtained through resonance-assisted tunneling (RAT) by taking into account the 2:1 and the 3:1 resonances drawn in red in panel (a). This curve is able to reproduce the tunneling rate peaks of the exact results in brown. The text above each peak in panel (b) represents the dominant contribution to the tunneling rate.

optical microcavities [70,71]. In the mixed regime, i.e. the regime where there is a coexistence between regular and chaotic trajectories in the phase space, it was applied to molecular system [69], the kicked Harper model [79], periodically-driven pendulum [84], the standard map [72,81–83] and optical microcavities [71,80].

This section proposes to add to this list the Bose-Hubbard system, here in the near-integrable regime as displayed in Fig. 4.3.4. In the quantum regime (N_p low), the transitions imply only one resonance. As one goes further in the semiclassical limit, the multiresonant processes cannot be put aside. The unperturbed case ($\delta/J = 0$) gives rise to an exponential decrease as specified in Eqs. (4.2.8) and (4.2.14). In the perturbed case, the average slope of the exponential curve decreases, and there are peaks in the tunneling rate, as indicates the brown and blue curves of Fig. 4.3.4(b). Above each peak is specified the dominant coupling path between the quasimodes concerned.

Figure 4.3.5 displays semiclassical computations implying only one resonance, namely the 2:1 for (a) and the 3:1 for (b). The one-resonance processes are able to reproduce some peaks but not all of them. Moreover, even if they reproduce the peak, they are not necessarily the dominant processes. That is why the multiresonance processes must be taken into account, especially in the semiclassical limit.

In order to determine the dominant path that enables one to reduce by several orders of magnitude the NOON time, the action of the NOON state (denoted by n) in the fixed-size

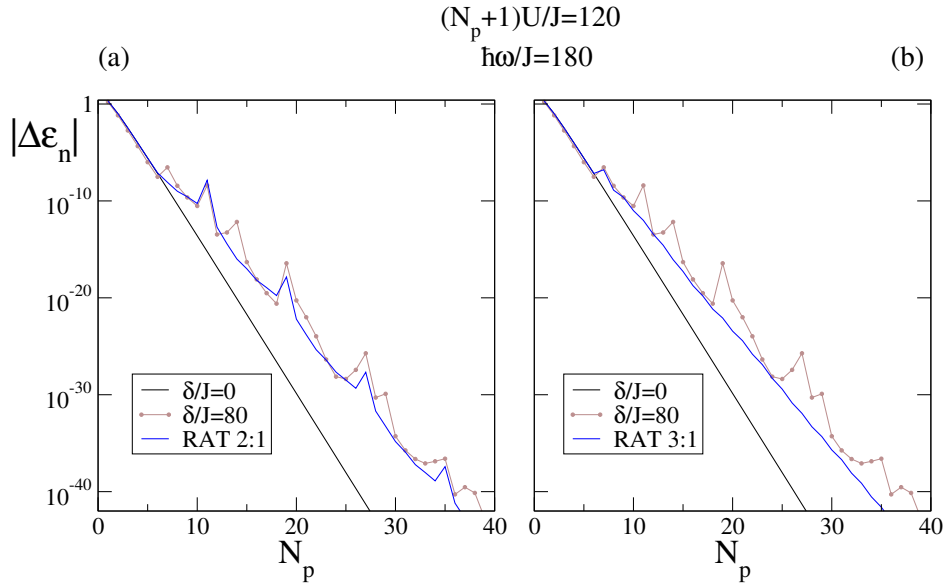


Figure 4.3.5: Both panels represents the tunneling rate of the NOON state as a function of the number of particles. The resonance-assisted tunneling (RAT) blue curves were obtained by taking only into account (a) the 2:1 resonance, (b) the 3:1 resonance. The exact calculation is represented by the brown curves. If the multiresonant processes are neglected, some peaks are missed or partially reproduced, especially in the semiclassical limit, i.e. for large N_p .

phase space (see Eq. (4.2.18))

$$\tilde{Y}_n = 1 - \frac{1}{N_p + 1} \quad (4.3.57)$$

must be connected with the quasimodes characterized by the actions (see Eq. (4.1.2))

$$\tilde{Y}_m = \hbar_{\text{eff}} \left(m + \frac{1}{2} \right) \quad m = 0, 1, 2, \dots, \frac{N_p - 1}{2}; \quad N_p \text{ odd}, \quad (4.3.58)$$

$$\tilde{Y}_m = \hbar_{\text{eff}}(m + 1) \quad m = 0, 1, 2, \dots, \frac{N_p}{2} - 1; \quad N_p \text{ even}. \quad (4.3.59)$$

Here we have $\hbar_{\text{eff}} = 2/(N_p + 1)$. The case $m = -1$ for N_p even corresponds to the Fock state $|n_1, n_1\rangle$. This case is not taken into account as there is no antisymmetric counterpart and so no unperturbed tunneling rate associated¹¹.

These connections are determined by the external frequency ω . The relation (4.3.3) claims that ω is able to produce a $r:s$ resonance with the action $\tilde{Y}_{r:s}$. By fixing the frequency, the positions of all resonances are fixed. From one $r_1:s_1$ resonance it becomes possible to find the position of another $r_2:s_2$ resonance through

$$\frac{r_1}{s_1} \tilde{Y}_{r_1:s_1} = \frac{r_2}{s_2} \tilde{Y}_{r_2:s_2}. \quad (4.3.60)$$

¹¹Actually, the coupling to the quasimode $|n_1, n_1\rangle$ would require modeling tunneling via a matrix (4.3.46) with an odd dimension where the central element would be the unperturbed energy of this quasimode. In this case, Eq. (4.3.47) must be modified. We didn't take into account this very specific coupling for the modeling of the tunneling rate.

In the case $(N_p + 1)U/J = 120$ and $\hbar\omega/J = 180$, the dimensionless actions produced by the external frequency read

$$\begin{aligned} \tilde{Y}_{3:2} &= 1, & \tilde{Y}_{5:2} &= \frac{3}{5}, \\ \tilde{Y}_{5:3} &= \frac{9}{10}, & \tilde{Y}_{3:1} &= \frac{1}{2}, \\ \tilde{Y}_{2:1} &= \frac{3}{4}, & \tilde{Y}_{4:1} &= \frac{3}{8}. \end{aligned} \quad (4.3.61)$$

The respective areas of these resonances will depend on the amplitude of the external perturbation δ . Clearly, the two prominent resonances in the phase space 4.3.4(a) are 2:1 and 3:1.

Concerning Fig. 4.3.4(b) for $N_p = 14$, the dominant coupling path reads

$$|6\rangle \xrightarrow{2:1} |4\rangle \xrightarrow{3:1} |1\rangle \quad (4.3.62)$$

such that the dominant term in the sum (4.3.55) is given by

$$\Delta\epsilon_6 \simeq \left| \mathcal{A}_{6,4}^{(2:1)} \right|^2 \left| \mathcal{A}_{4,1}^{(3:1)} \right|^2 \Delta\epsilon_1^{(0)}. \quad (4.3.63)$$

In this specific case, the 2:1 resonance with an action $\tilde{Y}_{2:1} = 5.625\hbar_{\text{eff}}$ is more or less symmetrically located between the quasimodes $\tilde{Y}_6 = 7\hbar_{\text{eff}}$ and $\tilde{Y}_4 = 5\hbar_{\text{eff}}$. Moreover, the 3:1 resonance with an action $\tilde{Y}_{3:1} = 3.75\hbar_{\text{eff}}$ is more or less symmetrically located between the quasimodes $\tilde{Y}_4 = 5\hbar_{\text{eff}}$ and $\tilde{Y}_1 = 2\hbar_{\text{eff}}$.

The arrangement of the action variables can be translated in terms of the arrangement of the unperturbed spectrum. Here only the antisymmetric eigenvalues are displayed for practical purpose,

$$\begin{aligned} \epsilon_6^- &= 728.135J, & \epsilon_3^- &= 464.286J, \\ \epsilon_5^- &= 624.161J, & \epsilon_2^- &= 408.465J, \\ \epsilon_4^- &= 536.205J, & \epsilon_1^- &= 368.877J, \\ & & \epsilon_0^- &= 341.871J. \end{aligned} \quad (4.3.64)$$

In this case, the energy difference $\epsilon_6^- - \epsilon_4^- = 191.93J$ is roughly equal to $\hbar\omega = 180J$ as well as the energy difference $\epsilon_4^- - \epsilon_1^- = 167.328J$. This means that $\epsilon_6^- - \epsilon_1^- = 359.258J \simeq 2\hbar\omega$, leading to a large value for the prefactor $|\mathcal{A}_{4,1}^{(3:1)}|$ in Eq. (4.3.63). Moreover, this two-resonance transition enables one to connect to the unperturbed tunneling rate $\Delta\epsilon_1^{(0)} = 0.297J$ which is much higher than $\Delta\epsilon_6^{(0)} = 8.167 \times 10^{-21}J$, the direct transition. Note that the conclusion would have been the same with the symmetric eigenenergies or those obtained through the canonical perturbation theory with the quantization.

4.4 Beyond weak perturbations

Perturbations were assumed to be weak in order to obtain the tunneling rate modifications (4.3.47) and (4.3.53). Because the transition matrix elements between quasimodes are not too strong, the tunneling rate modification can be obtained perturbatively. This means that the dynamics will be overwhelmingly determined by the two symmetrically-related quasimodes.

The purity of a NOON state is introduced in order to verify if the two-level approximation is still holding. This is defined as

$$p = M_0 + M_{N_p}, \quad (4.4.1)$$

with

$$M_n = \frac{1}{2T} \sum_{\sigma=\pm} \int_0^T |\langle n, N_p - n | u_\nu^\sigma(t) \rangle|^2 dt, \quad (4.4.2)$$

where $|u_\nu^\pm(t)\rangle$ are the eigenstates which refers to the NOON state. For more details, see Appx. A.2.2 for the Fock basis and Appx. A.3.4 for the symmetry-adapted basis. This definition of purity can formally be identified with the time average of the expectation value $\text{Tr}[\hat{P}\hat{\rho}]$ of the projector to the NOON doublet with respect to the density matrix $\hat{\rho} = |u_\nu^+(t)\rangle\langle u_\nu^+(t)| + |u_\nu^-(t)\rangle\langle u_\nu^-(t)|$, meaning that we have $p = 1/(2T) \int_0^T dt \text{Tr}[\hat{P}\hat{\rho}]$ with $\hat{P} = |0, N_p\rangle\langle 0, N_p| + |N_p, 0\rangle\langle N_p, 0|$

As indicated in Fig. 4.4.1(c) the purity for the 2:1 resonance stays close to 1 ($p \simeq 0.999$) indicating that the two-levels approximation is still holding. Note that (a), (c) and (e), which form a column, refer to the same combination of parameters. The two-level dynamics between $|0, 5\rangle$ and $|5, 0\rangle$ is corroborated by Fig. 4.4.1(e), which represents the temporal evolutions of the detection probabilities to obtain $|n_1, n_2\rangle$ knowing that the system was initially in $|\phi(t_0)\rangle = |0, 5\rangle$,

$$P_{|n_1, n_2\rangle}(t) = |\langle n_1, n_2 | \phi(t) \rangle|^2. \quad (4.4.3)$$

For the detailed expressions, see Appx. A.2.1 for the Fock basis and Appx. A.3.3 for the symmetry-adapted basis.

If the coupling matrix element between two quasimodes is sufficiently strong, the two-level approximation is no longer correct. For example, Fig. 4.4.1(d) indicates that the eigenvectors display a strong admixture between $1/\sqrt{2}(|0, 5\rangle \pm |5, 0\rangle)$ and $1/\sqrt{2}(|1, 4\rangle \pm |4, 1\rangle)$ for the set of parameters $N_p = 5$, $U/J = 20$, $\delta/J = 12$ and $\hbar\omega/J = 80$. This has consequences for the detection probabilities as seen in Fig. 4.4.1(f), where the oscillations take place between four levels. There are fast oscillations between $|0, 5\rangle$ and $|1, 4\rangle$, and slow oscillations between $|0, 5\rangle$ and $|5, 0\rangle$. The trigger in phase space of this phenomenon is the presence of a prominent 1:1 resonance with the action $Y_{1:1} \simeq 2$, i.e. symmetrically located between $|5, 0\rangle$ and $|4, 1\rangle$ as displayed in Fig. 4.4.1(b).

The idea behind the modeling of this phenomenon is to introduce a four-by-four matrix, which is centrosymmetric in order to reproduce the site-permutation symmetry,

$$H = \begin{pmatrix} E_0 & V & 0 & V_0 \\ V & E_1 & V_1 & 0 \\ 0 & V_1 & E_1 & V \\ V_0 & 0 & V & E_0 \end{pmatrix}. \quad (4.4.4)$$

In order to not overload the notation, the unperturbed energies in the absence of tunneling are denoted by E_m . The effective unperturbed couplings are given by V_m , and the coupling caused by the external perturbation is denoted by V .

As the system is centrosymmetric, it is common to introduce a symmetry-adapted basis,

$$\frac{1}{\sqrt{2}} \left\{ \begin{pmatrix} 1 \\ 0 \\ 0 \\ 1 \end{pmatrix}, \begin{pmatrix} 0 \\ 1 \\ 1 \\ 0 \end{pmatrix}, \begin{pmatrix} 1 \\ 0 \\ 0 \\ -1 \end{pmatrix}, \begin{pmatrix} 0 \\ 1 \\ -1 \\ 0 \end{pmatrix} \right\}, \quad (4.4.5)$$

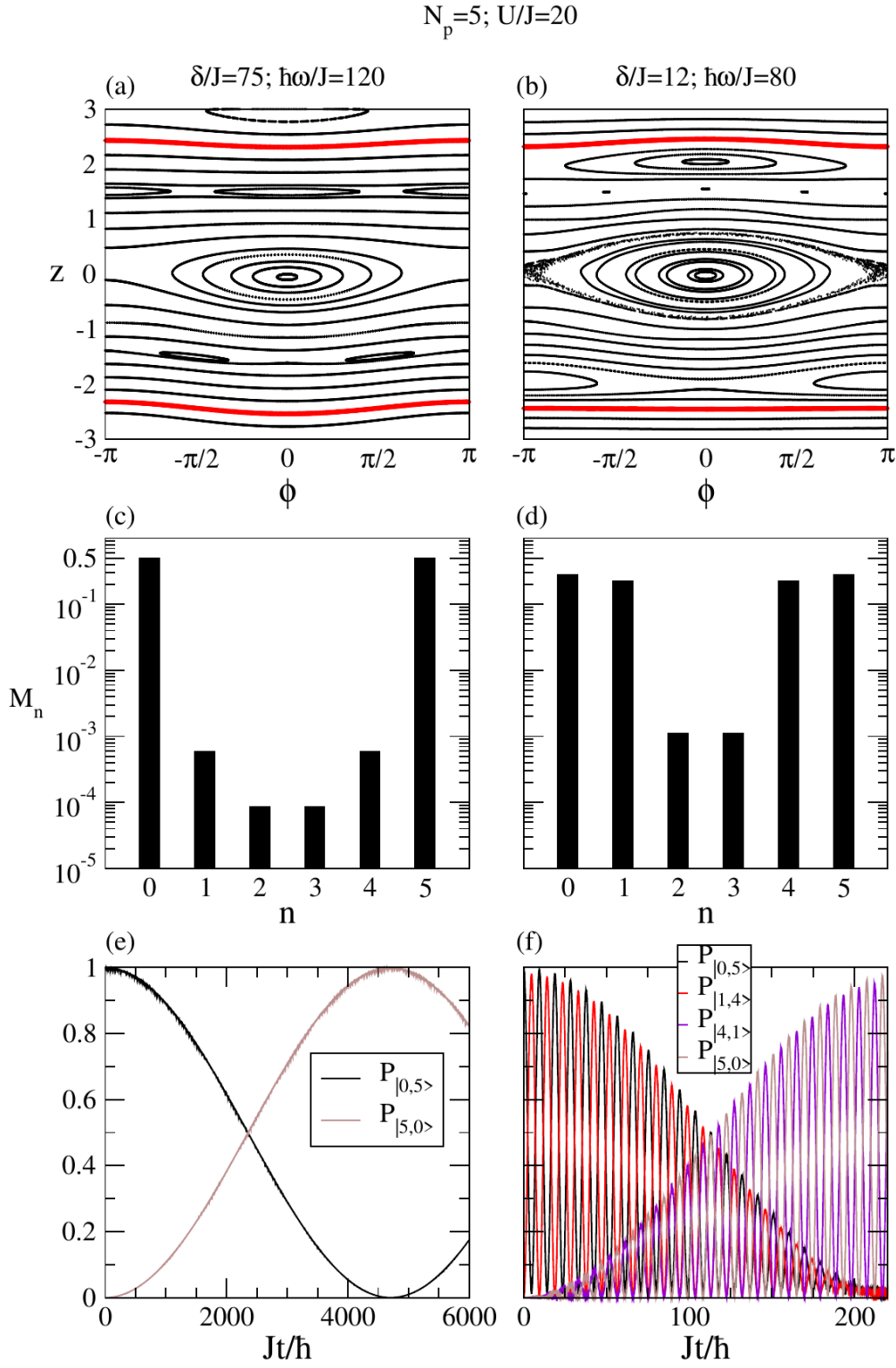


Figure 4.4.1: NOON states in the near-integrable regime. (a,b) Stroboscopic sections of the phase space. (c,d) Admixtures of quasimodes. (e,f) Time evolution of the detection probabilities. The left column represents the case where a 2:1 resonance situated in $z_{2:1} \simeq 1.5$ couples the quasimodes $|5,0\rangle$ and $|3,2\rangle$ while the right column represents the case where the 1:1 resonance located in $z_{1:1} \simeq -2$ couples the quasimodes $|0,5\rangle$ and $|1,4\rangle$. For the latter, the two-level approximation does not hold and the dynamic takes place on two timescales (see the relation (4.4.26) and the panels (d) and (f)). For the 2:1 resonance case, the NOON time is given by $\tau = 2.4 \times 10^3 \hbar/J$, with an excellent purity $p = 0.999$, while τ_s is equal to $112.3 \hbar/J$ in the 1:1 case. The tori in red represent the classical trajectories related to the NOON state.

to decompose the matrix in it,

$$H = \begin{pmatrix} S & 0 \\ 0 & A \end{pmatrix}, \quad (4.4.6)$$

$$S = \begin{pmatrix} E_0 + V_0 & V \\ V & E_1 + V_1 \end{pmatrix}, \quad A = \begin{pmatrix} E_0 - V_0 & V \\ V & E_1 - V_1 \end{pmatrix}. \quad (4.4.7)$$

Here S represents the symmetric block while A is the antisymmetric block. The eigenvalues are given by¹²

$$\epsilon_1^- = \frac{E_1 + E_0 - (V_1 + V_0)}{2} - \sqrt{\frac{(E_1 - E_0 - (V_1 - V_0))^2}{4} + V^2} \quad (\text{block } A), \quad (4.4.8)$$

$$\epsilon_2^+ = \frac{E_1 + E_0 + (V_1 + V_0)}{2} - \sqrt{\frac{(E_1 - E_0 + (V_1 - V_0))^2}{4} + V^2} \quad (\text{block } S), \quad (4.4.9)$$

$$\epsilon_3^- = \frac{E_1 + E_0 - (V_1 + V_0)}{2} + \sqrt{\frac{(E_1 - E_0 - (V_1 - V_0))^2}{4} + V^2} \quad (\text{block } A), \quad (4.4.10)$$

$$\epsilon_4^+ = \frac{E_1 + E_0 + (V_1 + V_0)}{2} + \sqrt{\frac{(E_1 - E_0 + (V_1 - V_0))^2}{4} + V^2} \quad (\text{block } S). \quad (4.4.11)$$

For example, the case shown in Fig. 4.4.1(f) can be approximately described by oscillations between the quasimodes $|0, 5\rangle$, $|1, 4\rangle$, $|4, 1\rangle$ and $|5, 0\rangle$. By assuming that

$$|0, 5\rangle \leftrightarrow \begin{pmatrix} 1 \\ 0 \\ 0 \\ 0 \end{pmatrix}, \quad |1, 4\rangle \leftrightarrow \begin{pmatrix} 0 \\ 1 \\ 0 \\ 0 \end{pmatrix}, \quad |4, 1\rangle \leftrightarrow \begin{pmatrix} 0 \\ 0 \\ 1 \\ 0 \end{pmatrix}, \quad |5, 0\rangle \leftrightarrow \begin{pmatrix} 0 \\ 0 \\ 0 \\ 1 \end{pmatrix}, \quad (4.4.12)$$

we have

$$E_0 = \epsilon_{0,5}^{(0)}, \quad (4.4.13)$$

$$E_1 = \epsilon_{1,4}^{(0)} + \hbar\omega. \quad (4.4.14)$$

Here $\epsilon_{n_1, n_2}^{(0)}$ refers to the quasimode $|n_1, n_2\rangle$ or the quasimode $|n_2, n_1\rangle$. The eigenvectors take the following form for $E_1 - E_0 \pm (V_1 - V_0) > 0$,

$$|1\rangle = \cos \theta^- \left(\frac{1}{\sqrt{2}}(|0, 5\rangle - |5, 0\rangle) \right) - \sin \theta^- \left(\frac{1}{\sqrt{2}}(|1, 4\rangle - |4, 1\rangle) \right), \quad (4.4.15)$$

$$|2\rangle = \cos \theta^+ \left(\frac{1}{\sqrt{2}}(|0, 5\rangle + |5, 0\rangle) \right) - \sin \theta^+ \left(\frac{1}{\sqrt{2}}(|1, 4\rangle + |4, 1\rangle) \right), \quad (4.4.16)$$

$$|3\rangle = \sin \theta^- \left(\frac{1}{\sqrt{2}}(|0, 5\rangle - |5, 0\rangle) \right) + \cos \theta^- \left(\frac{1}{\sqrt{2}}(|1, 4\rangle - |4, 1\rangle) \right), \quad (4.4.17)$$

$$|4\rangle = \sin \theta^+ \left(\frac{1}{\sqrt{2}}(|0, 5\rangle + |5, 0\rangle) \right) + \cos \theta^+ \left(\frac{1}{\sqrt{2}}(|1, 4\rangle + |4, 1\rangle) \right), \quad (4.4.18)$$

with

$$\tan(2\theta^\pm) = \frac{2V}{E_1 - E_0 \pm (V_1 - V_0)}. \quad (4.4.19)$$

¹²The assumptions $E_1 - E_0 \pm (V_1 - V_0) > 0$ ($\Rightarrow E_1 > E_0$), $V_1 > V_0$ and $V_0 > 0$ can be made in order to have $\epsilon_1^- < \epsilon_2^+ < \epsilon_3^- < \epsilon_4^+$. Note that the index m of ϵ_m^\pm doesn't refer to a specific quasimode as there are strong admixtures.

In the strong coupling case $|V| \gg \frac{1}{2}|E_1 - E_0 \pm (V_1 - V_0)|$, the eigenvalues can be developed in series according to

$$\epsilon_{1,3}^- = \frac{E_1 + E_0 - (V_1 + V_0)}{2} \mp |V| \left(1 + \frac{1}{8} \frac{(E_1 - E_0 - (V_1 - V_0))^2}{V^2} + \mathcal{O}(1/V^4) \right) \quad (4.4.20)$$

$$\epsilon_{2,4}^+ = \frac{E_1 + E_0 + (V_1 + V_0)}{2} \mp |V| \left(1 + \frac{1}{8} \frac{(E_1 - E_0 + (V_1 - V_0))^2}{V^2} + \mathcal{O}(1/V^4) \right). \quad (4.4.21)$$

This leads to

$$\epsilon_2^+ + \epsilon_3^- \simeq \epsilon_1^- + \epsilon_4^+ \quad (4.4.22)$$

$$|\theta^\pm| \simeq \pi/4. \quad (4.4.23)$$

Hence, with the additional assumption $V > 0$, we obtain¹³

$$\theta^\pm \simeq \pi/4. \quad (4.4.24)$$

From an initial state $|\phi(0)\rangle = |0, 5\rangle \simeq \frac{1}{2}(|1\rangle + |2\rangle + |3\rangle + |4\rangle)$, the time evolution reads^{14,15}

$$\begin{aligned} |\phi(t)\rangle &\simeq \frac{1}{2} \left(e^{-i\epsilon_1^- t/\hbar} |1\rangle + e^{-i\epsilon_2^+ t/\hbar} |2\rangle + e^{-i\epsilon_3^- t/\hbar} |3\rangle + e^{-i\epsilon_4^+ t/\hbar} |4\rangle \right) \\ &= \frac{1}{4} [e^{-i\epsilon_1^- t} (|0, 5\rangle - |5, 0\rangle - |1, 4\rangle + |4, 1\rangle) \\ &\quad + e^{-i\epsilon_2^+ t} (|0, 5\rangle + |5, 0\rangle - |1, 4\rangle - |4, 1\rangle) \\ &\quad + e^{-i\epsilon_3^- t} (|0, 5\rangle - |5, 0\rangle + |1, 4\rangle - |4, 1\rangle) \\ &\quad + e^{-i\epsilon_4^+ t} (|0, 5\rangle + |5, 0\rangle + |1, 4\rangle + |4, 1\rangle)] \\ &\simeq \cos\left(\frac{\Omega_s}{2}t\right) \left[\cos\left(\frac{\Omega_f}{2}t\right) |0, 5\rangle - i \sin\left(\frac{\Omega_f}{2}t\right) |1, 4\rangle \right] \\ &\quad - i \sin\left(\frac{\Omega_s}{2}t\right) \left[\cos\left(\frac{\Omega_f}{2}t\right) |5, 0\rangle - i \sin\left(\frac{\Omega_f}{2}t\right) |4, 1\rangle \right], \end{aligned} \quad (4.4.26)$$

¹³If $E_0 = E_1$ and $V_0 = V_1$, the results $\epsilon_2 + \epsilon_3 = \epsilon_1 + \epsilon_4$ and $\theta^\pm = \pi/4$ are exact. Nevertheless, it is expected to have $V_1 \gg V_0$ in the two site-optical lattice as the tunneling rate decreases significantly with the population imbalance.

¹⁴In summary, this result is valid if the following assumption is fulfilled,

$$V \gg \frac{1}{2}(E_1 - E_0 \pm (V_1 - V_0)) > 0. \quad (4.4.25)$$

¹⁵If we had assumed $V < 0$, we would have had $\theta^\pm \simeq -\pi/4$ and the temporal evolution would have been

$$\begin{aligned} |\phi(t)\rangle &\simeq \cos\left(\frac{\Omega_s}{2}t\right) \left[\cos\left(\frac{\Omega_f}{2}t\right) |0, 5\rangle + i \sin\left(\frac{\Omega_f}{2}t\right) |1, 4\rangle \right] \\ &\quad - i \sin\left(\frac{\Omega_s}{2}t\right) \left[\cos\left(\frac{\Omega_f}{2}t\right) |5, 0\rangle + i \sin\left(\frac{\Omega_f}{2}t\right) |4, 1\rangle \right]. \end{aligned}$$

Note that the detection probabilities are the same for both signs of V .

where the frequencies Ω_s and Ω_f refer respectively to the slow and the fast oscillations,

$$\Omega_s = \frac{\epsilon_4^+ - \epsilon_3^- + \epsilon_2^+ - \epsilon_1^-}{2\hbar}, \quad (4.4.27)$$

$$\Omega_f = \frac{\epsilon_4^+ - \epsilon_2^+ + \epsilon_3^- - \epsilon_1^-}{2\hbar}. \quad (4.4.28)$$

The probabilities of detection for the quasimodes, $P_{|n_1, n_2\rangle}(t) = |\langle n_1, n_2 | \phi(t) \rangle|^2$, exhibit the two timescales of the dynamics, which enables one to model the numerical results in Fig. 4.4.1(f),

$$\begin{aligned} P_{|0,5\rangle}(t) &= \cos^2\left(\frac{\Omega_s}{2}t\right) \cos^2\left(\frac{\Omega_f}{2}t\right), \\ P_{|1,4\rangle}(t) &= \cos^2\left(\frac{\Omega_s}{2}t\right) \sin^2\left(\frac{\Omega_f}{2}t\right), \\ P_{|5,0\rangle}(t) &= \sin^2\left(\frac{\Omega_s}{2}t\right) \cos^2\left(\frac{\Omega_f}{2}t\right), \\ P_{|4,1\rangle}(t) &= \sin^2\left(\frac{\Omega_s}{2}t\right) \sin^2\left(\frac{\Omega_f}{2}t\right). \end{aligned}$$

For the parameters $N_p = 5$, $U/J = 20$, $\delta/J = 12$ and $\hbar\omega/J = 80$, the perturbed quadruplet obtained through the exact diagonalization reads

$$\begin{aligned} \epsilon_4^+ &= 200.4351J, \\ \epsilon_3^- &= 200.4197J, \\ \epsilon_2^+ &= 199.7674J, \\ \epsilon_1^- &= 199.7548J, \end{aligned} \quad (4.4.29)$$

which enables one to measure the degree of deviation from the assumption (4.4.22),

$$\epsilon_4^+ + \epsilon_1^- - \epsilon_3^- - \epsilon_2^+ = 2.713 \times 10^{-3}J. \quad (4.4.30)$$

The spectrum (4.4.29) determines the characteristic times of the slow oscillations, τ_s , and the fast oscillations, τ_f ,

$$\begin{aligned} \tau_s &= \frac{\pi}{2|\Omega_s|} & \tau_f &= \frac{\pi}{2|\Omega_f|} \\ &= 112.3\hbar/J, & &= 2.357\hbar/J. \end{aligned} \quad (4.4.31)$$

Here τ_s represents the time required to obtain a NOON state, i.e. the NOON time. For typical optical lattice parameters filled with ^{87}Rb atoms (see Eq. (2.1.18)), the NOON time corresponds to $\tau_s = 0.49\text{s}$.

In order to obtain a perfectly balanced NOON state without impurities, i.e. with $P_{|0,5\rangle} = P_{|5,0\rangle} = 0.5$, on time τ_s , the frequency ratio Ω_f/Ω_s must be divisible by four according to Eq. (4.4.26). Fine-tuning of the amplitude of the driving δ is a way to achieve this purpose, but this may become very difficult in practice. Alternatively, if Ω_f/Ω_s is not exactly a multiple of four (such as $\Omega_f/\Omega_s = 47.62$ in our case), it is possible to create a NOON state without impurities ($P_{|0,5\rangle} + P_{|5,0\rangle} = 1$), but with a small bias between $P_{|0,5\rangle}$ and $P_{|5,0\rangle}$. By inspecting the zoom around τ_s shown in Fig. 4.4.2, the measurement time, t_m , can be chosen

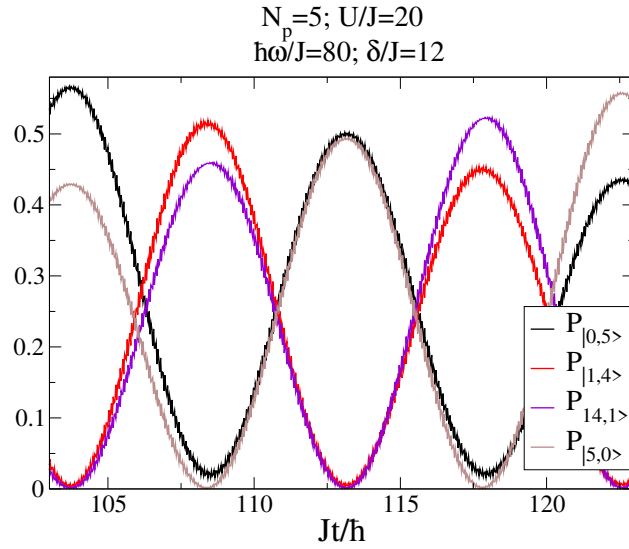


Figure 4.4.2: Close-up around τ_s of the detection probabilities for the 1:1 resonance case (see Fig. 4.4.1(f)). Even though this configuration is not able to produce a perfectly unbiased NOON state ($P_{|0,5\rangle} = P_{|5,0\rangle} = 0.5$), a slightly biased NOON state with almost no impurity, i.e. $P_{|0,5\rangle} + P_{|5,0\rangle} \simeq 1$ and $P_{|0,5\rangle} - P_{|5,0\rangle} = 8.5 \times 10^{-3}$, can be realized by choosing the measurement time slightly larger than $\tau_s = 112.3\hbar/J$, namely $t_m = 113.25\hbar/J$.

"by hand" in order to meet these criteria. For example, if we choose a $t_m = 113.25\hbar/J$ slightly larger than τ_s , we obtain $P_{|0,5\rangle} \approx P_{|5,0\rangle} \approx 0.5$ with $P_{|0,5\rangle} - P_{|5,0\rangle} = 8.5 \times 10^{-3}$ and $P_{|4,1\rangle} \approx P_{|1,4\rangle} \approx 10^{-3}$.

4.4.1 Semiclassical evaluation of the four-level oscillations

Even in the strong perturbation regime, the framework of resonance-assisted tunneling can still be used, as far as the matrix modeling (4.3.46) is concerned. Nevertheless, it becomes no longer possible to associate specific quasimodes to the results of the diagonalization, rendering invalid the relation (4.3.47).

More specifically, the effect of the 1:1 resonance (see Fig. 4.4.1(b)) on the new eigenvalues can be modeled by

$$\begin{pmatrix} \tilde{\epsilon}_2^{(0)} & V_1^{(1:1)} & 0 & \Delta_2 \\ V_0^{(1:1)*} & \tilde{\epsilon}_1^{(0)} & \Delta_1 & 0 \\ 0 & \Delta_1 & \tilde{\epsilon}_1^{(0)} & V_1^{(1:1)} \\ \Delta_2 & 0 & V_1^{(1:1)*} & \tilde{\epsilon}_2^{(0)} \end{pmatrix}, \quad (4.4.32)$$

where $V_1^{(1:1)}$ is defined in Eq. (4.3.44) and $\tilde{\epsilon}_m^{(0)} = \epsilon_m^{(0)} - \hbar\omega Y_m$. The unperturbed energies and splittings are respectively given by $\epsilon_m^{(0)}$ and $\Delta\epsilon_m^{(0)} = 2\Delta_m$. The exact diagonalization of this

matrix leads to the following eigenvalues,

$$\epsilon_{1,3}^- = \frac{\tilde{\epsilon}_1^{(0)} + \tilde{\epsilon}_2^{(0)} - (\Delta_1 + \Delta_2)}{2} \mp \sqrt{\frac{\left(\tilde{\epsilon}_1^{(0)} - \tilde{\epsilon}_2^{(0)} - (\Delta_1 - \Delta_2)\right)^2}{4} + \left|V_1^{(1:1)}\right|^2}, \quad (4.4.33)$$

$$\epsilon_{2,4}^+ = \frac{\tilde{\epsilon}_1^{(0)} + \tilde{\epsilon}_2^{(0)} + (\Delta_1 + \Delta_2)}{2} \mp \sqrt{\frac{\left(\tilde{\epsilon}_1^{(0)} - \tilde{\epsilon}_2^{(0)} + (\Delta_1 - \Delta_2)\right)^2}{4} + \left|V_1^{(1:1)}\right|^2}. \quad (4.4.34)$$

The purpose is to reproduce the two exact characteristic times (4.4.31) by means of the features of the phase space 4.4.1(b), especially the features of the 1:1 resonance.

$$Y_{1:1} = 2.0014 \quad (4.4.35)$$

$$V_{1:1} = 0.3285J \quad (4.4.36)$$

$$m_{1:1} = 0.02506J^{-1} \quad (4.4.37)$$

Moreover, the expression of the coupling matrix element $V_1^{(1:1)}$ obtained from Eq. (4.3.44) reads

$$V_1^{(1:1)} = V_{1:1} \sqrt{\frac{2}{Y_{1:1}}} e^{-i\varphi_{1:1}}. \quad (4.4.38)$$

The unperturbed splittings are computed either from the analytic continuation of the classical trajectories in the complex domain (4.2.8) or from the spectrum of the unperturbed system (2.1.14).

By using the antisymmetric block for the unperturbed energies, the timescales of the slow and the fast oscillations read respectively

$$\tau_s = 105.5\hbar/J, \quad \tau_f = 2.369\hbar/J, \quad (4.4.39)$$

which reproduce relatively well the exact results (4.4.31).

4.4.2 Improvement of the resonant condition

As pointed out in Eqs. (4.4.22) and (4.4.23), the strong coupling condition must be fulfilled in order to observe four-level oscillations. One method to reach that is to tune the driving frequency to an exact resonance in the Floquet spectrum. The canonical perturbation theory is a way to determine the frequency that will couple some specific quasimodes (see Eq. (4.3.49)). Another way is to choose a frequency that is a multiple of the energy difference between the unperturbed energies $\epsilon_n^{(0)}$ and $\epsilon_{n-kr}^{(0)}$ according to [72]

$$\hbar\omega = \frac{\epsilon_n^{(0)} - \epsilon_{n-kr}^{(0)}}{ks}, \quad (4.4.40)$$

where $r:s$ is the nonlinear resonance that couples both levels, and k is the number of steps to connect them. This relation is obtained by canceling the denominator of Eq. (4.3.36).

In this context, a precise determination of the unperturbed energies can help to obtain an ω that will fulfill the resonant condition. By using Eqs. (4.1.8) obtained in the framework of the canonical perturbation theory up to the second order, the unperturbed energies for

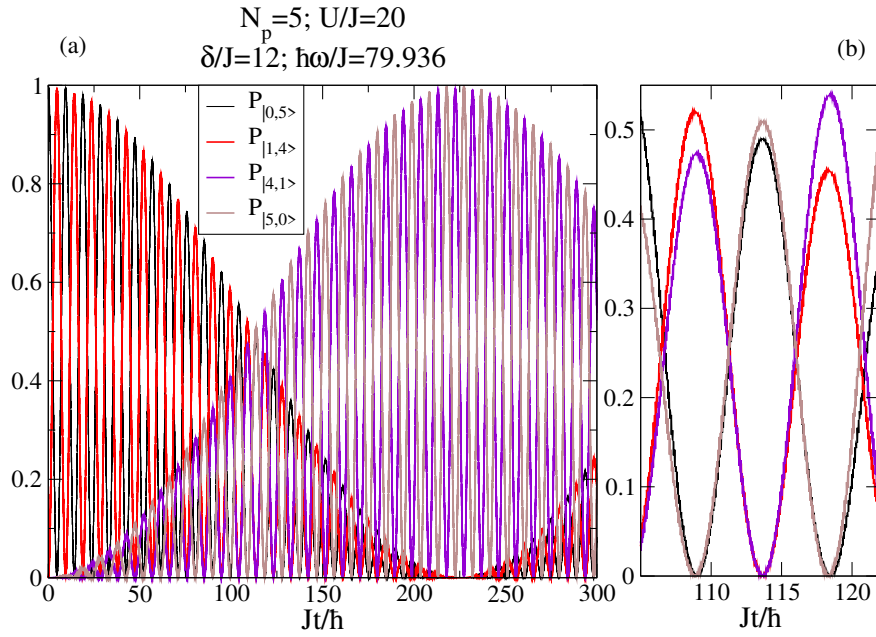


Figure 4.4.3: (a) Numerical detection probabilities as a function of time. (b) Zoom around $t_m = 113.7\hbar/J$, the time related to the formation of the NOON state. By tuning an external frequency as exact as possible to a resonance in the Floquet spectrum, it is possible to improve the strong coupling assumption (4.4.25), which leads to an improvement of the four-level oscillations as indicated by this figure and by the computation (4.4.41).

the parameters $N_p = 5$ and $U/J = 20$ read

$$\begin{aligned}\epsilon_2^{(0)} &= 200.061J, \\ \epsilon_1^{(0)} &= 120.125J, \\ \epsilon_0^{(0)} &= 80.925J.\end{aligned}$$

The assumption of strong perturbation for the 1:1 resonance of Fig. 4.4.1 can be improved with $\hbar\omega = \epsilon_2^{(0)} - \epsilon_1^{(0)} = 79.936J$ leading to an improvement of condition (4.4.22) such that

$$\epsilon_4^+ + \epsilon_1^- - \epsilon_3^- - \epsilon_2^+ = 2.429 \times 10^{-5}J, \quad (4.4.41)$$

for $\delta/J = 12$. Figure 4.4.3 displays the improved four-level oscillations with a driving frequency slightly different from $80J/\hbar$. Thanks to Fig. 4.4.3(b), which shows a zoom around the NOON time, it is possible to choose by hand a time, t_m , for the detection probabilities. With $t_m = 113.7\hbar/J$, we have $P_{|5,0>} + P_{|0,5>} \approx 0.999$ and $P_{|4,1>} + P_{|1,4>} \approx 10^{-3}$, which is similar to the results of the previous frequency. Nevertheless, the bias is more important and is equal to $P_{|5,0>} - P_{|0,5>} \approx 1.86 \times 10^{-2}$. Actually, we use the same amplitude δ to compute this case as the other one in Fig. 4.4.2. By fine-tuning the amplitude while adjusting t_m , it is possible to decrease the bias and the impurities. Moreover, the improvement of the condition $\epsilon_4^+ + \epsilon_1^- - \epsilon_3^- - \epsilon_2^+ = 0$ in Eq. (4.4.41) guarantees us that the purity can be enhanced.

4.5 Resonance- and chaos-assisted tunneling

4.5.1 NOON states in mixed phase spaces

Besides the resonances, chaos in phase space is expected to play a role on the tunneling rate. As shown Fig. 4.5.1 the combination between nonlinear resonances and chaos induces a significant decrease of the NOON time τ . Figure 4.5.1(d), (e) and (f) are the mean-field dynamics associated with panels (a), (b) and (c) respectively. The latter show the results of numerically simulated *in situ* measurements as a function of time of spinless bosonic atoms trapped in a double-well potential.

For the non-interacting conditions ($U = 0$), tunneling occurs through individual atomic transfer in a periodic way leading to Josephson oscillations [145,146]. The mean-field dynamics of Fig. 4.5.1(d) displays huge variations for the population imbalance. At the quantum level, it means that the eigenstates display non-negligible admixtures in terms of the quasi-modes. In this configuration, it is impossible to build a NOON state.

A regime of self-trapping [21,53–61], also called Fock regime, appears with sufficiently interacting atoms for high population imbalances as displayed in Figs. 4.5.1(e) and (f). In the case of Fig. 4.5.1(e), there is a coexistence between Josephson oscillations, where the hopping term dominates, and self-trapping, where the effective on-site interaction dominates, namely for low and high population imbalances respectively. In the self-trapping regime, the mismatches between the chemical potentials of both sites inhibit the one by one transition. Nevertheless, after a sufficiently long time, the system will experience a collective transfer of particles. This giant transfer of matter is due to the quasidegeneracy between the symmetric and antisymmetric superposition of $|N_p, 0\rangle$ and $|0, N_p\rangle$, i.e. the almost eigenstates related to the NOON state.

The dynamics schematized in Figs. 4.5.1(b) and (c) are qualitatively the same. Nevertheless, the order of magnitude of the NOON time is quite different: $\tau(\delta = 0) = 6.0 \times 10^5 \hbar/J$ in the unperturbed regime, and $\tau(\delta = 19.5J) = 1.9 \times 10^2 \hbar/J$ in the perturbed one characterized by $\delta/J = 19.5$ and $\hbar\omega/J = 20$. It is consistent with an abundant amount of literature [67,68,71–79,81–84] which suggests that nonlinear resonances and chaos have a huge impact on the tunneling rate. For a typical optical lattice characterized by a wavelength $\lambda = 1064$ nm filled with ^{87}Rb characterized by a mass $m = 1.443 \times 10^{-25}$ kg and a s-wave scattering length $a_s = 5.313$ nm, we obtain $\hbar/J = 4.4 \times 10^{-3}$ s (see Sec. 1.3.3 for the derivations). This leads to the NOON time $\tau(\delta = 19.5J) = 0.84$ s while we obtained in the unperturbed case $\tau(\delta = 0) = 2.6 \times 10^3$ s.

In the next section, the combined effects of the 1:4 resonance located at $z_{1:4} \simeq \pm 2$, the 1:3 resonance at $z_{1:3} \simeq \pm 1.5$ and the central chaotic sea (where the quasimodes displays strong admixture) will be able to explain semiclassically that decrease of the NOON time. The dominant path that speeds up the transition to the NOON states will be given by

$$|2\rangle \xrightarrow{1:4} |1\rangle \xrightarrow{1:3} \text{chaotic sea}, \quad (4.5.1)$$

where $|2\rangle$ and $|1\rangle$ correspond respectively to $|5, 0\rangle$ and $|4, 1\rangle$.

To build the phase space 4.5.1(f), the relation (4.3.49) was used to determine the frequency producing a 1:4 resonance in $z_{1:4} \simeq \pm 2$ symmetrically located between $|2\rangle$ and $|1\rangle$, i.e. $\hbar\omega = 20J$. Moreover, the interplay between the central unperturbed island in the phase space 4.5.1(e) and the 1:1 resonance in $z_{1:1} \simeq \pm 0.5$ leads to the central chaotic layer.

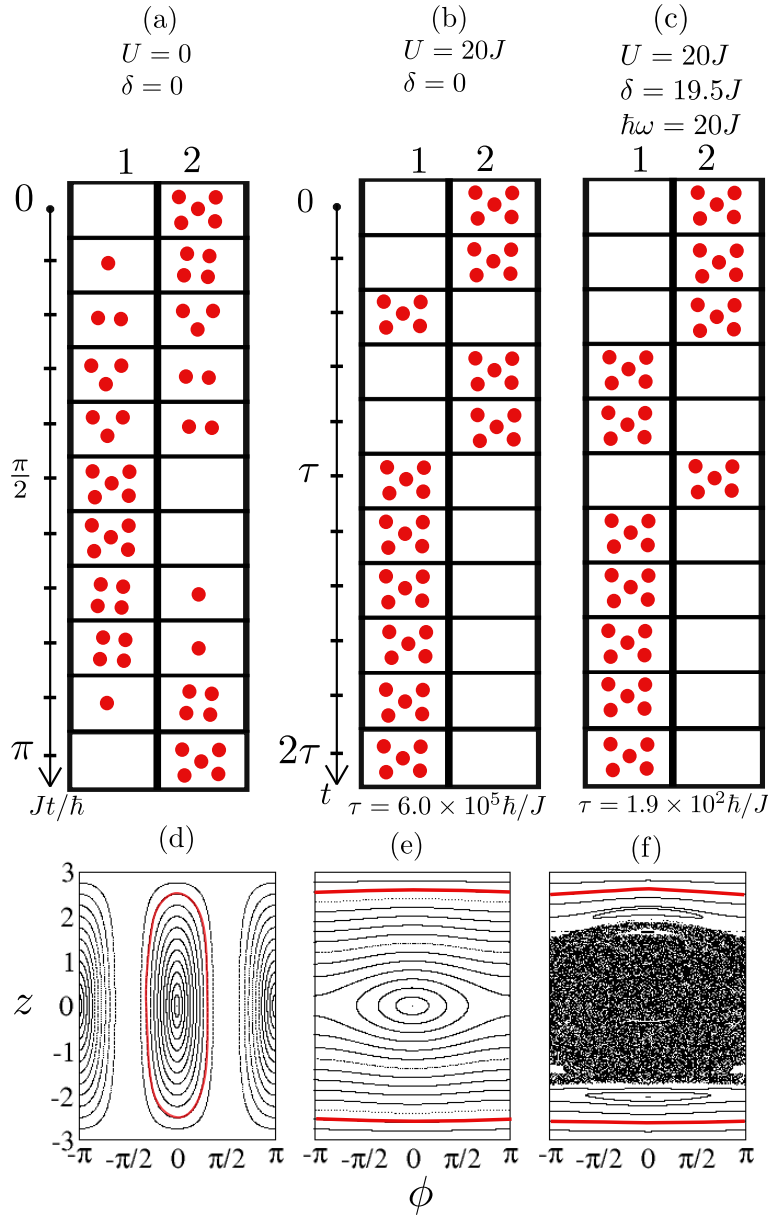


Figure 4.5.1: Sequential (a) and collective tunneling (b and c) of ultracold bosonic atoms in a double-well potential, in the absence (a and b) and in the presence (c) of a periodic driving. In the upper panels (a-c), a measurement process of the number of atoms within individual wells is numerically simulated for various evolved times, based on the numerical time evolution generated by the Hamiltonian (2.1.20). The lower panels (d-f) represent the corresponding phase spaces in the mean-field approximation (see the Hamiltonian (3.1.11)). The population imbalance and the phase difference between site 1 and 2 are respectively $z = (N_1 - N_2)/2$ and $\phi = \theta_1 - \theta_2$. The red trajectories are the classical counterparts of the upper quantum dynamics. (a,d) In the absence of interaction, tunneling occurs one by one, leading to Josephson oscillations. (b,e) In the presence of interaction ($U = 20J$), collective tunneling takes place, but on a very long timescale, $\tau = 6.0 \times 10^5 \hbar/J$. The phase space displays two qualitatively different dynamics, namely Josephson oscillations for low population imbalances and self-trapping for high population imbalance. (c,f) In the presence of a periodic shaking characterized by an amplitude $\delta/J = 19.5$ and a frequency $\hbar\omega/J = 20$, collective tunneling occurs on a much shorter timescale, $\tau = 1.9 \times 10^2 \hbar/J$. The presence of a central chaotic layer, a 1:4 resonance roughly situated at $z = \pm 2$ and a 1:3 one in $z \simeq \pm 1.5$ is able to explain the decrease of the NOON time.

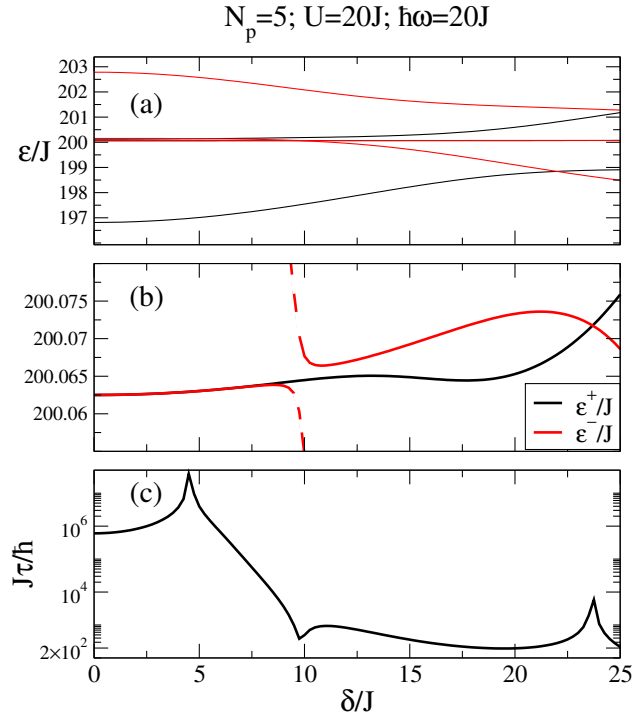


Figure 4.5.2: NOON doublet in the Floquet spectrum as a function of the driving amplitude. Panel (a) represents a block of the periodic Floquet spectrum (with even-parity levels being marked in black and odd-parity levels in red). Panel (b) displays a close-up of the block in (a) and panel (c) shows the NOON time calculated from panel (b) and the relation (2.1.17). The minimal τ appears roughly in $\delta/J \simeq 19.5$, which was used to produce Figs. 4.5.1(c) and (f). This result is robust in the sense that a range between $\delta/J \simeq 12$ and 22 can be chosen to observe the reduction by several orders of magnitude of the NOON time.

In order to find an optimal value of δ , all other parameters are fixed and the NOON time is computed as a function of δ . Figure 4.5.2(c) suggests that the a NOON-time minimum is reached for $\delta/J \approx 19.5$. This result is robust, meaning that there is a range between approximately $\delta/J = 12$ and 22 where the decrease of the NOON time is observable. This range begins roughly at a level repulsion near $\delta/J = 10$ for which the doublet of the symmetric and antisymmetric combination of $|0, 5\rangle$ and $|5, 0\rangle$ is crossed by the antisymmetric combination of $|1, 4\rangle$ and $|4, 1\rangle$ (see the dashed line of Fig. 4.5.2(b)). After that, the splitting gains several orders of magnitude. The more δ/J is increased, the larger the chaotic sea is. For $\delta/J > 25$, the quasimodes $|0, 5\rangle$ and $|5, 0\rangle$ begin to be diluted in the central chaotic layer. Beyond this point, the notions of splitting and NOON time are no longer meaningful.

In view of the latter considerations, a legitimate preoccupation could be the implication of the external driving on the purity of the NOON state. Indeed, the driving tends to decrease the NOON time, but tends also to increase the admixture between the NOON state and the other quasimodes. A time-independent indicator of the purity of the NOON state is given by the time-average (4.4.1). The time average over one driving period allows one to eliminate small periodic oscillations of the purity related to micromotions, which are not of interest here. Figure 4.5.3(b) suggests that the resulting purity is roughly equal to $p = 0.99$. Therefore, the two-level approximation seems to hold. Nevertheless, it is true that the introduction of the perturbation decreases the purity as this one is better for the unperturbed case (see Fig. 4.5.3(a)), i.e. $p = 0.999$. Figure 4.5.3 shows that the time evolution of the transition probabilities can be described in terms of two-state dynamics

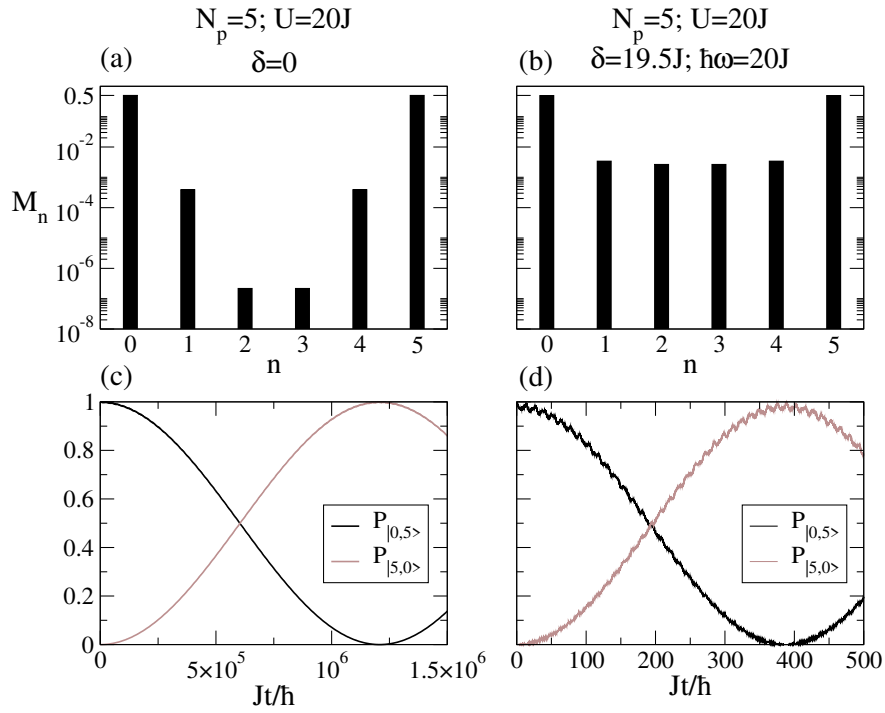


Figure 4.5.3: Overlap between the quasimodes $|n, N_p - n\rangle$ ($n = 0, 1, 2, 3, 4, 5$) and the Floquet eigenstates according to Eq. (4.4.2). Even for the perturbed system (b) and (d), the two-level approximation can still be justified as $M_0 = M_{N_p} \approx 0.5$. Panels (c) and (d) display the detection probabilities knowing that the system is prepared in $|0, 5\rangle$. While (a) and (c) show the unperturbed case, (b) and (d) display the situation with a frequency $\hbar\omega/J = 20$ that produces a chaotic layer and prominent 1:4 and 1:3 resonances as displayed in Fig. 4.5.1(f).

in both cases. This constitutes the advantage of the mixed phase space in comparison to the 1:1 resonance case in the near-integrable regime, Fig. 4.4.1(f), for which there are more constraints concerning the time precision of the NOON-state measure.

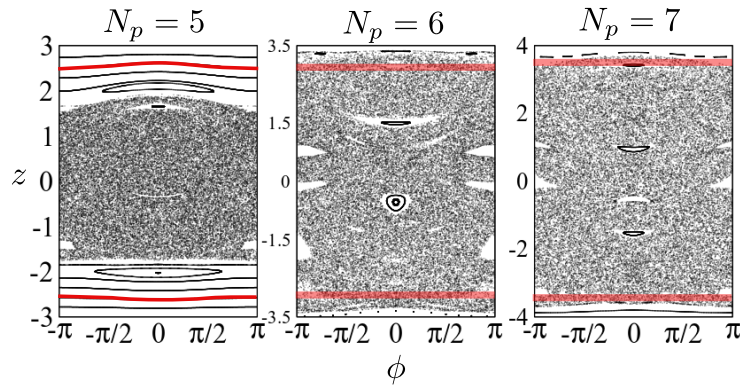


Figure 4.5.4: Evolution of the phase space with N_p . The nonlinear parameter $(N_p + 1)U/J$ and $\hbar\omega/J$ are kept constant in order to preserve the phase space for $\delta = 0$. Here δ/J is chosen such that a minimum of the NOON time is reached for $N_p = 5, 6, 7$. We choose $\delta/J = 19.5, 50, 44$ respectively. Note that for $N_p = 6$ and 7 the NOON states (highlighted by red shading on the phase space) are separated from the chaotic sea by partial barriers [72, 75, 76].

As pointed out in Eq. (4.2.14), the splitting between two related quasimodes is known to decrease exponentially with N_p , leading to an exponential increase of the NOON time. This is also the case for $\delta \neq 0$, but the increase is not so extreme. In Fig. 4.5.4, N_p is increased while keeping the nonlinear parameter $(N_p + 1)U/J$ and $\hbar\omega/J$ constant. From an experimental point of view, this particular scaling can be achieved by an adaptation of the lattice parameters without the need of modifying the s-wave scattering length a_s . Keeping the nonlinear parameter constant enables one to preserve the same phase space for $\delta = 0$.

N_p	$J\tau_{\delta=0}/\hbar$	$J\tau_{\delta\neq 0}/\hbar$	$p_{\delta\neq 0}$
5	6.0×10^5	1.9×10^2	0.988
6	2.3×10^7	5.5×10^2	0.968
7	9.2×10^8	1.4×10^3	0.987

Table 4.1: Comparison of the behaviors of the NOON time as a function of the total number of particles N_p in the unperturbed and perturbed systems. The NOON time is expected to exponentially increase with the semiclassical parameter N_p . The third column shows that this increase is softened by the external perturbation, suitably tuned in order to reach a minimum of the NOON time. These minima are obtained at $\delta/J = 19.5, 50, 44$ for $N_p = 5, 6, 7$ respectively. As shown in the fourth column, the purities stay reasonable in the perturbed case.

Figure 4.5.4 represents three phase spaces for $N_p = 5, 6, 7$ with $\delta/J = 19.5, 50, 44$, respectively, which correspond to minima of the NOON time τ . For $N_p=6$ and 7, the NOON states (in red) appear to be inside the chaotic region. However, they are still isolated from the chaotic part of the Floquet spectrum by the presence of partial barriers in the phase space [72,75,76]. As shown in Table 4.1, the NOON time with a perturbation increases with N_p as expected. Nevertheless, this increase is slowed down in comparison to the one in the unperturbed case. In addition to the reduction the NOON time, the external perturbation is also able to decrease the slope of τ as a function of N_p (see Table 4.1). Resonance- and chaos-assisted tunneling therefore opens interesting perspectives to create increasingly big entangled states.

4.5.2 Modeling of the chaotic sea

In the framework of resonance-assisted tunneling, the coupling matrix elements between the quasimodes are introduced as a function of the features of the nonlinear resonances. The chaotic sea can be modeled by introducing a block inside the matrix (4.3.46) describing the modification of the tunneling rate [72,78,79,84] such that

$$H_{\text{eff}} = \begin{pmatrix} \epsilon_n^{(0)} & V_{\text{eff}} & 0 & \cdots & 0 & \Delta_n \\ V_{\text{eff}} & \boxed{\text{chaos}} & & & & 0 \\ 0 & & & & & \vdots \\ \vdots & & & & & 0 \\ 0 & & & & & V_{\text{eff}} \\ \Delta_n & 0 & \cdots & 0 & V_{\text{eff}} & \epsilon_n^{(0)} \end{pmatrix}, \quad (4.5.2)$$

where V_{eff} is the effective coupling to the chaotic sea. This matrix must be compatible with the global symmetry of the system, i.e. it must commute with the operator associated with the discrete symmetry. In the case of the site-inversion symmetry, the matrix must be centrosymmetric.

The effective coupling V_{eff} takes into account all paths enabling to reach the chaotic sea with the m resonances $r_1:s_1, r_2:s_2, \dots, r_m:s_m$ [72],

$$V_{\text{eff}}^2 = \sum_{l=1}^m \sum_{k_1, k_2, \dots, k_m} \left| \mathcal{A}_{n, n+k_1 r_1}^{(r_1:s_1)} \right|^2 \left| \mathcal{A}_{n+k_1 r_1, n+k_1 r_1+k_2 r_2}^{(r_2:s_2)} \right|^2 \cdots \left| \mathcal{A}_{n+K_m, n+K_m+k_m r_m}^{(r_m:s_m)} \right|^2 \left| V_{n+K_m+k_m r_m-r_l}^{(r_l:s_l)} \right|^2 + \text{perm}(1, 2, \dots, m). \quad (4.5.3)$$

Here we have $K_m = k_1 r_1 + k_2 r_2 + \dots + k_{m-1} r_{m-1}$. If \bar{n} is the index of the last state inside the regular region, the last step to reach the chaotic sea must obey $n + K_m + k_m r_m - r_l < \bar{n}$ and $n + K_m + k_m r_m \geq \bar{n}$ ¹⁶. The $\text{perm}(1, 2, \dots, m)$ term takes into account all terms generated by the permutations between $r_1:s_1, r_2:s_2, \dots, r_m:s_m$. For $\text{perm}(1, 2, \dots, m)$, the terms with at least one $k_l = 0$ are removed in order to avoid multiple counting. Nevertheless, the $\text{perm}(1, 2, \dots, m)$ term is in general negligible if the $r_l:s_l$ are sorted according to their consecutive order of apparition in phase space. The amplitudes read

$$\mathcal{A}_{n+K_l, n+K_l+k_l r_l}^{(r_l:s_l)} = \prod_{j=\text{sgn}(k_l)}^{k_l} \frac{\langle n + K_l + j r_l | \hat{H}_{\text{res}}^{(r_l:s_l)} | n + K_l + (j - \text{sgn}(j)) r_l \rangle}{\epsilon_n^{(0)} - \epsilon_{n+K_l+j r_l}^{(0)} + (k_1 s_1 + k_2 s_2 + \dots + k_{l-1} s_{l-1} + j s_l) \hbar \omega} \quad k_l \neq 0, \quad (4.5.4)$$

with $K_l = k_1 r_1 + k_2 r_2 + \dots + k_{l-1} r_{l-1}$ and with the prescription $\mathcal{A}_{\nu, \nu}^{(r_l:s_l)} = 1$. Equation (4.5.3) can rapidly display numerous terms, especially with a lot of resonances for a high dimension of the Hilbert space. Nevertheless, it is still possible to have good insight as there exists in general one dominant coupling path.

Figure 4.5.5 displays the phase space studied in the preceding section, for which $N_p = 5$, $U = 20J$, $\delta = 19.5J$ and $\hbar\omega = 20J$. This phase space displays two prominent resonances, namely $r_1:s_1 = 1:4$ and $r_2:s_2 = 1:3$ characterized by the actions $Y_{r_l:s_l}$, the amplitudes $V_{r_l:s_l}$ and the effective masses $m_{r_l:s_l}$ (see the Hamiltonians (4.3.20) and (4.3.29)),

$$\begin{aligned} Y_{1:4} &= 2.004, & Y_{1:3} &= 1.511, \\ V_{1:4} &= 0.06857J, & V_{1:3} &= 0.3017J, \\ m_{1:4} &= 0.02491J^{-1}, & m_{1:3} &= 0.02491J^{-1}. \end{aligned} \quad (4.5.5)$$

The effective coupling to chaos (4.5.3) can be approximated by the term which contributes the most,

$$V_{\text{eff}}^2 \simeq \frac{\left| V_{n-r_1}^{(r_1:s_1)} \right|^2}{\left| \epsilon_n^{(0)} - \epsilon_{n-r_1}^{(0)} - s_1 \hbar \omega \right|^2} \left| V_{n-r_1-r_2}^{(r_2:s_2)} \right|^2. \quad (4.5.6)$$

The transition (4.5.6) can be schematically represented by the coupling path

$$|2\rangle \xrightarrow{1:4} |1\rangle \xrightarrow{1:3} \text{chaos}, \quad (4.5.7)$$

illustrated by the green and orange arrows in the phase space (4.5.5) while the red one represents the direct transition.

Visibly the quasimode $|1\rangle$ of Fig. 4.5.5 is embedded in the chaotic layer. However, there exists in mixed systems a kind of "gray zone", defined by the partial barriers [72, 74, 75], between the regular and the chaotic part of the phase space. The partial transport barriers

¹⁶This prescription is valid for the two-site Bose-Hubbard system for which K_m is negative. For some other systems (for example the standard map), the inequality symbols must be inverted [72].

are made of weakly connected chaotic subregions, where resonance chains, embedded in the chaotic part of the phase space, prevent the abrupt transition to the chaotic sea. In our specific case, the homoclinic tangle [65, 66] of the 1:3 resonance defines the innermost position of the partial barriers.

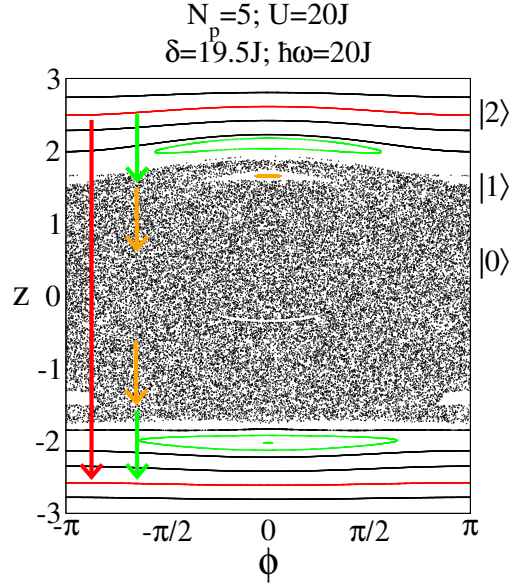


Figure 4.5.5: Stroboscopic map of the periodically-driven two-site Bose-Hubbard Hamiltonian. The red arrow represents the direct transition between both quasimodes related to the NOON state (red tori). The path defined by the green and orange arrows represents the dominant transition to chaos by means of the 1:4 resonance (in green) and the 1:3 (in orange).

Before describing a model of the chaotic block, the matrix (4.5.2) can be separated in its symmetric H_{eff}^+ and antisymmetric part H_{eff}^- ,

$$H_{\text{eff}}^{\pm} = \begin{pmatrix} \epsilon_n^{(0)} & V_{\text{eff}} \\ V_{\text{eff}} & \boxed{H_{\text{chaos}}^{\pm}} \end{pmatrix}. \quad (4.5.8)$$

Here the direct transition Δ_n is neglected. The chaotic block is characterized by the eigenvalues \mathcal{E}_j^{\pm} and the eigenvectors $|\Phi_j^{\pm}\rangle$,

$$\hat{H}_{\text{chaos}}^{\pm} |\Phi_j^{\pm}\rangle = \mathcal{E}_j^{\pm} |\Phi_j^{\pm}\rangle. \quad (4.5.9)$$

A way presented in [76, 77] to model the chaotic sea is to replace each chaotic block of (4.5.8) by a random matrix of the Gaussian orthogonal ensemble (GOE),

$$\boxed{H_{\text{chaos}}^{\pm}} \longrightarrow \boxed{\text{GOE}}.$$

The $(H_{\text{chaos}}^{\pm})_{ij}$ are the elements of the chaotic blocks, and, according to GOE, they are chosen randomly while preserving the symmetric structure of the Hamiltonian with real entries such that $(H_{\text{chaos}}^{\pm})_{ij} = (H_{\text{chaos}}^{\pm})_{ji}$. This assumption gives rise to the following modification of the eigenenergies [72, 79],

$$\epsilon_n^{\pm} = \epsilon_n^{(0)} + \sum_{j=1}^{N_c} \frac{|\langle \Phi_j^{\pm} | \hat{V}^{\pm} | n \rangle|^2}{\epsilon_n^{(0)} - \mathcal{E}_j^{\pm}}. \quad (4.5.10)$$

The splitting is obtained with $\Delta\epsilon_n = |\epsilon_n^- - \epsilon_n^+|$. Here (\hat{V}^\pm) is the coupling matrix after the prediagonalization of H_{chaos}^\pm ,

$$(\hat{V}^\pm) = \begin{pmatrix} 0 & v_1^\pm & \cdots & v_{N_c}^\pm \\ v_1^\pm & 0 & \cdots & 0 \\ \vdots & \vdots & \ddots & \vdots \\ v_{N_c}^\pm & 0 & \cdots & 0 \end{pmatrix}, \quad (4.5.11)$$

with N_c the number of chaotic states of a given parity and $H_{\text{eff}}^\pm = \text{diag}(\epsilon_n^{(0)}, \mathcal{E}_1^\pm, \dots, \mathcal{E}_{N_c}^\pm) + (\hat{V}^\pm)$. The chaotic eigenvectors display strong admixture such that the transition to the chaotic sea cannot favor a specific eigenstate from a statistical point of view. By performing a random matrix average concerning the eigenvectors, we obtain $v_j^\pm = |\langle \Phi_j^\pm | \hat{V}^\pm | n \rangle|^2 \sim V_{\text{eff}}^2 / N_c$. The chaotic eigenstates are coupled in a same way with $|n\rangle$ in average. From the phase space point of view, the chaotic eigenstates tend to be delocalized into the entire chaotic sea.

By performing a random matrix average over the chaotic eigenvalues \mathcal{E}_j^\pm , it was demonstrated in [77] that the splitting follows a Cauchy distribution,

$$P(\Delta\epsilon_n) = \frac{2}{\pi} \frac{\overline{\Delta\epsilon_n}}{\Delta\epsilon_n^2 + \overline{\Delta\epsilon_n}^2}, \quad (4.5.12)$$

with $\overline{\Delta\epsilon_n} = 2\pi V_{\text{eff}}^2 / (N_c \Delta_c)$. Here Δ_c is the mean-level spacing in the chaotic block. This distribution is valid for $\Delta\epsilon_n \ll V_{\text{eff}}$ and displays a cutoff at $\Delta\epsilon_n \sim 2V_{\text{eff}}$ in order to avoid divergences [77, 78]. In this framework, it is possible to infer that the geometric mean $\langle \Delta\epsilon_n \rangle_g \equiv \exp(\langle \ln(\Delta\epsilon_n) \rangle)$ is equal to $\overline{\Delta\epsilon_n}$ [72, 78, 79],

$$\langle \Delta\epsilon_n \rangle_g = \frac{2\pi V_{\text{eff}}^2}{N_c \Delta_c}. \quad (4.5.13)$$

In a time-periodic system, the chaotic eigenvalues are distributed on a Floquet block, i.e. $\zeta < \mathcal{E}_j^\pm \leq \hbar\omega + \zeta$ with $\zeta \in \mathbb{R}$ arbitrary, with level repulsion related to the GOE modeling [66]. This leads to the following expression for the mean-level spacing,

$$\Delta_c = \frac{\hbar\omega}{N_c}, \quad (4.5.14)$$

which gives rise to

$$\langle \Delta\epsilon_n \rangle_g = \frac{2\pi V_{\text{eff}}^2}{\hbar\omega}. \quad (4.5.15)$$

By computing the coupling matrix element with the chaotic block, it becomes possible to access the tunneling rate.

A relation similar to Eq. (4.5.15), which determines the direct tunneling to chaos, was derived in Ref. [160] by using Fermi golden rule. In Ref. [81], they generalized this approach for transitions combining resonances and chaos. The approach presented here (largely inspired by [72, 79]) is also able to model this combining effect. An alternative approach which doesn't use perturbative developments (such as Eqs. (4.3.35) or (4.3.47)) was proposed in Ref. [82]. This is based on another class of integrable approximation built from a series of canonical transformations in order to coincide the tori of the mixed phase space with the tori of the integrable approximation [161]. This opened the way to an evaluation of the resonance- and chaos-assisted tunneling by means of complex path [83]. We have to bear in

mind that our main purpose here in this thesis is to use semiclassical theory as a prescription for the quantum parameters in order to speed up tunneling. In this case, the variety of approaches to model resonance- and chaos-assisted tunneling are useful to obtain an insight of the main features of the quantum dynamics by means of the classical one.

For the combination of parameters $N_p = 5$, $U = 20J$, $\delta = 19.5J$ and $\hbar\omega = 20J$, the semiclassical evaluation of the NOON time reads

$$\tau = \frac{\pi\hbar}{2\langle\Delta\epsilon_2\rangle_g} = 140\hbar/J. \quad (4.5.16)$$

Note that the semiclassical prediction reproduces quite well the exact result $\tau = 190\hbar/J$ even though the dimension of the chaotic block is only equal to two.

Chapter 5

Unperturbed three-site Bose-Hubbard model

In the context of systems with one effective degree of freedom, the phase space has two dimensions, leading to the possibility to visualize the whole dynamics on a plane. An insight of the main resonance-assisted mechanisms can then be obtained by means of the global visualization of the classical dynamics. A detailed analysis of the phase space is even able to determine quantitatively the dominant coupling path for tunneling as exposed in Sec. 4.3.7.

In the context of system with at least two effective degree of freedom, some complications arise due to additional connections between the different parts of the phase space. In Ref. [88], resonance-assisted tunneling was studied in a three degree-of-freedom system by identifying the main resonances. Indeed, before studying resonance-assisted tunneling, a good insight into the classical dynamics, especially concerning the set of resonances, called the Arnold web, is required. Frequency analysis is a way to achieve that. This technique was used, for example, in the case of two coupled standard maps [85, 86]. Another technique to compute the Arnold web is called the fast Lyapunov indicator [89, 90] enabling one to discriminate between regular and chaotic dynamics. From this technique, resonance-assisted tunneling has been studied in high-dimensional molecular system in the context of intramolecular vibrational energy redistribution [91–93] or in the three-site Bose-Hubbard model weakly coupled with an additional fourth site [94].

An important breakthrough has been achieved with the 3D phase space slice on a 4D phase space [85, 86]. The idea is to project the orbits (q_1, q_2, p_1, p_2) on a reduced 3D space by defining a 2ε width around an arbitrary point \bar{p}_2 ,

$$\{(q_1, q_2, p_1, p_2) \mid |p_2 - \bar{p}_2| \leq \varepsilon\}. \quad (5.0.1)$$

The time-independent three-site Bose-Hubbard Hamiltonian presents two effective degrees of freedom owing to the conservation of the total number of particles on the lattice. That is why the phase space has four dimensions, and it can still be visualized through Poincaré section [66], knowing that the dynamics lies on a hypersurface of constant energy of three dimensions. Nevertheless, this representation is not very useful for our purpose because we are interested in the couplings between quasimodes characterized by different energies. In this context, the approach of 3D slice is suitable to obtain an insight into the underlying classical dynamics. Actually, as the system is time independent, the slices can be performed for $\varepsilon = 0$. In this case, a kind of Poincaré section is built according to a coordinate (here the coordinate p_2). This kind of visualization of 4D phase space by means of 3D space was obtained in Ref. [95] by fixing one coordinate to zero as the four-dimensional normal-form

Hamiltonians were time independent. The double-resonance structure studied in Ref. [95] had an impact on the proliferation of the resonance-assisted peaks in the tunneling rate. In the context of time-dependent system, finite size slices ($\varepsilon \neq 0$) are necessary for visualization. This case will be discussed in Chap. 6 when the perturbation will be turned on.

In the continuity of Chap. 4, the purpose here is to characterize tunneling between two congruent sites, meaning that the Hamiltonian is symmetric under the permutation of both sites. In the preceding sections, an additional time-periodic perturbation drove the system toward a destruction or an enhancement of tunneling. Here an alternative is proposed by the addition of a non-congruent third site, called the site 0, connected with site 1 and 2 through the coupling constant κ . This site is characterized by an on-site interaction γU and an on-site energy ξ . This chapter investigates the way the third site creates resonant channels, leading again to substantial modifications of the NOON time.

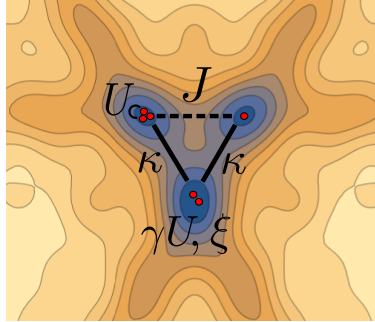


Figure 1: Contour plot of the triangular superlattice potential that was previously presented in Fig. 1.2.2(b). The on-site interaction γU and the on-site energy ξ of site 0 are different from the other sites. There is also a different coupling κ to the site 0. These differences can be introduced by a bias in the laser intensities used to generate the optical superlattice. The sites 1 and 2 are characterized by the on-site interaction U and no on-site energy. They are connected to each other via the hopping parameter J . The red dots represent ultracold atoms with two atoms on site 0, three atoms on site 1 and one atom on site 2.

5.1 Classical limit

The mean-field approximation of the general Bose-Hubbard Hamiltonian was developed in Sec. 1.3.4. This section investigates the particular case of a three-site system [162]. The Bose-Hubbard Hamiltonian describing Fig. 1 reads

$$\begin{aligned} \hat{H} = & -\kappa \left(\hat{a}_0^\dagger \hat{a}_1 + \hat{a}_1^\dagger \hat{a}_0 \right) - J \left(\hat{a}_1^\dagger \hat{a}_2 + \hat{a}_2^\dagger \hat{a}_1 \right) - \kappa \left(\hat{a}_2^\dagger \hat{a}_0 + \hat{a}_0^\dagger \hat{a}_2 \right) \\ & + \frac{U}{2} \left(\gamma \hat{a}_0^\dagger \hat{a}_0^\dagger \hat{a}_0 \hat{a}_0 + \hat{a}_1^\dagger \hat{a}_1^\dagger \hat{a}_1 \hat{a}_1 + \hat{a}_2^\dagger \hat{a}_2^\dagger \hat{a}_2 \hat{a}_2 \right) + \xi \hat{a}_0^\dagger \hat{a}_0. \end{aligned} \quad (5.1.1)$$

This Hamiltonian is invariant with respect to the inversion of the sites 1 and 2 while it is not invariant with respect to the permutation of the sites 1 or 2 with the site 0. In Ref. [128], the classical limit is obtained by introducing the quadrature operators, which can be seen as a Cartesian representation of the system. Otherwise, in the limit of an infinite number of particles the ladder operators can be replaced by complex numbers [129, 130],

which corresponds to the mean-field approximation,

$$\langle \hat{a}_l \rangle \sim \psi_l = \sqrt{I_l} e^{i\theta_l}, \quad (5.1.2)$$

$$\langle \hat{a}_l^\dagger \rangle \sim \psi_l^* = \sqrt{I_l} e^{-i\theta_l}. \quad (5.1.3)$$

Here the ψ_l ($l = 0, 1, 2$) represents the condensate amplitude on site l , θ_l the phase on site l and I_l is proportional to n_l , the number of particles on site l , such that $I_l = n_l + 1/2$. As the total number of particles N_p is conserved, the sum of the I_l amounts to a constant $N = N_p + 3/2$,

$$I_0 + I_1 + I_2 = N. \quad (5.1.4)$$

In this framework, the classical limit of the Hamiltonian (5.1.1) reads¹

$$\begin{aligned} H(\psi_l, \psi_l^*) = & -\kappa(\psi_0^* \psi_1 + \psi_1^* \psi_0) - J(\psi_1^* \psi_2 + \psi_2^* \psi_1) - \kappa(\psi_2^* \psi_0 + \psi_0^* \psi_2) \\ & + \frac{U}{2} (\gamma |\psi_0|^4 + |\psi_1|^4 + |\psi_2|^4 - 2\gamma |\psi_0|^2 - 2|\psi_1|^2 - 2|\psi_2|^2) + \xi |\psi_0|^2. \end{aligned} \quad (5.1.5)$$

The temporal evolution of the mean-field system is determined by the discrete Gross-Pitaevskii equation. It can be derived from the Hamiltonian (5.1.5).

$$\begin{aligned} i\hbar \frac{d\psi_0}{dt} &= -\kappa(\psi_1 + \psi_2) + \gamma U(|\psi_0|^2 - 1)\psi_0 + \xi \psi_0 \\ i\hbar \frac{d\psi_1}{dt} &= -(\kappa\psi_0 + J\psi_2) + U(|\psi_1|^2 - 1)\psi_1 \\ i\hbar \frac{d\psi_2}{dt} &= -(\kappa\psi_0 + J\psi_1) + U(|\psi_2|^2 - 1)\psi_2 \end{aligned} \quad (5.1.6)$$

Another convenient classical representation is the action-angle variables. It enables one to separate the angle-independent part from the angle dependent part such that

$$H(\boldsymbol{\theta}, \mathbf{I}) = H(\mathbf{I}) + V(\boldsymbol{\theta}, \mathbf{I}), \quad (5.1.7)$$

with

$$H(\mathbf{I}) = \frac{U}{2} (\gamma I_0^2 + I_1^2 + I_2^2) - U(\gamma I_0 + I_1 + I_2) + \xi I_0 \quad (5.1.8)$$

$$\begin{aligned} V(\boldsymbol{\theta}, \mathbf{I}) = & -2\kappa \sqrt{I_0 I_1} \cos(\theta_0 - \theta_1) - 2J \sqrt{I_1 I_2} \cos(\theta_1 - \theta_2) \\ & - 2\kappa \sqrt{I_0 I_2} \cos(\theta_0 - \theta_2). \end{aligned} \quad (5.1.9)$$

Like the pure quantum Hamiltonian (5.1.1), the classical one stays invariant under the permutation of site 1 and 2. This discrete symmetry enables one to consider the generation of a NOON state between both sites.

¹The constants in the Hamiltonian were removed. The general expression with the constants of motion can be found in Sec. 1.3.4.

5.2 Analysis of the phase space

If there is no hopping such that $J = \kappa = 0$, the system is described by the unperturbed Hamiltonian $H(\mathbf{I})$ and \hbar times the zeroth-order frequencies $\mathbf{\Omega} = (\Omega_0, \Omega_1, \Omega_2)$ read

$$\hbar\mathbf{\Omega}(\mathbf{I}) = \nabla_{\mathbf{I}}H(\mathbf{I}) = \begin{pmatrix} \gamma U(I_0 - 1) + \xi \\ U(I_1 - 1) \\ U(I_2 - 1) \end{pmatrix}. \quad (5.2.1)$$

The perturbative term can be written as

$$V(\boldsymbol{\theta}, \mathbf{I}) = -2 \sum_{l=0}^2 J_l \sqrt{I_l I_{l+1}} \cos(\mathbf{r}_l \cdot \boldsymbol{\theta}), \quad (5.2.2)$$

with $I_3 = I_0$, $J_0 = J_2 = \kappa$, $J_1 = J$ and

$$\mathbf{r}_0 = (1, -1, 0), \quad (5.2.3)$$

$$\mathbf{r}_1 = (0, 1, -1), \quad (5.2.4)$$

$$\mathbf{r}_2 = (1, 0, -1) \quad (5.2.5)$$

are called the resonance vectors.

When the hopping is turned on, the term $V(\boldsymbol{\theta}, \mathbf{I})$ becomes non-zero and the actions \mathbf{I} are no longer constants of motion. If the perturbation is slightly turned on, almost all tori in phase space are preserved and slightly deformed according to KAM theorem [65, 66]. The tori that are destroyed are those for which their frequencies are rationally related such that they fulfill

$$k_0\Omega_0 + k_1\Omega_1 + k_2\Omega_2 = 0, \quad (5.2.6)$$

with k_l integer and with at least one $k_l \neq 0$. In this case, the torus is resonant. A set of destroyed tori which fulfill Eq. (5.2.6) will give rise to a resonance that we will call the $k_0:k_1:k_2$ resonance. Indeed, Eq. (5.2.6) is a way to compute the Arnold web, i.e. the set of resonances. Actually, the main resonances are determined by the resonance vectors \mathbf{r}_l of the perturbation $V(\boldsymbol{\theta}, \mathbf{I})$ [87] according to

$$\mathbf{r}_0 \cdot \mathbf{\Omega} = 0, \quad (5.2.7)$$

$$\mathbf{r}_1 \cdot \mathbf{\Omega} = 0, \quad (5.2.8)$$

$$\mathbf{r}_2 \cdot \mathbf{\Omega} = 0. \quad (5.2.9)$$

These equations constitute the parametrization of the main resonance surfaces in the action space, also called the resonance center lines for a 2D action space [95]. From a geometrical point of view, the frequency is orthogonal to the unperturbed energy shell. Therefore, if a resonance vector is orthogonal to the frequency on a point of the action space, then it will lie on the tangent plane of the energy shell. More specifically, the parametrizations (5.2.7)–(5.2.9) read

$$I_1 - 1 - \gamma I_0 + \gamma - \frac{\xi}{U} = 0, \quad (5.2.10)$$

$$I_1 - I_2 = 0, \quad (5.2.11)$$

$$I_2 - 1 - \gamma I_0 + \gamma - \frac{\xi}{U} = 0. \quad (5.2.12)$$

If we set $\gamma = 1$ and $\xi = 0$ to facilitate the visualization, the unperturbed energy shells are spheres, which will be crossed by the resonance surfaces. Initial conditions for the slightly perturbed system will lead to a motion close to an unperturbed shell. These initial conditions can lie on a resonance surface. In that case, the trajectory will follow the resonance surface while respecting the energy conservation, and it is possible to reach another resonance surface by passing through a junction where the resonance surfaces intersect. More descriptions of this phenomenon can be found in Ref. [87].

The problem of this representation is the difficulty to visualize the dynamics as the phase space has six dimensions. However, N is a constant of motion which can play the role of a conjugate momentum in the Hamiltonian. With a canonical transformation such that N becomes a conjugate momentum in the new representation, the resonance surfaces encoded in the parametrizations (5.2.10)–(5.2.12) can be visualized with resonance center lines in a 2D action space in terms of the new momenta. Moreover, we can also take into account the fact that site 1 and 2 are congruent. That is why the following third class generating function that performs the transformation $(\boldsymbol{\theta}, \mathbf{I}) \mapsto (\boldsymbol{\phi}, \mathbf{z})$ is introduced,

$$F(\mathbf{I}, \boldsymbol{\phi}) = I_0 \phi_0 + \frac{1}{2}(I_1 - I_2)\phi_1 + (I_0 + I_1 + I_2)\phi_2, \quad (5.2.13)$$

characterized by the following relations,

$$\theta_l = \frac{\partial F}{\partial I_l}, \quad z_l = \frac{\partial F}{\partial \phi_l}. \quad (5.2.14)$$

The relations between the action-angle representation with and without a constant of motion read

$$\left\{ \begin{array}{l} \theta_0 = \phi_0 + \phi_2 \\ \theta_1 = \phi_2 + \frac{1}{2}\phi_1 \\ \theta_2 = \phi_2 - \frac{1}{2}\phi_1 \\ I_0 = z_0 \\ I_1 = \frac{1}{2}(2z_1 + (z_2 - z_0)) \\ I_2 = -\frac{1}{2}(2z_1 - (z_2 - z_0)) \end{array} \right. \Leftrightarrow \left\{ \begin{array}{l} \phi_0 = \theta_0 - \frac{1}{2}(\theta_1 + \theta_2) \\ \phi_1 = \theta_1 - \theta_2 \\ \phi_2 = \frac{1}{2}(\theta_1 + \theta_2) \\ z_0 = I_0 \\ z_1 = \frac{1}{2}(I_1 - I_2) \\ z_2 = I_0 + I_1 + I_2 = N \end{array} \right. . \quad (5.2.15)$$

The constant of motion (related to the total number of particles) reads

$$z_2 = N. \quad (5.2.16)$$

In this case, the phase space will be spanned by $(\phi_0, \phi_1, z_0, z_1)$ as z_2 is a parameter and ϕ_2 is a cyclic variable.

It becomes possible to write the Hamiltonian as a function of $(\boldsymbol{\phi}, \mathbf{z})$,

$$H(\boldsymbol{\phi}, \mathbf{z}) = H(\mathbf{z}) + V(\boldsymbol{\phi}, \mathbf{z}), \quad (5.2.17)$$

with

$$H(\mathbf{z}) = Uz_1^2 + \frac{U}{4}(N - z_0)^2 + \frac{\gamma U}{2}z_0^2 + (1 - \gamma)Uz_0 + \xi z_0, \quad (5.2.18)$$

$$\begin{aligned} V(\boldsymbol{\phi}, \mathbf{z}) = & -\sqrt{2\kappa}\sqrt{z_0(N - z_0 + 2z_1)} \cos\left(\phi_0 - \frac{1}{2}\phi_1\right) \\ & - 2J\sqrt{(N - z_0)^2/4 - z_1^2} \cos(\phi_1) \\ & - \sqrt{2\kappa}\sqrt{z_0(N - z_0 - 2z_1)} \cos\left(\phi_0 + \frac{1}{2}\phi_1\right). \end{aligned} \quad (5.2.19)$$

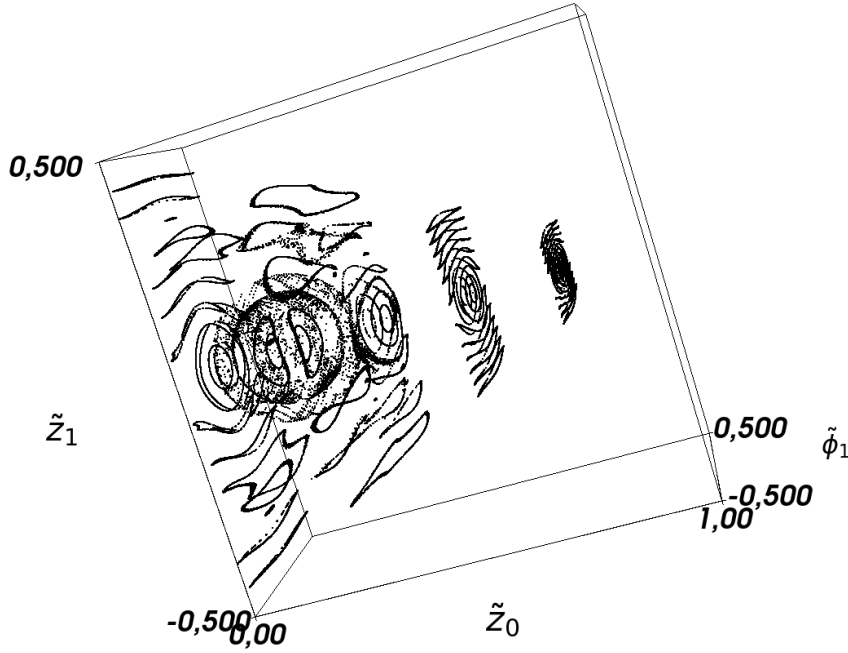


Figure 5.2.1: Phase space obtained through Eq. (5.2.20) of the three-site Bose-Hubbard model (5.2.17) for the parameters $N_p = 5$, $\kappa = 0.85J$, $\gamma = 1.5$, $U = 20J$, $\xi = 30J$. We have $\tilde{\phi}_1 = \phi_1/(2\pi)$, $\tilde{z}_0 = z_0/N$ and $\tilde{z}_1 = z_1/N$ and $\bar{\phi}_0 = 0$.

A 3D slice in the 4D phase space [85, 86] can be done beside ϕ_0 , for example, according to Eq. (5.0.1). As the system is time-independent the thickness of the slice ε can be chosen equal to 0. In this case, a coordinate Poincaré section is performed. It reads

$$\{(\phi_0, \phi_1, z_0, z_1) \mid |\phi_0 - \bar{\phi}_0| = 0\}, \quad (5.2.20)$$

with $\bar{\phi}_0$ an arbitrary point. Figure 5.2.1 displays the phase space of the unperturbed three-site Bose-Hubbard model for the parameters $N_p = 5$, $\kappa = 0.85J$, $\gamma = 1.5$, $U = 20J$ and $\xi = 30J$. If the connection to the site 0 is turned off, i.e. $\kappa = 0$, then the phase space is organized as a set of pendulum-like phase-space layers which are disconnected. In this case, the system can be described by the two-site Bose-Hubbard model with the canonical variables ϕ_1 and z_1 . Moreover, the resonance center line for $z_1 = 0$ is a collection of fixed points. Note that the size of each layer decreases as z_0 increases due to particle conservation. This leads to an action space with a triangular shape as displayed in Fig. 5.2.2(a). The connection to the zeroth site introduces temporal modifications of z_0 . Moreover, two other pendulum-like structures becomes present, and a junction is formed by the intersection of the three

resonance center lines, which can be parameterized in the action space by

$$z_1 = + \left(\gamma + \frac{1}{2} \right) z_0 - \left(\frac{N}{2} - \frac{\xi}{U} + \gamma - 1 \right), \quad (5.2.21)$$

$$z_1 = 0, \quad (5.2.22)$$

$$z_1 = - \left(\gamma + \frac{1}{2} \right) z_0 + \left(\frac{N}{2} - \frac{\xi}{U} + \gamma - 1 \right). \quad (5.2.23)$$

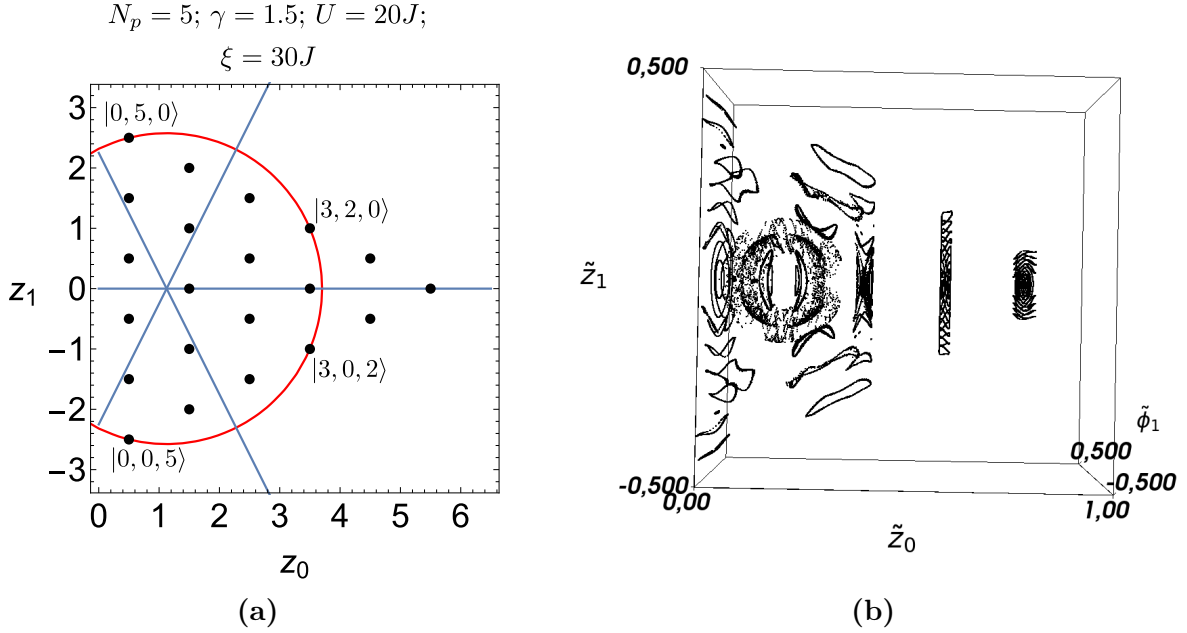


Figure 5.2.2: Panel (a) is schematic representation of the action space related to the phase space (b). The three resonance center lines are displayed in blue. The quasimodes $|n_0, n_1, n_2\rangle$ are represented by the dark dots. An energy shell of the unperturbed Hamiltonian is represented in red on which the quasimodes $|0, 5, 0\rangle$, $|3, 2, 0\rangle$, $|0, 0, 5\rangle$ and $|3, 0, 2\rangle$ are situated. The on-site energy ξ was fixed by means of Eq. (5.3.1) in order to have one resonance center line symmetrically located between $|0, 5, 0\rangle$ and $|3, 2, 0\rangle$, and another one symmetrically located between $|0, 0, 5\rangle$ and $|3, 0, 2\rangle$. The phase space of panel (b) is obtained for $N_p = 5$, $\kappa = 0.85J$, $\gamma = 1.5$, $U = 20J$ and $\xi = 30J$. We have $\tilde{\phi}_1 = \phi_1/(2\pi)$, $\tilde{z}_0 = z_0/N$ and $\tilde{z}_1 = z_1/N$.

Figure 5.2.2(a) displays the three resonance center lines in blue in the action space, the quasimodes $|n_0, n_1, n_2\rangle$ are represented by the dark dots and an unperturbed energy shell is represented in red. According to Eq. (5.2.19), the main resonance center lines are determined by the resonance vectors $\mathbf{s}_0 = (1, -1/2)$, $\mathbf{s}_1 = (0, 1)$ and $\mathbf{s}_2 = (1, 1/2)$. The resonance center line related to \mathbf{s}_1 fulfills the condition $\mathbf{s}_1 \cdot \boldsymbol{\phi} = \phi_1 = \text{const}$. In particular for the initial conditions $(\phi_0, \phi_1, z_0, z_1) = (\phi_0, 0, z_0, 0)$, the Hamiltonian equations of Eq. (5.2.17) read

$$\begin{aligned} \dot{\phi}_0 &= -U(N - z_0)/2 + \gamma U z_0 + (1 - \gamma)U + \xi \\ &\quad - \sqrt{2\kappa} \frac{(N - 2z_0)}{\sqrt{z_0(N - z_0)}} \cos \phi_0 + J, \end{aligned} \quad (5.2.24)$$

$$\dot{z}_0 = -2\sqrt{2\kappa} \sqrt{z_0(N - z_0)} \sin \phi_0, \quad (5.2.25)$$

with $\dot{\phi}_1 = 0$ and $\dot{z}_1 = 0$. The resonance center line $z_1 = 0$ with $\phi_1 = 0$ is therefore an invariant submanifold such that it becomes possible to draw a 2D phase space as displayed

in Fig. 5.2.3. Several fixed points are present at the resonance junction. Figure 5.2.3 clearly attests the presence of an elliptic-elliptic fixed point in $(\phi_0, \phi_1) = (0, 0)$, and a hyperbolic-elliptic fixed point in $(\pi, 0)$ at the junction. Far from the resonance junction, i.e. for z_1 small or large in the case of Figs. 5.2.1 or 5.2.2(b), the dynamics seems to be locally a pendulum-like phase space with few variations of z_0 . Closer to the resonance junction a chaotic layer with the shape of a bubble is formed. It results from the overlapping of the chaotic layers of the three pendulum-like structures in the context of the nonintegrable system, i.e. $\kappa \neq 0$. The phase space presented here displays some resemblances with the double pendulum in Ref. [95].

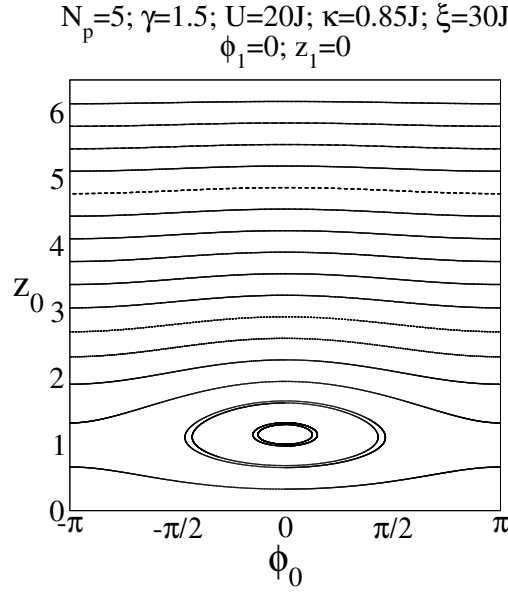


Figure 5.2.3: Phase space related to the Hamiltonian (5.2.17) for the initial conditions $(\phi_0, \phi_1, z_0, z_1) = (\phi_0, 0, z_0, 0)$. In this case, the Hamiltonian equations are given by (5.2.24) and (5.2.25) with $\dot{\phi}_1 = 0$ and $\dot{z}_1 = 0$. Thus, $(\phi_1, z_1) = (0, 0)$ leads to trajectories that stay on this submanifold, and it becomes possible to draw a 2D phase space. The elliptic-elliptic fixed point is situated in the center of the island as well as an elliptic-hyperbolic fixed point in $\phi_0 = \pi$.

The junction is located at the intersection between the three resonance center lines. Its parametrization reads

$$(z_0^*, z_1^*) = \left(\frac{1}{\gamma + \frac{1}{2}} \left(\frac{N}{2} - \frac{\xi}{U} + \gamma - 1 \right), 0 \right). \quad (5.2.26)$$

At this point, the unperturbed energy is minimum for repulsive atoms. By symmetry, it is logical to have $z_1^* = 0$. If the on-site energy ξ is high, the site 0 tends to be depopulated in order to minimize the energy. If the on-site energy is sufficiently large in absolute value, it is possible to have the junction outside the phase space, i.e. a junction with z_0^* negative or z_0^* larger than N . Concerning the combination of parameters of Fig. 5.2.2, the position of the junction is given by $(z_0^*, z_1^*) = (1.125, 0)$.

5.3 NOON states via resonance-assisted tunneling

The idea of this section is to use the connection to the zeroth site in order to speed up the production of a NOON state. By means of the relations (5.2.21) and (5.2.23), the parameters

of the site zero, namely γ and ξ , can be changed in order to tune the positions of the resonance center lines and, thus, to tune the tunneling rate. In particular, we would like to have one of the two resonance center lines that passes through an arbitrary point $(z_0^{(\xi)}, z_1^{(\xi)})$. We will see that the goal is to choose this point situated right in between two quasimodes in phase space. This point determines the value of ξ through the relations

$$\xi = U \left(\pm z_1^{(\xi)} - \left(\gamma + \frac{1}{2} \right) z_0^{(\xi)} + \frac{N}{2} + \gamma - 1 \right). \quad (5.3.1)$$

The sign $+$ in the previous relation corresponds to the resonance center line (5.2.21) while the sign $-$ corresponds to the one (5.2.23). Note that γ control the slope of the lines.

A resonance must be symmetrically located between two quasimodes in order to maximize the coupling matrix element between them [95]. To each Fock state $|n_0, n_1, n_2\rangle$, a classical torus can be associated whose position in action space is given by $(z_0, z_1) = (n_0 + 1/2, (n_1 - n_2)/2)$ with n_l the number of particles on site l . Let's assume that we want to induce a resonant coupling between the quasimodes $|n_0, n_1, n_2\rangle$ and $|n'_0, n'_1, n'_2\rangle$. In this case, the point $(z_0^{(\xi)}, z_1^{(\xi)})$ must be located in the middle of both quasimodes. The following associations can be made,

$$|n_0, n_1, n_2\rangle \longleftrightarrow (z_0, z_1), \quad (5.3.2)$$

$$|n'_0, n'_1, n'_2\rangle \longleftrightarrow (z'_0, z'_1). \quad (5.3.3)$$

The coordinates of the point $(z_0^{(\xi)}, z_1^{(\xi)})$, located in the middle of (z_0, z_1) and (z'_0, z'_1) , is given by

$$z_j^{(\xi)} = \frac{z_j + z'_j}{2}, \quad j = 0, 1. \quad (5.3.4)$$

By injecting these two relations in one of the Eqs. (5.3.1), it becomes possible to evaluate the on-site energy producing a resonance center line symmetrically located between $|n_0, n_1, n_2\rangle$ and $|n'_0, n'_1, n'_2\rangle$.

For example, Fig. 5.2.2(a) displays a resonant center line symmetrically located between $|0, 5, 0\rangle$ and $|3, 2, 0\rangle$, which correspond respectively to $(z_0, z_1) = (0.5, 2.5)$ and $(z_0, z_1) = (3.5, 1)$. Therefore, the point in the middle of both quasimodes is given by $(z_0^{(\xi)}, z_1^{(\xi)}) = (2, 1.75)$. By inserting these values in Eq. (5.3.1) for the $+$ sign with $\gamma = 1.5$, we obtain $\xi/J = 30$.

To access the transition probabilities $P_{|n_0, n_1, n_2\rangle}(t)$, a numerical diagonalization of the Hamiltonian (5.1.1) is performed. The basis of eigenvectors is given by

$$\{|\chi_\nu\rangle \mid \nu = 1, 2, \dots, D\}. \quad (5.3.5)$$

The dimension of the Hilbert space reads [162]

$$D = \frac{(N_p + 1)(N_p + 2)}{2}. \quad (5.3.6)$$

A convenient basis to decompose the Hamiltonian is the Fock basis. Note that the total number of particles is conserved such that $n_0 = N_p - n_1 - n_2$.

$$|\chi_\nu\rangle = \sum_{n_1=0}^{N_p} \sum_{n_2=0}^{N_p-n_1} F_{\nu, n_1, n_2} |n_0, n_1, n_2\rangle \quad (5.3.7)$$

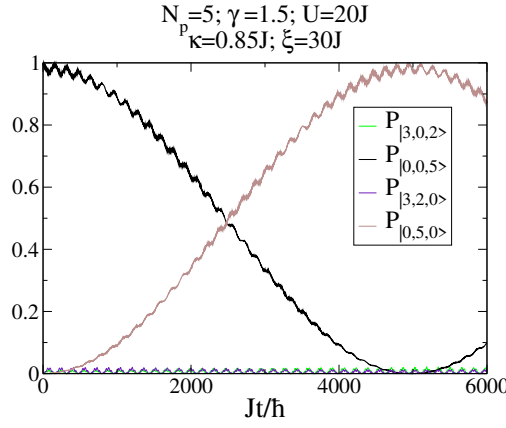


Figure 5.3.1: This figure displays the numerical detection probabilities of the quasimodes $|3, 0, 2\rangle$, $|0, 0, 5\rangle$, $|3, 2, 0\rangle$ and $|0, 5, 0\rangle$, knowing that the system is initially in $|0, 0, 5\rangle$. This figure corresponds to the phase space in Fig. 5.2.2(b). Figure 5.2.2(a) displays the positions of quantized actions in the action space (black dots), as well as the principal resonant center lines (blue lines). With a suitable value for ξ , a resonant center line becomes symmetrically located between $|0, 5, 0\rangle$ and $|3, 2, 0\rangle$. For $J\tau/\hbar = 2.5 \times 10^3$, the NOON state is formed. This is facilitated by the quasimodes of the same energy $|3, 0, 2\rangle$ and $|3, 2, 0\rangle$, which are also responsible for the micromotions in $P_{|0,0,5\rangle}(t)$ and $P_{|0,5,0\rangle}(t)$. With a purity equal to $p = 0.99$, the two-level approximation still holds.

It is also possible to take advantage of the discrete symmetry by decomposing the Hamiltonian in the symmetry-adapted basis (see Appx. D). The analytical and the numerical treatments are more complex, but the numerical calculation is faster owing to the smaller matrices to diagonalize. The numerical diagonalization gives access to F_{ν,n_1,n_2} . Any state can be decomposed in that basis, and the temporal evolution reads

$$|\phi(t)\rangle = \sum_{\nu=1}^D c_{\nu}(t_0) e^{-i\epsilon_{\nu}(t-t_0)/\hbar} |\chi_{\nu}\rangle, \quad (5.3.8)$$

with $c_{\nu}(t_0) = \langle \chi_{\nu} | \phi(t_0) \rangle$, and $\hat{H}|\chi_{\nu}\rangle = \epsilon_{\nu}|\chi_{\nu}\rangle$. The transition probability to the state $|n_0, n_1, n_2\rangle$, knowing that the system is initially in $|\phi(t_0)\rangle$, is given by

$$P_{|n_0,n_1,n_2\rangle}(t) = |\langle n_0, n_1, n_2 | \phi(t) \rangle|^2. \quad (5.3.9)$$

As displayed in Fig. 5.3.1, the probability transitions show typical NOON oscillations for the quasimodes $|0, 5, 0\rangle$ and $|0, 0, 5\rangle$. The NOON state is obtained after a time $\tau = 2.5 \times 10^3 \hbar/J$ while in the absence of site 0 (i.e. $\kappa = 0$) the result obtained was $\tau = 6.0 \times 10^5 \hbar/J$ as computed in Fig. 4.5.1. The result with a coupling via the zeroth site is comparable to the one obtained with the perturbed two-site system with a 2:1 resonance in the near-integrable regime (see Fig. 4.4.1), where we obtained $\tau = 2.4 \times 10^3 \hbar/J$.

The configuration in Fig. 5.3.1 is largely dominated by the oscillation between $|0, 0, 5\rangle$ and $|0, 5, 0\rangle$ with micromotions due to quasidegeneracy between the symmetric and antisymmetric combinations of $|3, 0, 2\rangle$ and $|3, 2, 0\rangle$ with the same combinations of $|0, 0, 5\rangle$ and $|0, 5, 0\rangle$. The purity of the main oscillations can be time-independently evaluated by means of

$$p = M_{0,N_p} + M_{N_p,0}, \quad (5.3.10)$$

with

$$M_{n_1, n_2} = \sum_{\sigma=\pm} |\langle n_0, n_1, n_2 | \chi_{\nu_\sigma} \rangle|^2. \quad (5.3.11)$$

Here $|\chi_{\nu_\pm}\rangle$ refers respectively to the symmetric and antisymmetric part of the NOON states such that $|\chi_{\nu_\pm}\rangle \sim 1/\sqrt{2}(|0, 0, N_p\rangle \pm |0, N_p, 0\rangle)$. We obtain $p = 0.99$ for $\kappa = 0.85J$, which is consistent with Fig. 5.3.1. This latter figure displays characteristic two-level oscillations between the quasimodes $|0, 5, 0\rangle$ and $|0, 0, 5\rangle$. The coupling matrix element with $|0, 3, 2\rangle$, induced by the coupling to the site 0, is responsible for the micromotions as well as the decrease of the NOON time, which amounts to $\tau = 2.5 \times 10^3 \hbar/J$. This result is comparable with the NOON time obtained with a two-site system in the near-integrable regime amounting to $\tau = 2.4 \times 10^3 \hbar/J$ as presented in Eq. (4.3.51).

Figure 5.3.2 displays a combination of parameters for which a resonance center line couples the quasimodes $|0, 5, 0\rangle$ and $|2, 3, 0\rangle$. In this context, Eq. (5.3.1) indicates that the on-site energy must be equal to $\xi = 55J$. Figure 5.3.3 displays the typical four-level oscillations that were previously described in the context of the periodically-perturbed two-site optical lattice (see Sec. 4.4 for a detailed description of this phenomenon). In this framework, the coupling between $|0, 5, 0\rangle$ and $|2, 3, 0\rangle$ is not a small perturbation and the two-level approximation must be abandoned. The transition probability dynamics is characterized by two timescales, namely the characteristic times of the slow oscillations τ_s and the fast oscillations τ_f (see Eqs. (4.4.31) for the definitions). The eigenenergies implied in the dynamics are given by

$$\begin{aligned} \epsilon_4^- &= 200.51509J, \\ \epsilon_3^+ &= 200.51114J, \\ \epsilon_2^- &= 200.03074J, \\ \epsilon_1^+ &= 200.02725J, \end{aligned} \quad (5.3.12)$$

which leads to $\tau_s = 422\hbar/J$ and to $\tau_f = 3.24\hbar/J$. According to the zoom in Fig. 5.3.3(b), if a measure is performed in τ_s , an entangled state between $|2, 0, 3\rangle$ and $|2, 3, 0\rangle$ will be obtained. A measurement time t_m can be chosen in order to obtain a NOON state. For $t_m = 428.3\hbar/J$, we obtain $P_{|0,5,0\rangle} + P_{|0,0,5\rangle} = 0.989$ with a bias $P_{|0,5,0\rangle} - P_{|0,0,5\rangle} = 6.7 \times 10^{-3}$. The time required to produce the NOON state is smaller than that required in the two-level oscillation case in Fig. 5.3.1. Nevertheless, the disadvantage related to the four-level oscillations is that t_m must be sufficiently precise, from an experimental point of view, in order to reach the NOON state.

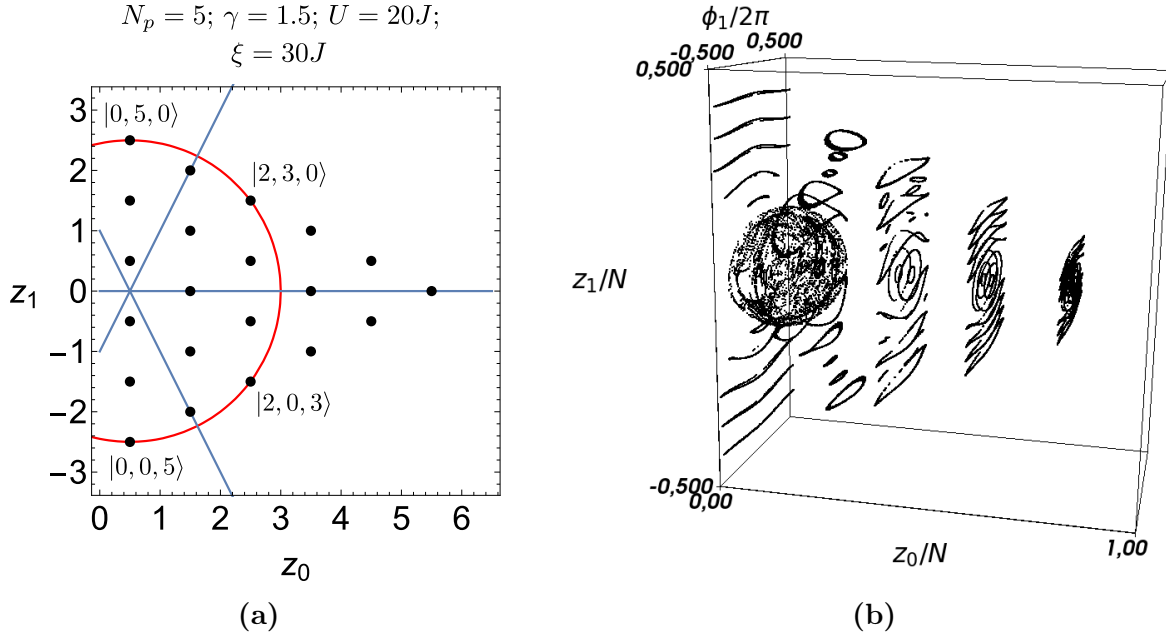


Figure 5.3.2: (a) Action space where the resonance center lines are represented in blue, the quasimodes with black dots and the unperturbed energy shell of the quasimodes $|3, 0, 2\rangle$, $|0, 0, 5\rangle$, $|3, 2, 0\rangle$ and $|0, 5, 0\rangle$ in red. (b) Phase space related to the action space of panel (a). The parameter $\xi = 55J$ is chosen by means of Eq. (5.3.1) in order to couple the quasimodes $|0, 5, 0\rangle$ and $|2, 3, 0\rangle$ with a resonant center symmetrically located between both quasimodes. The parameters of panel (b) are given by $N_p = 5$, $\kappa = J$, $\gamma = 1.5$, $U = 20J$ and $\xi = 55J$.

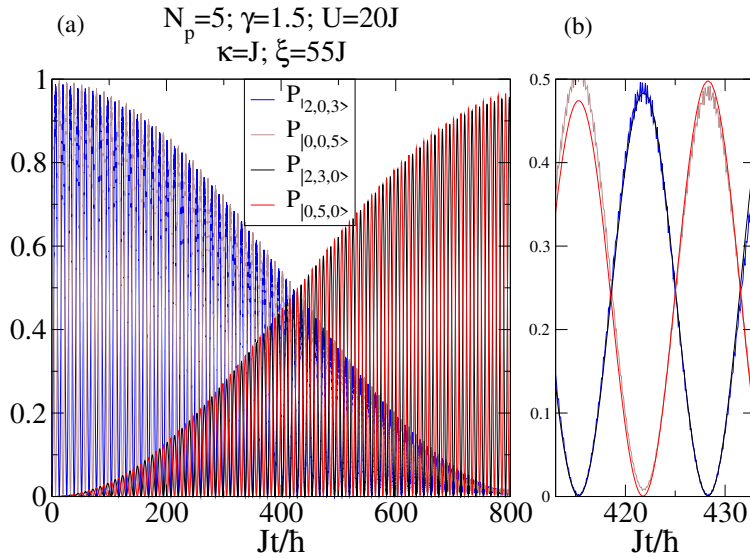


Figure 5.3.3: (a) Numerical detection probabilities knowing that the system is initially in $|0, 0, 5\rangle$. This is a typical four-level oscillation dynamics. (b) Zoom around τ_s the timescale of the slow oscillations. The coupling matrix element produced by the resonance center lines between $|0, 5, 0\rangle$ and $|2, 3, 0\rangle$ (see Fig. 5.3.2(a)) is sufficiently strong to invalidate the two-level approximation. In this case, the dynamics is described by four-level oscillations characterized by two timescales, namely $\tau_s = 422.4\hbar/J$ and $\tau_f = 3.245\hbar/J$.

Chapter 6

Triple-NOON states via resonance- and chaos-assisted tunneling

In the preceding two chapters, the formation of highly entangled states called the NOON states was investigated. This state is formed by the coherent superposition of two states $|N, 0\rangle$ and $|0, N\rangle$ where one mode is totally full of N quanta while the other is empty, i.e. $e^{i\phi_1}|N, 0\rangle + e^{i\phi_2}|0, N\rangle$. Another kind of entangled state can be built with three modes. A qutrit has been experimentally realized with biphotons according to their polarizations [163] and in a superconducting circuit [164], to mention two examples. In a triple-NOON state, one mode is totally full while two others are empty, leading to the state $e^{i\varphi_1}|N, 0, 0\rangle + e^{i\varphi_2}|0, N, 0\rangle + e^{i\varphi_3}|0, 0, N\rangle$ where N is the number of quanta. In the three-mode Bose-Hubbard model [162, 165–169], few proposals have been made. In Ref. [96], it is suggested to adiabatically generate the triple-NOON state with ultracold bosonic atoms that exhibit an attractive interaction. Apart from the enhanced instability of a Bose-Einstein condensate with attractive interaction [35–37], the generation of this triple-NOON state requires a very low temperature as it is the ground state [170]. Here we propose to build a triple-NOON state by initially loading all particles on a specific site in the self-trapping regime [53, 54, 166, 167], where the atomic repulsion is sufficiently strong to only authorize collective transfers of particles. The targeted entangled state is then obtained after the triple-NOON time. Besides the requirement of a perfectly symmetric optical trap, the main problem of this method is the prohibitively long time needed, especially for large populations.

This chapter investigates how the timescale of this process can be considerably reduced by modulating the optical lattice with a time-periodic driving. This phenomenon was demonstrated in Chap. 4 in the case of the NOON state in a two-site optical lattice [52]. Indeed, the driving is responsible for the emergence of nonlinear resonances in the phase space, leading to the phenomenon of resonance-assisted tunneling [67–71], as well as the production of chaotic layers, leading to the phenomenon of chaos-assisted tunneling [73–77]. Both phenomena can be combined to give rise to resonance- and chaos-assisted tunneling [71, 72, 78–84].

6.1 Structure of the spectrum

The purpose is to produce a perfectly balanced entangled state with three modes, namely $|N_p, 0, 0\rangle$, $|0, N_p, 0\rangle$ and $|0, 0, N_p\rangle$, in a three-site optical trap. For the two-site optical trap, the two sites must be congruent to produce a NOON state. In this case, the Hamiltonian is invariant under the permutation of the two sites. Therefore, it is logical to study an optical

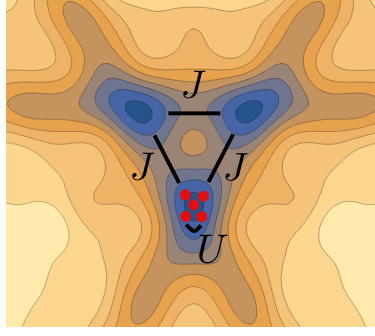


Figure 6.1.1: Contour plot of the triangular superlattice potential that was previously presented in Fig 1.2.2(b). All three sites are congruent, meaning they are characterized by the same on-site interaction U , the same on-site energy (equal to zero here) and each pair of sites is coupled by the same hopping parameter J . This site configuration can be achieved with lasers by means of superlattice techniques explained in Sec. 1.2.3. The red dots represent ultracold atoms trapped here on site 0.

lattice where the three sites are congruent in order to produce a triple-NOON state. The corresponding Hamiltonian is written as

$$\hat{H}_0 = -J \sum_{l=0}^2 (\hat{a}_l^\dagger \hat{a}_{l+1} + \hat{a}_{l+1}^\dagger \hat{a}_l) + \frac{U}{2} \sum_{l=0}^2 \hat{a}_l^\dagger \hat{a}_l^\dagger \hat{a}_l \hat{a}_l, \quad (6.1.1)$$

with $\hat{a}_3 \equiv \hat{a}_0$. This Hamiltonian is invariant under the permutation of any pair of sites. It describes the optical lattice schematized in Fig. 6.1.1. The eigenvalue equation reads

$$\hat{H}_0 |\psi_{n_0, n_1, n_2}^{(j)}\rangle = \epsilon_{n_0, n_1, n_2}^{(j)} |\psi_{n_0, n_1, n_2}^{(j)}\rangle, \quad (6.1.2)$$

with $j = 1$ or $j = 1, 2, 3$ or $j = 1, 2, 3, 4, 5, 6$ depending on the value of n_1 and n_2 , knowing that $n_0 = N_p - n_1 - n_2$. The first one refers to the singlets for which $n_0 = n_1 = n_2$, the second one to the triplets for which $n_0 \neq n_1 = n_2$ and the last one to the sextuplets for which $n_0 \neq n_1 \neq n_2 \neq n_0$. This nomenclature is appropriate for the strong interaction regime, where the nonlinear parameter is pretty high, $(N_p + 1)U/J \gg 1$. In this regime, the effective on-site interaction is strong compared to the hopping such that

$$\epsilon_{n_0, n_1, n_2}^{(j)} \simeq \frac{U}{2} \sum_{l=0}^2 n_l (n_l - 1). \quad (6.1.3)$$

The decomposition of the eigenvectors $|\psi_{n_0, n_1, n_2}^{(j)}\rangle$ will be overwhelmingly dominated by the Fock states $|n_0, n_1, n_2\rangle$, $|n_2, n_0, n_1\rangle$, $|n_1, n_2, n_0\rangle$, $|n_1, n_0, n_2\rangle$, $|n_2, n_1, n_0\rangle$ and $|n_0, n_2, n_1\rangle$ in the case of a sextuplet ($n_0 \neq n_1 \neq n_2 \neq n_0$). In the case of a triplet, the dominant coefficients of $|\psi_{n_0, n_1, n_1}^{(j)}\rangle$ will be determined by $|n_0, n_1, n_1\rangle$, $|n_1, n_0, n_1\rangle$ and $|n_1, n_1, n_0\rangle$ with $n_0 \neq n_1$. There is also the case of the singlet where $n_0 = n_1 = n_2$ such that $|\psi_{n_1, n_1, n_1}^{(j)}\rangle \simeq |n_1, n_1, n_1\rangle$. The triplet and sextuplet organization of the spectrum can be illustrated for $N_p = 5$ and

$$U = 20J,$$

$$\begin{aligned}
\epsilon_{0,0,5}^{(3)} &= 200.1234556J, & \epsilon_{0,1,4}^{(2)} &= 119.211J, & \epsilon_{0,2,3}^{(1)} &= 77.035J, \\
\epsilon_{0,0,5}^{(2)} &= 200.1234556J, & \epsilon_{0,1,4}^{(1)} &= 119.190J, & \epsilon_{1,1,3}^{(3)} &= 60.669J, \\
\epsilon_{0,0,5}^{(1)} &= 200.1234521J, & \epsilon_{0,2,3}^{(6)} &= 82.942J, & \epsilon_{1,1,3}^{(2)} &= 60.016J, \\
\epsilon_{0,1,4}^{(6)} &= 121.209J, & \epsilon_{0,2,3}^{(5)} &= 82.942J, & \epsilon_{1,1,3}^{(1)} &= 60.016J, \\
\epsilon_{0,1,4}^{(5)} &= 121.188J, & \epsilon_{0,2,3}^{(4)} &= 82.790J, & \epsilon_{2,2,1}^{(3)} &= 41.482J, \\
\epsilon_{0,1,4}^{(4)} &= 121.188J, & \epsilon_{0,2,3}^{(3)} &= 77.169J, & \epsilon_{2,2,1}^{(2)} &= 41.482J, \\
\epsilon_{0,1,4}^{(3)} &= 119.211J, & \epsilon_{0,2,3}^{(2)} &= 77.035J, & \epsilon_{2,2,1}^{(1)} &= 34.847J.
\end{aligned} \tag{6.1.4}$$

For example, the triplet $\epsilon_{0,0,5}^{(j)}$ displays a pair of two degenerate eigenvalues and a third one that is almost degenerate with this pair. This lifting of degeneracy is the signature that there is to some extent tunneling between $|5, 0, 0\rangle$, $|0, 5, 0\rangle$ and $|5, 0, 0\rangle$. For each triplet, this structure is the same. Sextuplets effectively appear as the combination of two triplets, i.e., we have two distinct pairs of degenerate eigenvalues and two further eigenvalues such that each one of them is close to one of the two pairs.

6.2 Three-level approximation

In the symmetric three-site optical lattice, the three states $|N_p, 0, 0\rangle$, $|0, N_p, 0\rangle$ and $|0, 0, N_p\rangle$ are sufficiently separated from the other part of the spectrum in the strong interaction regime. They can be seen as a triplet where V is the effective coupling. The main features of the dynamics can be captured with a three-level approximation characterized by the basis $\{|0\rangle, |1\rangle, |2\rangle\}$. Within this basis, the Hamiltonian is modeled as

$$M = \begin{matrix} & \begin{matrix} |0\rangle & |1\rangle & |2\rangle \end{matrix} \\ \begin{matrix} \langle 0| \\ \langle 1| \\ \langle 2| \end{matrix} & \begin{pmatrix} E & V & V \\ V & E & V \\ V & V & E \end{pmatrix} \end{matrix}. \tag{6.2.1}$$

This modeling is general and the connection with the Bose-Hubbard model can be done through

$$|0\rangle = |N_p, 0, 0\rangle, \tag{6.2.2}$$

$$|1\rangle = |0, N_p, 0\rangle, \tag{6.2.3}$$

$$|2\rangle = |0, 0, N_p\rangle. \tag{6.2.4}$$

This matrix takes into account the symmetries of the system and the fact that all sites are connected to each other. Indeed, the Hamiltonian is invariant under the permutation of any pair of sites. If $N_p = 1$, then $E = 0$, $V = -J$ and the result will be exact. The

eigenvalues and the related eigenvectors read

$$\begin{aligned}
E_1 &= E - V, & |X_1\rangle &= \frac{1}{\sqrt{2}} \begin{pmatrix} 0 \\ -1 \\ 1 \end{pmatrix} = \frac{1}{\sqrt{2}}(-|1\rangle + |2\rangle), \\
E_2 &= E - V, & |X_2\rangle &= \frac{1}{\sqrt{6}} \begin{pmatrix} -2 \\ 1 \\ 1 \end{pmatrix} = \frac{1}{\sqrt{6}}(-2|0\rangle + |1\rangle + |2\rangle), \\
E_3 &= E + 2V, & |X_3\rangle &= \frac{1}{\sqrt{3}} \begin{pmatrix} 1 \\ 1 \\ 1 \end{pmatrix} = \frac{1}{\sqrt{3}}(|0\rangle + |1\rangle + |2\rangle).
\end{aligned}$$

If all particles are initially located on site 0 such that

$$|\phi(0)\rangle = |0\rangle \quad (6.2.5)$$

$$= \langle X_1|0\rangle|X_1\rangle + \langle X_2|0\rangle|X_2\rangle + \langle X_3|0\rangle|X_3\rangle \quad (6.2.6)$$

$$= -\frac{2}{\sqrt{6}}|X_2\rangle + \frac{1}{\sqrt{3}}|X_3\rangle, \quad (6.2.7)$$

then the temporal evolution gives rise to

$$\begin{aligned}
|\phi(t)\rangle &= \frac{-2}{\sqrt{6}}e^{-iE_2t/\hbar}|X_2\rangle + \frac{1}{\sqrt{3}}e^{-iE_3t/\hbar}|X_3\rangle \\
&= \frac{e^{-iE_2t/\hbar}}{3}(2|0\rangle - |1\rangle - |2\rangle) + \frac{e^{-iE_3t/\hbar}}{3}(|0\rangle + |1\rangle + |2\rangle) \\
&= \frac{1}{3}\left(2e^{i\Delta\epsilon t/(2\hbar)} + e^{-i\Delta\epsilon t/(2\hbar)}\right)|0\rangle - \frac{2i}{3}\sin\left(\frac{\Delta\epsilon}{2\hbar}t\right)(|1\rangle + |2\rangle). \quad (6.2.8)
\end{aligned}$$

Here the splitting is given by $\Delta\epsilon = E_3 - E_2 = 3V$. From Eq. (6.2.8), it is possible to compute the temporal evolutions of the detection probabilities,

$$\begin{aligned}
P_{|0\rangle}(t) &= |\langle 0|\phi(t)\rangle|^2 & P_{|1\rangle}(t) &= P_{|2\rangle}(t) = |\langle 1|\phi(t)\rangle|^2 \\
&= \frac{1}{9}\left|1 + 2e^{i\Delta\epsilon t/\hbar}\right|^2, & &= \frac{4}{9}\sin^2\left(\frac{\Delta\epsilon}{2\hbar}t\right). \quad (6.2.9)
\end{aligned}$$

The detection probabilities for having all particles on site 1 or 2 are the same. This matches the intuition, as there is by symmetry no reason to favor the transition toward the site 1 or 2. The transition probabilities in Fig. 6.2.1 suggests that the dynamics is largely dominated by three-level oscillations for the parameters $N_p = 5$ and $U = 20J$.

From the previous relations (6.2.9), it is possible to compute the time τ required to reach the same detection probabilities for the three states, called the triple-NOON time. The condition $P_{|1\rangle}(\tau) = 1/3$ leads to

$$\tau = \frac{2\pi\hbar}{3\Delta\epsilon}. \quad (6.2.10)$$

At this time, the detection probabilities of each state are the same,

$$P_{|0\rangle}(\tau) = P_{|1\rangle}(\tau) = P_{|2\rangle}(\tau) = \frac{1}{3}. \quad (6.2.11)$$

The three-mode NOON time for the parameters $N_p = 5$ and $U = 20J$ is equal to $\tau = 5.9 \times 10^5 \hbar/J$ (see Fig. 6.2.1). In Sec. 1.3.3, the laboratory-unit evaluation gave rise $\hbar/J = 4.4 \times 10^{-3}$ s for a typical optical lattice filled with ^{87}Rb . This leads to a triple-NOON time of $\tau = 2600$ s. An additional periodic perturbation will be necessary to decrease this time above the lifetime of a condensate in an optical lattice, roughly equal to 10s [133].

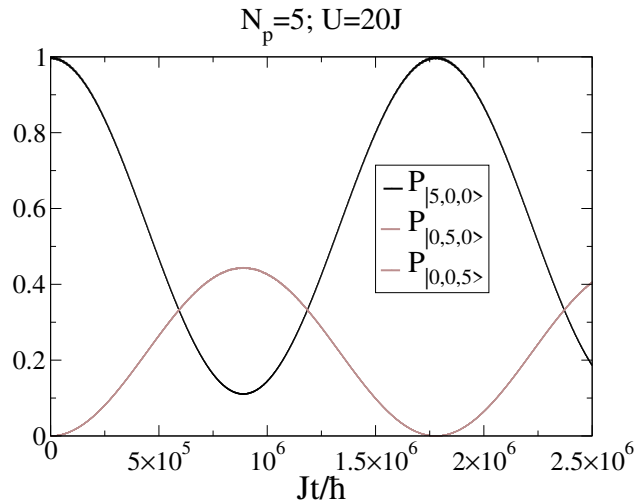


Figure 6.2.1: Numerical detection probabilities for the quasimodes $|5, 0, 0\rangle$, $|0, 5, 0\rangle$ and $|0, 0, 5\rangle$ knowing that all particles are initially located on site 0. In the strong interaction regime, i.e. $(N_p + 1)U/J \gg 1$, the dynamics can be approximated by the three-level dynamic and the detection probabilities are given by Eq. (6.2.9). The time required to obtain an entangled state with the same weight for $|5, 0, 0\rangle$, $|0, 5, 0\rangle$ and $|0, 0, 5\rangle$ amounts to $\tau = 5.9 \times 10^5 \hbar/J$.

6.3 Classical limit of the three-site Bose-Hubbard Hamiltonian

Before taking the classical limit, the Hamiltonian (6.1.1) will be amended by an additional time-periodic perturbation which must preserve the symmetries of the system. One way to achieve that is to have a time-dependent hopping such that

$$J(t) = J + \delta \cos(\omega t). \quad (6.3.1)$$

In this case, the time-dependent Hamiltonian reads [171]

$$\hat{H}(t) = -J(t) \sum_{l=0}^2 (\hat{a}_l^\dagger \hat{a}_{l+1} + \hat{a}_{l+1}^\dagger \hat{a}_l) + \frac{U}{2} \sum_{l=0}^2 \hat{a}_l^\dagger \hat{a}_l^\dagger \hat{a}_l \hat{a}_l. \quad (6.3.2)$$

Note that the Hamiltonian (6.3.2) is still symmetric with respect to the permutation of any pair of sites.

The classical limit is similar to that presented in Sec. 5.1. In the limit of an infinite number of particles the ladder operators can be replaced by complex numbers [129, 130],

which corresponds to the mean-field approximation,

$$\langle \hat{a}_l \rangle \sim \psi_l = \sqrt{I_l} e^{i\theta_l}, \quad (6.3.3)$$

$$\langle \hat{a}_l^\dagger \rangle \sim \psi_l^* = \sqrt{I_l} e^{-i\theta_l}. \quad (6.3.4)$$

Here ψ_l ($l = 0, 1, 2$) represents the condensate amplitude on site l , θ_l the phase on site l and I_l is proportional to n_l , the number of particles on site l , such that $I_l = n_l + 1/2$. As N_p is conserved, the sum of the I_l amounts to a constant $N = N_p + 3/2$,

$$I_0 + I_1 + I_2 = N. \quad (6.3.5)$$

In this framework, the classical limit of the Hamiltonian (6.3.2) reads¹

$$H(\psi_l, \psi_l^*) = -J(t) \sum_{l=0}^2 (\psi_l^* \psi_{l+1} + \psi_{l+1}^* \psi_l) + \frac{U}{2} \sum_{l=0}^2 |\psi_l|^4. \quad (6.3.6)$$

The temporal evolution of the mean-field system is determined by the discrete Gross-Pitaevskii equation. It can be derived from the Hamiltonian (6.3.6),

$$\begin{aligned} i\hbar \frac{d\psi_0}{dt} &= -J(t)(\psi_1 + \psi_2) + U|\psi_0|^2\psi_0, \\ i\hbar \frac{d\psi_1}{dt} &= -J(t)(\psi_0 + \psi_2) + U|\psi_1|^2\psi_1, \\ i\hbar \frac{d\psi_2}{dt} &= -J(t)(\psi_0 + \psi_1) + U|\psi_2|^2\psi_2. \end{aligned} \quad (6.3.7)$$

Another convenient classical representation is the action-angle variables. It enables one to separate the angle-independent part $H(\mathbf{I})$, the time-independent angle-dependent part $V(\boldsymbol{\theta}, \mathbf{I})$ and the time-dependent angle-dependent part $V(\boldsymbol{\theta}, \mathbf{I}, t)$,

$$H(\boldsymbol{\theta}, \mathbf{I}, t) = H(\mathbf{I}) + V(\boldsymbol{\theta}, \mathbf{I}) + V(\boldsymbol{\theta}, \mathbf{I}, t), \quad (6.3.8)$$

with

$$H(\mathbf{I}) = \frac{U}{2} (I_0^2 + I_1^2 + I_2^2), \quad (6.3.9)$$

$$\begin{aligned} &V(\boldsymbol{\theta}, \mathbf{I}) + V(\boldsymbol{\theta}, \mathbf{I}, t) \\ &= -2J(t) \underbrace{\left(\sqrt{I_0 I_1} \cos(\theta_0 - \theta_1) + \sqrt{I_1 I_2} \cos(\theta_1 - \theta_2) + \sqrt{I_0 I_2} \cos(\theta_0 - \theta_2) \right)}_{G(\boldsymbol{\theta}, \mathbf{I})}. \end{aligned} \quad (6.3.10)$$

Here we have $V(\boldsymbol{\theta}, \mathbf{I}) = -2JG(\boldsymbol{\theta}, \mathbf{I})$ and $V(\boldsymbol{\theta}, \mathbf{I}, t) = -2\delta \cos(\omega t)G(\boldsymbol{\theta}, \mathbf{I})$. Like the quantum Hamiltonian (6.3.2), the classical Hamiltonian remains invariant under the permutation of any pair of sites.

¹The constants in the Hamiltonian were removed. The general expression with the constant of motion can be found in Sec. 1.3.4.

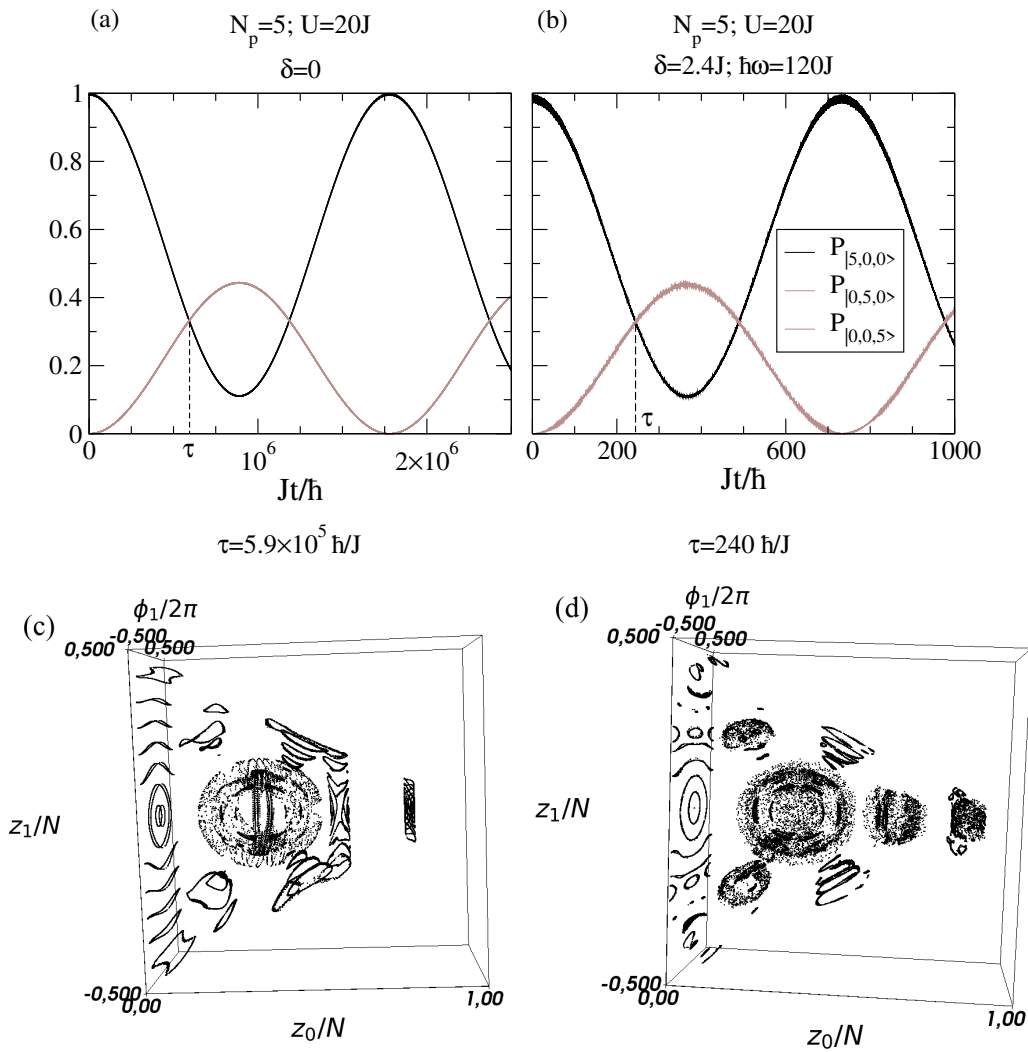


Figure 6.3.1: Numerical detection probabilities for (a) the unperturbed and (b) the periodically-driven three-site Bose-Hubbard system. The plots (c) and (d) are the phase spaces related respectively to the numerically simulated quantum dynamics (a) and (b). A perfectly balanced entangled state between the quasimodes $|5, 0, 0\rangle$, $|0, 5, 0\rangle$ and $|0, 0, 5\rangle$, called a triple-NOON state, can be obtained by preparing all particles on a specific site (here site 0) and then waiting the triple-NOON time τ . The timescale of τ time can be considerably reduced by means of a time-periodic external perturbation as displayed in (b). The main difference between (c) and (d) is the presence in (d) of a 2:1 resonance clearly visible for the layer $z_0 = 0$, which leads to the phenomenon of resonance-assisted tunneling.

6.4 Analysis of the phase space

As N is a constant of motion, it is interesting to perform a canonical transformation to reduce the number of degrees of freedom. As explained in Sec. 5.2, this procedure enables one to build an effective four-dimensional system by means of the generating function (5.2.13). Contrary to the standard action-angle representation (6.3.8), the Hamiltonian $H(\phi, \mathbf{z}, t) =$

$H(\mathbf{z}) + V(\boldsymbol{\phi}, \mathbf{z}) + V(\boldsymbol{\phi}, \mathbf{z}, t)$ defines a phase space of four dimensions with

$$H(\mathbf{z}) = Uz_1^2 + \frac{3U}{4} \left(z_0 - \frac{N}{3} \right)^2, \quad (6.4.1)$$

$$\begin{aligned} & V(\boldsymbol{\phi}, \mathbf{z}) + V(\boldsymbol{\phi}, \mathbf{z}, t) \\ &= -J(t) \left(\sqrt{2}\sqrt{z_0(N - z_0 + 2z_1)} \cos \left(\phi_0 - \frac{1}{2}\phi_1 \right) \right. \\ & \quad \left. + 2\sqrt{(N - z_0)^2/4 - z_1^2} \cos(\phi_1) \right. \\ & \quad \left. + \sqrt{2}\sqrt{z_0(N - z_0 - 2z_1)} \cos \left(\phi_0 + \frac{1}{2}\phi_1 \right) \right), \end{aligned} \quad (6.4.2)$$

$\underbrace{\hspace{15em}}_{G(\boldsymbol{\phi}, \mathbf{z})}$

such that $V(\boldsymbol{\phi}, \mathbf{z}) = -JG(\boldsymbol{\phi}, \mathbf{z})$ and $V(\boldsymbol{\phi}, \mathbf{z}, t) = -2\delta \cos(\omega t)G(\boldsymbol{\phi}, \mathbf{z})$. We have $N = N_p + 3/2$, and the links with the condensate amplitudes and phases are given by

$$\begin{aligned} \phi_0 &= \theta_0 - \frac{1}{2}(\theta_1 + \theta_2), & z_0 &= n_0 + \frac{1}{2}, \\ \phi_1 &= \theta_1 - \theta_2, & z_1 &= \frac{1}{2}(n_1 - n_2). \end{aligned} \quad (6.4.3)$$

Here z_0 represents the population of site 0 while z_1 is the population imbalance between site 1 and 2. Note that ϕ_1 and z_1 are the phase-space variables used for the study of the two-site system in Sec. 3.1.

The phase spaces 6.3.1(c) and (d) are 3D phase-space slices performed around $\bar{\phi}_0 = 0$ in a phase space of four dimensions. This visualization technique was proposed in Refs. [85,86] for the study of two coupled standard map and can be formalized in our case by slices of thickness 2ε around an arbitrary point $\bar{\phi}_0$ such that

$$\{(\phi_0, \phi_1, z_0, z_1) \mid |\phi_0 - \bar{\phi}_0| \leq \varepsilon\}. \quad (6.4.4)$$

The phase space 6.3.1(c) is characterized by three pendulum-like phase spaces, each of them defining a resonance center line [95] in action space (see also blue lines in Fig. 6.4.1(a)). The unperturbed frequencies of the tori will enable one to characterize these resonance center lines,

$$\boldsymbol{\Omega}(\mathbf{z}) = \frac{1}{\hbar} \nabla_{\mathbf{z}} H(\mathbf{z}) = \frac{1}{\hbar} \begin{pmatrix} \frac{3U}{2}(z_0 - N/3) \\ 2Uz_1 \end{pmatrix}. \quad (6.4.5)$$

As soon as the hopping J is different from zero, the system becomes perturbed through $V(\boldsymbol{\phi}, \mathbf{z})$, and the tori characterized by a resonant motion $\mathbf{r}_l \cdot \boldsymbol{\Omega}(\mathbf{z}) = 0$ will be destroyed [87] as explained in Sec. 5.2. The main resonance vector $\mathbf{r}_0 = (1, -1/2)$, $\mathbf{r}_1 = (0, 1)$ and $\mathbf{r}_2 = (1, 1/2)$ are determined by the arguments of the cosines of $V(\boldsymbol{\phi}, \mathbf{z})$ [87,95]. This leads to the parametrizations of the main resonant center lines,

$$z_1 = +\frac{3}{2}z_0 - \frac{N}{2}, \quad (6.4.6)$$

$$z_1 = 0, \quad (6.4.7)$$

$$z_1 = -\frac{3}{2}z_0 + \frac{N}{2}. \quad (6.4.8)$$

Each resonance center line passes through one of the quasimodes at stake, i.e. $|5, 0, 0\rangle$, $|0, 5, 0\rangle$, $|0, 0, 5\rangle$, and are symmetrically located between one pair of them as displayed in blue in Fig. 6.4.1(a). Moreover, these quasimodes lie on the same energy shell in red. At quantum level there is a small splitting $\Delta\epsilon$, which is the spectral signature of tunneling.

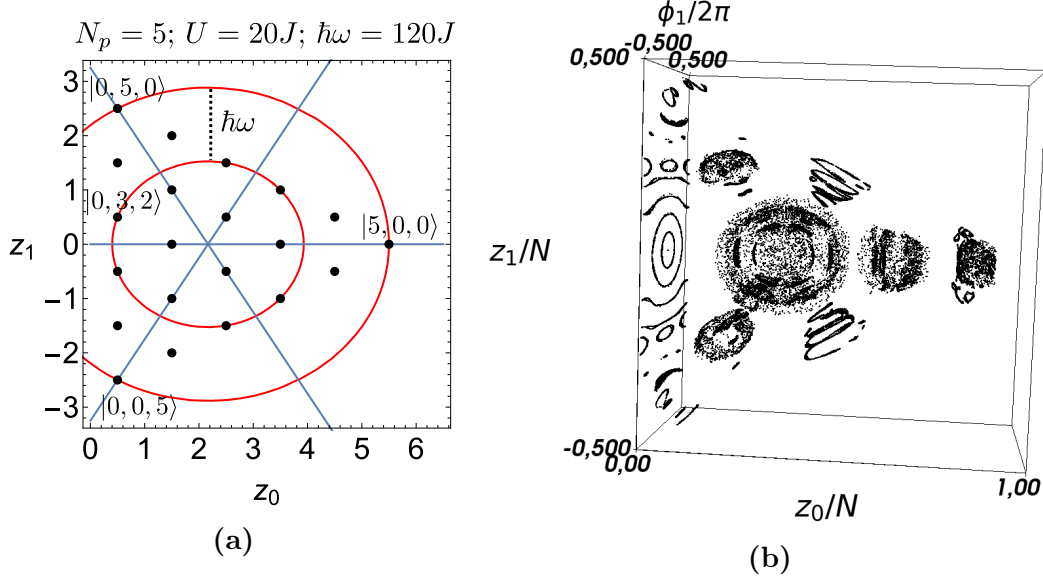


Figure 6.4.1: The resonance center lines are schematized in the action space in (a) by means of the blue color. The presence of an external perturbation of frequency $\omega = 120J/\hbar$ couples the two energy shells in red of the unperturbed system. This enables one to add a coupling matrix element between the quasimode $|0, 5, 0\rangle$ of the outer energy shell and the quasimode $|0, 3, 2\rangle$ of the inner energy shell. The manifestation of this coupling in the phase space (b) is the presence of a 2:1 resonance visible in $z_1 = \pm 1.5$ for the layers with z_0 between 0 and 1.25 roughly. For the phase space (b), we have $N_p = 5$, $U = 20J$, $\delta = 2.4J$ and $\hbar\omega/J = 120$.

At the intersection of the resonance center lines, there exists a junction made of several fixed points around which the phase space is organized. This junction is localized in action space in

$$(z_0^*, z_1^*) = \left(\frac{N}{3}, 0 \right), \quad (6.4.9)$$

which corresponds to the ground state for repulsive inter-atomic interactions. Far from them, the phase space is locally a 2D pendulum-like phase space as it is the case, for example, for the layer $z_0 = 0$. Closer to the junction, the interplay between the three pendulum-like degrees of freedom gives rise to a chaotic layer with the shape of a bubble. Note that due to particle conservation (N_p constant), the action space forms a triangle.

A careful analysis of the phase space is able to explain the role of the frequency ω for the emergence of the nonlinear resonances. Each unperturbed torus \mathbf{z} is characterized by two frequencies $\mathbf{\Omega} = (\Omega_0, \Omega_1)$ determined by Eq. (6.4.5). When the perturbation $V(\phi, \mathbf{z}, t)$ is slightly turned on, the Kolmogorov-Arnold-Moser theorem [65, 66, 87] states that if the frequencies are not rationally related, then the torus is preserved. The frequencies of a torus are rationally related if they obey the following relation [85, 86],

$$k_0\Omega_0 + k_1\Omega_1 = m\omega, \quad (6.4.10)$$

where $(k_0, k_1) \in \mathbb{Z}^2 \setminus \{(0, 0)\}$ and $m \in \mathbb{Z}$. A resonance is formed through the destruction of a set of tori and can be labeled by $k_0:k_1:m$. Resonances of the form $r:0:s$ and $0:r:s$ correspond

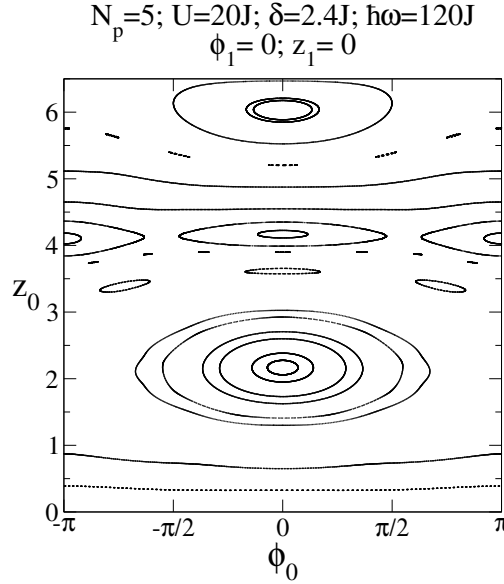


Figure 6.4.2: Phase space portrait of the classical dynamics confined to the invariant submanifold characterized by $\phi_1 = 0$ and $z_1 = 0$. It enables one to deduce the position of the central fixed points roughly situated in $(z_0, z_1) = (2.167, 0)$, one of them is elliptic-elliptic in $(\phi_0, \phi_1) = (0, 0)$ and another is hyperbolic-elliptic in $(\phi_0, \phi_1) = (\pi, 0)$.

to the relations $r\Omega_0 = s\omega$ and $r\Omega_1 = s\omega$, respectively. These two kinds of resonance are here called $r:s$ to shorten the notation. Indeed, both of them produce a $r:s$ resonance, the former perpendicular to the z_0 axis and the latter perpendicular to the z_1 axis. In this framework, the external frequencies ω that must be applied in order to build the $r:s$ nonlinear resonance characterized by $z_0 = z_0^{(r:s)}$ or $z_1 = z_1^{(r:s)}$ are given, respectively, by the relations

$$\hbar\omega = \frac{r}{s} \frac{3U}{2} \left(z_0^{(r:s)} - \frac{N}{3} \right), \quad (6.4.11)$$

$$\hbar\omega = \frac{r}{s} 2U z_1^{(r:s)}. \quad (6.4.12)$$

It is worthwhile to note that Eq. (6.4.12) is exactly the same as that obtained for the two-site optical lattice in Ref. [52].

For example, a 2:1 resonance situated in $z_1^{(2:1)} = 1.5$ symmetrically located between $|0, 5, 0\rangle$ in $(z_0, z_1) = (0.5, 2.5)$ and $|0, 3, 2\rangle$ in $(z_0, z_1) = (0.5, 0.5)$ leads to $\omega = 120J/\hbar$ for $U = 20J$. Thus, this combination of parameters leads to

$$z_0^{(2:1)} = 4.1666, \quad (6.4.13)$$

$$z_1^{(2:1)} = 1.5. \quad (6.4.14)$$

Actually, this resonance is clearly visible in Fig. 6.4.1(b) for the layer $z_0 \simeq 0$. Moreover, Eq. (6.4.13) gives access to the position of the 2:1 resonance along the $z_1 = 0$ resonance center line. Indeed, since trajectories that start with $\phi_1 = 0$ and $z_1 = 0$ remain confined along this submanifold, it is possible to build a 2D representation of the dynamics. This is displayed in Fig. 6.4.2 where the 2:1 resonance is clearly visible.

6.5 Triple-NOON states in near-integrable phase spaces

The triple-NOON time is expected to be modified with the addition of a time-periodic perturbation, for example, via the hopping parameter $J(t) = J + \delta \cos(\omega t)$ [171]. Even if the addition of a time-periodic perturbation breaks the conservation of energy, it is still possible to compute time-independent quasienergies ϵ_ν and to decompose any state $|\phi(t)\rangle$ in a time-periodic basis $\{|u_\nu(t)\rangle = |u_\nu(t + 2\pi/\omega)\rangle\}$ in the framework of the Floquet formalism [131, 138, 139],

$$\left(\hat{H}(t) - i\hbar \frac{d}{dt} \right) |u_\nu(t)\rangle = \epsilon_\nu |u_\nu(t)\rangle, \quad (6.5.1)$$

where $\nu = 1, 2, \dots, D$ with $D = (N_p + 1)(N_p + 2)/2$ the Hilbert space dimension of the unperturbed system [162]. Floquet theory is developed in detail in Sec. 2.2.

The Floquet basis can, for example, be expressed in terms of the Fock states $|n_0, n_1, n_2\rangle$,

$$\left\{ |u_\nu(t)\rangle = \sum_{k=-\infty}^{+\infty} e^{ik\omega t} \sum_{n_1=0}^{N_p} \sum_{n_2=0}^{N_p-n_1} F_{\nu,k,n_1,n_2} |n_0, n_1, n_2\rangle \mid \nu = 0, 1, \dots, D \right\}. \quad (6.5.2)$$

Here the value of n_0 is obtained through the particle conservation such that $n_0 = N_p - n_1 - n_2$. Any state $|\phi(t)\rangle$ can be decomposed in that basis,

$$|\phi(t)\rangle = \sum_{\nu=1}^D c_\nu(t_0) e^{-i\epsilon_\nu(t-t_0)/\hbar} |u_\nu(t)\rangle, \quad (6.5.3)$$

where $c_\nu(t_0) = \langle u_\nu(t_0) | \phi(t_0) \rangle$ and $|\phi(t_0)\rangle$ is the initial state. The probability amplitude to obtain the state $|n_0, n_1, n_2\rangle$, knowing that the system is initially in $|\phi(t_0)\rangle$, is given by

$$P_{|n_0, n_1, n_2\rangle}(t) = |\langle n_0, n_1, n_2 | \phi(t) \rangle|^2. \quad (6.5.4)$$

As illustrated in Fig. 6.3.1(b), a suitably tuned driving leads to a sharp decrease of the triple-NOON time such that $\tau = 240\hbar/J$ for $\delta = 2.4J$ and $\omega = 120J/\hbar$. The manifestation of this phenomenon is visible in the corresponding phase space of Fig. 6.3.1(d). Indeed, Figs. 6.3.1(c) and (d) are very similar except for the presence of a 2:1 nonlinear resonance in the perturbed case, which is clearly visible within the layer $z_0 = 0$. By the resonance-assisted tunneling mechanism [67, 68], a coupling matrix element is introduced between the quasimodes $|0, 5, 0\rangle$ and $|0, 3, 2\rangle$, which favors resonant perturbative transitions as the 2:1 resonance is symmetrically located between both quasimodes [72, 79]. In terms of the action space of Fig. 6.4.1(a), the energy shell in red related to $|5, 0, 0\rangle$, $|0, 5, 0\rangle$ and $|0, 0, 5\rangle$ is now connected to the one related to $|0, 3, 2\rangle$, $|3, 2, 0\rangle$, $|2, 0, 3\rangle$, $|3, 0, 2\rangle$, $|0, 2, 3\rangle$ and $|2, 3, 0\rangle$ via $\hbar\omega$. For a typical optical lattice² filled with atoms of the ⁸⁷Rb species, we have $\hbar/J = 4.4 \times 10^{-3}$ s such that the triple-NOON time is given by $\tau = 1.1$ s compared to $\tau = 2600$ s for the unperturbed case. This reduction of three orders of magnitude could render possible an experimental observation of the triple-NOON state.

As it remains one free parameter, namely the amplitude δ , the triple-NOON time is computed as a function of this one to obtain an optimal choice. As displayed in Fig. 6.5.1(a), the triple-NOON time only decreases after the peak in $\delta = 0.05J$. Nevertheless, the purity decreases at the same time. This time-independent indicator is useful to quickly test the

²The details for the derivations can be found in Sec. 1.3.3.

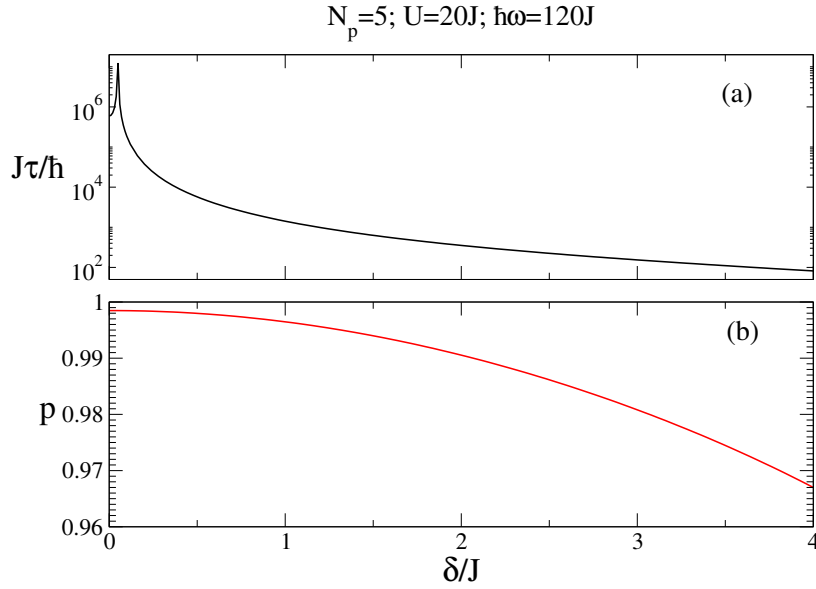


Figure 6.5.1: (a) Triple-NOON time as a function of the amplitude δ . (a) The purity p defined in Eq. (6.5.5) as a function of δ . The triple-NOON time τ decreases continually from $\delta = 0.05J$ without reaching a minimum (expect for $\delta = 0$). The more it decreases, the more the purity decreases as well as seen in panel (b). In this context, the convenient choice of δ is a trade-off. For $\delta = 2.4J$, we have $\tau = 240\hbar/J$ with a purity of $p = 0.987$ while for $\delta = 0$, we have $\tau = 5.9 \times 10^5 \hbar/J$ with $p = 0.998$.

validity of the three-level approximation. The purity is defined as

$$p = M_{N_p,0,0} + M_{0,N_p,0} + M_{0,0,N_p}, \quad (6.5.5)$$

with

$$M_{n_0,n_1,n_2} = \frac{1}{3T} \sum_{j=1}^3 \int_0^T |\langle n_0, n_1, n_2 | u_{\nu_j}(t) \rangle|^2 dt. \quad (6.5.6)$$

Here $|u_{\nu_j}(t)\rangle$ are the eigenstates related to the triple-NOON state. If they are close to the eigenvectors of the three-level approximation such that

$$|u_{\nu_1}(t)\rangle \sim \frac{1}{\sqrt{2}}(-|0, N_p, 0\rangle + |0, 0, N_p\rangle), \quad (6.5.7)$$

$$|u_{\nu_2}(t)\rangle \sim \frac{1}{\sqrt{6}}(-2|N_p, 0, 0\rangle + |0, N_p, 0\rangle + |0, 0, N_p\rangle), \quad (6.5.8)$$

$$|u_{\nu_3}(t)\rangle \sim 1/\sqrt{3}(|N_p, 0, 0\rangle + |0, N_p, 0\rangle + |0, 0, N_p\rangle), \quad (6.5.9)$$

the purity is expected to be close to 1. In view of these considerations, the choice of δ is a trade-off for the parameters in Fig. 6.5.1. By choosing $\delta = 2.4J$, the three-level approximation is still valid with a purity of $p = 0.987$.

6.6 Triple-NOON states in mixed phase spaces

The time-independent indicator of purity defined in Eq. (6.5.5) enables one to obtain quickly a representation of the main features of the dynamics without being obliged to compute a

time evolution of the transition probabilities. Indeed, we have

$$M_{n_0, n_1, n_2} = \frac{1}{3} \sum_{j=1}^3 \sum_{k=-\infty}^{\infty} |F_{\nu_j, k, n_1, n_2}|^2. \quad (6.6.1)$$

This indicator assumes that the system is prepared in one the three Floquet states involved in the three-level approximation, namely $|u_{\nu_j}(t_0)\rangle$ with $j = 1, 2, 3$. Then, the temporal mean over one period of the transition probabilities from these three states is performed.

Nevertheless, the question asked by Fig. 6.3.1(a) is how much the transition probabilities $P_{|N_p, 0, 0\rangle}$, $P_{|0, N_p, 0\rangle}$ and $P_{|0, 0, N_p\rangle}$ dominates the dynamics in order to test the validity of the three-level approximation. This question makes sense from an experimental point of view if the system is initially prepared in $|\phi(t_0)\rangle = |N_p, 0, 0\rangle$. Thus, the time-independent indicator related to Fig. 6.3.1(a) and (b) is properly speaking given by

$$\bar{p} = \bar{P}_{|N_p, 0, 0\rangle} + \bar{P}_{|0, N_p, 0\rangle} + \bar{P}_{|0, 0, N_p\rangle}, \quad (6.6.2)$$

with

$$\bar{P}_{|n_0, n_1, n_2\rangle} = \frac{1}{t} \int_0^t dt' |\langle n_0, n_1, n_2 | \phi(t') \rangle|^2. \quad (6.6.3)$$

The \bar{p} indicator is more pertinent for the question asked. The main drawback is that it required to compute the time-evolution of the system and to perform a temporal mean on a sufficiently long time t . Luckily, both indicators p and \bar{p} are in general very close to each other. Nevertheless, we remarked some notable deviations for the three-site Bose-Hubbard model when a prominent chaotic sea is present (see Fig. 6.6.1). That is why, the values of \bar{p} are displayed in the last column of Table 6.1.

N_p	$J\tau_{\delta=0}/\hbar$	$p_{\delta=0}$	$J\tau_{\omega=60J/\hbar}/\hbar$	$\bar{p}_{\omega=60J/\hbar}$
5	5.9×10^5	0.998	5.8×10^2 ($\delta = 0.95J$)	0.978
7	1.0×10^9	0.998	4.8×10^3 ($\delta = 1.3J$)	0.974
9	1.9×10^{12}	0.998	4.3×10^6 ($\delta = 1.5J$)	0.972

Table 6.1: As expected, the triple-NOON time τ increases with N_p , but this increase can be considerably reduced for $\omega = 60J/\hbar$. Creating a central chaotic layer in phase space (see Fig 6.6.1) is able to slow down the exponential increase with N_p of the triple-NOON time. In order to keep the unperturbed phase space unchanged, we keep $NU/J = 130$ for each result.

Besides the resonance-assisted mechanisms, chaos-assisted tunneling is a credible alternative to speed up the production of a triple-NOON state. A smaller frequency, for example $\omega = 60\hbar/J$ in Fig. 6.6.1, is able to produce a prominent central chaotic layer due to the interplay between the chaotic bubble structure at the junction and the low-rank 1:s non-linear resonances. As indicated in Fig. 6.6.2, this produces a triple-NOON time amounting to $\tau = 580\hbar/J$ with a purity $\bar{p} = 0.978$, which is comparable to the one obtained through the 2:1 resonance in Fig. 6.3.1(b) and (d). This corresponds to $\tau = 2.6$ s for ^{87}Rb atoms in the lattice that is studied in Sec. 1.3.3. Moreover, Table 6.1 suggests that the phase-space structure made of a central chaotic sea as displayed, for example, in Fig. 6.6.1, is valuable for the triple-NOON time reduction as the number of particles increases. Indeed, the exponential increase with N_p is slowed down. This is due to the fact that the states of the chaotic sea are strongly mixed such that they cannot really be distinguished from each other. The transition between quasimodes $|N_p, 0, 0\rangle$, $|0, N_p, 0\rangle$ and $|0, 0, N_p\rangle$ is then facilitated by their coupling with the chaotic sea. It means that chaos-assisted tunneling is

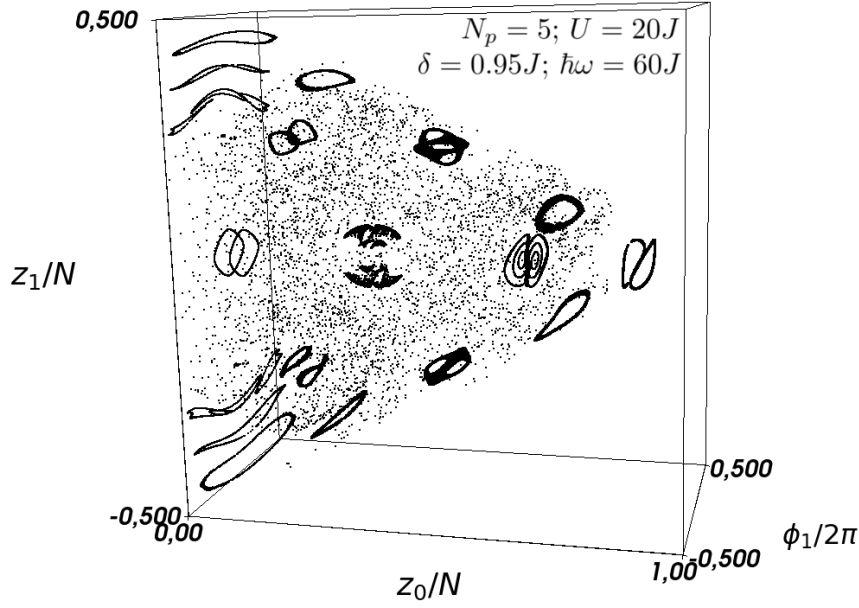


Figure 6.6.1: Phase space of the periodically-driven three-site Bose-Hubbard system in the mixed regime. A central prominent chaotic layer can be generated by means of smaller external frequency ω . The three corners of the phase space are still regular and greet the three quasimodes involved in the triple-NOON state, namely $|5, 0, 0\rangle$, $|0, 5, 0\rangle$ and $|0, 0, 5\rangle$, which are strongly coupled by means of this chaotic sea. This specific figure corresponds at the quantum level to $\tau = 580\hbar/J$ with $\bar{p} = 0.978$ (see Fig. 6.6.2), which corresponds roughly to the same orders of magnitude as the near-integrable case in Fig. 6.3.1(b). As illustrated in Table 6.1, we can take advantage of this phase-space structure as the number of particles increases. Embedded in the chaotic sea, regular structures tends to stabilize, from the purity point of view, the states located at each corner.

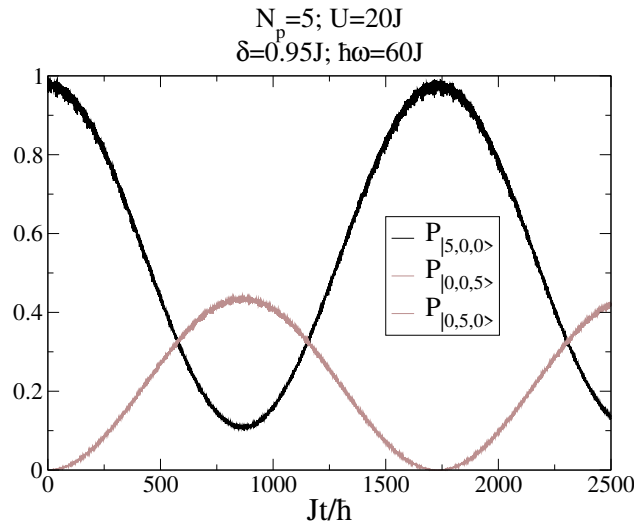


Figure 6.6.2: Numerical detection probabilities of the quasimodes $|5, 0, 0\rangle$, $|0, 0, 5\rangle$ and $|0, 5, 0\rangle$ knowing that all particles are prepared on the site 0 initially. This figure corresponds to the phase space of Fig. 6.6.1. The central chaotic layer is able to facilitate the transition to the triple-NOON state. For this specific combination of parameters, the triple-NOON time is given by $\tau = 580\hbar/J$ for a purity $\bar{p} = 0.978$.

surely a promising tool to investigate the triple-NOON production with higher populations. The results of Table 6.1 were obtained by fixing $NU/J = 130$ constant in order to preserve the unperturbed phase space. The central chaotic region of Fig. 6.6.1 is not homogeneous as it displays regular islands embedded in the chaotic sea. This may indicate the presence of some resonance-assisted tunneling phenomena besides the chaos-assisted tunneling one. Moreover, these regular islands would tend to stabilize the regular eigenstates located at the three corners of the phase owing to the presence of partial transport barriers.

Conclusion

This dissertation theoretically investigates the production of entangled states with a Bose-Einstein condensate trapped in several sites of an optical lattice. The protocol proposed here is quite simple. All atoms are loaded on any site of a symmetric optical trap. In this case, the temporal evolution of the ultracold atoms leads to a NOON state, after the NOON time, in the case of a double-well potential as explored partially in Chap. 2 and extensively in Chap. 4. One of the main drawback is the prohibitively long time necessary to obtain the coherent and equivalent superposition between the states $|N_p, 0\rangle$ and $|0, N_p\rangle$, called the NOON state, where N_p is the total number of ultracold atoms. For example, in the strong on-site interaction regime where the effective atom-atom interaction is quite large compared to the hopping J , i.e. $(N_p + 1)U \gg J$, we theoretically obtain the NOON time $\tau = 2600$ s for $N_p = 5$ and $U/J = 20$ in Sec. 2.1.2. This time is obtained for ^{87}Rb atoms with the assumptions that are presented in Sec. 1.3.3. This result, computed in the unperturbed case, is clearly larger than the typical lifetime of a condensate, which is roughly 10 s [133].

As it is explained in Chap. 4, this problem can be bypassed by subjecting the double-well potential to a periodic tilting characterized by an amplitude δ and a frequency ω . In Sec. 4.3.5, we obtain $\tau = 11$ s for $N_p = 5$, $U/J = 20$, $\delta/J = 75$ and $\hbar\omega/J = 120$ by introducing a perturbative coupling between the Fock states $|n_1, n_2\rangle$ with a 2:1 nonlinear resonance. It is also possible to improve this result by combining couplings with the chaotic sea and multiple perturbative couplings via the 1:4 and 1:3 resonances. This configuration gives rise to $\tau = 0.84$ s and is obtained for $N_p = 5$, $U/J = 20$, $\delta/J = 19.5$ and $\hbar\omega/J = 20$. This result is presented in Sec. 4.5.

Indeed, the increase of the tunneling rate (or equivalently the decrease of the NOON time) is the consequence of the presence of chaos and nonlinear resonances in the phase space. These structures are able to produce coupling matrix elements at the quantum level between the quasimodes $|n_1, n_2\rangle$, which can speed up the NOON-state generation without altering too much the regular tori related to this NOON state. This is described in Secs. 4.3 and 4.5. In this context, the semiclassical theory of resonance- and chaos-assisted tunneling, which is introduced in Chap. 4, can be used as a guideline to find the optimal parameters. This is particularly the case for the frequency of the periodic driving, which determines the positions of the nonlinear resonances in the phase space. Moreover, integrable systems are known to display an exponential decrease of tunneling rates according to the semiclassical parameter (here N_p). This is illustrated in Sec. 4.2 for the unperturbed two-site Bose-Hubbard model. Nevertheless, with a prominent chaotic sea, the average slope of the exponential decrease is slowed down, and there are peaks in the tunneling rate. This opens the way for realizing NOON states with an increasing number of particles.

We can ask the opposite question, namely if it is possible to coherently suppress tunneling in the optical trap by means of an external perturbation. Actually, it is possible, and this phenomenon has been known for several decades. Obviously, this suppression doesn't have a lot of interest for the NOON state as the NOON time is already prohibitively large for the

unperturbed case. Nevertheless, this question makes sense for entangled states with smaller population imbalances as they have smaller entanglement times. As it is shown in Chap. 2, the external perturbation is also able to totally suppress the entangled-state formation, especially for large frequency compared to the width of the unperturbed spectrum. Stated differently, the entanglement time can become infinite for suitable amplitudes and frequencies. In this context, we present our original contribution by deriving the renormalization of the tunneling rate related to the two-site Bose-Hubbard model as shown in Sec. 2.4.

As it is explained in Chap. 6, a natural way to study entanglement in a three-site optical trap is to introduce the notion of triple-NOON state, which corresponds to the coherent and equivalent superposition between $|N_p, 0, 0\rangle$, $|0, N_p, 0\rangle$ and $|0, 0, N_p\rangle$. The protocol here is the same as in the two-site trap. The Bose-Einstein condensate is loaded on one site of the symmetric three-site optical trap, and the triple-NOON state is obtained after the triple-NOON time τ . For example, we compute $\tau = 2600$ s for $N_p = 5$ and $U/J = 20$ with the unperturbed three-site Bose-Hubbard model in Sec. 6.5. This time is too long compared to the timescale of a typical experiment. Here the time-periodic perturbation is added in the hopping parameter in order to preserve the symmetry of the lattice. The result $\tau = 1.1$ s is obtained in the near-integrable regime, where perturbative couplings between the Fock states $|n_0, n_1, n_2\rangle$ is induced by a 2:1 resonance. This result is presented in Sec. 6.5. The related parameters are $N_p = 5$, $U/J = 20$, $\delta/J = 2.4$ and $\hbar\omega/J = 120$. Here too, resonance-assisted tunneling can be seen as a guiding mechanism. As in the two-site case, the presence of a prominent chaotic layer in phase space is a valuable ingredient to obtain triple-NOON states. For this phase-space structure, the regular regions, on which the states $|N_p, 0, 0\rangle$, $|0, N_p, 0\rangle$ and $|0, 0, N_p\rangle$ are anchored, are separated by a huge chaotic layer. This structure favors the transitions between these three states. Specifically, we obtain $\tau = 2.6$ s for $N_p = 5$, $U/J = 20$, $\delta/J = 0.95$ and $\hbar\omega/J = 60$ as presented Sec. 6.6. Moreover, the exponential increase with N_p of the triple-NOON time tends to be damped by means that huge chaotic layer. This paves the way to obtain a triple-NOON state with an increasing number of particles.

Perspectives

From the present work, some perspectives can be drawn. At the end of Chap. 6, we suggest that a huge layer of chaotic motion in phase space is the path to follow to produce triple-NOON states with higher populations. Nevertheless, resonance-assisted tunneling could be another way to achieve this goal, and our present lack of knowledge concerning its inherent mechanisms at higher dimensions prevents us to use it in a valuable way. Indeed, resonance- and chaos-assisted tunneling has not been studied much so far for several degree-of-freedom systems. We initiate this study for the three-site Bose-Hubbard model subjected to a periodic driving by identifying a valuable indicator, namely the triple-NOON time. Moreover, the 3D slices in a 4D phase space enable one to have a clear representation of the classical dynamics. The idea would be to develop a semiclassical theory that generalizes resonance- and chaos-assisted tunneling for two or any degree-of-freedom systems. This should reproduce the semiclassical theory exposed in Chap. 4 valid for the one degree-of-freedom system. With this framework, it would be possible to explore quantitatively and qualitatively the semiclassical limit of the three-site Bose-Hubbard model. With this theory, it should be possible to combine the effect of chaos and resonances in an optimal way to produce triple-NOON states with higher populations.

This dissertation focuses exclusively on the generation of double- and triple-NOON states with ultracold bosonic atoms. Quite naturally, we can ask the question concerning the

generation of a n -tuple-NOON state. Actually, the protocol proposed here can be generalized for this kind of state. All atoms are loaded on a specific site of a symmetric optical lattice composed of N_s sites. The formation of the n -tuple-NOON state is obtained after the n -tuple-NOON time. From a theoretical point of view, this state can be modeled by generalizing the matrix (6.2.1) to a $N_s \times N_s$ matrix where all diagonal elements, i.e. the unperturbed energies, are the same and are coupled to each other with the same coupling matrix element V . From an experimental point of view, this kind of state is quite challenging. Indeed, it requires a symmetric optical lattice, in a sense that the on-site interaction must be the same for each site as well as the hopping between any pair of sites. This requirement is more easily fulfilled for the two- and three-site optical traps as they can be produced in a plane. For a quadruple NOON state, for example, the four-site optical trap must be considered in three dimensions such that it can be generated for a lattice with the shape of a tetrahedron.

The protocol proposed to produce a NOON state (or a triple-NOON state) assumes a nearby perfect symmetry of the optical lattice maintained during several seconds. This requirement could lead to experimental complications. These complications are not addressed in this dissertation. One way to overcome this potential problem would be to use the notion of time crystal for which the symmetry is guaranteed by construction [172]. Specifically, the ultracold atoms are confined in a ring-shaped trap [173]. By means of 2:1 resonance produces by an external perturbation, the condensate displays two possible rotational states of motion. The idea would be to load the ultracold atoms in one of them and wait the NOON time in order to obtain the coherent superposition between these two rotational states. From a phase space point of view, it means that the initial wave packet is localized on a specific island of the 2:1 resonance. This protocol can also be used for a 3:1 resonance to produce a triple-NOON state, implying three rotational states of motion, as the islands are still connected in the same way. In this context, the coupling between these islands is a chaos-assisted tunneling mechanism such that this theory is directly required to evaluate the hopping parameter. Moreover, the on-site (or on-island) interaction can depend on time because the spatial localization of the wave packet can vary on one period of the time crystal. That is why the parameter of the Bose-Hubbard model would require more effort to be determined.

Appendix A

Floquet theory and two-site Bose-Hubbard Hamiltonian

A.1 General solutions of Floquet systems

The purpose of this appendix is to demonstrate that the solutions of the Schrödinger equation characterized by a time-periodic Hamiltonian with a period T , i.e. $\hat{H}(t+T) = \hat{H}(t)$, is the combination an imaginary exponential and a function characterized by a period T . We assume that the $|\psi_\nu(t)\rangle$ are the solutions of the Schrödinger equation,

$$i\hbar \frac{d}{dt} |\psi_\nu(t)\rangle = \hat{H}(t) |\psi_\nu(t)\rangle, \quad (\text{A.1.1})$$

where ν labels the different solutions. As the Hamiltonian is periodic, the $|\psi_\nu(t+T)\rangle$ are also solutions,

$$i\hbar \frac{d}{dt} |\psi_\nu(t+T)\rangle = \hat{H}(t) |\psi_\nu(t+T)\rangle. \quad (\text{A.1.2})$$

In this case, the solutions are related by a phase factor [174],

$$|\psi_\nu(t)\rangle = e^{-i\epsilon_\nu T} |\psi_\nu(t+T)\rangle. \quad (\text{A.1.3})$$

We define the quasienergies ϵ_ν such that

$$\epsilon_\nu = \frac{\hbar \alpha_\nu}{T}. \quad (\text{A.1.4})$$

The function $|u_\nu(t)\rangle$ defined as

$$|u_\nu(t)\rangle = e^{i\epsilon_\nu t/\hbar} |\psi_\nu(t)\rangle \quad (\text{A.1.5})$$

is then periodic, $|u_\nu(t)\rangle = |u_\nu(t+T)\rangle$. In this framework the solutions of (A.1.1) are given by the combination of an imaginary exponential and a function with the periodicity of the Hamiltonian,

$$|\psi_\nu(t)\rangle = e^{-i\epsilon_\nu t/\hbar} |u_\nu(t)\rangle. \quad (\text{A.1.6})$$

A.2 Two-site Bose-Hubbard Hamiltonian in the Fock basis

The purpose of this appendix is to decompose the two site Bose-Hubbard Hamiltonian,

$$\begin{aligned}\hat{H}(t) = & -J(\hat{a}_1^\dagger \hat{a}_2 + \hat{a}_2^\dagger \hat{a}_1) + \frac{U}{2}(\hat{a}_1^\dagger \hat{a}_1^\dagger \hat{a}_1 \hat{a}_1 + \hat{a}_2^\dagger \hat{a}_2^\dagger \hat{a}_2 \hat{a}_2) \\ & + \delta \cos(\omega t)(\hat{a}_1^\dagger \hat{a}_1 - \hat{a}_2^\dagger \hat{a}_2),\end{aligned}\quad (\text{A.2.1})$$

into the Fock basis,

$$\{|n, N_p - n\rangle \mid n = 0, 1, 2, \dots, N_p\}, \quad (\text{A.2.2})$$

in order to build the Floquet matrix (2.3.4). The following frame indicates the action of the different operators on the Fock states with $n_1 + n_2 = N_p$ and with $l = 1, 2$.

$$\begin{aligned}-J\hat{a}_1^\dagger \hat{a}_2 |n_1, n_2\rangle &= -J\sqrt{n_2(n_1 + 1)} |n_1 + 1, n_2 - 1\rangle \\ -J\hat{a}_2^\dagger \hat{a}_1 |n_1, n_2\rangle &= -J\sqrt{n_1(n_2 + 1)} |n_1 - 1, n_2 + 1\rangle \\ \frac{U}{2}\hat{a}_l^\dagger \hat{a}_l^\dagger \hat{a}_l \hat{a}_l |n_1, n_2\rangle &= \frac{U}{2}n_l(n_l - 1) |n_1, n_2\rangle \\ \frac{\delta}{2}\hat{a}_l^\dagger \hat{a}_l |n_1, n_2\rangle &= \frac{\delta}{2}n_l |n_1, n_2\rangle\end{aligned}$$

The Fourier decomposition of Eq. (A.2.1) is given by $\hat{H}(t) = \hat{H}_0 + \hat{H}_1(e^{i\omega t} + e^{-i\omega t})$, and the mode one of the Fourier coefficients is diagonal,

$$(\hat{H}_1) = \begin{pmatrix} -\frac{\delta}{2}N_p & 0 & \dots & \dots & 0 \\ 0 & \ddots & & & \vdots \\ \vdots & & \frac{\delta}{2}(n_1 - n_2) & & \vdots \\ \vdots & & & \ddots & 0 \\ 0 & \dots & \dots & 0 & \frac{\delta}{2}N_p \end{pmatrix}. \quad (\text{A.2.3})$$

Concerning the specific case of $N_p = 3$, the central diagonal block reads

$$(\hat{H}_0) = \begin{pmatrix} 3U & -\sqrt{3}J & 0 & 0 \\ -\sqrt{3}J & U & -2J & 0 \\ 0 & -2J & U & -\sqrt{3}J \\ 0 & 0 & -\sqrt{3}J & 3U \end{pmatrix}. \quad (\text{A.2.4})$$

A.2.1 Measurement

A basis of solutions of the Schrödinger equation (2.2.5), where the Fourier coefficients $|\tilde{u}_{\nu,k}\rangle$ of $|u_{\nu}(t)\rangle$ are decomposed in the Fock basis, is given by

$$\left\{ |u_{\nu}(t)\rangle = \sum_{k=-\infty}^{+\infty} e^{ik\omega t} \sum_{n=0}^{N_p} F_{\nu,k,n} |n, N_p - n\rangle \mid \nu = 0, 1, \dots, N_p \right\}. \quad (\text{A.2.5})$$

The eigenstates $|f_\nu\rangle$ of the eigenvalue equation (2.2.8) are made of the coefficients F_{ν,k,n_1} such that

$$(|f_\nu\rangle) = \begin{pmatrix} \vdots \\ F_{\nu,k-1,N_p} \\ F_{\nu,k,0} \\ \vdots \\ F_{\nu,k,N_p} \\ F_{\nu,k+1,0} \\ \vdots \end{pmatrix}. \quad (\text{A.2.6})$$

Any state can be decomposed in that basis,

$$|\phi(t)\rangle = \sum_{\nu=0}^{N_p} c_\nu(t_0) e^{-i\epsilon_\nu(t-t_0)/\hbar} |u_\nu(t)\rangle \quad (\text{A.2.7})$$

with $c_\nu(t_0) = \langle u_\nu(t_0) | \phi(t_0) \rangle$. The probability to be in the state $|n'_1, n'_2\rangle$, knowing that the system is initially in the state $|\phi(t_0)\rangle = |n_1, n_2\rangle$, is given by

$$P_{n'_1}(t) = |\langle n'_1, n'_2 | \phi(t) \rangle|^2 \quad (\text{A.2.8})$$

$$= \left| \sum_{\nu=0}^{N_p} c_\nu(t_0) e^{-i\epsilon_\nu(t-t_0)/\hbar} B_{\nu,n'_1} \right|^2, \quad (\text{A.2.9})$$

where the different elements read

$$c_\nu(t_0) = \sum_{k=-\infty}^{\infty} e^{-ik\omega t_0} F_{\nu,k,n_1}^*, \quad (\text{A.2.10})$$

$$B_{\nu,n'_1} = \sum_{k=-\infty}^{\infty} e^{ik\omega t} F_{\nu,k,n'_1}. \quad (\text{A.2.11})$$

A.2.2 Average of the measurements

In the symmetric case, meaning that the Hamiltonian is invariant under the permutation of both sites, the temporal evolution can be dominated by two symmetrically related basis elements such that

$$|\phi(t)\rangle \sim e^{-i\epsilon_{\nu_+}(t-t_0)/\hbar} |u_{\nu_+}(t)\rangle + e^{-i\epsilon_{\nu_-}(t-t_0)/\hbar} |u_{\nu_-}(t)\rangle, \quad (\text{A.2.12})$$

where the symmetric and antisymmetric parts are roughly given by $|u_{\nu_\pm}(t)\rangle \sim 1/\sqrt{2}(|n_1, n_2\rangle \pm |n_2, n_1\rangle)$ with $\epsilon_{\nu_+} \sim \epsilon_{\nu_-}$. The purity is a time-independent indicator of the global dynamics defined as

$$p = M_{n_1} + M_{n_2}, \quad (\text{A.2.13})$$

with $n_1 + n_2 = N_p$ and

$$M_n = \frac{1}{2T} \sum_{\sigma=\pm} \int_0^T |\langle n, N_p - n | u_{\nu_\sigma}(t) \rangle|^2 dt. \quad (\text{A.2.14})$$

If the purity is close to 1, the dynamic is largely dominated by the states $|n_1, n_2\rangle$ and $|n_2, n_1\rangle$.

A.3 Two-site Bose-Hubbard Hamiltonian in the symmetry-adapted basis

The purpose of this appendix is to decompose the two-site Bose-Hubbard Hamiltonian,

$$\begin{aligned}\hat{H}(t) = & -J(\hat{a}_1^\dagger \hat{a}_2 + \hat{a}_2^\dagger \hat{a}_1) + \frac{U}{2}(\hat{a}_1^\dagger \hat{a}_1^\dagger \hat{a}_1 \hat{a}_1 + \hat{a}_2^\dagger \hat{a}_2^\dagger \hat{a}_2 \hat{a}_2) \\ & + \delta \cos(\omega t)(\hat{a}_1^\dagger \hat{a}_1 - \hat{a}_2^\dagger \hat{a}_2),\end{aligned}\tag{A.3.1}$$

into a symmetric and antisymmetric basis, i.e. a basis of the permutation operator \hat{P} , which is defined as $\hat{P}|n_1, n_2\rangle = |n_2, n_1\rangle$. This will lead to the Floquet matrix (2.3.4) related to the two-site Bose-Hubbard system. The following frame indicates the action of the different operators on some symmetric and antisymmetric states ($l = 1, 2$) with $n_1 + n_2 = N_p$.

$$\begin{aligned}& \bullet - J(\hat{a}_2^\dagger \hat{a}_1 + \hat{a}_1^\dagger \hat{a}_2)(|n_1, n_2\rangle \pm |n_2, n_1\rangle) \frac{1}{\sqrt{2}} \\ & = -J\sqrt{n_1(n_2 + 1)}(|n_1 - 1, n_2 + 1\rangle \pm |n_2 + 1, n_1 - 1\rangle) \frac{1}{\sqrt{2}} \\ & \quad - J\sqrt{n_2(n_1 + 1)}(|n_1 + 1, n_2 - 1\rangle \pm |n_2 - 1, n_1 + 1\rangle) \frac{1}{\sqrt{2}} \\ & \bullet - J(\hat{a}_2^\dagger \hat{a}_1 + \hat{a}_1^\dagger \hat{a}_2)|n, n\rangle \\ & = -J\sqrt{2n(n + 1)}(|n - 1, n + 1\rangle + |n + 1, n - 1\rangle) \frac{1}{\sqrt{2}}\end{aligned}$$

$$\begin{aligned}& \sum_{l=1,2} \frac{U}{2} \hat{a}_l^\dagger \hat{a}_l^\dagger \hat{a}_l \hat{a}_l (|n_1, n_2\rangle \pm |n_2, n_1\rangle) \frac{1}{\sqrt{2}} \\ & = \frac{U}{2} (n_1(n_1 - 1) + n_2(n_2 - 1)) (|n_1, n_2\rangle \pm |n_2, n_1\rangle) \frac{1}{\sqrt{2}}\end{aligned}$$

$$\begin{aligned}& \frac{\delta}{2} (\hat{a}_1^\dagger \hat{a}_1 - \hat{a}_2^\dagger \hat{a}_2) (|n_1, n_2\rangle \pm |n_2, n_1\rangle) \frac{1}{\sqrt{2}} \\ & = \frac{\delta}{2} (n_1 - n_2) (|n_1, n_2\rangle \mp |n_2, n_1\rangle) \frac{1}{\sqrt{2}}\end{aligned}$$

A.3.1 N_p odd

The chosen basis reads (with $n_2 = N_p - n_1$)

$$\left\{ \dots, \frac{1}{\sqrt{2}}(|n_1, n_2\rangle + |n_2, n_1\rangle), \dots, \frac{1}{\sqrt{2}}(|n_1, n_2\rangle - |n_2, n_1\rangle), \dots \mid n_1 = 0, 1, \dots, (N_p - 1)/2 \right\}. \quad (\text{A.3.2})$$

The particular case $N_p = 3$ gives rise to

$$(\hat{H}_0) = \left(\begin{array}{cc|cc} 3U & -\sqrt{3}J & & \\ -\sqrt{3}J & U - 2J & & \\ \hline & & 3U & -\sqrt{3}J \\ & & -\sqrt{3}J & U + 2J \end{array} \right), \quad (\text{A.3.3})$$

$$(\hat{H}_1) = \left(\begin{array}{cc|cc} & & \frac{-3\delta}{2} & 0 \\ & & 0 & \frac{-\delta}{2} \\ \hline \frac{-3\delta}{2} & 0 & & \\ 0 & \frac{-\delta}{2} & & \end{array} \right). \quad (\text{A.3.4})$$

By combining these blocks, the Floquet matrix will take the form (2.3.10).

A.3.2 N_p even

The chosen basis reads (with $n_2 = N_p - n_1$)

$$\left\{ \dots, \frac{1}{\sqrt{2}}(|n_1, n_2\rangle + |n_2, n_1\rangle), \dots, |N_p/2, N_p/2\rangle, \dots, \frac{1}{\sqrt{2}}(|n_1, n_2\rangle - |n_2, n_1\rangle), \dots \mid n_1 = 0, 1, \dots, N_p/2 - 1 \right\}. \quad (\text{A.3.5})$$

The particular case $N_p = 4$ gives rise to

$$(\hat{H}_0) = \left(\begin{array}{ccc|cc} 6U & -2J & 0 & & \\ -2J & 3U & -\sqrt{12}J & & \\ 0 & -\sqrt{12}J & 2U & & \\ \hline & & & 6U & -2J \\ & & & -2J & 3U \end{array} \right), \quad (\text{A.3.6})$$

$$(\hat{H}_1) = \left(\begin{array}{ccc|cc} & & & \frac{-4\delta}{2} & 0 \\ & & & 0 & \frac{-2\delta}{2} \\ & & & 0 & 0 \\ \hline \frac{-4\delta}{2} & 0 & 0 & & \\ 0 & \frac{-2\delta}{2} & 0 & & \end{array} \right). \quad (\text{A.3.7})$$

By combining these blocks, the Floquet matrix will take the form (2.3.10).

A.3.3 Measurement

In the framework of the symmetric and antisymmetric basis, the Schrödinger equation (2.2.5) can be written as

$$\left(\hat{H}(t) - i\hbar\partial_t \right) |u_\nu^\sigma(t)\rangle = \epsilon_\nu^\sigma |u_\nu^\sigma(t)\rangle, \quad (\text{A.3.8})$$

where $\sigma = \pm$. The symbol $+$ refers to the block F_S in the relation (2.3.10), i.e. the Floquet block where S is central. The symbol $-$ refers to the block F_A in the relation (2.3.10), i.e. the Floquet block where A is central. By abuse of language, we can call F_S the symmetric block and F_A the antisymmetric block.

A basis of solution of the Schrödinger equation (A.3.8), where the Fourier coefficients $|\tilde{u}_{\nu,k}^\sigma\rangle$ of $|u_\nu^\sigma(t)\rangle$ are decomposed in the symmetric and antisymmetric basis (A.3.2) or (A.3.5), is given by

$$\left\{ |u_\nu^\sigma(t)\rangle = \sum_{k=-\infty}^{+\infty} e^{ik\omega t} \sum_{n_1=0}^{D_k^\sigma-1} F_{\nu,k,n_1}^\sigma \frac{1}{\sqrt{2}} (|n_1, n_2\rangle + p_k^\sigma |n_2, n_1\rangle) \middle| \sigma = \pm; \nu = 1, 2, \dots, D^\sigma \right\}, \quad (\text{A.3.9})$$

where $D^+ = \dim S$ and $D^- = \dim A$ are the dimensions of the symmetric and antisymmetric blocks of \hat{H}_0 respectively (see the relation (2.1.9)). It means that $N = D^+ + D^- = N_p + 1$ with N the dimension of the Hilbert space. Moreover, we have

$$N_p \text{ odd: } D_k^\pm = D^+ = D^- = N/2, \quad (\text{A.3.10})$$

$$N_p \text{ even: } D^+ = (N+1)/2 \text{ and } D^- = (N-1)/2, \quad (\text{A.3.11})$$

$$D_k^\pm = \begin{cases} D^\pm & \text{if } k \% 2 = 0 \\ D^\mp & \text{if } k \% 2 \neq 0 \end{cases}. \quad (\text{A.3.12})$$

The values of p_k^\pm are given by $p_k^\pm = \pm(-1)^k$ for $n_1 \neq n_2$. The case $n_1 = n_2$ gives rise to $p_k^+ = \sqrt{2} - 1$.

Any state can be decomposed in that basis,

$$|\phi(t)\rangle = \sum_{\sigma=\pm} \sum_{\nu=1}^{D^\sigma} c_\nu^\sigma(t_0) e^{-i\epsilon_\nu^\sigma(t-t_0)/\hbar} |u_\nu^\sigma(t)\rangle, \quad (\text{A.3.13})$$

where $c_\nu^\sigma(t_0) = \langle u_\nu^\sigma(t_0) | \phi(t_0) \rangle$. The probability to be in the state $|n'_1, n'_2\rangle$, knowing that the system is initially in the state $|\phi(t_0)\rangle = |n_1, n_2\rangle$, is given by

$$P_{n'_1}(t) = |\langle n'_1, n'_2 | \phi(t) \rangle|^2 \quad (\text{A.3.14})$$

$$= \left| \sum_{\sigma=\pm} \sum_{\nu=1}^{D^\sigma} e^{-i\epsilon_\nu^\sigma(t-t_0)} c_\nu^\sigma(t_0) B_{\nu,n'_1}^\sigma \right|^2, \quad (\text{A.3.15})$$

with $B_{\nu,n'_1}^\sigma = \langle n'_1, n'_2 | u_\nu^\sigma(t) \rangle$.

The coefficients read

$$c_\nu^\sigma(t_0) = \begin{cases} \sum_{k=-\infty}^{+\infty} e^{-ik\omega t_0} \frac{F_{\nu,k,n_1}^{\sigma*}}{\sqrt{2}} & n_1 < n_2 \\ \sum_{k=-\infty}^{+\infty} e^{-ik\omega t_0} F_{\nu,k,n_1}^{\sigma*} (\delta_{\sigma,+} \delta_{k\%2,0} + \delta_{\sigma,-} \delta_{k\%2,|0}) & n_1 = n_2 \\ \sum_{k=-\infty}^{+\infty} e^{-ik\omega t_0} p_k^\sigma \frac{F_{\nu,k,n_1}^{\sigma*}}{\sqrt{2}} & n_1 > n_2, \end{cases} \quad (\text{A.3.16})$$

$$B_{\nu,n'_1}^\sigma = \begin{cases} \sum_{k'=-\infty}^{\infty} e^{ik'\omega t} \frac{F_{\nu,k',n'_1}^\sigma}{\sqrt{2}} & n'_1 < n'_2 \\ \sum_{k'=-\infty}^{\infty} e^{ik'\omega t} F_{\nu,k',n'_1}^\sigma (\delta_{\sigma,+} \delta_{k'\%2,0} + \delta_{\sigma,-} \delta_{k'\%2,|0}) & n'_1 = n'_2 \\ \sum_{k'=-\infty}^{\infty} e^{ik'\omega t} p_{k'}^\sigma \frac{F_{\nu,k',n'_2}^\sigma}{\sqrt{2}} & n'_1 > n'_2. \end{cases} \quad (\text{A.3.17})$$

Here we have $\delta_{k\%2,|0} = 1$ if $k\%2 \neq 0$ and $\delta_{k\%2,|0} = 0$ in the other cases.

A.3.4 Average of the measurements

In the symmetric case, meaning that the Hamiltonian is invariant under the permutation of both sites, the temporal evolution can be dominated by two symmetrically related basis elements such that

$$|\phi(t)\rangle \sim e^{-i\epsilon_\nu^+(t-t_0)/\hbar} |u_\nu^+(t)\rangle + e^{-i\epsilon_\nu^-(t-t_0)/\hbar} |u_\nu^-(t)\rangle, \quad (\text{A.3.18})$$

where $|u_\nu^\pm(t)\rangle \sim 1/\sqrt{2}(|n_1, n_2\rangle \pm |n_2, n_1\rangle)$ with $\epsilon_\nu^+ \sim \epsilon_\nu^-$. In this context, having a global vision of the dynamics can be achieved by computing the purity

$$p = M_{n_1} + M_{n_2}, \quad (\text{A.3.19})$$

based on the overlap

$$M_{n_1}^\sigma = \frac{1}{T} \int_0^T dt |\langle n_1, n_2 | u_\nu^\sigma(t) \rangle|^2 = \begin{cases} \frac{1}{2} \sum_{k=-\infty}^{+\infty} |F_{\nu,k,n_1}^\sigma|^2 & n_1 < n_2 \\ \sum_{k=-\infty}^{+\infty} |F_{\nu,k,n_1}^\sigma|^2 (\delta_{\sigma,+} \delta_{k\%2,0} + \delta_{\sigma,-} \delta_{k\%2,|0}) & n_1 = n_2 \\ \frac{1}{2} \sum_{k=-\infty}^{+\infty} |F_{\nu,k,n_2}^\sigma|^2 & n_1 > n_2. \end{cases} \quad (\text{A.3.20})$$

Here we have $M_{n_1} = (M_{n_1}^+ + M_{n_1}^-)/2$ and $n_1 + n_2 = N_p$. If the purity is close to 1, it means that the dynamics is largely dominated by the states $|n_1, n_2\rangle$ and $|n_2, n_1\rangle$.

Appendix B

Monodromy matrix

The monodromy matrix characterizes the stability of a fixed point by tracking the dynamics around it. Here $\mathcal{P} : z \mapsto z'$ denotes the mapping of a point $z = \begin{pmatrix} q \\ p \end{pmatrix}$ on a stroboscopic map or a Poincaré section to the next point z' . A fixed point of order r , denoted by z^* , obeys the relation

$$\mathcal{P}_r(z^*) = z^*, \quad (\text{B.0.1})$$

where $\mathcal{P}_r = \mathcal{P} \circ \dots \circ \mathcal{P}$ refers to r times the application of the mapping \mathcal{P} .

As the point $z = z^* + \delta z$ is assumed to be close to the fixed point, the map can be linearized around z^* ,

$$\mathcal{P}_r(z^* + \delta z) = z'(z) \quad (\text{B.0.2})$$

$$\simeq z^* + \left. \frac{\partial z'(z)}{\partial z} \right|_{z=z^*} \delta z \quad (\text{B.0.3})$$

$$= z^* + M(z^*)\delta z. \quad (\text{B.0.4})$$

Here $M(z^*)$ is the Jacobian matrix which links z and z' . In this context, this matrix is called the monodromy matrix or the tangent map.

The knowledge of this matrix gives precious information about the dynamics around the fixed point. In the two-dimensional map case, the elliptic fixed points, for which the motion in its vicinity is stable, are characterized by $|\text{Tr}(M)| < 2$ while the hyperbolic fixed points, for which the unstable motion in its vicinity is described by an exponential separation with respect to the fixed point, are characterized by $|\text{Tr}(M)| > 2$. For more details, see [65, 66].

Appendix C

Two-level approximation

The two-level model presented here has the purpose to describe the transitions between the states $|a\rangle$ and $|b\rangle$ by means of the coupling parameter V . It is important to point out that this simple system can still be suitable even for a Hilbert space dimension larger than two. For instance, it can be applied for the two-site Bose-Hubbard model as detailed in Sec. 2.1.2. In this context, V describes an effective coupling, which incorporates the direct transition between both states and the indirect transitions via the other states. The two-level Hamiltonian reads

$$(\hat{H}) = \begin{pmatrix} E_a & V \\ V & E_b \end{pmatrix}.$$

The eigenvalues read

$$E_{1,2} = \frac{E_b + E_a}{2} \mp \sqrt{\frac{(E_b - E_a)^2}{4} + V^2}.$$

In the case where $E_b > E_a$, the eigenvectors read

$$\begin{aligned} |1\rangle &= \cos \theta |a\rangle - \sin \theta |b\rangle \\ |2\rangle &= \sin \theta |a\rangle + \cos \theta |b\rangle, \end{aligned} \tag{C.0.1}$$

with

$$\tan(2\theta) = \frac{2V}{E_b - E_a}. \tag{C.0.2}$$

The states $|a\rangle$ and $|b\rangle$ can be expressed in terms of $|1\rangle$ and $|2\rangle$,

$$\begin{aligned} |a\rangle &= \cos \theta |1\rangle + \sin \theta |2\rangle, \\ |b\rangle &= -\sin \theta |1\rangle + \cos \theta |2\rangle. \end{aligned} \tag{C.0.3}$$

If $E_a = E_b$ and $V > 0$, the eigenvectors read

$$\begin{aligned} |1\rangle &= \frac{1}{\sqrt{2}}(|a\rangle - |b\rangle), \\ |2\rangle &= \frac{1}{\sqrt{2}}(|a\rangle + |b\rangle), \end{aligned} \tag{C.0.4}$$

which, respectively, correspond to the antisymmetric and the symmetric combination of the states $|a\rangle$ and $|b\rangle$. The system is assumed to be initially in the state $|a\rangle$,

$$|\phi(0)\rangle = |a\rangle = \frac{1}{\sqrt{2}}(|1\rangle + |2\rangle). \quad (\text{C.0.5})$$

The temporal evolution leads to periodic oscillations between both states,

$$|\phi(t)\rangle = \frac{1}{\sqrt{2}} (e^{-iE_1 t/\hbar}|1\rangle + e^{-iE_2 t/\hbar}|2\rangle) \quad (\text{C.0.6})$$

$$= \cos\left(\frac{\Delta E}{2\hbar}t\right) |a\rangle + i \sin\left(\frac{\Delta E}{2\hbar}t\right) |b\rangle, \quad (\text{C.0.7})$$

where $\Delta E = E_1 - E_2$.

In this framework, it is possible to define a frequency $\Omega = |\Delta E|/\hbar$, called the Rabi frequency, which determines the time to obtain a complete transfer of population from $|a\rangle$ to $|b\rangle$. The detection probabilities to obtain $|a\rangle$ and $|b\rangle$ read respectively

$$P_{|a\rangle}(t) = \cos^2\left(\frac{\Omega}{2}t\right), \quad (\text{C.0.8})$$

$$P_{|b\rangle}(t) = \sin^2\left(\frac{\Omega}{2}t\right). \quad (\text{C.0.9})$$

This simple model will be used as an approximation throughout this thesis. Let us imagine a gas of ultracold bosonic atoms, characterized by N_p particles, defined on two states which correspond to two spatially separated orbitals. These two orbitals can be modeled by the dynamics of $|a\rangle$ and $|b\rangle$ in certain circumstances explained in Sec. 2.1.2.

Appendix D

Matrix representation of the unperturbed three-site Bose-Hubbard Hamiltonian

The purpose of this appendix is to decompose the unperturbed three-site Bose-Hubbard Hamiltonian in the symmetry-adapted basis. This Hamiltonian reads

$$\begin{aligned}\hat{H} = & -\kappa \left(\hat{a}_0^\dagger \hat{a}_1 + \hat{a}_1^\dagger \hat{a}_0 \right) - J \left(\hat{a}_1^\dagger \hat{a}_2 + \hat{a}_2^\dagger \hat{a}_1 \right) - \kappa \left(\hat{a}_2^\dagger \hat{a}_0 + \hat{a}_0^\dagger \hat{a}_2 \right) \\ & + \frac{U}{2} \left(\gamma \hat{a}_0^\dagger \hat{a}_0^\dagger \hat{a}_0 \hat{a}_0 + \hat{a}_1^\dagger \hat{a}_1^\dagger \hat{a}_1 \hat{a}_1 + \hat{a}_2^\dagger \hat{a}_2^\dagger \hat{a}_2 \hat{a}_2 \right) + \xi \hat{a}_0^\dagger \hat{a}_0.\end{aligned}\quad (\text{D.0.1})$$

The symmetry-adapted basis is an eigenbasis of the permutation operator between site 1 and 2. It reads

$$\{ |n_0, n_1, n_2\rangle_+ \dots |n'_0, n'_1, n'_1\rangle \dots |n_0, n_1, n_2\rangle_- \dots \}, \quad (\text{D.0.2})$$

with

$$\begin{aligned}n_1 &= 0, 1, \dots, d & n'_1 &= 0, 1, \dots, D_{\text{ne}} - 1 \\ n_2 &= n_1 + 1, \dots, N_p - n_1 & n'_0 &= N_p - 2n'_1, \\ n_0 &= N_p - n_1 - n_2\end{aligned}\quad (\text{D.0.3})$$

$$d = \begin{cases} \frac{N_p - 1}{2} & N_p \text{ odd} \\ \frac{N_p}{2} - 1 & N_p \text{ even.} \end{cases} \quad (\text{D.0.4})$$

By definition, we have

$$|n_0, n_1, n_2\rangle_\pm \equiv \frac{1}{\sqrt{2}} (|n_0, n_1, n_2\rangle \pm |n_0, n_2, n_1\rangle). \quad (\text{D.0.5})$$

The dimension of the Hilbert space is given by [162]

$$D = \frac{(N_p + 2)(N_p + 1)}{2} = D^+ + D^-, \quad (\text{D.0.6})$$

with D^\pm the dimension of the symmetric and antisymmetric subspaces respectively. The following table displays the different dimensions related to the system.

$$\begin{array}{ll}
 N_p \text{ even :} & N_p \text{ odd :} \\
 D_{\text{ne}} = \frac{N_p + 2}{2} & D_{\text{ne}} = \frac{N_p + 1}{2} \\
 D_{\text{e}} = \frac{D - D_{\text{ne}}}{2} & D_{\text{e}} = \frac{D - D_{\text{ne}}}{2} \\
 = \frac{N_p^2}{4} + \frac{N_p}{2} & = \frac{N_p^2}{4} + \frac{N_p}{2} + \frac{1}{4} \\
 D^+ = D_{\text{e}} + D_{\text{ne}} & D^+ = D_{\text{e}} + D_{\text{ne}} \\
 = \frac{N_p^2}{4} + N_p + 1 & = \frac{N_p^2}{4} + N_p + \frac{3}{4} \\
 D^- = D_{\text{e}} & D^- = D_{\text{e}} \\
 = \frac{N_p^2}{4} + \frac{N_p}{2} & = \frac{N_p^2}{4} + \frac{N_p}{2} + \frac{1}{4}
 \end{array} \tag{D.0.7}$$

As the Hamiltonian (D.0.1) is unchanged under the permutation between site 1 and 2, its form is block diagonal in the basis (D.0.2) such that $(\hat{H}) = \text{diag}(S, A)$, with S and A the symmetric and antisymmetric block, respectively. For $N_p = 1$, it takes the form

$$S = \begin{array}{c} +\langle 0, 0, 1 | \\ \langle 1, 0, 0 | \end{array} \begin{array}{cc} |0, 0, 1\rangle_+ & |1, 0, 0\rangle \\ \left(\begin{array}{cc} -J & -\sqrt{2}\kappa \\ -\sqrt{2}\kappa & \xi \end{array} \right), & A = \begin{array}{c} |0, 0, 1\rangle_- \\ -\langle 0, 0, 1 | \end{array} \left(\begin{array}{c} +J \end{array} \right). \tag{D.0.8}$$

For $N_p = 2$, it takes the form

$$\begin{aligned}
 S &= \begin{array}{c} +\langle 1, 0, 1 | \\ +\langle 0, 0, 2 | \\ \langle 2, 0, 0 | \\ \langle 0, 1, 1 | \end{array} \begin{array}{cccc} |1, 0, 1\rangle_+ & |0, 0, 2\rangle_+ & |2, 0, 0\rangle & |0, 1, 1\rangle \\ \left(\begin{array}{cccc} \xi - J & -\sqrt{2}\kappa & -2\kappa & -\sqrt{2}\kappa \\ -\sqrt{2}\kappa & U & 0 & -2J \\ -2\kappa & 0 & \gamma U + 2\xi & 0 \\ -\sqrt{2}\kappa & -2J & 0 & 0 \end{array} \right), \\
 A &= \begin{array}{c} -\langle 1, 0, 1 | \\ -\langle 0, 0, 2 | \end{array} \begin{array}{cc} |1, 0, 1\rangle_- & |0, 0, 2\rangle_- \\ \left(\begin{array}{cc} \xi + J & -\sqrt{2}\kappa \\ -\sqrt{2}\kappa & U \end{array} \right).
 \end{aligned}$$

For $N_p = 3$, it takes the form

$$\begin{aligned}
 S = & \begin{array}{c} |2, 0, 1\rangle_+ \quad |1, 0, 2\rangle_+ \quad |0, 0, 3\rangle_+ \quad |0, 1, 2\rangle_+ \quad |3, 0, 0\rangle \quad |1, 1, 1\rangle \\ +\langle 2, 0, 1| \left(\begin{array}{cccccc} \gamma U + 2\xi - J & -2\kappa & 0 & 0 & -\sqrt{2 \times 3}\kappa & -\sqrt{2 \times 2}\kappa \\ -2\kappa & U + \xi & -\sqrt{3}\kappa & -\kappa & 0 & -\sqrt{2 \times 2}J \\ 0 & -\sqrt{3}\kappa & 3U & -\sqrt{3}J & 0 & 0 \\ 0 & -\kappa & -\sqrt{3}J & U - 2J & 0 & -\sqrt{2 \times 2}\kappa \\ -\sqrt{2 \times 3}\kappa & 0 & 0 & 0 & 3\gamma U + 3\xi & 0 \\ -\sqrt{2 \times 2}\kappa & -\sqrt{2 \times 2}J & 0 & -\sqrt{2 \times 2}\kappa & 0 & \varepsilon \end{array} \right) \\ +\langle 1, 0, 2| \\ +\langle 0, 0, 3| \\ +\langle 0, 1, 2| \\ +\langle 3, 0, 0| \\ +\langle 1, 1, 1| \end{array} \\
 A = & \begin{array}{c} |2, 0, 1\rangle_- \quad |1, 0, 2\rangle_- \quad |0, 0, 3\rangle_- \quad |0, 1, 2\rangle_- \\ -\langle 2, 0, 1| \left(\begin{array}{cccc} \gamma U + 2\xi + J & -2\kappa & 0 & 0 \\ -2\kappa & U + \xi & -\sqrt{3}\kappa & -\kappa \\ 0 & -\sqrt{3}\kappa & 3U & -\sqrt{3}J \\ 0 & -\kappa & -\sqrt{3}J & U + 2J \end{array} \right) \\ -\langle 1, 0, 2| \\ -\langle 0, 0, 3| \\ -\langle 0, 1, 2| \end{array}
 \end{aligned}$$

The general eigenbasis reads

$$\{|\chi_\nu^\sigma\rangle \mid \sigma = \pm; \nu = 1, 2, \dots, D^\sigma\}, \quad (\text{D.0.9})$$

with the decomposition in the symmetry-adapted basis ($n_0 = N_p - n_1 - n_2$),

$$|\chi_\nu^\sigma\rangle = \sum_{n_1=0}^d \sum_{n_2=n_1+1}^{N_p-n_1} F_{\nu, n_1, n_2}^\sigma \frac{1}{\sqrt{2}} (|n_0, n_1, n_2\rangle + \sigma |n_0, n_2, n_1\rangle) \quad (\text{D.0.10})$$

$$+ \delta_{\sigma,+} \sum_{n_1=0}^{D_{\text{ne}}-1} F_{\nu, n_1, n_1}^\sigma |n_0, n_1, n_1\rangle. \quad (\text{D.0.11})$$

Any state $|\phi(t_0)\rangle$ can be decomposed in that basis and its temporal evolution reads

$$|\phi(t)\rangle = \sum_{\sigma=\pm} \sum_{\nu=1}^{D^\sigma} c_\nu^\sigma(t_0) e^{-i\epsilon_\nu^\sigma(t-t_0)/\hbar} |\chi_\nu^\sigma\rangle, \quad (\text{D.0.12})$$

with $c_\nu^\sigma(t_0) = \langle \chi_\nu^\sigma | \phi(t_0) \rangle$ and $\hat{H}|\chi_\nu^\sigma\rangle = \epsilon_\nu^\sigma |\chi_\nu^\sigma\rangle$. This gives access to the transition probabilities,

$$P_{|n_0, n_1, n_2\rangle}(t) = |\langle n_0, n_1, n_2 | \phi(t) \rangle|^2. \quad (\text{D.0.13})$$

It can be interesting to have an indicator which captures time-independently the main features of the dynamics. That is why the purity is defined as

$$p = M_{0, N_p} + M_{N_p, 0}, \quad (\text{D.0.14})$$

with $M_{n_1, n_2} = M_{n_1, n_2}^+ + M_{n_1, n_2}^-$ and

$$M_{n_1, n_2}^\sigma = |\langle n_0, n_1, n_2 | \chi_\nu^\sigma \rangle|^2 \quad (\text{D.0.15})$$

$$= \begin{cases} \frac{1}{2} |F_{\nu, n_1, n_2}^\sigma|^2 & n_1 \neq n_2 \\ \delta_{\sigma,+} |F_{\nu, n_1, n_1}^\sigma|^2 & n_1 = n_2. \end{cases} \quad (\text{D.0.16})$$

If the purity is close to 1, it means that the dynamics is overwhelmingly dominated by the transitions between $|0, 0, N_p\rangle$ and $|0, N_p, 0\rangle$.

Bibliography

- [1] J. S. Bell, *Speakable and Unspeakable in Quantum Mechanics: Collected Papers on Quantum Philosophy*. Cambridge University Press, 1987.
- [2] A. Einstein, B. Podolsky, and N. Rosen, “Can quantum-mechanical description of physical reality be considered complete?,” *Phys. Rev.*, vol. 47, pp. 777–780, May 1935.
- [3] S. J. Freedman and J. F. Clauser, “Experimental test of local hidden-variable theories,” *Phys. Rev. Lett.*, vol. 28, no. 14, p. 938, 1972.
- [4] A. Aspect, P. Grangier, and G. Roger, “Experimental tests of realistic local theories via Bell’s theorem,” *Phys. Rev. Lett.*, vol. 47, pp. 460–463, Aug. 1981.
- [5] C. A. Kocher and E. D. Commins, “Polarization correlation of photons emitted in an atomic cascade,” *Phys. Rev. Lett.*, vol. 18, pp. 575–577, Apr. 1967.
- [6] J. S. Bell, “On the Einstein Podolsky Rosen paradox,” *Phys. Phys. Fiz.*, vol. 1, pp. 195–200, Nov. 1964.
- [7] B. Hensen, H. Bernien, A. E. Dréau, A. Reiserer, N. Kalb, M. S. Blok, J. Ruitenbergh, R. F. Vermeulen, R. N. Schouten, C. Abellán, *et al.*, “Loophole-free Bell inequality violation using electron spins separated by 1.3 kilometres,” *Nature*, vol. 526, no. 7575, pp. 682–686, 2015.
- [8] Y. Lin, D. R. Leibbrandt, D. Leibfried, and C.-w. Chou, “Quantum entanglement between an atom and a molecule,” *Nature*, vol. 581, no. 7808, pp. 273–277, 2020.
- [9] K. C. Lee, M. R. Sprague, B. J. Sussman, J. Nunn, N. K. Langford, X.-M. Jin, T. Champion, P. Michelberger, K. F. Reim, D. England, D. Jaksch, and I. A. Walmsley, “Entangling macroscopic diamonds at room temperature,” *Science*, vol. 334, no. 6060, pp. 1253–1256, 2011.
- [10] I. Afek, O. Ambar, and Y. Silberberg, “High-NOON states by mixing quantum and classical light,” *Science*, vol. 328, p. 879, 2010.
- [11] Y. Israel, S. Rosen, and Y. Silberberg, “Supersensitive Polarization Microscopy Using NOON States of Light,” *Phys. Rev. Lett.*, vol. 112, p. 103604, Mar. 2014.
- [12] J. Zhang, M. Um, D. Lv, J.-N. Zhang, L.-M. Duan, and K. Kim, “NOON states of nine quantized vibrations in two radial modes of a trapped ion,” *Phys. Rev. Lett.*, vol. 121, p. 160502, 2018.
- [13] M. H. Anderson, J. R. Ensher, M. R. Matthews, C. E. Wieman, and E. A. Cornell, “Observation of Bose-Einstein condensation in a dilute atomic vapor,” *Science*, vol. 269, no. 5221, pp. 198–201, 1995.
- [14] K. B. Davis, M. O. Mewes, M. R. Andrews, N. J. van Druten, D. S. Durfee, D. M. Kurn, and W. Ketterle, “Bose-Einstein condensation in a gas of sodium atoms,” *Phys. Rev. Lett.*, vol. 75, pp. 3969–3973, Nov. 1995.
- [15] A. Einstein, “Quantentheorie des einatomigen idealen gases,” *Sitzungsberichte der Preussischen Akademie der Wissenschaften, Physikalisch-mathematische Klasse*, vol. 22, pp. 261–267, 1924.
- [16] A. Einstein, “Quantentheorie des einatomigen idealen gases: Zweite abhandlung,” *Sitzungsberichte der Preussische Akademie der Wissenschaften*, vol. 1, p. 3, 1925.
- [17] S. N. Bose, “Plancks gesetz und lichtquantenhypothese,” *Z. Phys.*, vol. 26, pp. 178–181, 1924.

- [18] O. Morsch and M. Oberthaler, “Dynamics of Bose-Einstein condensates in optical lattices,” *Rev. Mod. Phys.*, vol. 78, pp. 179–215, Feb. 2006.
- [19] I. Bloch, J. Dalibard, and W. Zwerger, “Many-body physics with ultracold gases,” *Rev. Mod. Phys.*, vol. 80, pp. 885–964, Jul. 2008.
- [20] C. J. Pethick and H. Smith, *Bose-Einstein Condensation in Dilute Gases*. Cambridge University Press, 2e ed., 2008.
- [21] M. Albiez, R. Gati, J. Fölling, S. Hunsmann, M. Cristiani, and M. K. Oberthaler, “Direct observation of tunneling and nonlinear self-trapping in a single bosonic Josephson junction,” *Phys. Rev. Lett.*, vol. 95, p. 010402, 2005.
- [22] L. Santos, M. A. Baranov, J. I. Cirac, H.-U. Everts, H. Fehrmann, and M. Lewenstein, “Atomic quantum gases in kagomé lattices,” *Phys. Rev. Lett.*, vol. 93, p. 030601, Jul. 2004.
- [23] B. Damski, H. Fehrmann, H.-U. Everts, M. Baranov, L. Santos, and M. Lewenstein, “Quantum gases in trimerized kagomé lattices,” *Phys. Rev. A*, vol. 72, p. 053612, Nov. 2005.
- [24] S. Fölling, S. Trotzky, P. Cheinet, M. Feld, R. Saers, A. Widera, T. Müller, and I. Bloch, “Direct observation of second-order atom tunnelling,” *Nature*, vol. 448, no. 7157, pp. 1029–1032, 2007.
- [25] J. Hubbard, “Electron correlations in narrow energy bands,” *Proc. R. Soc. A*, vol. 276, no. 1365, pp. 238–257, 1963.
- [26] H. A. Gersch and G. C. Knollman, “Quantum cell model for bosons,” *Phys. Rev.*, vol. 129, pp. 959–967, Jan. 1963.
- [27] M. P. A. Fisher, P. B. Weichman, G. Grinstein, and D. S. Fisher, “Boson localization and the superfluid-insulator transition,” *Phys. Rev. B*, vol. 40, pp. 546–570, Jul. 1989.
- [28] D. Jaksch, C. Bruder, J. I. Cirac, C. W. Gardiner, and P. Zoller, “Cold bosonic atoms in optical lattices,” *Phys. Rev. Lett.*, vol. 81, pp. 3108–3111, Oct. 1998.
- [29] M. Greiner, O. Mandel, T. Esslinger, T. W. Hänsch, and I. Bloch, “Quantum phase transition from a superfluid to a Mott insulator in a gas of ultracold atoms,” *Nature*, vol. 415, no. 6867, pp. 39–44, 2002.
- [30] J. P. Dowling, “Quantum optical metrology – the lowdown on high-NOON states,” *Contemp. Phys.*, vol. 49, no. 2, pp. 125–143, 2008.
- [31] L. Pezzè, A. Smerzi, M. K. Oberthaler, R. Schmied, and P. Treutlein, “Quantum metrology with nonclassical states of atomic ensembles,” *Rev. Mod. Phys.*, vol. 90, p. 035005, Sep. 2018.
- [32] J. A. Jones, S. D. Karlen, J. Fitzsimons, A. Ardavan, S. C. Benjamin, G. A. D. Briggs, and J. J. L. Morton, “Magnetic field sensing beyond the standard quantum limit using 10-spin NOON states,” *Science*, vol. 324, pp. 1166–1168, May 2009.
- [33] C. Song, K. Xu, W. Liu, C. p. Yang, S.-B. Zheng, H. Deng, Q. Xie, K. Huang, Q. Guo, L. Zhang, P. Zhang, D. Xu, D. Zheng, X. Zhu, H. Wang, Y.-A. Chen, C.-Y. Lu, S. Han, and J.-W. Pan, “10-qubit entanglement and parallel logic operations with a superconducting circuit,” *Phys. Rev. Lett.*, vol. 119, p. 180511, 2018.
- [34] J. I. Cirac, M. Lewenstein, K. Mølmer, and P. Zoller, “Quantum superposition states of Bose-Einstein condensates,” *Phys. Rev. A*, vol. 57, p. 1208, 1998.
- [35] J. M. Gerton, D. Strekalov, I. Prodan, and R. G. Hulet, “Direct observation of growth and collapse of a Bose-Einstein condensate with attractive interactions,” *Nature*, vol. 408, no. 6813, pp. 692–695, 2000.
- [36] E. A. Donley, N. R. Claussen, S. L. Cornish, J. L. Roberts, E. A. Cornell, and C. E. Wieman, “Dynamics of collapsing and exploding Bose-Einstein condensates,” *Nature*, vol. 412, no. 6844, pp. 295–299, 2001.
- [37] R. J. Dodd, M. Edwards, C. J. Williams, C. W. Clark, M. J. Holland, P. A. Ruprecht, and K. Burnett, “Role of attractive interactions on Bose-Einstein condensation,” *Phys. Rev. A*, vol. 54, pp. 661–664, Jul. 1996.

- [38] D. Gordon and C. M. Savage, “Creating macroscopic quantum superpositions with Bose-Einstein condensates,” *Phys. Rev. A*, vol. 59, p. 4623, 1999.
- [39] A. Sørensen, L.-M. Duan, J. I. Cirac, and P. Zoller, “Many-particle entanglement with Bose-Einstein condensates,” *Nature*, vol. 409, no. 6816, pp. 63–66, 2001.
- [40] J. A. Dunningham and K. Burnett, “Proposals for creating Schrödinger cat states in Bose-Einstein condensates,” *J. Mod. Opt.*, vol. 48, p. 1837, 2001.
- [41] A. Micheli, D. Jaksch, J. I. Cirac, and P. Zoller, “Many-particle entanglement in two-component Bose-Einstein condensates,” *Phys. Rev. A*, vol. 67, p. 013607, 2003.
- [42] K. W. Mahmud, H. Perry, and W. P. Reinhardt, “Phase engineering of controlled entangled number states in a single component Bose-Einstein condensate in a double well,” *J. Phys. B: At. Mol. Opt. Phys.*, vol. 36, p. L265, 2003.
- [43] K. W. Mahmud, H. Perry, and W. P. Reinhardt, “Quantum phase-space picture of Bose-Einstein condensates in a double well,” *Phys. Rev. A*, vol. 71, p. 023615, Feb. 2005.
- [44] T. Zibold, E. Nicklas, C. Gross, and M. K. Oberthaler, “Classical bifurcation at the transition from Rabi to Josephson dynamics,” *Phys. Rev. Lett.*, vol. 105, no. 20, p. 204101, 2010.
- [45] J. Ruostekoski, M. J. Collett, R. Graham, and D. F. Walls, “Macroscopic superpositions of Bose-Einstein condensates,” *Phys. Rev. A*, vol. 57, p. 511, 1998.
- [46] I. Mazets, G. Kurizki, M. Oberthaler, and J. Schmiedmayer, “Creation of macroscopic quantum superposition states by a measurement,” *EPL*, vol. 83, no. 6, p. 60004, 2008.
- [47] H. Cable, F. Laloë, and W. J. Mullin, “Formation of NOON states from Fock-state Bose-Einstein condensates,” *Phys. Rev. A*, vol. 83, p. 053626, 2011.
- [48] A. A. Bychek, D. N. Maksimov, and A. R. Kolovsky, “NOON state of Bose atoms in the double-well potential via an excited-state quantum phase transition,” *Phys. Rev. A*, vol. 97, p. 063624, Jun. 2018.
- [49] N. Teichmann and C. Weiss, “Coherently controlled entanglement generation in a binary Bose-Einstein condensate,” *EPL*, vol. 78, p. 10009, 2007.
- [50] C. Weiss and Y. Castin, “Creation and detection of a mesoscopic gas in a nonlocal quantum superposition,” *Phys. Rev. Lett.*, vol. 102, p. 010403, 2009.
- [51] A. I. Streltsov, O. E. Alon, and L. S. Cederbaum, “Scattering of an attractive Bose-Einstein condensate from a barrier: Formation of quantum superposition states,” *Phys. Rev. A*, vol. 80, p. 043616, 2009.
- [52] G. Vanhaele and P. Schlagheck, “NOON states with ultracold bosonic atoms via resonance- and chaos-assisted tunneling,” *Phys. Rev. A*, vol. 103, p. 013315, Jan. 2021.
- [53] A. Smerzi, S. Fantoni, S. Giovanazzi, and S. R. Shenoy, “Quantum coherent atomic tunneling between two trapped Bose-Einstein condensates,” *Phys. Rev. Lett.*, vol. 79, p. 4950, Dec. 1997.
- [54] G. J. Milburn, J. Corney, E. M. Wright, and D. F. Walls, “Quantum dynamics of an atomic Bose-Einstein condensate in a double-well potential,” *Phys. Rev. A*, vol. 55, p. 4318, 1997.
- [55] M. J. Steel and M. J. Collett, “Quantum state of two trapped Bose-Einstein condensates with a Josephson coupling,” *Phys. Rev. A*, vol. 57, no. 4, p. 2920, 1998.
- [56] R. W. Spekkens and J. E. Sipe, “Spatial fragmentation of a Bose-Einstein condensate in a double-well potential,” *Phys. Rev. A*, vol. 59, no. 5, p. 3868, 1999.
- [57] E. A. Ostrovskaya, Y. S. Kivshar, M. Lisak, B. Hall, F. Cattani, and D. Anderson, “Coupled-mode theory for Bose-Einstein condensates,” *Phys. Rev. A*, vol. 61, p. 031601, Feb. 2000.
- [58] A. J. Leggett, “Bose-Einstein condensation in the alkali gases: Some fundamental concepts,” *Rev. Mod. Phys.*, vol. 73, pp. 307–356, 2001.
- [59] D. Ananikian and T. Bergeman, “Gross-Pitaevskii equation for Bose particles in a double-well potential: Two-mode models and beyond,” *Phys. Rev. A*, vol. 73, p. 013604, 2006.
- [60] L. Fu and J. Liu, “Quantum entanglement manifestation of transition to nonlinear self-trapping for Bose-Einstein condensates in a symmetric double well,” *Phys. Rev. A*, vol. 74, no. 6, p. 063614, 2006.

- [61] B. Juliá-Díaz, D. Dagnino, M. Lewenstein, J. Martorell, and A. Polls, “Macroscopic self-trapping in Bose-Einstein condensates: Analysis of a dynamical quantum phase transition,” *Phys. Rev. A*, vol. 81, no. 2, p. 023615, 2010.
- [62] A. N. Salgueiro, A. F. R. de Toledo Piza, G. B. Lemos, R. Drumond, M. C. Nemes, and M. Weidemüller, “Quantum dynamics of bosons in a double-well potential: Josephson oscillations, self-trapping and ultralong tunneling times,” *Eur. Phys. J. D*, vol. 44, no. 3, pp. 537–540, 2007.
- [63] G. Watanabe, “Efficient creation of maximally entangled states by modulation of tunneling rates,” *Phys. Rev. A*, vol. 81, no. 2, p. 021604, 2010.
- [64] G. Watanabe and H. Mäkelä, “Floquet analysis of the modulated two-mode Bose-Hubbard model,” *Phys. Rev. A*, vol. 85, no. 5, p. 053624, 2012.
- [65] M. Tabor, *Chaos and integrability in nonlinear dynamics : An introduction*. Wiley New York, 1989.
- [66] S. Wimberger, *Nonlinear dynamics and quantum chaos. An introduction*. Springer, 2014.
- [67] O. Brodier, P. Schlagheck, and D. Ullmo, “Resonance-assisted tunneling in near-integrable systems,” *Phys. Rev. Lett.*, vol. 87, p. 064101, 2001.
- [68] O. Brodier, P. Schlagheck, and D. Ullmo, “Resonance-assisted tunneling,” *Ann. Phys.*, vol. 300, p. 88, 2002.
- [69] S. Keshavamurthy, “On dynamical tunneling and classical resonances,” *J. Chem. Phys.*, vol. 122, no. 11, p. 114109, 2005.
- [70] J. Kullig and J. Wiersig, “ Q spoiling in deformed optical microdisks due to resonance-assisted tunneling,” *Phys. Rev. E*, vol. 94, p. 022202, Aug. 2016.
- [71] F. Fritzsche, R. Ketzmerick, and A. Bäcker, “Resonance-assisted tunneling in deformed optical microdisks with a mixed phase space,” *Phys. Rev. E*, vol. 100, p. 042219, Oct. 2019.
- [72] P. Schlagheck, A. Mouchet, and D. Ullmo, “Resonance-assisted tunneling in mixed regular-chaotic systems,” in *Dynamical Tunneling: Theory and Experiment* (S. Keshavamurthy and P. Schlagheck, eds.), Boca Raton: Taylor & Francis CRC, 2011.
- [73] W. A. Lin and L. E. Ballentine, “Quantum tunneling and chaos in a driven anharmonic oscillator,” *Phys. Rev. Lett.*, vol. 65, p. 2927, 1990.
- [74] O. Bohigas, D. Boosé, R. Eydio de Carvalho, and V. Marvulle, “Quantum tunneling and chaotic dynamics,” *Nucl. Phys. A*, vol. 560, p. 197, 1993.
- [75] O. Bohigas, S. Tomsovic, and D. Ullmo, “Manifestation of classical phase space structures in quantum mechanics,” *Phys. Rep.*, vol. 223, p. 43, 1993.
- [76] S. Tomsovic and D. Ullmo, “Chaos-assisted tunneling,” *Phys. Rev. E*, vol. 50, p. 145, 1994.
- [77] F. Leyvraz and D. Ullmo, “The level splitting distribution in chaos-assisted tunneling,” *J. Phys. A*, vol. 29, p. 2529, 1996.
- [78] C. Eltschka and P. Schlagheck, “Resonance- and chaos-assisted tunneling in mixed regular-chaotic systems,” *Phys. Rev. Lett.*, vol. 94, p. 014101, Jan. 2005.
- [79] P. Schlagheck, C. Eltschka, and D. Ullmo, “Resonance- and chaos-assisted tunneling,” in *Progress in Ultrafast Intense Laser Science I* (K. Yamanouchi, S. L. Chin, P. Agostini, and G. Ferrante, eds.), (Berlin), pp. 107–131, Springer, 2006.
- [80] A. Bäcker, R. Ketzmerick, S. Löck, J. Wiersig, and M. Hentschel, “Quality factors and dynamical tunneling in annular microcavities,” *Phys. Rev. A*, vol. 79, no. 6, p. 063804, 2009.
- [81] S. Löck, A. Bäcker, R. Ketzmerick, and P. Schlagheck, “Regular-to-chaotic tunneling rates: From the quantum to the semiclassical regime,” *Phys. Rev. Lett.*, vol. 104, p. 114101, 2010.
- [82] N. Mertig, J. Kullig, C. Löbner, A. Bäcker, and R. Ketzmerick, “Perturbation-free prediction of resonance-assisted tunneling in mixed regular-chaotic systems,” *Phys. Rev. E*, vol. 94, p. 062220, Dec. 2016.
- [83] F. Fritzsche, A. Bäcker, R. Ketzmerick, and N. Mertig, “Complex-path prediction of resonance-assisted tunneling in mixed systems,” *Phys. Rev. E*, vol. 95, p. 020202, Feb. 2017.

- [84] A. Mouchet, C. Eltschka, and P. Schlagheck, “Influence of classical resonances on chaotic tunnelling,” *Phys. Rev. E*, vol. 74, p. 026211, Aug. 2006.
- [85] M. Richter, S. Lange, A. Bäcker, and R. Ketzmerick, “Visualization and comparison of classical structures and quantum states of four-dimensional maps,” *Phys. Rev. E*, vol. 89, p. 022902, Feb. 2014.
- [86] S. Lange, M. Richter, F. Onken, A. Bäcker, and R. Ketzmerick, “Global structure of regular tori in a generic 4D symplectic map,” *Chaos*, vol. 24, no. 2, p. 024409, 2014.
- [87] A. J. Lichtenberg and M. A. Lieberman, *Regular and chaotic dynamics*, vol. 38. Springer Science & Business Media, 2013.
- [88] S. Keshavamurthy, “Resonance-assisted tunneling in three degrees of freedom without discrete symmetry,” *Phys. Rev. E*, vol. 72, p. 045203, Oct. 2005.
- [89] C. Froeschlé, E. Lega, and R. Gonczi, “Fast lyapunov indicators. application to asteroidal motion,” *Celest. Mech. and Dyn. Astron.*, vol. 67, no. 1, pp. 41–62, 1997.
- [90] C. Froeschlé, M. Guzzo, and E. Lega, “Graphical evolution of the arnold web: from order to chaos,” *Science*, vol. 289, no. 5487, pp. 2108–2110, 2000.
- [91] S. Karmakar and S. Keshavamurthy, “Relevance of the resonance junctions on the arnold web to dynamical tunneling and eigenstate delocalization,” *J. Phys. Chem. A*, vol. 122, no. 43, pp. 8636–8649, 2018.
- [92] S. Karmakar and S. Keshavamurthy, “Intramolecular vibrational energy redistribution and the quantum ergodicity transition: a phase space perspective,” *Phys. Chem. Chem. Phys.*, vol. 22, no. 20, pp. 11139–11173, 2020.
- [93] S. Karmakar, P. K. Yadav, and S. Keshavamurthy, “Stable chaos and delayed onset of statisticality in unimolecular dissociation reactions,” *Commun. Chem.*, vol. 3, no. 1, pp. 1–11, 2020.
- [94] S. Karmakar and S. Keshavamurthy, “Arnold web and dynamical tunneling in a four-site Bose-Hubbard model,” *Physica D*, vol. 427, p. 133006, 2021.
- [95] M. Firmbach, F. Fritzsche, R. Ketzmerick, and A. Bäcker, “Resonance-assisted tunneling in four-dimensional normal-form Hamiltonians,” *Phys. Rev. E*, vol. 99, no. 4, p. 042213, 2019.
- [96] F. Yao, Y.-M. Du, H. Xing, and L. Fu, “Two-parameter estimation with three-mode NOON state in a symmetric three-well,” *arXiv:2107.02459 [quant-ph]*, Jul. 2021. arXiv: 2107.02459.
- [97] A. Einstein, “Über einen die erzeugung und verwandlung des lichtes betreffenden heuristischen gesichtspunkt,” *Ann. phys.*, vol. 4, pp. 132–148, 1905.
- [98] L. de Broglie, *Recherche sur la théorie des quanta*. PhD thesis, Paris, 1924.
- [99] C. Davisson and L. H. Germer, “The scattering of electrons by a single crystal of nickel,” *Nature*, vol. 119, no. 2998, pp. 558–560, 1927.
- [100] C. J. Davisson and L. H. Germer, “Reflection of electrons by a crystal of nickel,” *Proc. Natl. Acad. Sci. U.S.A.*, vol. 14, no. 4, pp. 317–322, 1928.
- [101] E. Schrödinger, “An undulatory theory of the mechanics of atoms and molecules,” *Phys. Rev.*, vol. 28, pp. 1049–1070, Dec. 1926.
- [102] W. Ketterle, “Nobel lecture: When atoms behave as waves: Bose-Einstein condensation and the atom laser,” *Rev. Mod. Phys.*, vol. 74, pp. 1131–1151, Nov. 2002.
- [103] C. C. Bradley, C. A. Sackett, J. J. Tollett, and R. G. Hulet, “Evidence of Bose-Einstein condensation in an atomic gas with attractive interactions,” *Phys. Rev. Lett.*, vol. 75, pp. 1687–1690, Aug. 1995.
- [104] D. G. Fried, T. C. Killian, L. Willmann, D. Landhuis, S. C. Moss, D. Kleppner, and T. J. Greytak, “Bose-Einstein condensation of atomic hydrogen,” *Phys. Rev. Lett.*, vol. 81, pp. 3811–3814, Nov. 1998.
- [105] A. Robert, O. Sirjean, A. Browaeys, J. Poupard, S. Nowak, D. Boiron, C. I. Westbrook, and A. Aspect, “A Bose-Einstein condensate of metastable atoms,” *Science*, vol. 292, no. 5516, pp. 461–464, 2001.

- [106] G. Modugno, G. Ferrari, G. Roati, R. J. Brecha, A. Simoni, and M. Inguscio, “Bose-Einstein condensation of potassium atoms by sympathetic cooling,” *Science*, vol. 294, no. 5545, pp. 1320–1322, 2001.
- [107] L. Pitaevskii and S. Stringari, *Bose-Einstein condensation and superfluidity*, vol. 164. Oxford University Press, 2016.
- [108] M. Greiner, C. A. Regal, and D. S. Jin, “Emergence of a molecular Bose-Einstein condensate from a Fermi gas,” *Nature*, vol. 426, no. 6966, pp. 537–540, 2003.
- [109] S. Jochim, M. Bartenstein, A. Altmeyer, G. Hendl, S. Riedl, C. Chin, J. H. Denschlag, and R. Grimm, “Bose-Einstein condensation of molecules,” *Science*, vol. 302, no. 5653, pp. 2101–2103, 2003.
- [110] M. W. Zwierlein, C. A. Stan, C. H. Schunck, S. M. F. Raupach, S. Gupta, Z. Hadzibabic, and W. Ketterle, “Observation of Bose-Einstein condensation of molecules,” *Phys. Rev. Lett.*, vol. 91, p. 250401, Dec. 2003.
- [111] A. G. Truscott, K. E. Strecker, W. I. McAlexander, G. B. Partridge, and R. G. Hulet, “Observation of Fermi pressure in a gas of trapped atoms,” *Science*, vol. 291, no. 5513, pp. 2570–2572, 2001.
- [112] J. R. Anglin and W. Ketterle, “Bose-Einstein condensation of atomic gases,” *Nature*, vol. 416, no. 6877, pp. 211–218, 2002.
- [113] B. DeMarco and D. S. Jin, “Onset of Fermi degeneracy in a trapped atomic gas,” *Science*, vol. 285, no. 5434, pp. 1703–1706, 1999.
- [114] B. DeMarco, S. B. Papp, and D. S. Jin, “Pauli blocking of collisions in a quantum degenerate atomic Fermi gas,” *Phys. Rev. Lett.*, vol. 86, pp. 5409–5412, Jun. 2001.
- [115] F. Schreck, G. Ferrari, K. L. Corwin, J. Cubizolles, L. Khaykovich, M.-O. Mewes, and C. Salomon, “Sympathetic cooling of bosonic and fermionic lithium gases towards quantum degeneracy,” *Phys. Rev. A*, vol. 64, p. 011402, Jun. 2001.
- [116] E. A. Cornell and C. E. Wieman, “Nobel lecture: Bose-Einstein condensation in a dilute gas, the first 70 years and some recent experiments,” *Rev. Mod. Phys.*, vol. 74, pp. 875–893, Aug. 2002.
- [117] O. Penrose and L. Onsager, “Bose-Einstein condensation and liquid helium,” *Phys. Rev.*, vol. 104, no. 3, p. 576, 1956.
- [118] M. Lohse, C. Schweizer, O. Zilberberg, M. Aidelsburger, and I. Bloch, “A Thouless quantum pump with ultracold bosonic atoms in an optical superlattice,” *Nat. Phys.*, vol. 12, no. 4, pp. 350–354, 2016.
- [119] C. J. Foot *et al.*, *Atomic physics*, vol. 7. Oxford University Press, 2005.
- [120] W. Niedenzu, *Microscopic description and simulation of ultracold atoms in optical resonators*. PhD thesis, University of Innsbruck, 2012.
- [121] W. Zwerger, “Mott Hubbard transition of cold atoms in optical lattices,” *J. Opt. B: Quantum and Semiclass. Opt.*, vol. 5, pp. S9–S16, Apr. 2003.
- [122] I. Bloch, “Ultracold quantum gases in optical lattices,” *Nat. Phys.*, vol. 1, no. 1, pp. 23–30, 2005.
- [123] A. Garg, “Tunnel splittings for one-dimensional potential wells revisited,” *Am. J. of Phys.*, vol. 68, no. 5, pp. 430–437, 2000.
- [124] A. Mouchet, *Effet tunnel chaotique - Méthode différentielle*. Habilitation à diriger des recherches, Université François Rabelais - Tours, Dec. 2006.
- [125] E. Michon, C. Cabrera-Gutiérrez, A. Fortun, M. Berger, M. Arnal, V. Brunaud, J. Billy, C. Petitjean, P. Schlagheck, and D. Guéry-Odelin, “Phase transition kinetics for a Bose-Einstein condensate in a periodically driven band system,” *New J. Phys.*, vol. 20, no. 5, p. 053035, 2018.
- [126] M. A. García-March, D. R. Dounas-Frazer, and L. D. Carr, “Macroscopic superposition of ultracold atoms with orbital degrees of freedom,” *Phys. Rev. A*, vol. 83, p. 043612, Apr. 2011.

- [127] M. A. Garcia-March, D. R. Dounas-Frazer, and L. D. Carr, “Macroscopic superposition states of ultracold bosons in a double-well potential,” *Front. Phys.*, vol. 7, no. 1, pp. 131–145, 2012.
- [128] G. Vanhaele, *Chaos quantique et classique dans une chaîne d’oscillateurs non linéaires*. Master thesis, Université de Liège, 2016.
- [129] A. P. Itin and P. Schmelcher, “Semiclassical spectrum of small Bose-Hubbard chains: A normal-form approach,” *Phys. Rev. A*, vol. 84, p. 063609, Dec. 2011.
- [130] É. Tisserond, *Dynamique, régulière et chaotique, de condensats de Bose-Einstein dans des réseaux optiques finis*. Internship report, Université Paris-Sud XI, 2012–2013.
- [131] A. Eckardt, C. Weiss, and M. Holthaus, “Superfluid-insulator transition in a periodically driven optical lattice,” *Phys. Rev. Lett.*, vol. 95, p. 260404, Dec. 2005.
- [132] B. J. Dalton and S. Ghanbari, “Two mode theory of Bose-Einstein condensates: interferometry and the Josephson model,” *J. Mod. Opt.*, vol. 59, no. 4, pp. 287–353, 2012.
- [133] H. K. Andersen, *Bose-Einstein condensates in optical lattices*. PhD thesis, Department of Physics and Astronomy University of Aarhus, 2008.
- [134] C. E. Creffield and T. S. Monteiro, “Tuning the Mott transition in a Bose-Einstein condensate by multiple photon absorption,” *Phys. Rev. Lett.*, vol. 96, p. 210403, Jun. 2006.
- [135] H. Lignier, C. Sias, D. Ciampini, Y. Singh, A. Zenesini, O. Morsch, and E. Arimondo, “Dynamical control of matter-wave tunneling in periodic potentials,” *Phys. Rev. Lett.*, vol. 99, p. 220403, Nov. 2007.
- [136] C. Sias, H. Lignier, Y. P. Singh, A. Zenesini, D. Ciampini, O. Morsch, and E. Arimondo, “Observation of photon-assisted tunneling in optical lattices,” *Phys. Rev. Lett.*, vol. 100, p. 040404, Feb. 2008.
- [137] G. Floquet, “Sur les équations différentielles linéaires à coefficients périodiques,” *Ann. Sci. de l’Ecole Norm. Supérieure*, vol. 2, no. 12, pp. 47–88, 1883.
- [138] J. H. Shirley, “Solution of the Schrödinger Equation with a Hamiltonian Periodic in Time,” *Phys. Rev.*, vol. 138, pp. B979–B987, May 1965.
- [139] H. Sambe, “Steady states and quasienergies of a quantum-mechanical system in an oscillating field,” *Phys. Rev. A*, vol. 7, pp. 2203–2213, Jun. 1973.
- [140] J. Gong, L. Morales-Molina, and P. Hänggi, “Many-body coherent destruction of tunneling,” *Phys. Rev. Lett.*, vol. 103, p. 133002, Sep. 2009.
- [141] D. H. Dunlap and V. M. Kenkre, “Dynamic localization of a charged particle moving under the influence of an electric field,” *Phys. Rev. B*, vol. 34, pp. 3625–3633, Sep. 1986.
- [142] F. Großmann, P. Jung, T. Dittrich, and P. Hänggi, “Tunneling in a periodically driven bistable system,” *Z. Phys. B*, vol. 84, no. 2, pp. 315–325, 1991.
- [143] A. Rapp, X. Deng, and L. Santos, “Ultracold lattice gases with periodically modulated interactions,” *Phys. Rev. Lett.*, vol. 109, p. 203005, Nov. 2012.
- [144] F. Meinert, M. J. Mark, K. Lauber, A. J. Daley, and H.-C. Nägerl, “Floquet engineering of correlated tunneling in the Bose-Hubbard model with ultracold atoms,” *Phys. Rev. Lett.*, vol. 116, p. 205301, May 2016.
- [145] I. Zapata, F. Sols, and A. J. Leggett, “Josephson effect between trapped Bose-Einstein condensates,” *Phys. Rev. A*, vol. 57, pp. R28–R31, Jan. 1998.
- [146] S. Levy, E. Lahoud, I. Shomroni, and J. Steinhauer, “The ac and dc Josephson effects in a Bose-Einstein condensate,” *Nature*, vol. 449, no. 7162, pp. 579–583, 2007.
- [147] T. Anker, M. Albiez, R. Gati, S. Hunsmann, B. Eiermann, A. Trombettoni, and M. K. Oberthaler, “Nonlinear self-trapping of matter waves in periodic potentials,” *Phys. Rev. Lett.*, vol. 94, p. 020403, Jan. 2005.
- [148] K. Husimi, “Some formal properties of the density matrix,” *J. Phys. Soc. Jpn.*, vol. 22, no. 4, pp. 264–314, 1940.

- [149] V. Maslov, M. Fedoriuk, M. Fedoriuk, J. Niederle, and J. Tolar, *Semi-Classical Approximation in Quantum Mechanics*. Mathematical Physics and Applied Mathematics, Springer Netherlands, 1981.
- [150] L. D. Carr, D. R. Dounas-Frazer, and M. A. Garcia-March, “Dynamical realization of macroscopic superposition states of cold bosons in a tilted double well,” *EPL*, vol. 90, p. 10005, 2010.
- [151] L. D. Landau and E. M. Lifshitz, *Quantum mechanics: non-relativistic theory*, vol. 3. Elsevier, 2013.
- [152] S. C. Creagh, “Tunnelling in multidimensional systems,” *J. Phys. A: Math. Gen.*, vol. 27, pp. 4969–4993, Jul. 1994.
- [153] A. N. Kolmogorov, “On the conservation of conditionally periodic motions under small perturbation of the Hamiltonian,” *Dokl. Akad. Nauk SSSR*, vol. 98, pp. 527–530, 1954.
- [154] J. Moser, “On invariant curves of area-preserving mappings of an annulus,” *Matematika*, vol. 6, no. 5, pp. 51–68, 1962.
- [155] V. I. Arnold, “Proof of a theorem of A. N. Kolmogorov on the preservation of conditionally periodic motions under a small perturbation of the Hamiltonian,” *Russ. Math. Surv.*, vol. 18, no. 5, pp. 9–36, 1963.
- [156] V. I. Arnold, *Mathematical methods of classical mechanics*, vol. 60. Springer Science & Business Media, second ed., 1989.
- [157] H. Poincaré, “Sur un théoreme de géométrie,” *Rend. Circ. Mat. Palermo*, vol. 33, no. 1, pp. 375–407, 1912.
- [158] G. D. Birkhoff, “Proof of Poincaré’s geometric theorem,” *Trans. Amer. Math. Soc.*, vol. 14, no. 1, pp. 14–22, 1913.
- [159] S. Tomsovic, M. Grinberg, and D. Ullmo, “Semiclassical trace formulas of near-integrable systems: Resonances,” *Phys. Rev. Lett.*, vol. 75, pp. 4346–4349, Dec. 1995.
- [160] A. Bäcker, R. Ketzmerick, S. Löck, and L. Schilling, “Regular-to-chaotic tunneling rates using a fictitious integrable system,” *Phys. Rev. Lett.*, vol. 100, p. 104101, Mar. 2008.
- [161] J. Kullig, C. Löbner, N. Mertig, A. Bäcker, and R. Ketzmerick, “Integrable approximation of regular regions with a nonlinear resonance chain,” *Phys. Rev. E*, vol. 90, p. 052906, Nov. 2014.
- [162] M. Hiller, T. Kottos, and T. Geisel, “Wave-packet dynamics in energy space of a chaotic trimeric Bose-Hubbard system,” *Phys. Rev. A*, vol. 79, p. 023621, Feb. 2009.
- [163] Y. I. Bogdanov, M. V. Chekhova, S. P. Kulik, G. A. Maslennikov, A. A. Zhukov., C. H. Oh, and M. K. Tey, “Qutrit state engineering with biphotons,” *Phys. Rev. Lett.*, vol. 93, p. 230503, Dec. 2004.
- [164] V. I. Shnyrkov, A. A. Soroka, and O. G. Turutanov, “Quantum superposition of three macroscopic states and superconducting qutrit detector,” *Phys. Rev. B*, vol. 85, p. 224512, Jun. 2012.
- [165] K. Nemoto, C. A. Holmes, G. J. Milburn, and W. J. Munro, “Quantum dynamics of three coupled atomic Bose-Einstein condensates,” *Phys. Rev. A*, vol. 63, p. 013604, Dec. 2000.
- [166] R. Franzosi and V. Penna, “Self-trapping mechanisms in the dynamics of three coupled Bose-Einstein condensates,” *Phys. Rev. A*, vol. 65, p. 013601, Dec. 2001.
- [167] R. Franzosi and V. Penna, “Chaotic behavior, collective modes, and self-trapping in the dynamics of three coupled Bose-Einstein condensates,” *Phys. Rev. E*, vol. 67, p. 046227, Apr. 2003.
- [168] H. Cao, Q. Wang, and L.-B. Fu, “Quantum transition and parity effects of three coupled Bose-Einstein condensates subjected to an artificial gauge potential,” *Laser Phys.*, vol. 25, p. 065501, Jun. 2015.

- [169] A. A. Bychek, P. S. Muraev, D. N. Maksimov, E. N. Bulgakov, and A. R. Kolovsky, “Chaotic and regular dynamics in the three-site Bose-Hubbard model,” *AIP Conf. Proc.*, vol. 2241, p. 020007, 2020.
- [170] L. Dell’Anna, G. Mazzarella, V. Penna, and L. Salasnich, “Entanglement entropy and macroscopic quantum states with dipolar bosons in a triple-well potential,” *Phys. Rev. A*, vol. 87, p. 053620, May 2013.
- [171] G. Pieplow, C. E. Creffield, and F. Sols, “Protected cat states from kinetic driving of a boson gas,” *Phys. Rev. Res.*, vol. 1, p. 033013, Oct. 2019.
- [172] K. Sacha, “Modeling spontaneous breaking of time-translation symmetry,” *Phys. Rev. A*, vol. 91, p. 033617, Mar. 2015.
- [173] Y. Shin, G.-B. Jo, M. Saba, T. A. Pasquini, W. Ketterle, and D. E. Pritchard, “Optical weak link between two spatially separated Bose-Einstein condensates,” *Phys. Rev. Lett.*, vol. 95, p. 170402, Oct. 2005.
- [174] Y. B. Zel’Dovich, “The quasienergy of a quantum-mechanical system subjected to a periodic action,” *Soviet Physics JETP*, vol. 24, no. 5, pp. 1006–1008, 1967.